2014

New Synthetic Strategies for Improved Gas separation by Nanoporous Organic Polymers

Suha Altarawneh
Virginia Commonwealth University

New Synthetic Strategies for Improved Gas Separation by Nanoporous Organic Polymers

A dissertation submitted in partial fulfillment of the requirements for the degree of Doctor of Philosophy at Virginia Commonwealth University

By

Suha S. Altarawneh

M.Sc. at Mutah University, 2004

Director: Dr. Hani M. El-Kaderi

Associate Professor, Department of Chemistry

Virginia Commonwealth University

Richmond, Virginia

August, 2014

Acknowledgments

I would like to express my deepest appreciation for the continued support, encouragement and guidance of Professor Hani M. El-Kaderi, whose ideas and constructive recommendations helped lead to the successful completion of this project. I would also like to offer my sincere appreciation for the learning opportunities provided by my committee members Professor Purusottam Jena, Professor Everett E. Carpenter, and Professor Julio C. Alvarez. I wish to thank Professor Purusottam Jena, and Rosy Behera from the physics department at VCU for their contribution to this project by carrying out DFT calculations, Dr. Indika U. Arachchige and Lamia Nahar from the chemistry department for their help in collecting the photoluminsence data and for the valuable discussions. Special thanks should be given to the chemistry department faculty, staff, and people who helped me to handle the instruments. I am very thankful to the members of the El-Kaderi Group who have been extremely supportive of me during my work. I would like to express my special thanks to Dr. Mohammad Rabbani who established the method of my project under the leadership of Dr. El-Kaderi, Ali Kemal for running TGA, SEM, and XRD measurements, and Timur Islamoglu for training me on the mathematical calculations of the ideal adsorption solution theory (IAST) and heats of adsorption (Q_{st}). Finally, I am grateful to Tafila Technical University-Jordan for their financial support. I would also like to thank my loving sister, Dr. Ruba Darweesh, for her encouragement and support during the rough times over the past four years. I am grateful to my caring, loving, and supportive family and parents, without whose prayers and tears I am sure that reaching this point would not have been possible.

Table of Contents

List of Tables……..vi

List of Figures……..……viii

Abstract…….…xiv

Chapter: 1 Introduction

1.1 Global Energy Concerns and Proposed Solutions……...1

1.2 Current Materials for CO_2 Capture……..……4

1.2.1 Physical Sorbents…….……..7

1.2.2 Adsorption Materials…….……....8

1.3 Functionalized Porous Organic Polymers……..…12

1.4 Benzimidazole-Linked Polymers (BILPs)……...…..15

1.5 Interpenetration Effect and the Control Methods……..……25

1.6 Porosity Measurements, Principles, and Instrumentation……..31

1.7 Theoretical Calculations and Mathematical Methods……34

1.7.1 Heats of Adsorption Calculations……...……..34

1.7.2 Selectivity Calculations……..……..36

1.8 Dissertation Problem…….……..39

Chapter 2: New Insights into Carbon Dioxide Interactions with Benzimidazole-Linked Polymers

2.1 Introduction…….……41

2.2 Experimental and Computational Studies……42

2.3 Results and Discussions……..……48

2.3.1 Porosity Measurements, Gas Uptake and Relate Calculations…..**.....**……...55

2.3.2 Heats of Adsorption Calculations…….61

2.3.3 Selective Gas Uptake Studies……..…….63

2.4 Computational Study……..…….71

2.4.1 Results and Discussions Computational Studies…….…….72

2.5 Conclusions…….…….76

Chapter 3: Acid-Catalyzed Formation of Benzimidazole-Linked Polymers: Impact on Porosity and Selective Gas Admission and Uptake

3.1 Introduction……..……77

3.2 Experimental……..……..78

3.3 Results and Discussions……..…….80

3.3.1 Impact of Acid-Catalyzed Process on Porosity……...….89

3.3.2 Porosity Measurements and Gas Uptakes…….……94

3.4 Gas Selectivity Studies…….…….101

3.5 Conclusions……..…..105

Chapter 4: Highly Porous and Photoluminescent Pyrazine-Derived Benzimidazole-Linked Polymers

4.1 Introduction…….……..…..106

4.2 Experimental……..107

4.3 Results and Discussions……...……..109

4.3.1 Porosity and Low Pressure Gas Uptake Measurements..……...…121

4.3.2 Gas Selectivity Studies……..….131

4.4 Photoluminescence Study……..……136

4.4.1 Experimental Methods and Measurements…….……...137

4.4.2 Results and Discussions……..…138

4.5 Conclusions……..…...……...141

Chapter 5: Alkoxy-Functionalized Benzimidazole-Linked Polymers

5.1 Introduction……..……..142

5.2 Experimental……..……143

5.3 Synthesis of Alkoxy-Functionalized BILPs…….……..……154

5.4 Alkoxy-Functionalized BILP-14-OR Derivatives……...……..155

5.4.1 Results and Discussions……. 158

5.4.2 Porosity and Low Pressure Gas Uptake Measurements.……..…..168

5.4.3 Gas Selectivity Studies……..…….181

5.5 Alkoxy-Functionalized BILP-15-OR Derivatives……...……..187

5.5.1 Results and Discussions…….…….190

5.5.2 Porosity and Low Pressure Gas Uptake Measurements…….…199

5.5.3 Gas Selectivity Studies……...……212

5.6 Conclusions……..……..218

Chapter 6: Conclusions……...…….…….……219

References…….…….....……222

Vita……..…….…….……..240

List of Tables

1.1: Typical gas composition (by wt) in post- and pre-combustion process……..….3

1.2: Gas Uptake and Selectivity data of all Reported BILPs……..…24

2.1: Gas sorption uptakes of BILP-14 and BILP-15……..59

2.2: Surface areas and heats of Adsorption of BILP-14 and BILP-15……..……61

2.3: Initial slope and IAST selectivity of BILP-14 and BILP-15 ……..…..……..70

2.4: CO_2 Binding energies calculated at the LDA/6-311+G* and M06/6-311+G* and the Atomic charges on C-atom of CO_2 and N-atom of the imidazole…….....……..75

3.1: The impact of different acid concentrations on the porosity of BILP-16C at 1:1 HCl/DAB……91

3.2: The impact of different acid concentrations on the porosity of BILP-16C at 2:1 of HCl/DAB ……...…….……92

3.3: Impact of different HCl:DBA mole ratios on the porosity of BILP-16C at constant acid concentration……..93

3.4: BET values for non-catalyzed and acid-catalyzed BILPs calculated from Ar adsorption isotherms at 87 K……..……..……...97

3.5: Gas uptake and Heats of adsorptions of acid-catalyzed and non-catalyzed BILPs……..100

4.1: BET and Langmuir values pyrazine-derived BILPs were calculated from Ar adsorption isotherms at 87 K……..…123

4.2: Initial slope selectivity of pyrazine-derived BILPs at 273 K (298 K)……..130

4.3: Gas Uptake and heats of adsorption data of pyrazine-derived BILPs……..…132

5.1: BET values for BILP-14 and BILP-14-OR derivatives calculated from Ar adsorption isotherms at 87 K…….....172

5.2: IAST and initial slope selectivity of BILP-14 and BILP-14-OR derivatives…….....182

5.3: Gas Uptake and heats of adsorption data of BILP-14 and BILP-14-OR derivatives…….186

5.4: BET and Langmuir surface areas for BILP-15 and BILP-15-OR derivatives calculated from the Ar adsorption isotherm at 87 K……..**.....**….....203

5.5: Initial slope selectivity of BILP-15 and BILP-15-OR derivatives at 273 K (298 K), and the IAST selectivity of BILP-15 and BILP-15-OR derivatives at 298 K for the binary mixtures of (CO_2/N_2: 10:90) and (CO_2/CH_4: 50:50)……..….213

5.6: Gas Uptake and heats of adsorption data for BILP-15 and ILP-15OC derivatives……..217

List of Figures

1.1: New materials and technologies for CO_2 capture……...5

1.2: (A) BET surface area, small gas uptakes, selectivity values, and heat of adsorptions of reported Benzimidazole-Linked Polymers……23

1.3: Different degrees of interpenetration in three different network topologies observed using very similar ligands……..……..…30

1.4: Schematic Representation for a quantachrome Autosorb IQ2 Low Pressure Sorption Instrument……..…34

2.1: Suggested interactions between CO_2 and the imidazole moieties in BILPs……..…41

2.2: ^{1}H-NMR and ^{13}C-NMR of 1,2,4,5-Tetrakis-(4-formylphenyl)benzene……....45

2.3: Scanning electron microscopy images of BILP-14 and BILP-15……..…50

2.4: X-ray diffraction pattern (XRD) and Thermogravimetirc analysis (TGA)……...…..…51

2.5: FT-IR spectra of BILP-14 and BILP-15 (4500-500 cm^{-1})……..……...…53

2.6: Solid state ^{13}C CP-MAS NMR spectra of BILP-14 and BILP-15……..……54

2.7: Argon isotherms and pore size distribution of BILP-14 and BILP-15……..……..56

2.8: BET plots for BILP-14 and BILP-15 ……57

2.9: CH_4, CO_2 and H_2 uptake isotherms for BILP-14 and BILP-15……..…60

2.10: Heats of adsorption of H_2, CH_4 and CO_2 for BILP-14 and BILP-15 from the virial analysis……...……62

2.11: Gas sorption capacities for BILP-14 and BILP-15……..……..64

2.12A: The initial slope calculations for BILP-14……..…65

2.12B: The initial slopecalculations for BILP-15…….……...…..66

2.12C: IAST selectivities of CO_2/ CH_4 for 50/50 and CO_2/ N_2 10/90 at 298 K for BILP-14 and BILP-15……..69

2.13: Fully optimized geometries of BILPs-CO_2 interactions calculated at M06/6-311+G* level of theory……..……...……73

3.1: Thermogravimetric analysis (TGA) of BILP-15, BILP-16, BILP-15C, and BILP-16C……...……..84

3.2: FT-IR spectra of BILP-15, BILP-16, BILP-15C and BILP-16C and their starting building units……..……...……85

3.3: Solid state ^{13}C CP-MAS NMR spectra for BILP-16…….……86

3.4: Scanning electron microscopy (SEM) images BILP-15, BILP-15C, BILP-16, and BILP-16C…….……..……..87

3.5: X-ray diffraction pattern (XRD) for BILP-15C, BILP-16 and BILP-16C…….88

3.6: Possible rotations around the imidazole rings in rigid BILP-14 and flexible BILP-15 and BILP-16……..……...…….89

3.7: Porosity of BILP-16C at different acid concentrations and different HCl:DAB mole ratios…….……..91

3.8: Argon isotherms and pore size distribution of acid-catalyzed and non-catalyzed BILPs…….……96

3.9: BET surface area plots for non-catalyzed and acid-catalyzed BILPs…….97

3.10: Gas uptake isotherms: CO_2 and CH_4 at 273/298 K, and H_2 at 87/77 K……...98

3.11: Heats of adsorption of acid-catalyzed and non-catalyzed BILPs……...…..…99

3.12: Gas sorption capacities for BILP-15C, BILP-16C, and BILP-16…….…….102

3.13: Adsorption selectivity of CO_2 over N_2 and CH_4 for BILPs from initial slope calculations for BILP-15C, BILP-16C, and BILP-16……..103

3.14: IAST selectivity data for CO_2/N_2 and CO_2/CH_4 at different binary mixture ratios for BILP-15, BILP-15C, BILP-16, BILP-16C……..……..……104

4.2: Thermal gravimetric profiles of pyrazine-derived BILPs measured under N_2 air and Pattern X-ray diffraction of pyrazine-derived BILPs…….…….….112

4.3: SEM images of BILP-17, BILP-18, BILP-19, and BILP-20……..…….….113

4.4: FT-IR spectra of BILP-17 and its corresponding starting materials……..…..115
4.5: FT-IR spectra of BILP-18 and its corresponding starting materials in the range (A) (4100-500 cm^{-1}) and (B) (2200-500 cm^{-1})…….……...…..116

4.6: FT-IR spectra of BILP-19 and its corresponding starting materials in the range (A) (4100-500 cm^{-1}) and (B) (2200-500 cm^{-1})…….……...……..117

4.7: FT-IR spectra of BILP-20 and its corresponding starting materials in the range (A) (4100-500 cm^{-1}) and (B) (2200-500 cm^{-1})…….……...……..118

4.8: Solid state ^{13}C CP-MAS NMR spectra of (A) BILP-17, (B) BILP-18, (C) BILP-19, and (D) BILP-20……..…….….120
4.9: Ar adsorption isotherms for pyrazine-derived BILPs were measured at 87 K…….122

4.10: BET plots and Langmuir surface area for pyrazine-derived BILPs……..….123

4.11: Pore Size Distribution of pyrazine-derived BILPs was calculated from the Ar adsorption isotherms……..……..…..124

4.12: CO_2, CH_4, and H_2 gas uptake isotherms for pyrazine-derived BILPs at 273 K and 298 K……...……...…….126

4.13: Isosteric heats of adsorption (Q_{st}) for pyrazine-derived BILPs ……....129

4.14: Gas sorption capacities of pyrazine-derived BILPs…….……..133

4.15: Initial slope calculations of pyrazine-derived BILPs and the adsorption selectivity of CO_2 over N_2 and CH_4 at 273 K……134

4.16: IAST selectivity data for CO_2/N_2 and CO_2/CH_4 at 273 K and different binary mixture ratios for BILP-17, BILP-18, BILP-19, and BILP-20……..……...……..135

4.17: The structures of Phenazine-tetraamine, BILP-17 and BILP-18……...….136

4.18: UV-visible absorption, and emission, spectra of the BILP-17 BILP-18 and the corresponding monomer units……..……139

5.1A: ^{1}H-NMR and ^{13}C-NMR of $(OMe)_2$TFPB……..150

5.1B: ^{1}H-NMR and ^{13}C-NMR of $(OEt)_2$TFPB……...….151

5.1C: ^{1}H-NMR and ^{13}C-NMR of $(OBu)_2$TFPB……..….152

5.1D: ^{1}H-NMR and ^{13}C-NMR of $(OBu)_2$TFPB……...……..153

5.2: Molecular building units of alkoxy-functionalized BILPs……...……154

5.3: Thermal gravimetric profiles of BILP-14 and BILP-14-OR derivatives measured under N_2……..……...……161

5.4: SEM images of BILP-14 and BILP-14-OR derivatives…….....…..162

5.5: FT-IR spectra of BILP-14 and BILP-14-OR derivatives and their aryl-aldehydes starting building units…….…….…….165

5.6: Solid state ^{13}C CP-MAS NMR spectra of BILP-14-OR derivatives……..……..167

5.7: Ar adsorption isotherms for BILP-14 and BILP-14-OR derivatives ……...…....171

5.8: BET surface area plots for BILP-14 and BILP-14-OR derivatives……...……..….172

5.9: Pore Size Distribution of BILP-14 and BILP-14-OR derivatives were calculated from the Ar adsorption isotherms……...…….173

5.10A: CO_2 uptake isotherms of BILP-14 and BILP-14-OR derivatives at 273 K and 298 K……...……...……...175

5.10B: CH_4 uptake isotherms of BILP-14 and BILP-14-OR derivatives……...……...…..178

5.10C: H_2 uptake isotherms of BILP-14 and BILP-14-OR derivatives …….....……179

5.11: CO_2, CH_4 and H_2 isosteric heats of adsorption (Q_{st}) for BILP-14 and BILP-14-OR derivatives……..……..180

5.12A: Gas sorption capacities for BILP-14-OMe and BILP-14-OEt derivatives and the adsorption selectivity of CO_2 over N_2 and CH_4 from initial slope calculations……..….183

5.12B: Gas sorption capacities for BILP-14-OBu and BILP-14-OiBu derivatives and the adsorption selectivity of CO_2 over N_2 and CH_4 for from initial slope calculations.....…..184

5.13: IAST selectivities of CO_2/ N_2 10/90 and CO_2/ CH_4 for 50/50 binary mixtures at 298 K for BILP-14 and BILP-14-OR derivatives……...…….…….185

5.14: Thermal gravimetric profiles of BILP-15 and BILP-15-OR derivatives measured under N_2…….…….192

5.15: SEM images of BILP-15 and BILP-15-OR derivatives……...……..193

5.16: FT-IR spectra of BILP-15 and BILP-15-OR derivatives and their aryl-aldehydes starting building units……..…….……196

5.17: Solid state ^{13}C CP-MAS NMR spectra of BILP-15-OR derivatives……..……198

5.18: Ar adsorption isotherm for BILP-15 and BILP-15-OR derivatives ……...…...202

5.19: BET plots for BILP-15 and BILP-15-OR derivatives calculated from the Ar adsorption isotherm at 87 K……...……..……..203

5.20: The Pore Size Distribution of BILP-15 and BILP-15-OR derivatives…..……...……..204

5.21A: CO_2 uptake isotherms of BILP-15 and BILP-15-OR derivatives …….……..206

5.21B: CH_4 uptake isotherms of BILP-15 and BILP-15-OR derivatives……207

5.21C: H_2 uptake isotherms of BILP-15 and BILP-15-OR derivatives …….…….208

5.22: CO_2, CH_4 and H_2 isosteric heat of adsorption (Q_{st}) for BILP-15 and BILP-15-OR derivatives……..……..211

5.23: Gas sorption capacities for BILP-15 and BILP-15-OR derivatives and the adsorption selectivity of CO_2 over N_2 and CH_4 from initial slope calculations……...……215

5.24: IAST selectivities of CO_2/ N_2 10/90 and CO_2/ CH_4 for 50/50 binary mixtures at 298 K for BILP-15 and BILP-15-OR derivatives……..……..216

Abstract

NEW SYNTHETIC STRATEGIES FOR IMPROVED GAS SEPARATION BY NANOPOROUS ORGANIC POLYMERS

Suha S. Altarawneh, Ph.D.

A dissertation submitted in partial fulfillment of the requirements for the degree of Doctor of Philosophy at Virginia Commonwealth University.

Virginia Commonwealth University, 2014

Director: Dr. Hani M. El-Kaderi, Associate Professor, Department of Chemistry

The emission of carbon dioxide (CO_2) from fossil fuel combustion is a major cause of climate change. Therefore, the efficient separation of CO_2 from mixtures of gases such as flue gas and impure sources of CH_4 (e.g. natural gas and landfill gas) is an essential step in meeting the ever increasing demands on natural gas and creating a cleaner environment. Carbon capture and storage technology (CCS) is one of the methods employed for gas separation using chemisorption and/or physisorption processes. Several materials such as porous polymers and amine solutions have been used as gas adsorbents. However, the amount of energy required for the adsorbent regeneration is one of the main concerns that needs to be addressed. In this regard, porous organic polymers (POPs) with defined porosity and preferential binding affinity for CO_2 over N_2 and CH_4 are some of the most attractive materials that could fulfill the above requirement and are also applicable for use in gas storage and separation. Suitable POPs that can be used for gas storage applications need to have high porosity and mechanical stability under high pressure conditions (~100 bar). Alternatively, the most effective POPs in gas separation are

those that have preferential binding affinity for CO_2 over other gases present at low pressure settings. In all cases, the chemical nature of POPs and their textural properties are key parameters, however, the modest surface area of most POPs limits their efficiency.

With the above considerations in mind, the aim of our research is to develop benzimidazole–linked polymers (BILPs) that have variable porosity levels and chemical functionality to enhance gas separation (CO_2/CH_4, CO_2/N_2). We have established new synthetic routes that utilize polycondensation reactions between aryl-aldehydes and aryl-o-diamine building units to construct new BILPs with improved gas separation properties. Our strategy targeted structural and textural modifications of BILPs. We used longer linkers (building units) to improve porosity; however, the flexible linkers offered only low porosity due to network interpenetration. To overcome this challenge, a more controlled network growth rate was assessed by adjusting imine-bond formation rates through different acid loading. The acid, HCl, was used to catalyze imine-bond formation. The new resulting acid-catalyzed BILPs have shown an improved porosity up to 92% compared to the non-catalyzed BILPs. We also used the "rational ligand design" approach to introduce new functionalities into BILPs (-OR) to alter the hydrophobic nature of their pores. In this regard, we have illustrated the applicability of this strategy to BILPs containing flexible aryl-o-diamine linkers. The bulky alkoxy groups were incorporated into the aryl-aldehyde building unit prior to polymerization. The resulting polymers have proven that the presence of the bulky pendant alkoxy-chains plays a significant role during the polymerization process which allows for increased control over network formation, and in turn, porosity. Sorption measurements, selectivity, and heats of adsorption data have confirmed the positive impact of the alkoxy-groups and shown that varying the pendant groups is a promising method for designing highly porous BILPs.

In addition to pore functionalization with alkoxy-chains, we used pi-conjugated and N-rich building units to prepare new BILPs that have semiconducting properties in addition to their porous nature. This class of BILPs has shown that the extended-conjugated system improved BILPs electronic properties. The other studies performed in this research, involved the use of DFT theory to investigate CO_2/BILPs interaction sites and binding affinities. The computational outcomes of DFT have shown that (C-H) bond of the aryl system is a possible site for CO_2 interaction beside the free-N side and hydrogen bonding. All new polymers were characterized by spectral and analytical characterization methods and their sorption data were collected to evaluate their capability as candidates for gas separation applications.

Chapter 1

Introduction

1.1 Global Energy Concerns, Sources and Proposed Solutions

The escalating level of atmospheric carbon dioxide (CO_2) generated from the anthropogenic emissions is one of the major economic and environmental concerns in this age.[1] The predominant source of these emissions is the combustion of oil, coal and natural gas, which has generated approximately 80% of CO_2 emission worldwide between 1970 and 2004.[1b] This high percentage is also projected to continue to increase, especially in developing nations, due to economic and industrial growth.[2] Thus, finding efficient strategies to overcome this issue and reduce the global atmospheric concentration of greenhouse gases becomes an urgent project. In the long term, one of the most vital solutions is finding alternative fuel sources.

Renewable energy sources are greatly preferred because of their abundance and their minimal negative environmental impact, such as natural gas (NG)[3] and /or hydrogen (H_2).[4] Hydrogen is among the most promising alternative fuels, especially in automobile applications; it is abundant and burns cleanly in fuel cells to generate only electricity and water as byproducts.[5] However, the high density of the liquid hydrogen (70.8 g L^{-1}),[6] and the safety concerns of the gaseous hydrogen are significant challenges that prevent the worldwide use. Accordingly, extensive efforts are being made to study H_2 storage systems using chemical hydrides,[7] and metal hydrides.[8] However, these systems are problematic due to their irreversible hydrogenation-dehydrogenation nature,[9] which makes the need to find other alternative systems even more pressing.

On the other hand, natural gas (NG) consists of methane (> 95%) and a mixture of ethane, nitrogen, carbon dioxide and heavier hydrocarbons. As such it has the lowest carbon-footprint among all petroleum-based fuels. However, several limitations have been encountered in the widespread use of (NG), such as the requirements for liquefaction of the gas, with temperatures reaching -82 ºC and compression to 200-300 bar, preventing its use as an alternative fuel.[3] Other short term proposed mechanisms were considered to reduce the effect of CO_2 emission including: (1) increasing the reduction efficiency up to 20%, (2) co-firing biomass with coal up to 10% and most importantly, (3) employing carbon capture and storage technology (CCS). The CCS technology is the central strategy of these scenarios. It offers the chance to meet fossil fuel needs in the long term, reduces the emission of CO_2 and hence, suppresses global warming.[10]

This technology allows the continued use of fossil fuels without release of CO_2 to the atmosphere by separation and purification of the gas from the combustion process and application of a long term disposal process such as a geological storage system. CCS is subdivided into different technologies including pre- and post-combustion capture and oxyfuel combustion processes.[11] In post-combustion technology, CO_2 is selectively removed from flue gas, which consists of CO_2 (15-16%) and N_2 (70-75%) along with other impurities such as hydrocarbons and inorganic components (SO_x, NO_x, HCl, Hg) among others (Table 1.1).[12] Therefore, the stream of gas will contain a wide range of solid and gaseous components. In the Pre-combustion capture, the process produces a high pressure gas containing H_2 and CO_2, which can be easily separated compared to CO_2 and N_2 in the post-combustion process (Table 1.1).[13]

Table 1.1: Typical gas composition (by weight) in post-combustion and pre-combustion processes

Composition	Post-combustion	Pre-combustion
N_2	70-75%	0.25%
CO_2	15-16%	35.5%
H_2O	5-7%	0.2%
O_2	3-4%	-
H_2	-	61.5%
SO_x	< 800 ppm	-
NO_X	500 ppm	-
H_2S	100 ppm	1.1%
Conditions :Temperature and pressure	50-75 ºC, 1 bar	40 ºC, 30 bar

Once CO_2 is separated from the gas mixture, H_2 will be ready for use in fuel cell applications.[14] The significant advantage of pre-combustion capture over the post-combustion is that the higher component concentrations and elevated pressures reduce the energy capture penalty of the process to 10–16 %, roughly half that for post-combustion CO_2 capture.[13a] Oxyfuel process is a separation process, which refers to the ignition of coal or any other carbon-base fuel in a pure O_2 environment where nitrogen is completely excluded from the combustion process through a preliminary air separation step. The main difference and advantage in this process over the post- and pre-combustion processes is that the combustion output is entirely CO_2, which simplifies the capture step of the gas. However, each technology faces challenges and limitations when attempting to meet the CO_2 capture demands. For post-combustion capture, the low pressure application (up to 1 bar) and low CO_2 concentration of the flue gas require a high volume of gas

to be treated, as a result, additional energy is required to compress the captured CO_2 and a high energy input is required for the regeneration of the sorbent. In the case of pre-combustion capture, the main drawback includes poor availability and operability, especially for a large scale operation including multi-operational steps, which results in a high cost process. For oxy-fuel combustion capture, the technology is still at a developmental stage and the use of pure oxygen in the air-separation process consumes significant energy.[15] Thus, to overcome these limitations, new technologies and materials need to be developed to improve the CO_2 capture.

1.2 Current Materials for CO_2 Capture

Several classes of materials have been developed to date, to meet the requirements of high performance CO_2 capture configurations for installation in coal- and gas-fired power plants. Examples of these materials include: aqueous alkanolamine solutions, physical absorbents, adsorption on solids using pressure and/or temperature swing adsorption processes, membranes, cryogenic distillation, gas hydrate formation, and chemical-looping combustion using metal oxides (Figure 1.1).[15c]

To design these materials some specific parameters should be tuned to fulfill the CO_2 capture requirements.[15c] The most crucial performance parameters for any CO_2 capture material are the selectivity toward CO_2 and low heat capacity. Optimization of these parameters should minimize the energy penalty and the cost of CO_2 capture to allow the designed materials to be applicable for CO_2 capture and separation processes.[1b]

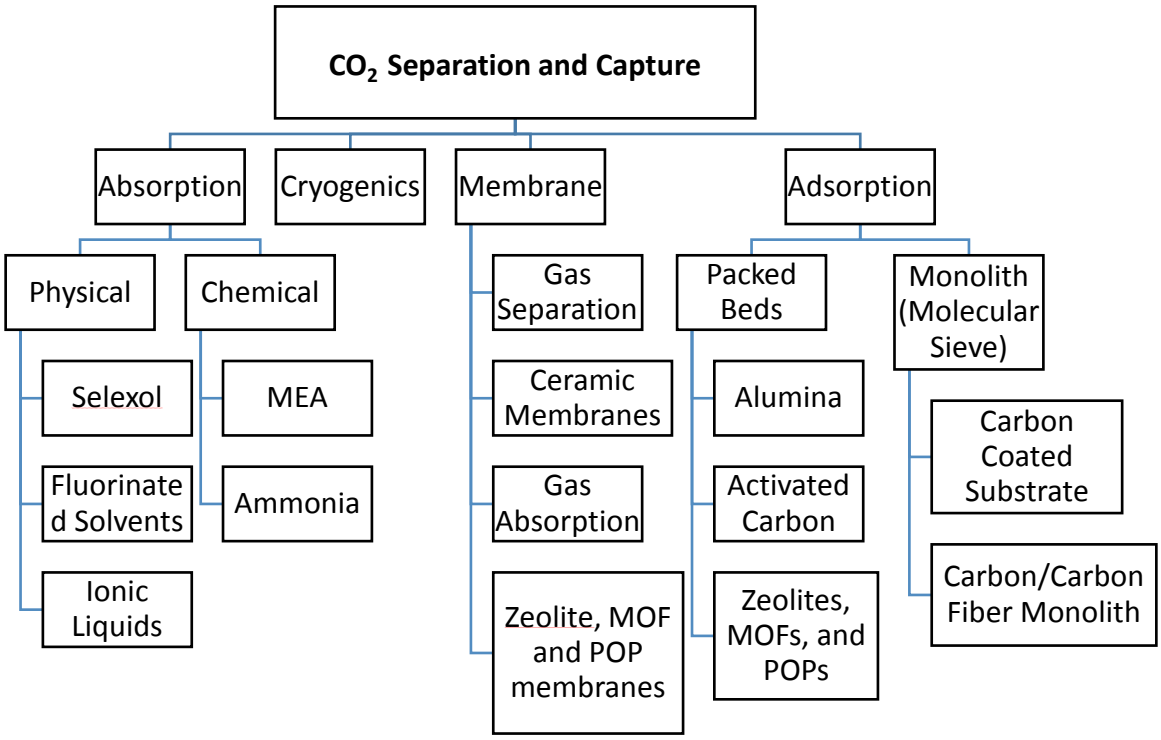

Figure 1.1: New Materials and technologies for CO_2 capture

Aqueous alkanolamine (~ 30% in H_2O) as "amine solvent scrubbing"[16] is one of the most established technologies that has been used in post-combustion CO_2 capture from flue gas.[3-5, 17] These absorbents are widely used for CO_2 capture and the process depends on the formation of a C-N bond from the nucleophilic attack of the amine on the CO_2 carbon to generate carbamate or bicarbonate as shown in Scheme 1.1.[1b, 18]

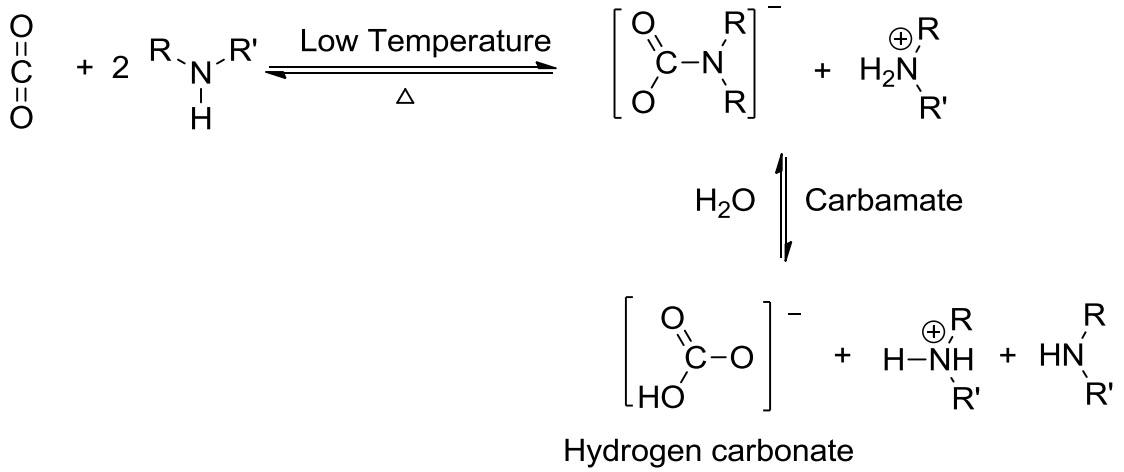

Scheme1.1: General reaction scheme for the chemical absorption of CO_2 by secondary amine

The formation of the C-N bond allows the CO_2 capture by alkanolamines to fall into the chemisorption regime where the enthalpy of absorption lies in the range of -50 to -100 kJ mol^{-1}.[19] Alkanolamines have several significant limitations as adsorbents for large-scale CO_2 capture. These drawbacks are related to, (1) high energy consumption for the materials regeneration in which the material should be heated to liberate CO_2, which leads to high energy penalty,[20] (2) low absorption/desorption rate; (3) solvent loss due to degradation and evaporation during regeneration processes, as a result of the presence of the SO_x and NO_x by-product in flue gas stream, and (4) corrosion caused by the high pH liquid amine solution.[13b] On the other hand, a low amine concentration will introduce a high volume of water to the system, which must be heated in order to regenerate the material and reduces CO_2 capture capacity.

Thus, several strategies have been proposed to overcome these limitations, such as: the use of liquids with lower heats of adsorption, increasing the concentration of the adsorbent molecules and improving the mass transfer and reaction kinetics. Therefore, the use of substituted amines (e.g. secondary and tertiary)[14] amine-based molecules with lower regeneration temperatures has been considered for chemical absorption in order to make the regeneration step for the amines more viable. To address these limitations, physical sorbents and adsorption materials have been designed to be more applicable for the post- and pre-combustion and the oxyfuel processes.

1.2.1 Physical Sorbents

Using physical absorbents, in which the solvent binds selectively to CO_2 at high partial pressure and low temperature, is a promising alternative to the use of chemical absorption. Ionic liquids are a class of physical solvents consisting of combinations of large organic cations and smaller inorganic anions with high viscosity near room temperature that are well known for selective CO_2 absorption.[21] They are non-flammable, environmentally benign, thermally stable solvents and have extremely high vapor pressure. The gas capture mechanism is based on physisorption (Van der waal). This process involves weak association between the ionic liquid and CO_2 molecules with heats of adsorption about -11 kJ mol^{-1}. Thus, minimal energy is required for the solvent regeneration.[13a, 22] However, it should be mentioned that some ionic liquids react with both CO_2 and SO_2 in a chemisorption fashion (covalent bonding) and, hence, they are applicable for removing CO_2 and SO_2, which may not be considered advantageous due to the requirement of more additional steps for CO_2 separation from SO_2. However, the high viscosity of the solvents minimizes solvent loss from the gas stream and that limits the mass transfers and

lowers the rate of absorption. To overcome this limitation the introduction of functional groups such as amines has been suggested to enhance CO_2 capture at low pressure settings (up to 1 bar).[23]

1.2.2 Adsorption Materials

Solid physical adsorbents are solid materials that exist as packed or fluidized adsorbent beds and possess significant advantages for energy efficiency compared to chemical and physical absorption approaches.[24] The CO_2 adsorption process can be divided into either physisorption or chemisorption interactions between the gas molecules and the surface of a material. Physisorption is the adsorption mechanism wherein the gas molecules are attracted to the pore and the surface of the sorbent by van der Waals forces, and have a low heat of adsorption that is only slightly greater than the heat of sublimation of the adsorbate. In contrast, in chemisorption interactions, the adsorbate molecules undergo a chemical reaction to bind to certain sites on the sorbent covalently with a much greater heat of adsorption, roughly equal to the heat of reaction.[25] Thus, to take advantage of the chemisorption and physisorption processes, the main target is to design materials that combine high CO_2 binding affinity and low heat of regeneration.

The most promising materials to fulfill these requirements are porous solid adsorbents. Porous solid adsorbents can be organic-inorganic hybrid materials classified according to pore size (microporous < 2 nm, mesoporous 2-50 nm and macroporous materials > 50 nm).[26] Moreover, porous materials can be divided into crystalline and amorphous materials,[27] according to their solid pattern. Crystalline materials have well-ordered structures and uniform pore sizes, while amorphous materials have disordered structure and a wider pore size range. Different classes of organic and inorganic porous materials, with diverse variety in their building blocks

and porosity ranges, have been synthesized and investigated as candidates for CO_2 capture and separation applications. Examples include: zeolites,[28] activated carbons,[29] metal organic frameworks (MOFs),[30] and porous organic polymers (POPs).[31] Zeolites are porous aluminosilicate materials that possess high chemical and thermal stability. They have been evaluated by studying the hydrogen and CO_2 separation using high pressure settings.[32]

Most of the moderate surface area and microporous zeolites have shown promising CO_2 capture capabilities at room temperature such as zeolite 13X, which has relatively high surface area (726 m^2 g^{-1}). It has been proven that the variety of compositions, the structural, and the chemical features of different zeolites play a significant role in affecting the material adsorption performance. However, zeolites are expensive and difficult to produce on a large scale. Also, many of the well-known zeolites become readily saturated with water vapor from the flue gas, which reduce their CO_2 capacity.[28] It is worthwhile to mention that the CO_2 adsorption temperature (normally < 60 °C) of these materials is slightly lower than that of real flue gases (normally ~90 °C), and the current choice is to first cool down the flue gas, which is also energy consuming and makes the overall process less efficient.

Therefore, developing new classes of CO_2 adsorbents with high capacity, high selectivity, and high regenerability in an energy efficient method and at moderate temperatures is highly recommended. The required materials should have CO_2 capacity of 3-4 mmol g^{-1} under ambient conditions to be competitive with alkanolamine technology, also they need to bind to CO_2 selectively over other flue gas components.[33]

Activated carbons are amorphous porous materials prepared by pyrolysis of various carbon-containing resins, fly ash, or biomass.[29] These materials have low CO_2 capacities at lower pressure compared to zeolites due to their high porosity and non-functionalized pores, which

leads to lower binding affinity. In contrast, porous activated carbons have high surface area and can store significant amounts of CO_2 at high pressure. Two advantages should be considered for activated carbons over zeolites, the hydrophobicity of porous carbons, which are not affected by hydrated conditions,[34] and the lower heat of adsorption, which will lower the amount of heat required for materials regeneration.

In addition to the carbon-based materials and zeolites, other classes of porous materials have been considered as potential CO_2 adsorbents including: covalent-organic frameworks (COFs),[35] porous organic polymers (POPs),[31] and MOFs.[17, 36] MOFs are hybrid organic-inorganic porous materials that can capture CO_2, particularly at higher pressures (>15 bar) due to their adjustable pore functionality and high porosity.[1a, 17, 37] Moreover, they have a tunable pore surface, which facilitates CO_2 binding and requires a minimum amount of energy for material regeneration. MOFs have a strong accessibility for pore and surface functionalization by incorporating new heterogeneous functionality through post-synthetic modification, without affecting the porosity.

However, the working temperature of MOFs is still below the range of the gas adsorption temperature in the actual systems, for instance, the temperature swing adsorption.[38] The chemical and physical stability of MOFs is generally lower than that of zeolites and other porous inorganic solids due to the weak coordination bonds between the metal and the ligand.[39] Furthermore, they need to be handled carefully under inert atmosphere due to their high air and moisture sensitivity. Thus, the main target in this field is to design highly porous and pore functionalized materials that have attractive properties for gas capture inside the pores and selective uptake of CO_2 over the other flue gas components.[40] Porous organic polymers, or nanoporous organic polymers[35, 41] are another branch of porous materials that found applications in areas of storage,[42] separation,[43]

and catalysis.[44] The use of the nanoporous texture encompasses the micro- and the meso-porous materials. POPs include several sub-classes of materials such as: COFs,[45] hyper-crosslinked polymers (HCPs),[46] conjugated microporous polymers (CMPs),[47] and polymers of intrinsic microporosity (PIMs).[48] All of these materials are promising candidates for gas storage and separation due to their high porosity, high surface areas, low density, and high chemical and physical stability.[5, 31, 43, 49]

COFs are, highly porous microcrystalline materials, synthesized from organic monomers linked by strong covalent bonds such as: B-O, C-N, and B-N bonds. The first, and the simplest, network of COFs is COF-1, which has been synthesized via the self-condensation of benzene-1,4-diboronic acid.[45] COFs can be synthesized as 2D or 3D frameworks, while their 2D networks exhibit favorable π–π stacking interactions that can enhance the network interpenetration and hinder the accessibility of boron sites.[45, 50] Recently, El-Kaderi et.al. has synthesized a new 2D triptycene-based porous material, possessing a mesoporous network with high surface area, accessible boron sites, and enhanced gas storage capacity.[51] However, this class of polymers, especially B-O linked COFs, requires inert conditions for handling due to the reversible nature and the moisture sensitivity of the B-O bond. They have shown remarkable capacities for H_2, CO_2, and CH_4 gas storage at high pressure settings.

In particular, the selective uptake of CO_2 over CH_4 or N_2 is believed to arise from enhanced CO_2 framework interactions through hydrogen bonding and/or dipole-quadrupole interactions.[52] Hypercrosslinked polymers (HCPs) are a large group of materials developed by extending the crosslinking of the networks to enhance their rigidity and prevent their collapse. On the other hand, conjugated microporous polymers (CMPs) are considered a subclass of hypercrosslinked polymers, while they differ only in the content of multiple C-C bonds and/or

aromatic rings that form the extended conjugated network.[53] The first reported CMPs were synthesized by using Sonogashira-Hagihara palladium coupling to link aromatic halides with aromatic alkynes and form poly(aryleneethynylene) (PAE).[54]

Consequently, series of CMPs were synthesized and resulted in surface areas in the range of 522-834 $m^2 g^{-1}$. The high porosity, structure rigidity, and stability of HCPs, CMPs, and PIMs allow for potential use of these materials for gas storage and separation applications. For instance, PPN-4 has the records of the highest surface area (6460 $m^2 g^{-1}$) and high capacity for CO_2 at high pressure settings among all known POPs.[55] Furthermore, the introduction of other functionalities to the backbone of PPN-4 resulted in PPN-6-SO_3H (1254 $m^2 g^{-1}$),[56] PPN-6-SO_3Li (1186 $m^2 g^{-1}$),[56] and PPN-6-CH_2DETA (555 $m^2 g^{-1}$),[57] which exhibit improved CO_2 captures and heats of adsorption. It was notable that the incorporation of the new functional groups in MOFs or POPs has improved the CO_2 capture by adding new surface atoms that act as adsorption sites and provide alteration of the electronic structure (e.g. polarity and polarizability of the organic linkers). However, it increased the density of the materials, which leads to a decrease in the gravimetric adsorption capacity of the polymers and, hence compromises the high porosity.[58] Combining a high porosity and high CO_2 binding affinity is still challenging for POPs and new strategies to design suitable materials are required to achieve these targets.

1.3 Functionalized Porous Organic Polymers

The introduction of new functional groups to the surface and the pores of POPs is one of the most vital modification steps, which has been applied to improve CO_2 capture and binding affinity. Thus, the strategies that have been investigated to achieve these goals are as follows: (1) providing more CO_2 interaction sites on the surface and in the pores of the networks by increasing the surface area; and (2) improving the heats of adsorption (binding affinity to CO_2).

The second strategy was accomplished by introducing new functionalities, and/or by engineering the pore size of the materials.[59] However, improving the CO_2 capture by increasing the surface area of the polymer to produce large pores and non-functionalized surface is only effective at high pressure settings and in CO_2 pre-combustion technology. For example, the highest surface area PPN-4 (6460 m^2 g^{-1}) and PPN-6 (4023 m^2 g^{-1}), or PAF-1 (5600 m^2 g^{-1}) have a reported excess CO_2 of (38.86 mmol g^{-1} at 295 K and 50 bar) and (29.55 mmol g^{-1} at 298 K and 40 bar), respectively.[59a] On the other hand, the introduction of pore functionality has improved the CO_2 uptake and lowered the surface area of the polymers under the same conditions. For example, the surface area and CO_2 uptake of PPN-6-SO_3H is 1254 m^2 g^{-1} and 3.60 mmol g^{-1} at 1 bar, while for the non-sulfonated PPN-6 it is 4023 m^2 g^{-1} and 1.16 mmol g^{-1} at 1 bar.

Other functionalized POPs have shown high heats of adsorption and moderate to low surface area. Examples of these POPs, including their surface areas and heats of adsorption, are conjugated microporous polymers such as: CMP-NH_2CH_3, 653 m^2 g^{-1}, 26.5 kJ mol^{-1}, CMP-1-NH_2, 710 m^2 g^{-1} and 29.5 kJ mol^{-1}, and CMP-1-COOH, 522 m^2 g^{-1} and 32.6 kJ mol^{-1}.[24] The series of the functionalized PPN-6 and CMP-1 polymers have shown a tradeoff between CO_2 uptake, binding affinity, and porosity. In general, the pore functionalization avenues are subdivided into pre- (as-synthesized) and post-synthesis functionalization processes. In the functionalized PPN-6 and CMP-1 the new polymers were accomplished by the post-synthetic avenue, which loads the network with new functionality and lowers the porosity. On the other hand, other examples of adamantane-based microporous polymers have displayed that the impact of the functionality on the CO_2 uptake and porosity depends on the length of linker and the bulkiness of the functional groups.

For example, in the functionalization process of adamantane-based microporous polymers, the incorporation of the nitrobenzoyl- group to phenyl-, biphenyl- and terphenyl-adamantane-based polymers have resulted in higher CO_2 uptake (from 1.74 to 2.19 mmol g^{-1} at 298 K and 1 bar). Moreover, it has shown lower porosity for the first two polymers and much higher porosity for the third polymer compared to the non-functionalized polymers.[60] Alcohol-containing networks (e.g. POF1B) have shown uptake of (2.14 mmol g^{-1} at 298 K and 1 bar).[61] NPOF-4 is another example of nitrogen-rich porous organic polymers, which was synthesized via acid catalyzed cyclotrimerization reaction followed by nitration and reduction of the parent NPOF-4. The resulted NPOF-4-NO_2 and NPOF-4-NH_2 have shown higher CO_2 uptake and lower porosity.[62]

In contrast to the post-synthetic strategy, the pre-functionalization process depends on the incorporation of the functionality prior to the polymerization. Nitrogen-rich porous organic polymers are examples ~~on~~ of this synthesis method and include: microporous triazine-based polymers (TPM),[63] triazine-based polyimides (TPIs),[64] triptycene-based polymers of intrinsic microporosity (Trip(Et)-PIM),[65] polycarbazoles (CPOPs)[66] imine-linked microporous polymers,[67] azo-linked polymers,[68] and benzimidazole-linked polymers (BILPs).[69] All of the above classes of N-rich polymers have shown moderate to high porosity and high CO_2 uptakes.

In this study, we have investigated the porosity and the gas uptake properties of benzimidazole-linked polymers, (BILPs) and studied several suggested strategies to enhance their porosity and binding affinity. Basically, benzimidazole-linked polymers are known as amine-decorated polymers. This class of polymers was developed by El-Kaderi and coworkers, and has shown that the introduction of amines to the pores enhances the performance of this class of porous materials with regard to CO_2 capture.[69]

1.4 Benzimidazole-Linked Polymers (BILPs)

The design of new porous polybenzimidazole-linked polymers (PBIs) has increased dramatically due to their potential in the fields of heterogeneous catalysis, sensing, proton conductivity, proton-exchange membrane fuel cells, and gas storage and separation applications.[41, 70] There are several well-known synthetic strategies for PBIs, which usually apply polycondensation reactions and result in the formation of the imidazole moiety. One of the early synthetic methods of PBIs is the polycondensation reaction between diamine moieties and benzene carboxylic acids or their derivatives, (e.g., esters) or aldehydes in the presence of templating agents such as silica nanoparticles in polyphosphoric acid.[71] Other PBIs were synthesized using the ionothermal method in the presence of an ionic medium (e.g. LiCl/KCl solution) and melt-condensation routes.[72] Wang et al. has reported on PBIs by applying facile one-step polycondensation of 3,3'-diaminobenzidine and silane carboxylic acids.[73] The surface areas of the resulting polymers are around 200 $m^2 g^{-1}$ and their pore sizes are within the range of the macroporous and microporous sizes. Recently, El-Kaderi et al. has developed a new class of amine-decorated benzimidazole-linked polymers (BILPs) and investigated their capability in gas storage and separation applications.[69] BILPs have been synthesized by a metal-free polymerization process that led to the formation of imidazole linkages. The synthetic approach was demonstrated by polycondensation reaction between aryl-o-diamines and aryl-aldehydes, as shown in Schemes 1.2.

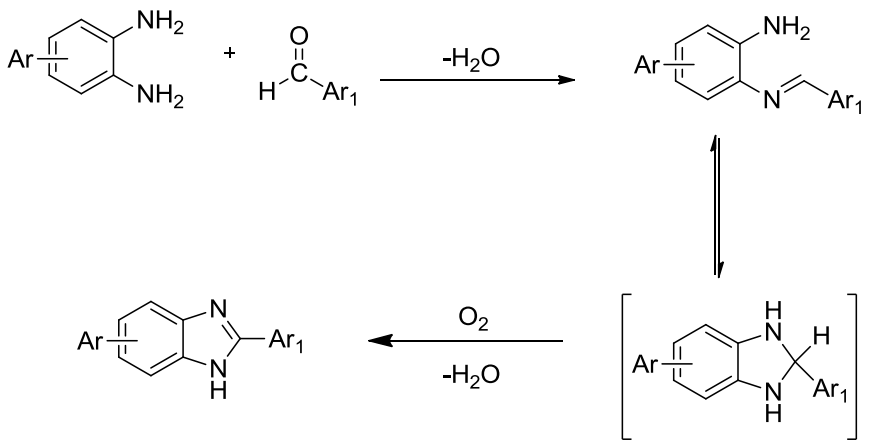

Scheme 1.2: General polycondensation reaction between aryl-o-diamines and aryl-aldehydes

This metal-free synthetic avenue facilitates polymer purification and avoids the use of expensive metal catalysts.[74] To date, several BILPs have been synthesized from 2D and 3D building units by varying the combinations of the aryl-o-diamines and aryl-aldehydes as shown in Schemes 1.3 & 1.4.[69] In general, the synthetic protocol of BILPs depends on the dropwise treatment of the aryl-o-diamine with homogeneous solution of the aryl-aldehyde in dimethylformamide (DMF) over 3 hrs under N_2 atmosphere at -30 ºC followed by stirring to reach RT. Applying an oxidative step[75] by bubbling the reaction mixture with O_2 and heating for 3 days leads to BILPs formation.

The role of the slow addition step is to slowdown the rate of the imine formation reaction, while the oxidative step assists ring closure. The first synthesized polymer is BILP-1.[69d] This polymer was prepared by a polycondensation reaction between hexaaminotriphenelene and tetrakis(4-formylphenyl)methane. Consequently, the triptycene-based BILPs (BILP-3 and BILP-6) were synthesized from the combinations of hexaaminotriptycene, and tetrakis(4-formylphenyl)methane, and terephthalaldehyde respectively.[69b] The other series of the reported

BILPs (BILP-2, BILP-4, BILP-5, and BILP-7)[69c] were synthesized according to the same method by varying the combination of linkers and resulted in favorable yields.

More recently, a new pyrene-based BILP (BILP-10) was synthesized from the polycondensation reaction between Tetrakis(4-formylphenyl)pyrene and benzenetetraamine. The incorporation of the pyrene moiety in BILP-10 has shown new texture properties that resulted in remarkable binding affinity for CO_2.[69a] The successful formation of the imidazole linkage in the polymers' backbones has been confirmed by using spectral and analytical characterization methods.

The thermogravimetric analysis showed their high stability up to 400 ºC, while the X-ray diffraction analysis confirmed their amorphous nature. Scanning Electron Microscopy (SEM) of BILPs revealed aggregated particles with variable size differs for different BILPs, while BILP-10 showed a unique morphology of nanofibers due to the presence of the pyrene core.

The chemical connectivity and the presence of the imidazole moiety were evidenced by elemental analysis, FT-IR, and ^{13}C solid state NMR spectroscopy. BILPs have several attractive properties such as high chemical and physical stabilities that are superior to those of MOFs; they also have considerable CO_2 and H_2 uptakes as well as high CO_2 selectivity over N_2 and CH_4.[15a] The common feature of BILPs is the formation of the amphoteric imidazole moieties, which are the most vital part of the polymers' backbone and increased the importance of BILPs as an attractive class of POPs, especially for CO_2 capture and separation applications.[76] The introduction of amine functionality and the incorporation of accessible nitrogen sites on the walls of the polymers enhanced the performance of the polymers to capture small gases (CO_2, N_2 and

CH_4) selectively.

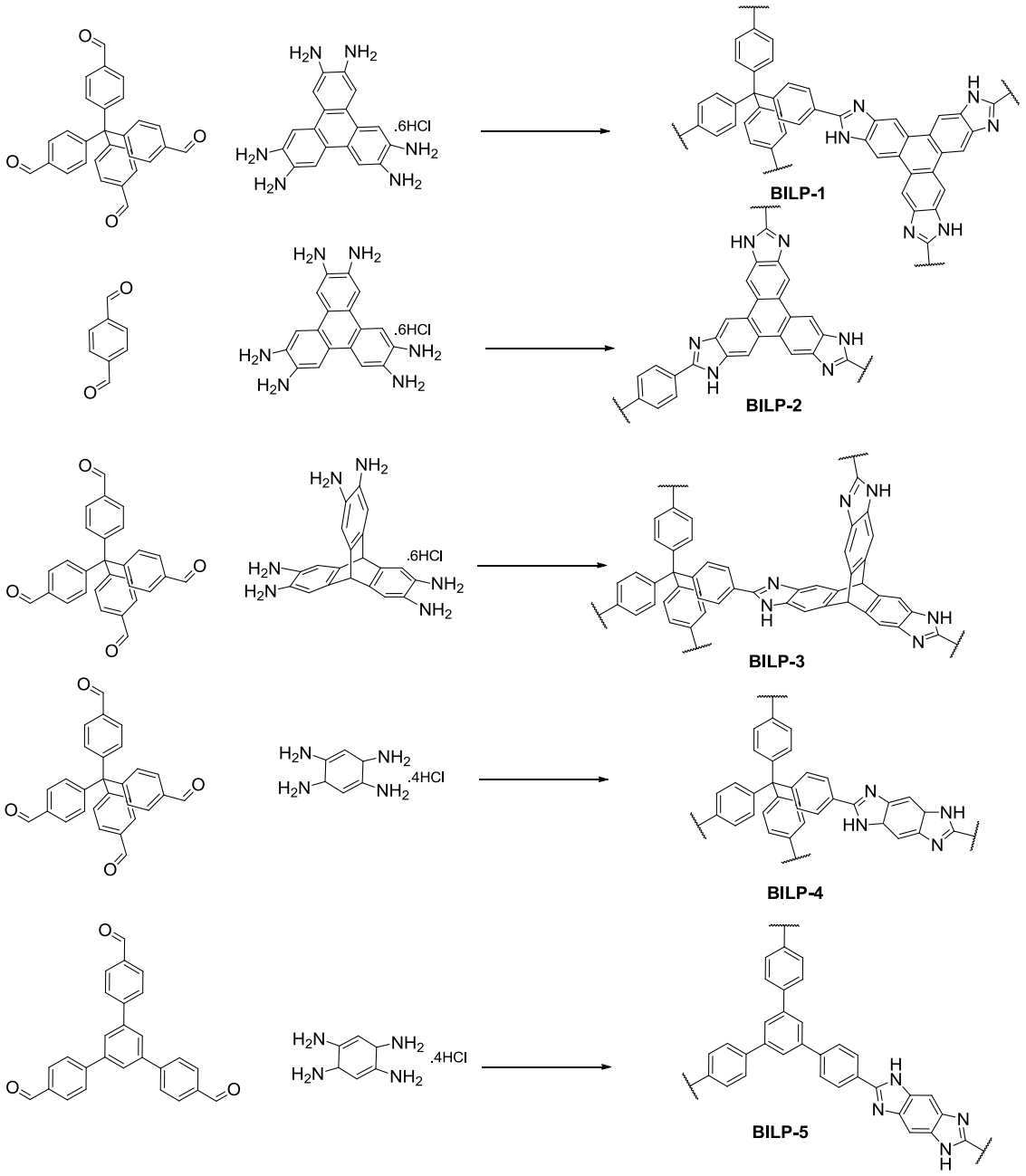

Polymerization conditions ; (i) DMF, -30 ^{O}C, 3 hrs. (ii) DMF, RT, 6 hrs under N_2 flow, (iii) 3. 130 ^{O}C, 3 days under O_2

Scheme 1.3: General synthetic method of the reported BILP-1 – BILP-5.

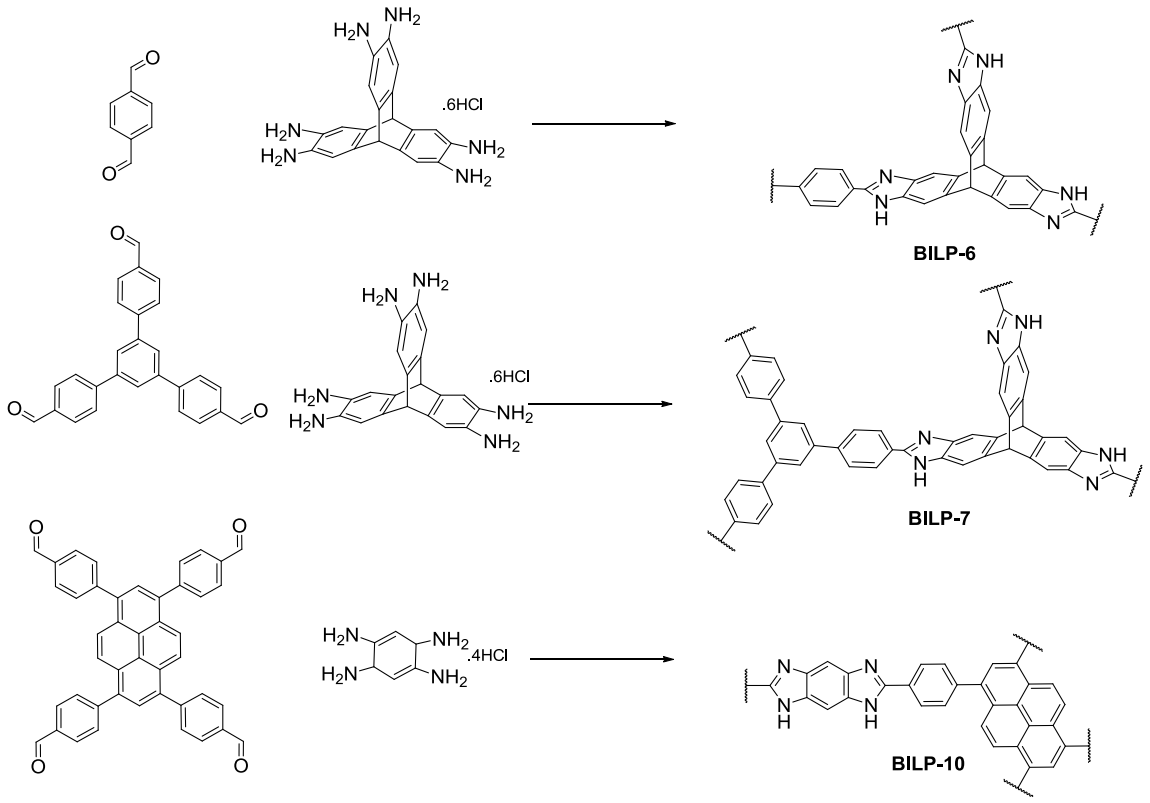

Polymerization conditions ; (i) DMF, -30 ^{O}C, 3 hrs. (ii) DMF, RT, 6 hrs under N_2 flow, (iii) 3. 130 ^{O}C, 3 days under O_2

Scheme 1.4: General synthetic method of the reported BILP-6 – BILP-7 and BILP-10

The porosity of BILPs was investigated by argon and/or nitrogen sorption desorption measurements and showed that all BILPs are microporous polymers (Type-I-Type II isotherms). The surface area data for the polymers was gathered using the Brunauer-Emmett-Teller (BET) model within the pressure range of P/P_0 = 0.01- 0.15 and summarized in Figure 1.2, Table 1.2. The fully reversible Type-I-Type II isotherms indicate the permanent microporosity nature of the polymers. The surface areas of BILPs depend on the dimensionality of the building units. The apparent surface areas for the 2D BILPs are lower than 3D BILPs, this can be attributed to the

favorable π-π stacking in 2D polymers, the possible hydrogen bonding between the imidazole moieties, and the flexible nature of the polymers, which leads to greater network interpenetration and lower porosity. Thus far, the highest reported surface area (SA) was for BILP-3 (SA_{BET} =1306 m^2g^{-1}) a triptycene-derived BILP, while the lowest surface area was for BILP-5 (SA_{BET} = 599 m^2g^{-1}). The pore size distribution (PSD) of the polymers was examined by fitting the uptake branch of argon or nitrogen to the nonlocal density functional theory (NLDFT) which resulted in the PSD less than 8 Å for all BILPs. The impact of the microporosity, the incorporated amine functionality, and the small pore size were investigated by studying the uptake of small gases (CO_2, N_2 and CH_4) and the selectivity of the polymers.

The small gas uptake measurements were applied at 273 K and 298 K by collecting adsorption/desorption isotherms of pure gas components. The notable enhanced CO_2 capture and selectivity of BILPs, compared to other purely organic or organic-inorganic hybrid materials such as MOFs, has been attributed to their subnanopore dimensions and imidazole-functionalized pore walls that facilitate selective CO_2 capture and storage. These textural properties of BILPs resulted in the highest CO_2 uptake by porous organic materials (5.3 mmol g^{-1}), for BILP-4, with high CO_2 isosteric heats of adsorption ~26-28 kJ mol^{-1} for BILP-1-BILP-7, and 38 kJ mol^{-1} for BILP-10 as shown in Table 1.2& Figure 1.2, and high CO_2/N_2 (113) selectivity for BILP-2 from the initial slope calculations. The heat of adsorption (Q_{st}) of the polymers was calculated using the adsorption data collected at 273 K and 298 K using the virial method. The methods and mathematical equations used for the heats of adsorption and selectivity calculations are discussed in the next section of this chapter.

The reversible sorption/desorption behavior and moderate Q_{st} values reveal that the interactions of CO_2 with the pores are weak enough to allow for the material regeneration

without applying heat. The binding of CO_2 to the pore walls was proposed as Lewis acid-base interaction between the electron lone pair on imine-nitrogen of the imidazole ring and the carbon of CO_2 or the polarizable nature of CO_2 molecules through hydrogen bonding and/or dipole-quadrupole interactions, which consists of the protonated and proton-free nitrogen sites of imidazole rings (Figure 1.3). However, the presence of the non-functionalized aryl moieties in BILPs needs to be considered and investigated as a potential binding site. To gain insight into the electronic nature of the benzimidazole and the aromatic benzene building units in the polymers, two new BILPs (BILP-14 and BILP-15) were synthesized and studied to investigate the possible interactions of CO_2 with the BILPs building units, as discussed in Chapter 2.[69e, 77]

The moderate surface area and the pore functionality of BILPs make them preferable candidates for CO_2 capture and separation applications under ambient conditions. In contrast, the highly porous materials that feature high surface areas and pore volumes such MOFs,[37] COFs,[50] and PPNs[55] are more applicable at high pressure settings for gas storage applications. Thus, the design of new BILPs suitable for gas separation and storage application is required combining the pore functionality and high porosity features.

Theoretically, and by applying the material studio visualizer,[78] BILPs exhibit high surface area, however, the applied experimental approach always results in moderate to low surface areas compared to the theoretical results. For example, the calculated surface area for BILP-5 is around 2361 $m^2 g^{-1}$, while the experimental surface area of BILP-5 reached only 599 $m^2 g^{-1}$. Thus, new efforts need to be invested to improve the porosity and the gas binding affinity of BILPs. Examples of some proposed steps include: (1) modify the synthetic strategy of BILPs to improve the porosity of the polymers for high pressure settings and dynamic gas storage, and/or (2) functionalize the pores with functional groups that have a high binding affinity for

CO_2 to increase its uptake and selectivity. The proposed modified synthetic strategy should provide control over the formation rate of the imidazole ring by slowing down the coupling step of the aldehyde functional group and amine during the condensation step. This approach may limit the network interpenetration, which can arise from high polymerization rate and the use of expanded building blocks.

It has been reported that the formation of the imidazole ring during the condensation reaction between the aldehyde and amines can be facilitated by the catalytic effects of acids and bases such as polyphosphoric acid, mineral acids, acetic acid, and aniline.[25, 74] Moreover, this process can be catalyzed in the presence of metals such as cerium (IV)/ cerium (III)-redox-mediated oxidation process.[74, 79] Improving the porosity of BILPs has been studied by synthesizing new BILPs and introducing longer organic linkers, studying the catalytic impact of acids on the formation of the imidazole ring and pre-functionalizing the building blocks to suppress network interpenetration and improve the gas uptake affinity of the materials as discussed in the following chapters.

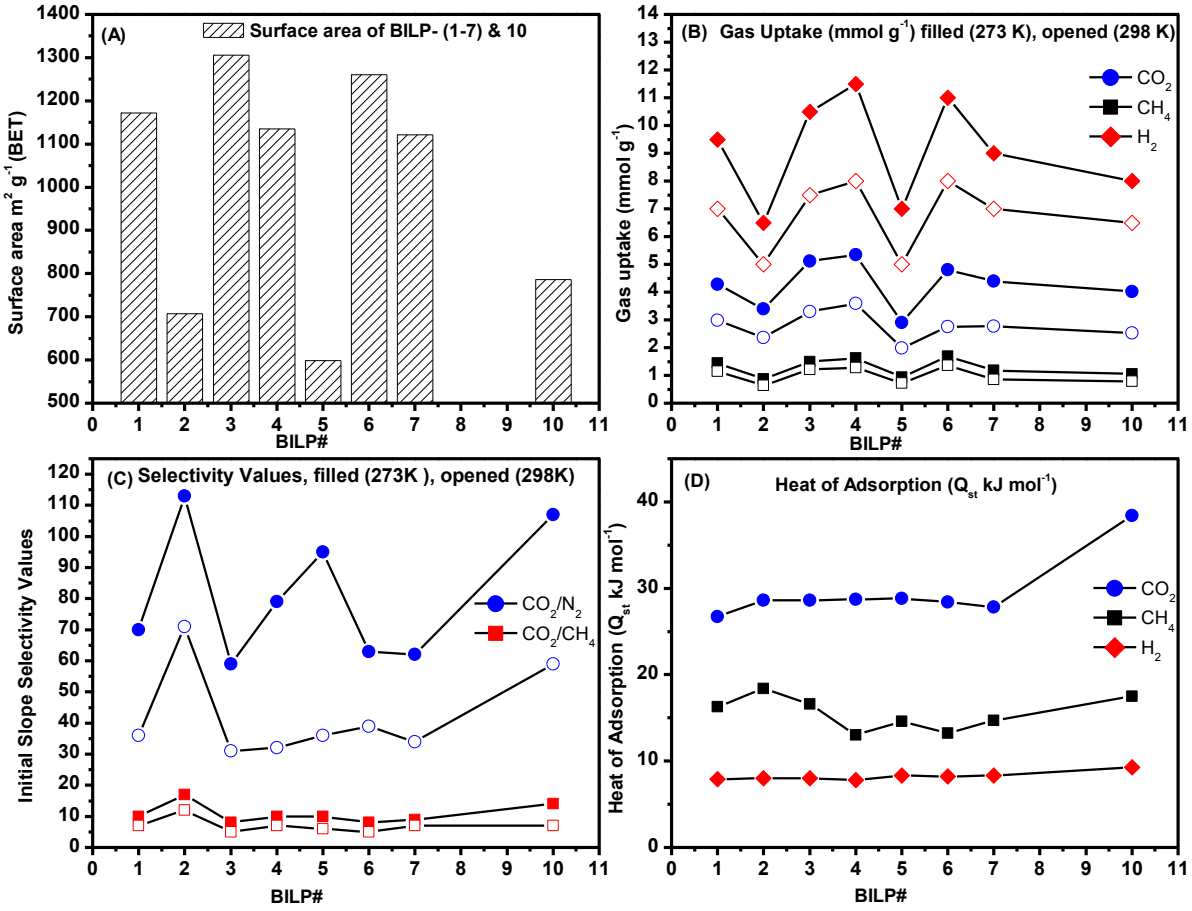

Figure 1.2: (A) BET surface area (m^2 g^{-1}) of the reported BILPs; (B) small gas uptakes (mg g^{-1}) at 273 K and 298 K; (C) Selectivity values at 273 K and 298 K resulted from the initial slope calculations; and (D) Heat of adsorptions (kJ mol^{-1}).

Table 1.2: Gas Uptake and Selectivity data of all Reported Benzimidazole-Linked Polymers (BILPs)

polymer	SA^{a}_{BET}	H_2 at 1 bar[b]			CO_2 at 1 bar[b]			CH_4 at 1 bar[b]			N_2 at 1 bar[b]		Selectivity[c]	
		77 K	87 K	Q_{st}	273 K	298 K	Q_{st}	273K	298 K	Q_{st}	273 K	298 K	CO_2/N_2	CO_2/CH_4
BILP-1	**1172**	19	14	7.9	188	131	26.7	23	16	16.3	5.0	7.3	70(36)	10(7)
BILP-2	**708**	13	10	8.0	149	104	28.6	14	9	18.4	3.4	2.5	113(71)	17(12)
BILP-3	**1306**	21	15	8.0	225	145	28.6	24	17	16.6	3.3	2.4	59(31)	8(5)
BILP-4	**1135**	23	16	7.8	235	158	28.7	26	18	13.0	1.1	3.8	79(32)	10(7)
BILP-5	**599**	14	10	8.3	128	87	28.8	15	10	14.6	0.2	2.7	95(36)	10(6)
BILP-6	**1261**	22	16	8.2	211	121	28.4	27	19	13.2	6.8	6.7	63(39)	8(5)
BILP-7	**1122**	18	14	8.3	193	122	27.8	19	12	14.7	5.63	5.4	62(34)	9(7)
BILP-10	**787**	16	13	9.3	177	111	38.4	17	11	17.5	1.0	3.9	107(59)	14(7)

[a]Surface area ($m^2\ g^{-1}$) was calculated from Ar isotherm. [b]Gas uptake in mg g^{-1} and isosteric enthalpies of adsorption (Q_{st}) in kJ mol^{-1}. [c]Selectivity (mol mol^{-1}) was calculated from initial slope calculations at 273 K and (298 K).

1.5 Interpenetration Effect and the Control Methods

The applications of POPs, MOFs, and COFs, include catalysis, sensing, and gas separation. It is a requirement that materials have well-defined structure, the largest possible pore cavity, and retained porosity. In principle, the simplest way to design highly porous materials with large pore size is to increase the length of the organic linkers.[80] However, the longer linkers may lead to the formation of large voids, which can lead to structure collapse after the activation and solvent removal. The longer linkers can also accommodate organic linker, metal, and guest molecules inside the voids and allow for the formation of a new network coexisting with the original network. This new formation will result in interpenetrated networks.[80a] There are two recent proposed solutions to prevent structure collapse; supercritical activation and the density-based separation method.

The supercritical activation is a thermal activation method, which has been applied as an exchange process in solvent-containing MOF materials with liquid and supercritical carbon dioxide.[81] On the other hand, the density-based separation is a method that allows the separation of MOFs based on density difference, however, it does not address the problem that results in the formation of multiphased products, such as interpenetrated materials.[82] Thus, the design of a single network (non-interpenetrated MOF) has been proven to be a major problem especially with long linkers. Therefore, the interpenetration problem needs to be addressed, to control the factors that lead to designing materials with high porosity and large free pore cavities.

Interpenetration is an intriguing phenomenon that has been noticed in MOFs and COFs wherein there is a formation of interwoven or catenation of two separate structures within each other.[83] It has a negative impact on the porosity and the functional applications of the polymers; although it makes the network more robust and thermodynamically stable. On the other hand, it

plays a positive role in the selective separation of small gas molecules due to the decreased pore size of the interpenetrated network. Interpenetration is very common in coordination polymers, specifically in structures that consist of flexible linkers. Specific types of interpenetration such as polycatenation, polythreading, and polyknotting have been recognized in MOFs by studying the X-ray diffraction patterns of the polymers.[84] Moreover, it can occur within the structures of different dimensionalities (1D (chains), 2D, and 3D polymers) without forming a new bond connection.[83] However, there is no chemical bond formation between the interpenetrated networks; there is no way to separate them without the breakage of the bonds. Thus, the only way to avoid this effect is to modify the synthetic methods and the building units to prohibit interpenetration during synthesis.

Several strategies have been developed to suppress the interpenetration in MOFs in order to isolate high surface area MOFs when long linkers are used. These strategies include: (1) reaction temperature and concentration control,[85] (2) template directed control,[86] and (3) ligand design/modification-induced control.[80b, 87] Control over temperature and concentration has shown a strong impact on the suppression of the interpenetration in MOFs. For example, a MOF structure has been synthesized by solvothermal reaction of 4,4-bipyridine (long linker), 1,4-benezendicarboxylic acid and cadmium nitrate hydrated salt using different concentrations and reaction temperatures. These conditions afforded materials having two different X-ray diffraction patterns, a non-interpenetrating pillared MOF and a 2-fold interpenetrated MOF.

The non-interpenetrating structure was isolated from a low concentration (~ 0.012 M) and 85 ºC, while the interpenetrated MOF was isolated from (0.1M and 125 ºC). At elevated temperature, the denser MOF and the lower porosity could be attributed to the possibility of the faster crystal growth and the sublattice formation in the voids.[85, 88] In contrast, at lower

temperature and lower starting material concentrations, the proposed mechanism relies on the slow polymerization rate over a long period of time. Accordingly, this would contribute to suppressing the sublattice formation and prevent the collapse of the structure.[85, 88]

The second control strategy is the template-directed method. In this method the formation of non-interpenetrated material depends on the incorporation of a hard or soft template during the polymerization process. The template in this case can be used as a surface of the structure construction, which should be leached out after the polymerization. Several materials have been used as templates, such as oxalates, silica, and small solvent molecules (e.g. DMF, toluene, benzene and dioxane).[86, 89] For example, Weber et al. has synthesized mesoporous benzimidazole-linked polymers using a 13 nm silica template, which resulted in a mesoporous polymer with 11 nm pore diameter.[71] Thus, to avoid interpenetration by applying the template methodology, several factors need to be considered such as, the type of the template (soft or hard), the size of the template, the pore size of the desired polymer (micro-, meso-, and macro-porous) and the reaction conditions.

More recently, several studies have reported non-interpenetrated MOFs through the rational modification and design of the ligand before the polymerization. It has been proven that the presence of stericly bulky groups on the organic linker could effectively suppress network interpenetration. Therefore, to apply this strategy, a selective modification of the organic linker with pendant groups differing in size and/or length is the leading step to afford non-interpenetrated networks. For example, the hydrothermal reaction between a dicarboxylate linker with uranyl cation (UO_2^{+2}) led to doubly interpenetrated layered structure. This interpenetration has been prevented by pre-introduction of naphthalene substituent on the dicarboxylate linker and resulted in a non-interpenetrated structure.[90] Moreover, a series of pillared-layer MOFs have

been synthesized by solvothermal reactions and resulted in interpenetrated and non-interpenetrated frameworks by using a non-substituted (aryl-H) and bromine-substituted (aryl-Br) organic linker, respectively. The pre-introduction of the (aryl-Br) group has led to suppression of the interpenetration compared to the (aryl-H) due to the bulkiness effect of the bromine group.[80b] Furthermore, the numbers of the incorporated bulky groups on the linker play a significant role in avoiding interpenetration. For instance, the pre-introduction of one and two azolium moieties on biphenyl dicarboxylate linker have led to interpenetrated and non-interpenetrated structures respectively.[87a]

Interestingly, this strategy has also shown multifunctional bulky groups, which suppress the interpenetration and assist in the introduction of new functionality. For example, the pre-introduction of a tert-butylcarbamate (NHBoc) group on the biphenyldicarboxylate linker has played roles of interpenetration suppression and protected amino group, which has been de-protected later and resulted in more stable and higher porous amino-functionalized MOF.[91] The size and the length of the groups, also, have a significant impact on the degree of interpenetration. One example is the ligand-elaboration method wherein a series of 4,4'-ethylenedibenzoic acids have been synthesized by incorporation of different functional groups such as (-CH_3, -Br and –CH_2OH). In this example, the similar substituents size (-CH_3, -Br) resulted in three-fold, interpenetrated structure, while the longer (-CH_2OH) led to a more open two-fold, interpenetrated framework (Figure 1.3).[92] Several examples have shown the importance of each strategy, while all belong to well-defined structures of MOFs and COFs where the degree of interpenetration can be indicated by X-ray diffraction. Thus, these strategies are invaluable in crystalline networks, due to the fact that crystalline materials have well-defined pore structure with monodisperse size distribution, stable pores, and tunable metrics. However,

applying these methods on amorphous materials may enhance the porosity and lead to the synthesis of new materials capable of working for gas separation and storage applications.

In this study, and motivated by the impact of the pre-functionality introduction method on the porosity of MOFs, we have applied the third strategy, “rational ligand design”, on amorphous BILPs by incorporating different lengths of alkoxy (e.g. methoxy, ethoxy, butoxy and isobutoxy) functional groups. The impact of the new functionality on the porosity and the CO_2 binding affinity were concluded from sorption measurements. We have shown that the incorporation of the new hydrophobic and steric bulky groups introduced little control over the network formation and enhanced the porosity of the functionalized compared to the non-functionalized BILPs. The detailed study of the functionalized BILPs and their rational design of the monomers are mentioned in chapter 5.

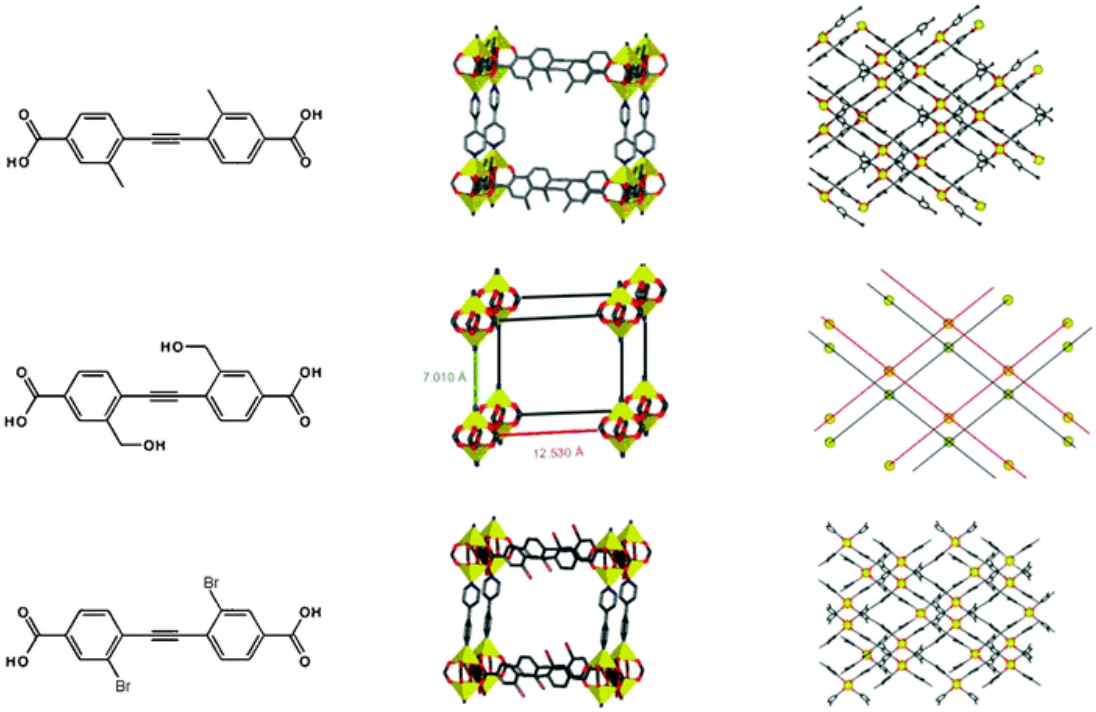

Figure 1.3: Different degrees of interpenetration in three different network topologies observed using very similar ligands. This figure used with permission from RSC.[92]

1.6 Porosity measurements, principles and instrumentations

Applying the porosity measurements is the main technique to evaluate the porosity nature and help in determining the performance of porous materials in terms of gas storage and separation applications. These measurements require sorption equipment capable of collecting the data either at high pressure or low pressure ranges. The high pressure equipment allows the assessment of gas storage from 1-200 bar, while the low pressure assesses the sorption measurements at range (10^{-6}-1 bar) using low pressure equipment. It is notable that, the high pressure measurements are important for the highly porous materials (high surface area) to indicate their performance in the pre-combustion technology and for storage applications.

In contrast, the low pressure settings are more practical for low porous materials and the post-combustion applications. A physisorption apparatus is used to collect the gas isotherms, (e.g. CO_2, N_2, H_2 and CH_4). The output of the measurements is the isotherm, which shows the amount of gas uptake at constant temperature and a specific range of pressure. The applicable temperatures range is from 77 K to 315 K. The choice of the temperature is related to the experiments' conditions. For example, at low pressure settings the isotherms are collected at 77 K, 87 K, 273 K or 298 K at pressure range 10^{-6}-1.0 bar by immersing the samples' cell in a bath compatible with the desired temperature and keeping it constant over the period of the measurement. The pressure variation point can be reached, basically, by a dosing process which depends on taking a specific volume of the gas and applying a repetitive process to reach the requested pressure point. For this research a Qunatachrome Autosorb IQ2 was used for all sorption experiments as shown in Figure 1.4.

The surface area (SA) measurements can be obtained from the sorption isotherms, by applying the same experiment at 77 K, where the adsorbent is nitrogen (N_2) or at 87 K where the

adsorbent is argon (Ar) and this provides the information about the accessible area of binding. Two methods are used to measure the surface area: Langmuir and BET. The Langmuir model was developed by Irving Langmuir in 1916 and determined by the equation:

$$\frac{\mathbf{1}}{\boldsymbol{x}} = \left(\frac{\mathbf{1}}{\boldsymbol{K}*\boldsymbol{x}_\circ}\right) * \left(\frac{\mathbf{1}}{\boldsymbol{P}}\right) + \frac{\mathbf{1}}{\boldsymbol{x}_\circ} \qquad \text{(Eq.1.1)}$$

Where $\boldsymbol{x}$ is the surface area covered with the gas, $\boldsymbol{K}$ is the ratio of the adsorption and desorption rate constants, $\boldsymbol{P}$ is the pressure and $\boldsymbol{x_0}$ is the total surface area. Nevertheless, this equation is based on four assumptions including: (1) the surface of the material is uniform; (2) the adsorbate molecules do not interact with each other; (3) all adsorption occurs by the same mechanism; and (4) at the maximum adsorption only one single layer is formed. However, in reality these assumptions are rarely true due to the surface non-ideality, multistage adsorption mechanism, and multilayer formation scenarios.

In 1938 Emmett and Teller derived the BET theory, which resulted in the assumption of the multilayer formation and, hence lower surface area compared to Langmuir. It is noteworthy that the surface area calculations by using these two methods are limited to the microporous materials since the adsorption mechanism of the mesoporous materials include the molecule-molecule interaction and molecule-wall interaction. However, this restriction is often ignored in research applications.

The pore size distribution (PSD) calculations can be gained from the argon or nitrogen isotherms. PSD calculations are applied by using the Non-Local Density Functional Theory (NLDFT) to show how often pores of every size are distributed in the porous material. The thickness of the distribution can be an indication of the consistency of the work. Two methods are typically used to calculate pore size distribution, Barrett-Joyner-Halenda (BJH) and Non-

Local Density Functional Theory (NLDFT). The first method has a tendency to bias the distribution high, while the only method used in this study to calculate PSD is NLDFT.

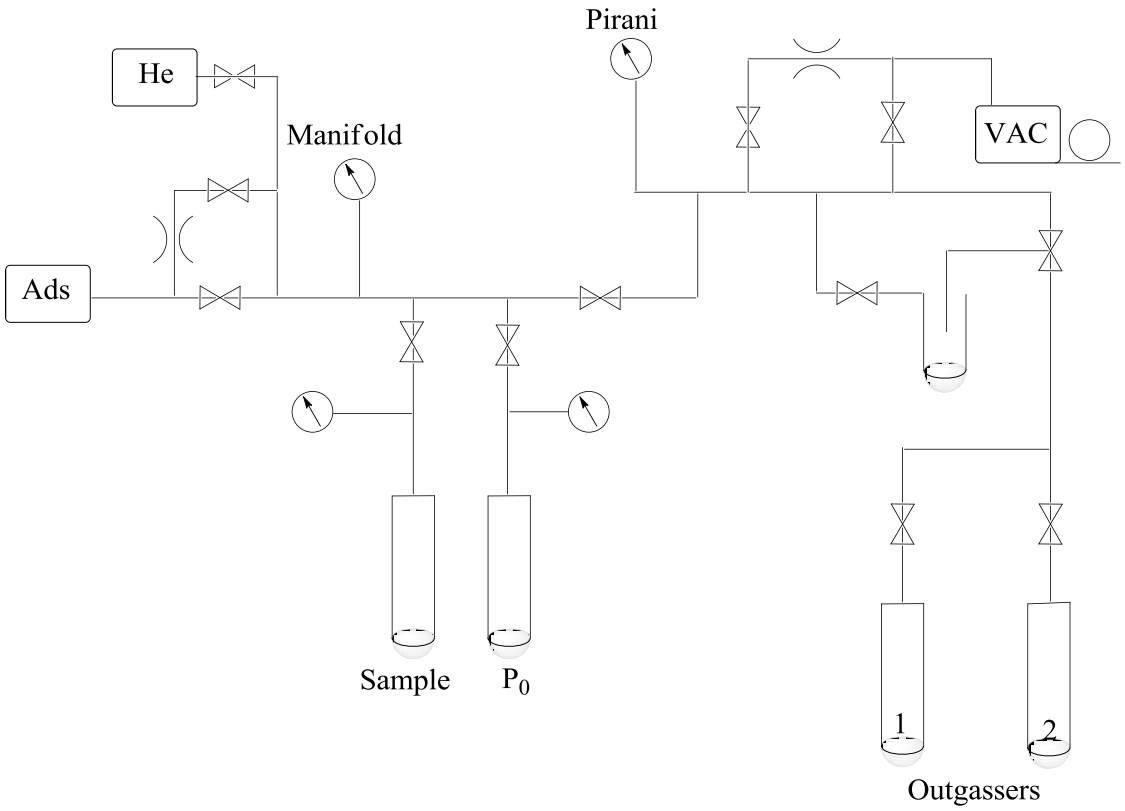

Figure 1.4: Schematic Representation for a quantachrome Autosorb IQ2 Low Pressure Sorption Instrument. **He** and **Ads** represent the inlets for helium gas and the adsorbate gas, respectively. **VCA** represents the vacuum. Circled arrows represent pressure gauges, and bow-tie shapes represent valves. The up/ down small curves near the ads and the **pirani** represent the valves for fine flow.

1.7 Theoretical Calculations and Mathematical Methods

1.7.1 Heats of Adsorption Calculations

An Isosteric heat of adsorption (Q_{st}) is a useful tool assessing the capabilities of the polymers to store a particular gas. For porous adsorbents, Q_{st} dictates the affinity of the pore surface and the surface coverage. It is usually estimated using two or more gas adsorption

isotherms, which describe the pressure as a function of loading, collected at different temperatures. The zero-coverage heat of adsorption parameter gives an indication about the binding affinity of the gas to the surface and the wall of the porous materials. Accordingly, the resulted values can be tuned by changing the chemical nature of the material through the functionalization or changing the porosity. The calculation of isosteric heats of adsorption is based on experimental isotherms. The isotherms are fitted to mathematical models that are designed to describe the data. There are three different types of models used to calculate Q_{st}, (1) Langmuir model, (2) Langmuir-Freundlich model, and (3) virial model. The first two models use the Clausius-Clapeyron equation to evaluate the fitted model. The mathematical calculations and equations of the first two models reported elsewhere.[93] The only method mentioned and applied in this study is the virial calculation method. The Virial equation, as shown below, is an expansion of summation equation, where, the number of summation iterations is unknown.

$$\ln P = \ln N + \frac{1}{T}\sum_{i=0}^{m} a_i N^i + \sum_{i=0}^{n} b_i N^i \qquad \text{(Eq.1.2)}$$

The parameters mentioned in the equation are: P the pressure in Torr, T the temperature in Kelvin and N the mmol of the gas adsorbed per gram of sample. The values (n) and (m) are undefined since the number of the summations is unknown, while, $m \geq n$. The fitting parameters are $a_0, a_1, \ldots a_m$ and $b_0, b_1, \ldots b_n$, used for the calculation of the heats of adsorption values after the fitting by using the equation bellow.

$$Q_{st} = -R\sum_{i=0}^{m} a_i N^i \qquad \text{(Eq.1.3)}$$

Where the value of (m) matches the value found for the preceding equation such that all a_i values are used. Following the previous equation, the calculated values are then plotted as they relate to the surface coverage, *N*, while the isosteric heats of adsorption at the point of zero-coverage is

reported as the mean of comparison. The large number of fitting parameters gives better description of the isothermal data compared to the other methods.[94] The Q_{st} values were calculated and reported in this study.

1.7.2 Selectivity Calculations

The selective binding of one gas over the other is the most significant parameter in the solid adsorbents design. Therefore, the best materials that fulfill the environmental demands are those which have the best performing properties regarding the binding of CO_2 ~~from~~ over other small gases (N_2, CH_4 and H_2). There are specific evaluation methods, which give numerical data to indicate the selectivity value (where higher values mean more selective). Calculations for the selectivity capabilities of the porous polymers depend on the pure gas isotherms.

These calculation methods include: (1) initial slope calculations, (2) Henry's Law constants, and (3) ideal adsorbed solution theory (IAST). The first method employs the calculations at a low pressure range (0 – 0.1 bar) and takes the slope of the linear relation between the low pressure range and the gas uptake (mmol g^{-1}). The slope ratios of the respective gases provide the numerical selectivity value. For example, the initial slope selectivity value of (CO_2/N_2) at 273 K will be calculated by taking the slope of each CO_2 and N_2 pure gas isotherm at 273 K in the low pressure range, then calculate the slope ratio between the pure gas isotherms.[95]

This method is the fastest and the simplest method to evaluate the selectivity, but it is limited due to the assumption that the isotherms are linear in the low pressure range. Calculating the selectivity by applying Henry's Law constant gives a more precise measure of the true initial slope value of each gas isotherm. Henry's Law calculation uses the virial-type expansion, which

has been used in the isosteric heats of adsorption calculations above. The resulted fitting parameters $a_0, a_1, \ldots a_m$ and $b_0, b_1, \ldots b_n$ will be used to calculate the constants and hence the selectivity according to the following equations.[15b, 96]

$$K_H = e^{-b^\circ} * e^{\left(\frac{-a^\circ}{T}\right)} \qquad \text{(Eq.1.4)}$$

$$S_{ij} = \frac{K_{Hi}}{K_{Hj}} \qquad \text{(Eq.1.5)}$$

Where K_H is Henry's constant and a_0, b_0 are the fitting parameters from the virial equation, while, i, j are the gas components (e.g. i = CO_2 and j = N_2), K_{Hi} is the constant for the first gas, K_{Hj} is the constant for the other gas and S_{ij} is the final selectivity value. Although this method is more time consuming, it is more accurate compared to the initial slope.

The third method is the ideal adsorbed solution theory (IAST), which is used to evaluate the capability of porous materials to separate the gases from the real gas mixtures. This theory is based on the fact that "in an ideal solution the partial pressure of an adsorbed component is given by the product of its mole fraction in the adsorbed phase and the pressure, which it would exert as a pure adsorbed component at the same temperature and spreading pressure as those of the mixture."[97] Applying the mathematical derivations based on the thermodynamics as mentioned in the selectivity results in Chapter 1, will result in the final selectivity value which represents the ratio of the molar ratios of the bulk phase and the adsorbed phase as mentioned in the following equation.[98]

$$S_{1,2} = \frac{(x_1/y_1)}{\left(x_2/y_2\right)} \qquad \text{(Eq.1.6)}$$

Where y_1, y_2 are the bulk phase molar ratios of gas 1 and 2, while, x_1, x_2 are the adsorbed phase molar ratios of gas 1 and 2. In this study all selectivity data were calculated by using the initial slope calculations and the IAST calculations, and interestingly, the resulting data are consistent between both methods, as will be shown.

1.8 Dissertation Problem

The high concentration of CO_2 in the atmosphere is significantly contributing to global warming. Thus, CO_2 capture and sequestration (CCS) has been proposed to maintain or lower CO_2 concentration in the atmosphere. To do this, CO_2 capture from flue gas or removal from methane rich gases is essential. The current technology involves the use of amine solutions that enable CO_2 capture by chemisorption. However, the high amount of energy required for adsorbent regeneration, solvent decomposition and evaporation, and toxicity remain major concerns. As such, developing new technologies that would enable CO_2 capture while also addressing the aforementioned concerns is vital for environmental protection and natural gas utalization. Among the promising alternatives is the use of porous materials that trap CO_2 with moderate binding affinity (physisorption) and enable regeneration of adsorbents with affordable costs. Additionally, porous adsorbents should possess high selectivity for CO_2 over other gases present in gas mixtures, high physicochemical stability, and high CO_2 capacity.

There are several classes of porous materials that show promise for CCS and they include metal-organic frameworks (MOFs), purely organic discrete cage molecules, and porous organic polymers (POPs). Although MOFs have been widely investigated, their limited stability in general remains a major drawback. On the other hand, porous organic polymers are more chemically robust and can be functionalized to have high selectivity for CO_2 over CH_4 and N_2. Never the less, most porous organic polymers have low gas binding energies and low surface area that leads to low CO_2-uptake capacity and CO_2/N_2 selectivity. Thus, the lack of finding a suitable design of porous material, which combines high surface area, high CO_2 capacity, and high selectivity, needs to be addressed. Benzimidazole-linked polymers (BILPs) developed recently by El-Kaderi have structural features that mitigate most of these issues. In particular, the

N-rich aspect of BILPs coupled with their moderate porosity led to an impressive CO_2/N_2 selectivity and CO_2 uptake at ambient pressure. However, the surface area of the reported BILPs is still much lower than those of highly porous MOFs and POPs limiting their potential application in gas storage under high pressure conditions. Furthermore, BILPs/CO_2 interaction is not well understood and can be affected by the hydrophobic nature of the pores. These new directions in BILPs assessment can lead to new polymers with improved functions.

The moderate porosity of BILPs can be attributed to rapid pore formation and network interpenetration during the synthesis. Accordingly, the general scope of this study is centered about new synthetic strategy to improve BILPs surface area and selectivity. The new modifications consist of controlling the formation rate of BILPs by applying acid-catalyzed processes and introducing new functionalities capable of enhancing gas capture and separation. Furthermore, at the electronic level, new BILPs with extended pi-conjugated units may open the door for new applications such as sensing and optoelectronics.

Chapter 2

New Insights into Carbon Dioxide Interactions with Benzimidazole-Linked Polymers

2.1 Introduction

As we discussed earlier, porous organic polymers (POPs) having basic sites that can bind considerable amounts of CO_2 with moderate binding energies, such as BILPs, are among the promising materials for CO_2 capture.[69] In contrast to the well-established MOFs, the interaction between POPs and CO_2, to a large extent, has been limited to routine physisorption studies because of the amorphous nature of POPs, which precludes theoretical studies and investigation by powder X-ray diffraction or inelastic neutron scattering techniques.[99] Overcoming such limitations would be essential to pinpoint factors that govern CO_2 interaction with host POPs, which can aid in the design of enhanced CO_2 adsorbents. For example, earlier studies on BILPs suggested that the main CO_2 interaction sites would be limited to the electron lone pair on the imidazole nitrogen and hydrogen bonding through the (N-H) bond (Figure 2.1).

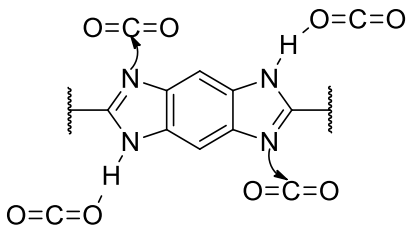

Figure 2.1: Suggested interactions between CO_2 and the imidazole moieties in BILPs.

However, such interactions do not consider the possible participation of the non-functionalized moiety (e.i. aryl-groups or C-H bonds) in the interaction of the host materials with CO_2. Thus, further studies are required to explore the role of the aryl groups in CO_2 interactions with the backbone of BILPs.

In this Chapter, we describe the synthesis of two BILPs containing benzo-bis(imidazole) and 3,3'-bibenzimidazole moieties and determine their CO_2 capture capacity and selectivity over CH_4 and N_2. Moreover, we highlight the impact of the electronic nature of imidazole-containing units on the binding site and affinity for CO_2 using density functional theory (DFT).

2.2 Experimental and Computational Studies

Materials, Methods and Experimental Procedures

All starting materials and solvents were obtained from Acros Organics, Sigma- Aldrich or Frontier Scientific, unless otherwise noted, and used without further purification. 1,2,4,5-Tetrabromobenzene, 3,3'-Diaminobenzidine tetrahydrochloride-hydrate (DABA), 1,2,4,5-Benzentetraamine tetrahydrochloride (BTA), 1,4-Dioxane (extra dry over molecular sieves) and ethylacetate were obtained from Acros organic. Chloroform (stabilized with amylene) was purchased from Aldrich Company and used without further purification. Tetrahydrofuran (THF) was dried by distillation from Na/benzophenone. Tetrakis(4-formylphenyl)benzene(TFPB), was synthesized and recrystallized over ethylacetate and dichloromethane/hexane (1:1) mixture as mentioned in their published methods.[69e, 100] All reactions were handled under an inert atmosphere of nitrogen using Schlenk line technique. Elemental microanalyses were performed at the Midwest Microlab, LLC. Liquid ^{1}H and ^{13}C NMR spectra were obtained on a Varian Mercury-300 MHz NMR spectrometer (75 MHz carbon frequency). Solid-state ^{13}C cross-

polarization magic angle spinning (CP-MAS) NMR spectra for solid samples were taken at Spectral Data Services, Inc. Spectra were obtained using a Tecmag-based NMR spectrometer operating at a H-1 frequency of 363 MHz, using a contact time of 1ms and a delay of three seconds for the CPMAS experiment. All samples were spun at 7.0 kHz. For Scanning Electron Microscopy imaging (SEM), samples were prepared by dispersing the material onto a sticky carbon surface attached to a flat aluminum sample holder. The samples were then coated with platinum at $1x10^{-4}$ mbar of pressure in a nitrogen atmosphere for 120 seconds before imaging. Images were taken on a Hitachi SU-70 Scanning Electron Microscope. Powder X-ray diffraction data were collected on a Panalytical X'pert pro multipurpose diffractometer (MPD). Samples were mounted on a sample holder and measured using Cu Kα radiation with a 2θ range of 1.5-35. FT-IR spectra were obtained as KBr pellets using Nicolet-Nexus 670 spectrometer. Porosity and gas sorption experiments were collected using a Quantachrome Autosorb IQ2 volumetric analyzer using adsorbates of UHP grade. In a typical experiment, a sample of BILPs (~ 60 mg) was loaded into a 9 mm large bulb cell (from Quantachrome) of known weight and then hooked up to the Autosorb-IQ2 and degassed at 120 °C for 12 hours. The degassed sample was refilled with helium, weighed precisely, and then transferred back to the analyzer. The temperatures for adsorption measurements were controlled by using a refrigerated bath of liquid nitrogen (77 K), liquid argon (87 K), or temperature controlled system (273 and 298 K).

Synthesis of BILPs and their Starting Materials

Synthesis of 1,2,4,5-Tetrakis-(4-formylphenyl)benzene (TFPB)

A mixture of 1,2,4,5-Tetrabromobenzene (1.5 g, 3.85 mmol), 4-formylphenylboronic acid (3.4 g, 22.7 mmol), palladium tetrakis(triphenylphosphine) (0.12 g, 0.10 mmol, 5.2 mol%), and potassium carbonate (4.2 g, 30.4 mmol) in dry 1,4-Dioxane (50 mL) was stirred under nitrogen atmosphere for 3 days at 90 °C. The white suspension reaction mixture was poured into slurry of ice containing 80 mL concentrated hydrochloric acid. The solid product was filtered and washed with water and 2 M HCl three times. The final product was obtained after extraction of the crude product with chloroform (4 × 50 mL). The extracted organic layer was dried over $MgSO_4$, filtered and evaporated under reduced pressure. The resultant solid was recrystallized from hot ethylacetate to afford (TFPB) as a yellowish powder (1.3 g, 68%). Anal. Calcd for $C_{34}H_{22}O_4$: C, 82.58%; H, 4.48%; O, 12.94% Found: C, 82.27%; H, 4.59%; O, 13.00%. ^{1}H NMR (300 MHz, $CDCl_3$, δ (ppm)): (s, 4H, formyl H), (s, 4H, Ar H), (d, 8H, Ar H) and (d, 8H, Ar H).^{13}C NMR ($CDCl_3$, 75 MHz) δ (ppm) 191.0, 146.0, 140.0, 136.0, 133.0, 130.0, 131.0.

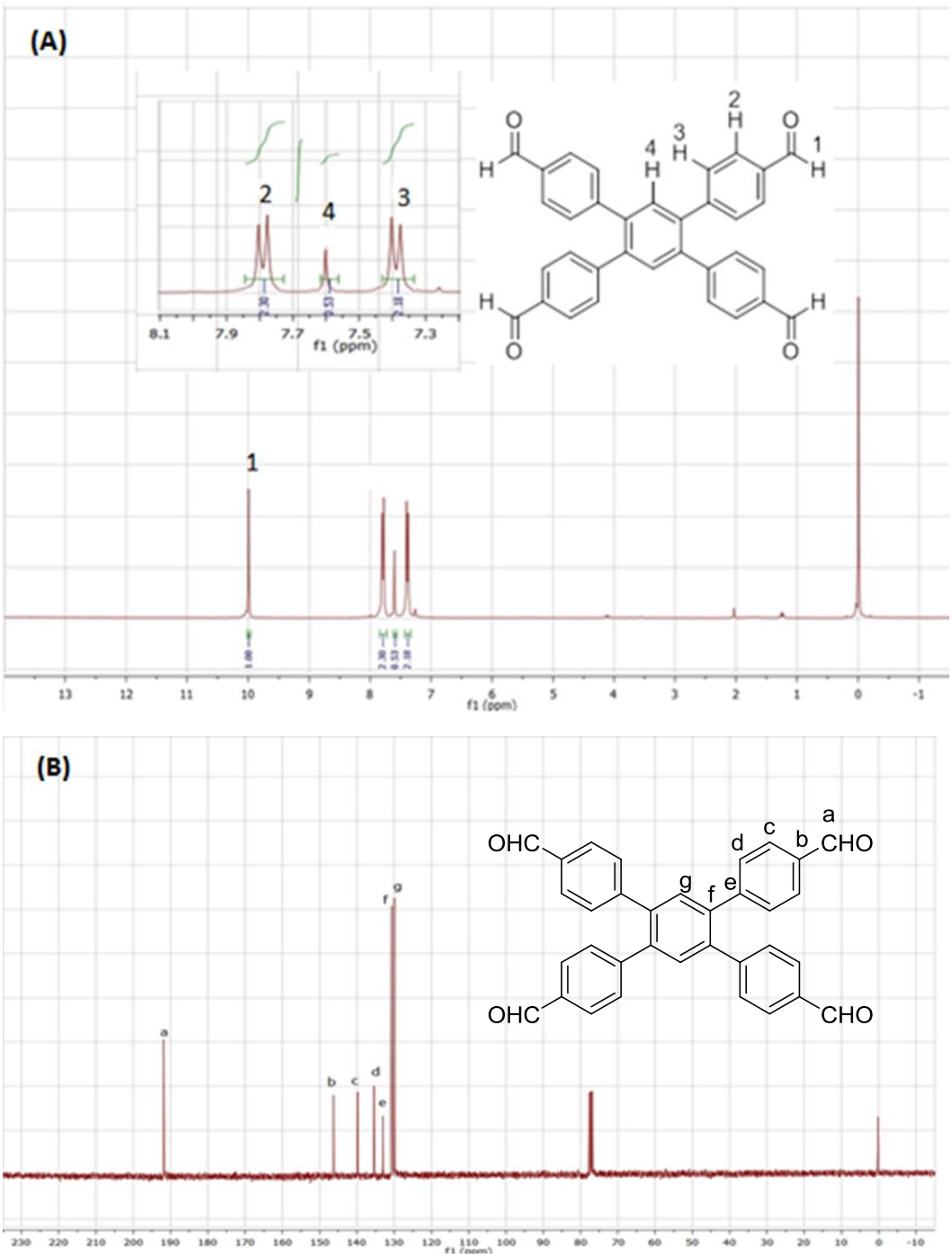

Figure 2.2: (A) ^{1}H-NMR and (B) ^{13}C-NMR of 1,2,4,5-Tetrakis-(4-formylphenyl)benzene (TFPB).

Synthesis of Bezimidazole-Linked Polymers

Synthesis of BILP-14

A 100 mL Schlenk flask was charged with (60 mg, 0.211 mmol) of 1,2,4,5-Benzenetetramine tetrahydrochloride salt and 30 mL of anhydrous DMF. The solution was cooled to around -30 °C and a solution of 1,2,4,5-tetrakis(4-formylphenyl)benzene (50 mg, 0.10 mmol) in 25 mL anhydrous DMF was added dropwise to the pervious charged solution over 3 hrs. Temperature was maintained around -30 °C until yellowish brown solid product formation was complete and then the temperature was raised to RT and kept overnight. The flask containing the reaction mixture was flashed with air for 15 minutes and capped. The reaction mixture was then heated in an oven at 130 °C (0.5 °C/min) for 3 days to afford a fluffy brownish polymer which was isolated by filtration over a glass frit. The product was immersed in DMF (20 mL overnight) and then in (20 mL) acetone. The product was dried under vacuum at 120 °C and 1.0 x 10^{-5} Torr for 20 hrs to give BILP-14 as a brown fluffy solid (56 mg, 73%). Anal. Calcd for $C_{46}H_{26}N_8.4H_2O$: C, 72.44%; H, 3.41%; N, 14.70 %. Found: C, 71.82%; H, 4.98%; N, 13.11%.

Synthesis of BILP-15

A 100 mL Schlenk flask was charged with (65 mg, 0.181 mmol) 3,3'-Diaminobenzidine tetrahydrochloride hydrate (used in excess due to the presence of 10% hydrate in the structure) and 30 mL of anhydrous DMF. The solution was cooled to around -30 °C and a solution of (40 mg, 0.081 mmol) 1,2,4,5-tetrakis(4-formylphenyl)benzene in 25 mL anhydrous DMF was added dropwise to the pervious charged solution over 3 hrs. Temperature was maintained around -30 °C until yellowish brown solid product formation was complete and then the temperature was raised to RT and kept overnight. The flask containing the reaction mixture was flashed with air

for 15 minutes and capped. The reaction mixture was then heated in an oven at 130 °C (0.5 °C/min) for 3 days to afford a fluffy brownish polymer which was isolated by filtration over a glass frit. The product was immersed in DMF (20 mL overnight) and then in (20 mL) acetone. The product was dried under vacuum at 120 °C and 1.0 x 10^{-5} Torr for 20 hrs to give BILP-15 as a brownish fluffy solid (60 mg, 81%) (Scheme 2.1) Anal. Calcd for $C_{58}H_{34}N_8.4H_2O$: C, 76.15%; H, 4.60%; N, 12.25%. Found: C, 75.90%; H, 4.66%; N, 12.60%.

2.3 Results and Discussion

Physical Characterizations of Benzimidazole-Linked Polymers (BILPs)

The new synthesized BILP-14 and BILP-15 were obtained by metal-free condensation reactions between 1,2,4,5-tetrakis(4-formylphenyl)benzene, 1,2,4,5-benzenetetramine tetrahydrochloride and 3,3'-diaminobenzidine tetrahydrochloride, respectively. The synthetic procedure was discussed in detail in the experimental section. After isolation and purification of the polymers, the resulting products were obtained in good yields and their structural aspects and chemical composition were established using spectral and analytical methods and the results were consistent with all reported BILPs.[69]

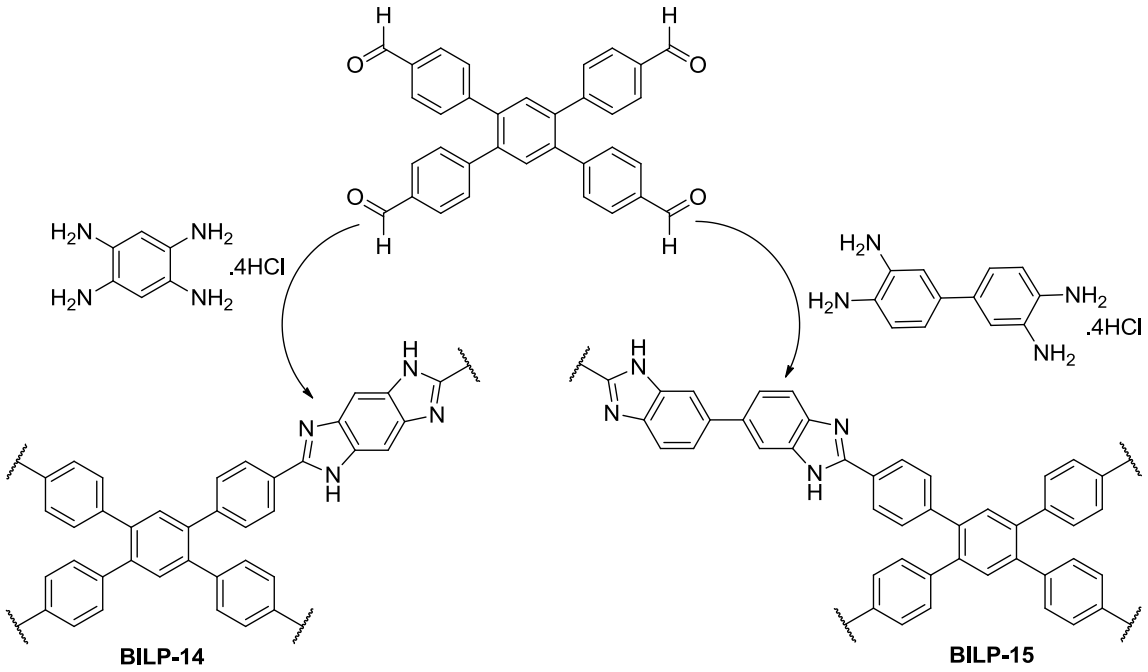

(i) DMF, -30 ^{o}C, 3h; (ii) DMF, 25 ^{o}C, 6 hr under N_2; (iii) DMF, 130 ^{o}C, 72 hr under O_2

Scheme 2.1: Synthesis of BILP-14 and BILP-15

In order to determine the phase purity of the products, scanning electron microscopy (SEM) was used to scan the morphology present in the polymers. The sample preparation step was mentioned in the materials and methods section. The SEM images of as-prepared polymers revealed agglomerated particles ca. 0.5-0.3 μm in size for both BILP-14 and BILP-15 (Figure 2.3). Powder x-ray diffraction studies on the activated polymers indicated that both polymers are amorphous (Figure 2.4A). The thermal stability of the polymers was confirmed by thermo-gravimetric analysis (TGA), which indicated that both BILPs are thermally stable up to 400 °C under N_2 (Figure 2.4B). Both polymers are chemically stable and remained intact upon treatment with aqueous HCl and NaOH (4M), which is consistent with the covalent nature of all BILPs.

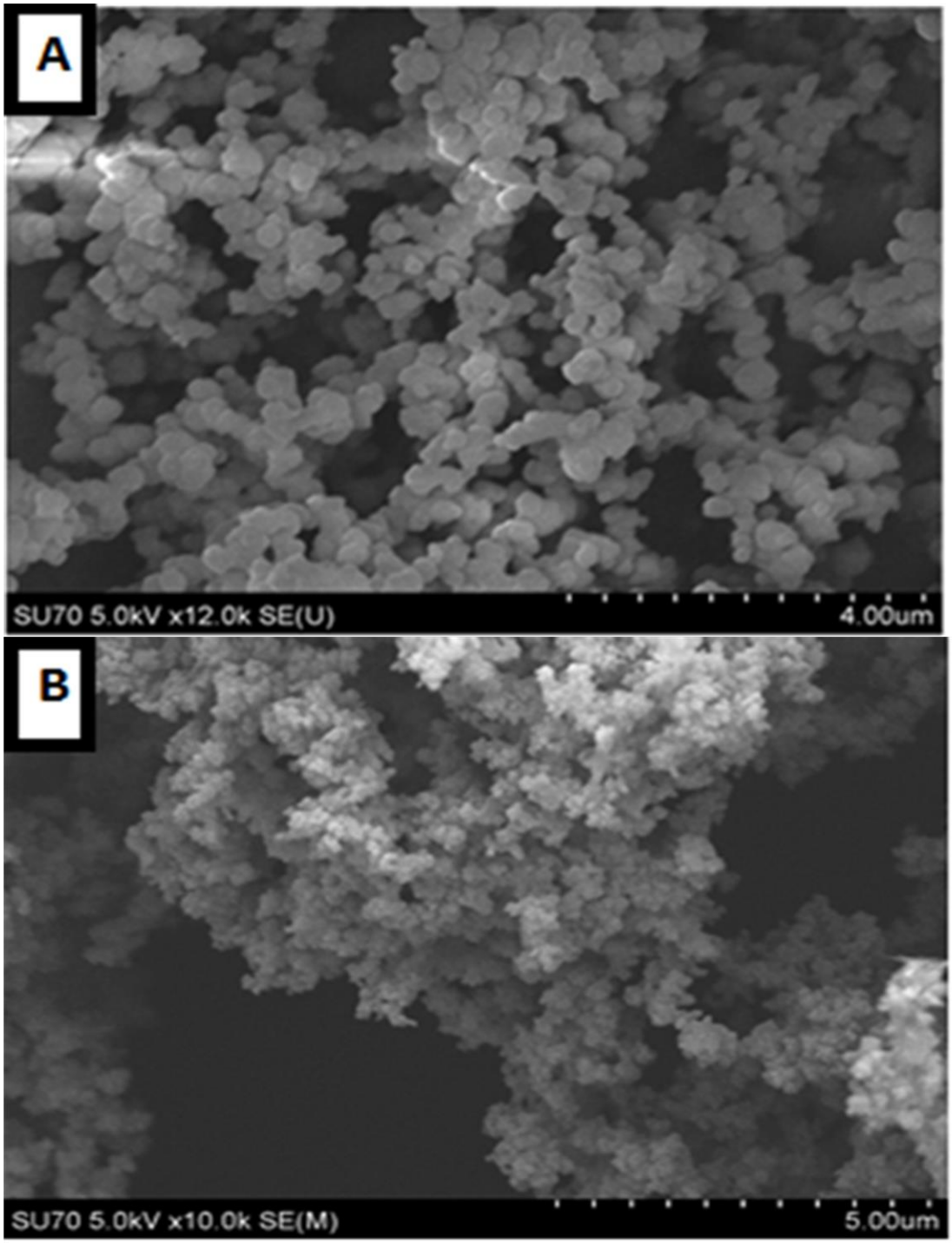

Figure 2.3: Scanning electron microscopy images of BILP-14 (A) and BILP-15 (B).

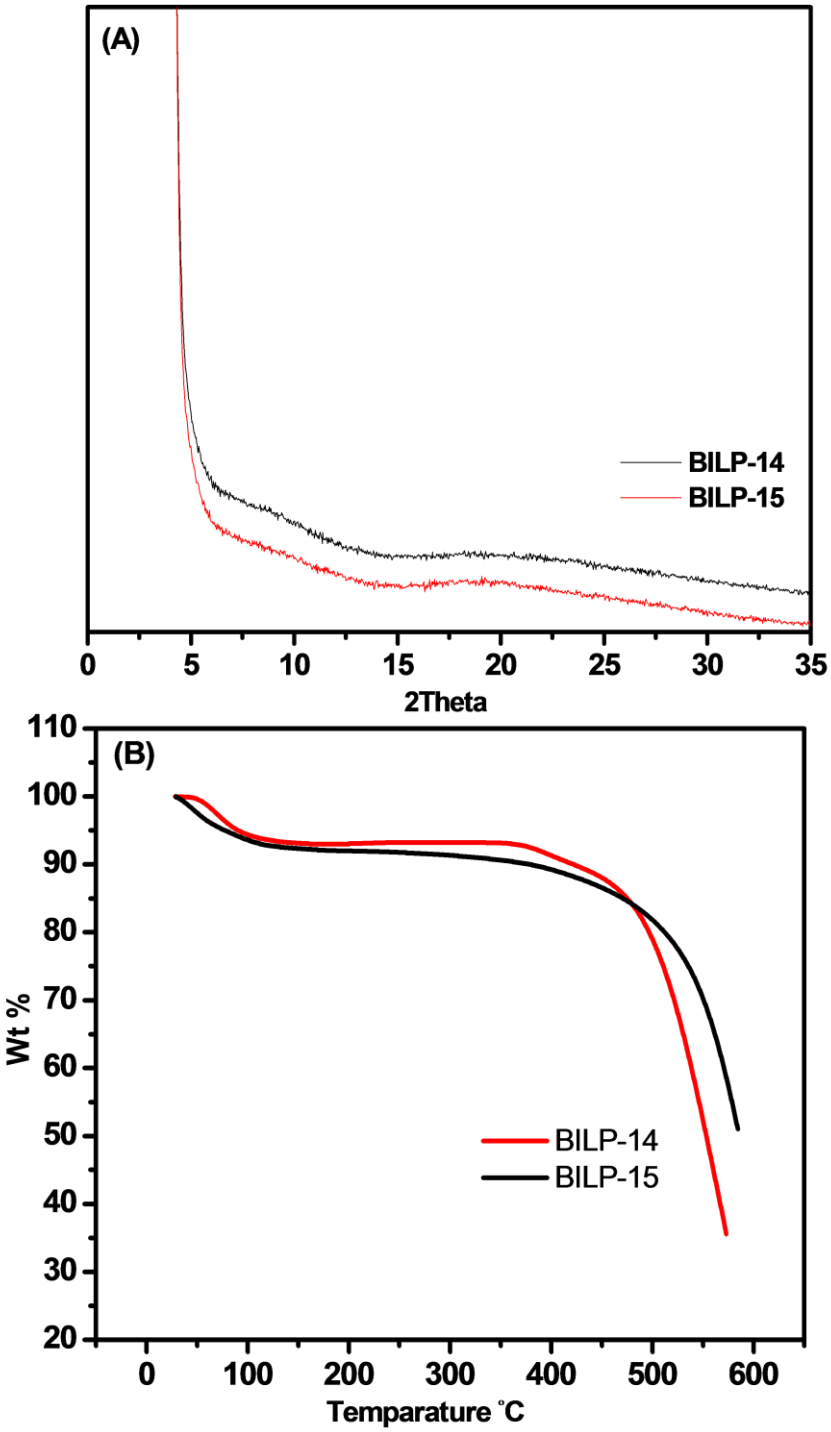

Figure 2.4: (A) X-ray diffraction pattern XRD pattern and (B) Thermogravimetirc analysis TGA

The chemical composition and connectivity of building blocks and the polymers BILP-14 and BILP-15 were investigated by spectral and analytical methods, which include: FT-IR, solid state ^{13}C CP-MAS and elemental analysis. The FT-IR spectra (Figure 2.5) confirmed the consummation of the aryl-aldehyde functional group at 1700 cm^{-1}, which disappeared completely upon condensation. Moreover, It showed broad bands at 3425 cm^{-1} (N-H stretching), 3220 cm^{-1} (hydrogen bonded N-H), new bands at 1620 cm^{-1} (C=N), and new vibrations at 1620, 1480 and 1435 cm^{-1}, which are attributed to the skeleton of the imidazole ring. The new band at 1640 cm^{-1} is due to the N-H bending and the bands ranging from 2750-3030 cm^{-1} are due to aromatic CH stretching. The region from 2000-400 cm^{-1} is expanded to show the characteristic vibrations of imidazole ring and the consumption of the aldehyde C=O functional group.

The ^{13}CP-MAS spectra (Figure 2.6) revealed characteristic peaks of the imidazole ring (NC(Ph)N) at ~151 ppm along with other peaks in the range (100-148 ppm) that correspond to the aryl units of BILPs.

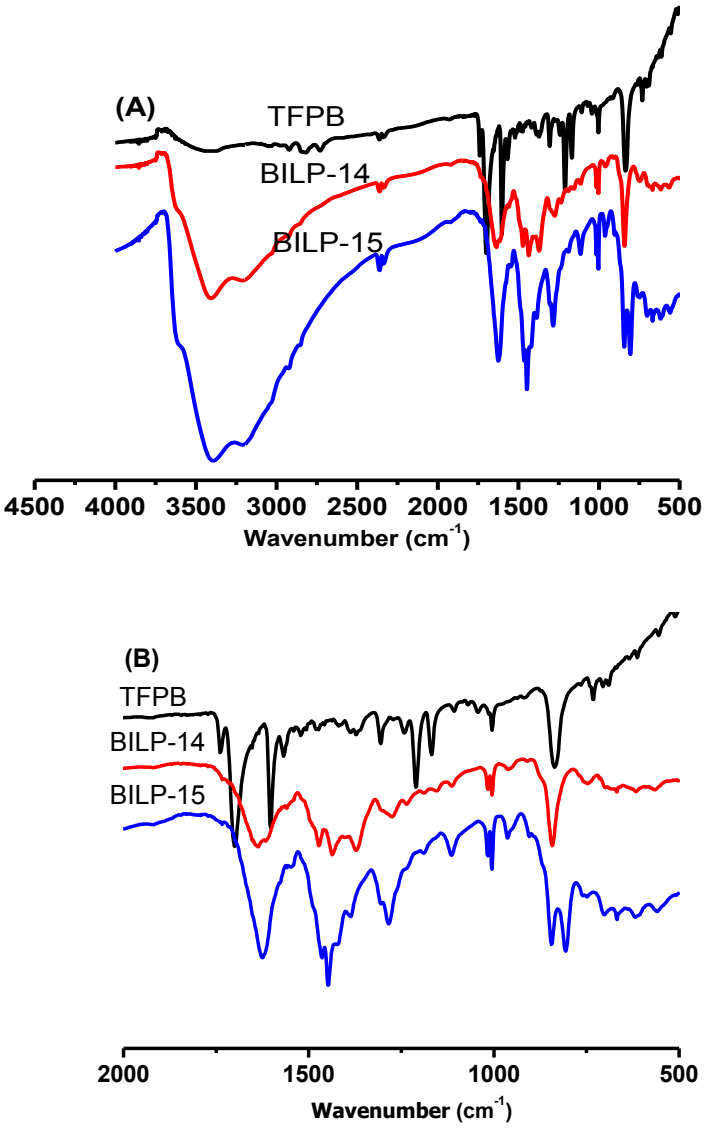

Figure 2.5: (A) FT-IR spectra of BILP-14 and BILP-15 (4500-500 cm^{-1}) and their aryl-aldehydes starting building unit, (B) FT-IR spectra of BILP-14 and BILP-15 and their aryl-aldehydes starting building unit in the range (2000-200 cm^{-1}).

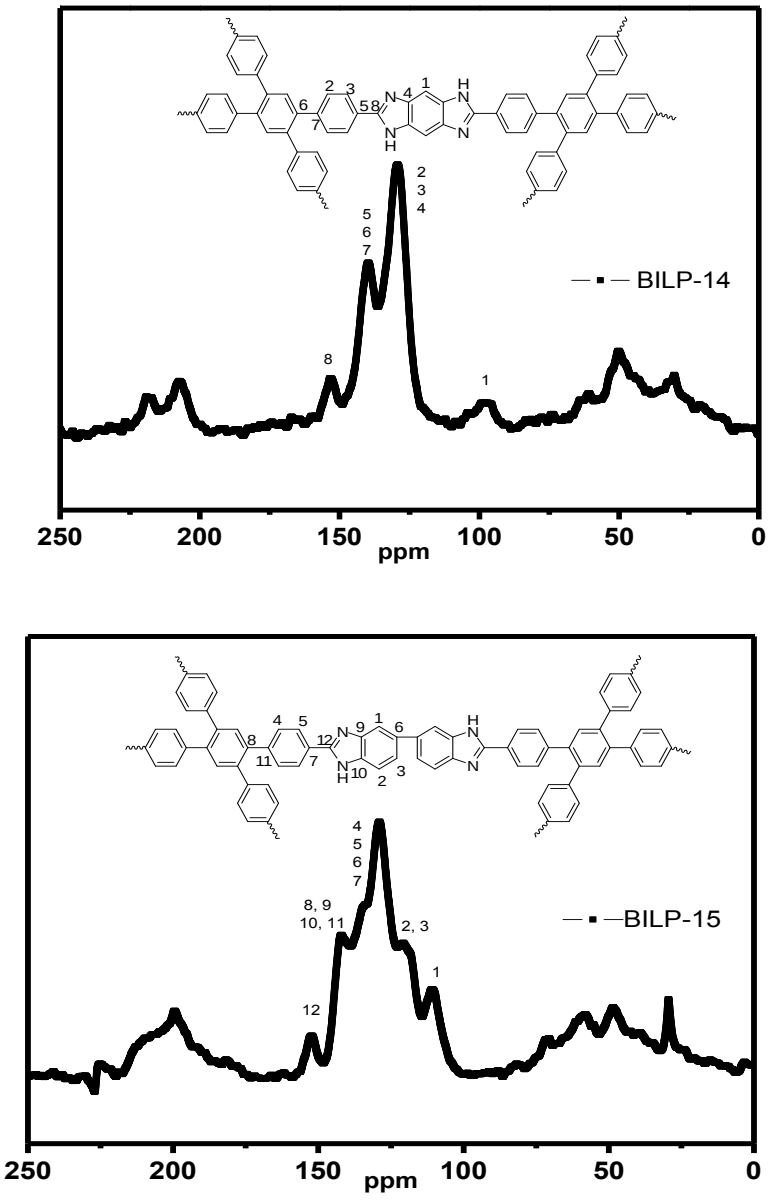

Figure 2.6: Solid state ^{13}C CP-MAS NMR spectra of BILP-14 and BILP-15.

2.3.1 Porosity Measurements, Gas Uptake and Related Calculations

Low-Pressure (0 – 1.0 bar) Gas Adsorption Measurements

To investigate the permanent porosity and assess the gas uptake capabilities of BILP-14 and BILP-15, the isotherms of argon, carbon dioxide, methane, and hydrogen and nitrogen sorption data were collected by the use of Quantachrome Autosorb IQ2. The gas isotherms were collected at different temperatures and used to evaluate the porosity, gas uptake properties, binding selectivity (S) and binding energy (Q_{st}). Argon isotherms were collected at 87 K and used to calculate the surface area by applying the Brunauer-Emmett-Teller (BET) model at P/P_0 between 0.05 and 0.15, pore size distribution (PSD) was estimated using the Non-Local Density Functional Theory (NLDFT), while the pore volume (Vp) was calculated from the isotherm at single pressure point. The NLDFT was able to calculate the pore size distribution on the adsorption branch with a cylindrical pore model on argon isotherm. The small gas isotherms (CO_2, CH_4, H_2 and N_2) were collected and used to evaluate the storage capacity of the polymers, the binding selectivity of CO_2/N_2 and CO_2/CH_4 and calculate the heats of adsorptions (Q_{st}).

Surface area measurements and pore size distributions

The porosity of BILP-14 and BILP-15 was evaluated from argon isotherms at 87 K. The isotherms are fully reversible with a minor hysteresis consistent with the powdery and flexible nature of BILPs (Figure. 2.7A). The surface areas of the polymers were calculated using the Brunauer-Emmett-Teller (BET) model at P/P_o between 0.05 and 0.15 and resulted in surface areas of 1005 $m^2\ g^{-1}$ for BILP-14 and 448 $m^2\ g^{-1}$ for BILP-15 (Figure 2.8). The notably low surface area for BILP-15 may arise from network interpenetration facilitated by the longer and flexible nature of the bibenzimidazole linker.

The pore volume (Vp) was calculated at P/P_o =0.95 bar and found to be 0.55 and 0.27 cc g^{-1} for BILP-14 and BILP-15, respectively. Pore size distribution curves were derived from (NLDFT) and found to be centered at about 7.0 Å for BILP-14 and 5.6 Å for BILP-15, which confirmed their microporous nature (Figure. 2.7B).

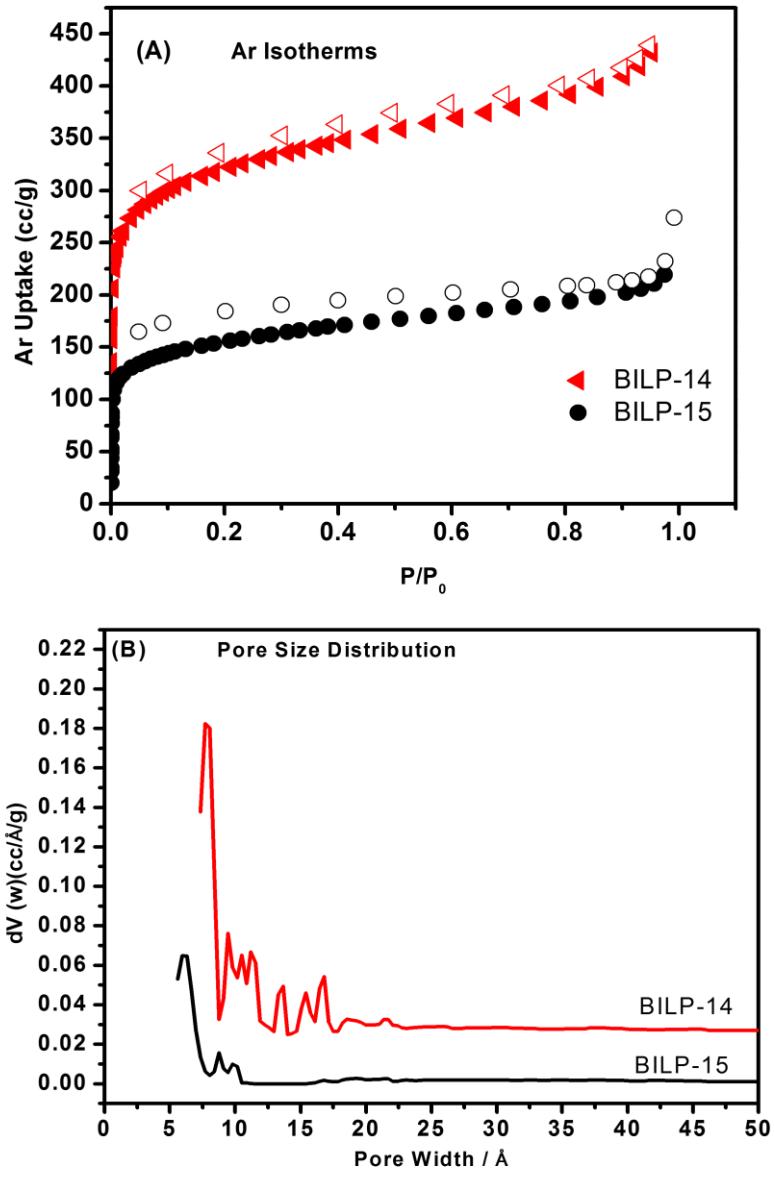

Figure 2.7: (A) Argon isotherms and (B) pore size distribution of BILP-14 and BILP-15.

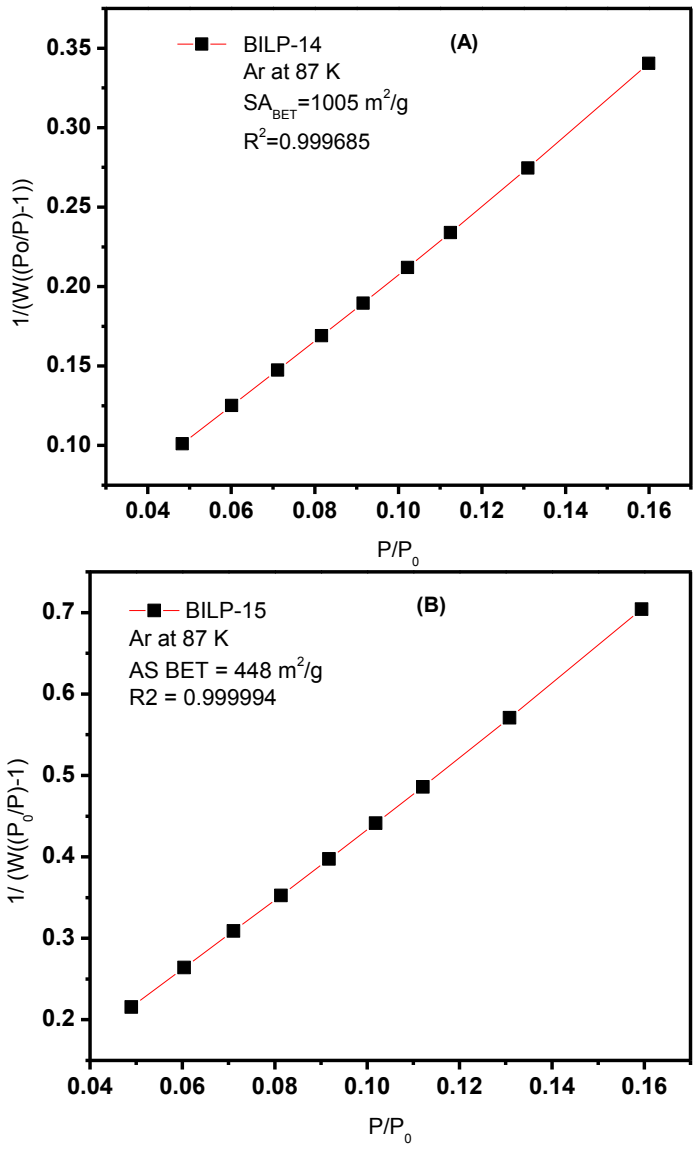

Figure 2.8: BET plots for BILP-14 and BILP-15 calculated from Ar adsorption isotherm at 87 K.

Low pressure gas uptake measurements

The performance of BILPs in gas separation and storage was considered after the porosity has been established. Accordingly, the low pressure carbon dioxide, hydrogen, methane, and nitrogen were measured at various temperatures and used to calculate the selectivity and heat of adsorption for BILP-14 and BILP-15. Low pressure CO_2, CH_4, and N_2 measurements were collected at 273 K and 298 K, while H_2 isotherms were collected at 77 K and 87 K. Interest in storing CH_4 stems from its potential in automotive applications due to its abundance and low carbon footprint, whereas CO_2 capture or separation from flue gases or coal-fired plants is highly attractive for environmental and economic reasons. The isotherms are fully reversible and exhibit a steep rise at low pressure and significant uptake at 1.0 bar. BILP-14 and BILP-15 gas uptake data are summarized in Table 2.2 and Figure 2.9. The low gas uptake data for BILP-15 can be attributed to the modest surface area and pore volume. The uptake of BILP-14 is similar to the best performing 2D BILPs (Table 1.1). Thus, the subnanometer porosity, and the chemical heterogeneity of the pores can significantly enhance the gas uptake capabilities.

Table 2.1: Gas sorption uptakes of BILP-14 and BILP-15

polymer	[a]SA BET	[b]H_2 uptake		[b]CO_2 uptake		[b]CH_4 uptake		[b]N_2 uptake	
		77 K	87 k	273 K	298 K	273K	298 K	273 K	298 K
BILP-14	1005	17	14	170	114	19	11	9.0	4.0
BILP-15	448	17	15	118	80	13.5	7.2	5.7	2.4

[a]Surface area (m^2 g^{-1}) and [b]Gas uptake in mg g^{-1} at 1 bar

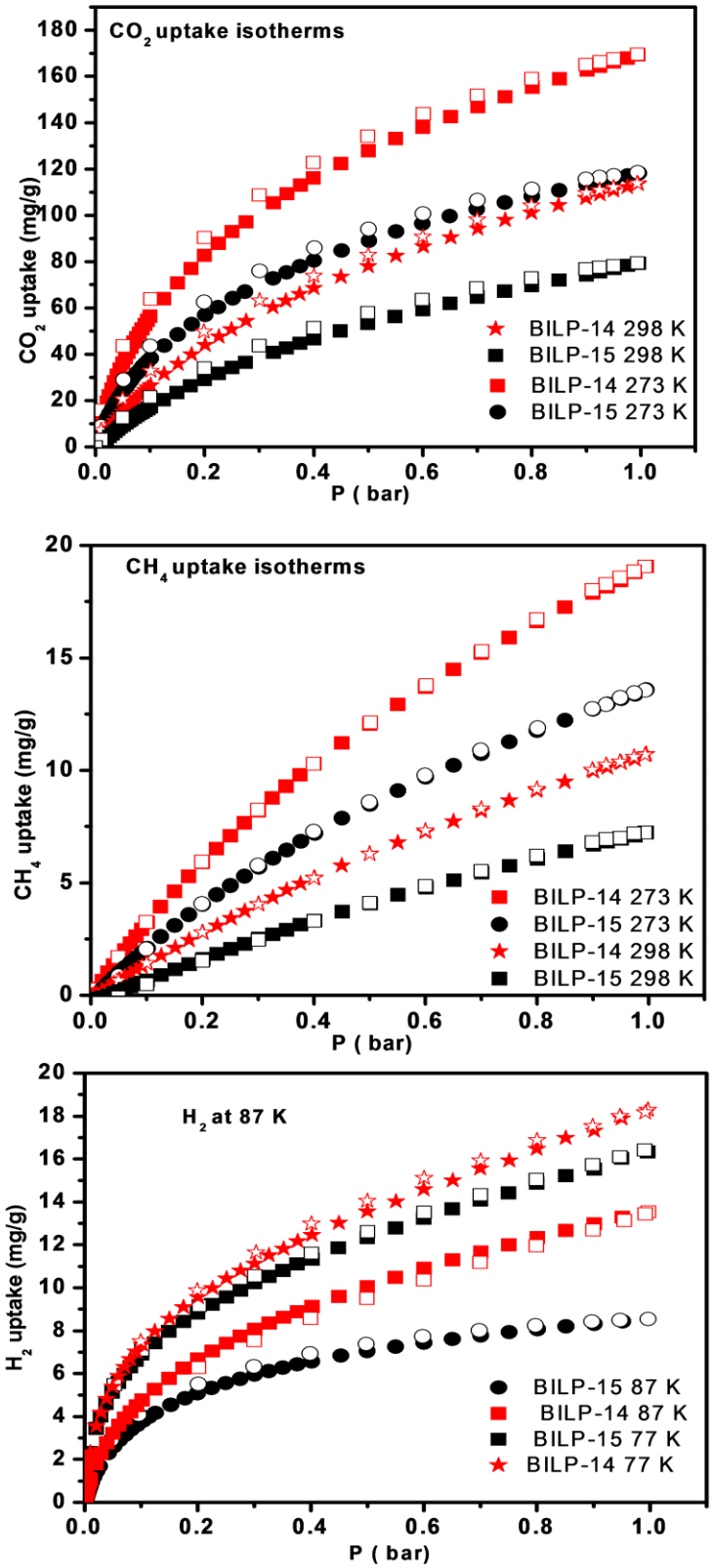

Figure 2.9: Methane, Carbon dioxide and Hydrogen uptake isotherms for BILP-14 and BILP-15 Adsorption filled, desorption (empty).

2.3. 2 Heats of Adsorption Calculations

The binding affinity (Q_{st}) of the small gases was calculated by fitting the pure isotherms on the virial equation (Eq.1.2), as discussed in Chapter 1 and listed in Table 2.2. The Q_{st} values for CO_2 at zero coverage fall in a very narrow range (33-33.5 kJ mol^{-1}) (Figure 2.1) and drop with higher loading at higher pressure up to 1.0 bar. These values are comparable to CO_2 selective MOFs which generally feature $–NH_2$ and –OH functionalized pores.[1b] In this study, we have attributed the high CO_2 binding affinity to the physical interactions which related to the hydrogen bonding or the dipole-quadrupole interactions between CO_2 molecules and imidazole moieties, while the other possible interactions related to (aryl(C-H)) bond interaction with CO_2 molecules according to DFT calculations. These interactions are weak enough to regenerate the polymer after the adsorption process without applying heat. On the other hand, the binding affinities for CH_4 and H_2 were calculated by applying the virial equation and resulted in Q_{st} values in the range of 21.0-27.0 kJ mol^{-1} for CH_4 and 7.1- 8.0 kJ mol^{-1} for H_2 as shown in Figure 2.10.

Table 2.2: Surface areas and Heats of Adsorption of BILP-14 and BILP-15

polymer	SA_{BET} $m^2 g^{-1}$	Q_{st} for H_2 kJ mol^{-1}	Q_{st} for CO_2 kJ mol^{-1}	Q_{st} for CH_4 kJ mol^{-1}
BILP-14	1005	7.1	33.0	23.3
BILP-15	448	8.0	33.5	26.5

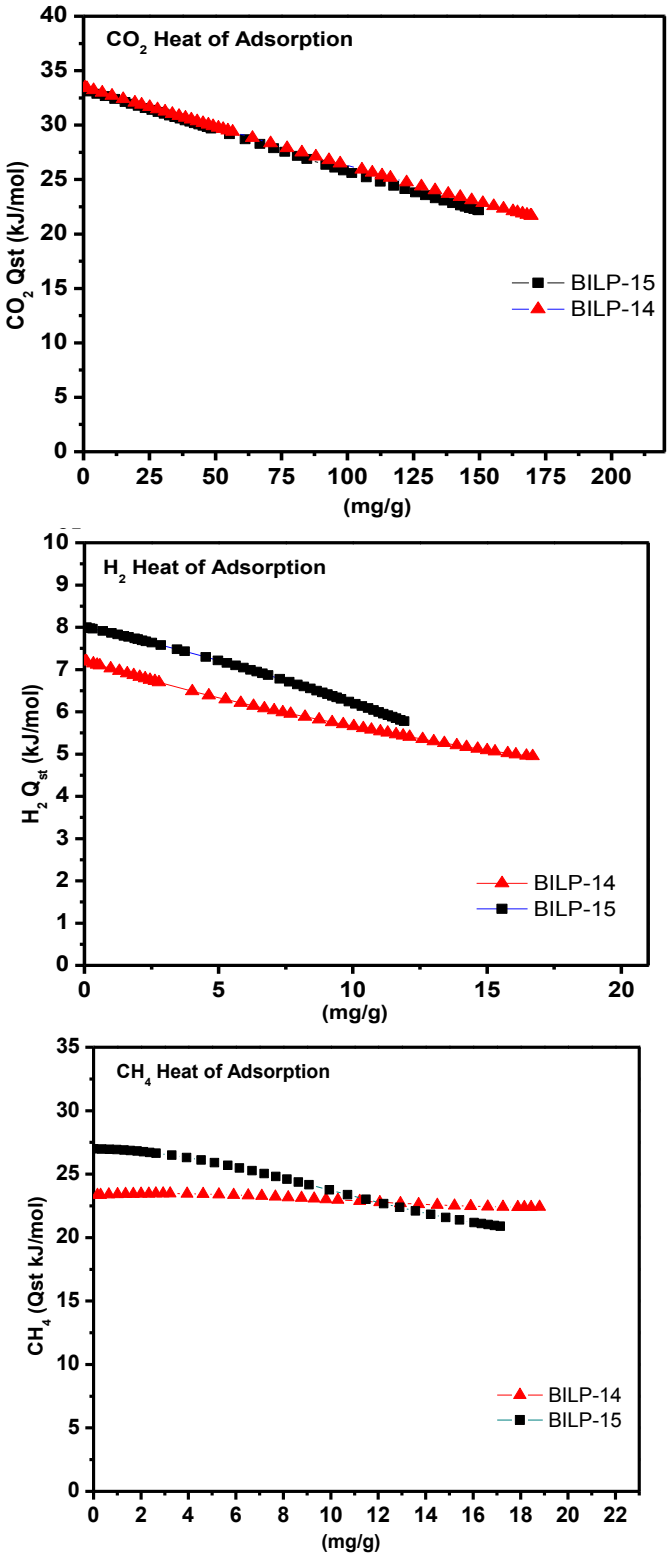

Figure 2.10: Heats of adsorption of H_2, CH_4 and CO_2 for BILP-14 and BILP-15 from the virial analysis

2.3.3 Selective Gas Uptake Studies

1. Initial Slope calculations

The selectivity of BILPs toward CO_2/N_2 and CO_2/CH_4 was calculated because CO_2 removal from flue gas or methane-rich gases (natural gas and landfill gas) is needed to mitigate climate change and to enhance the quality and energy density of methane-rich fuels. Based on that, selectivity studies were performed using the initial slope of pure gas isotherms collected at 273 K and 298 K and the pressure range (0- 1.0 bar) (Figure. 2.11). The steep rise in CO_2 compared to CH_4 and N_2 is due to the more favorable interactions between CO_2 molecules and the accessible nitrogen sites of imidazole moieties through H-bonding and/or dipole-quadrupole interactions. The initial slope selectivity values CO_2/N_2 (273 K/298 K) for BILP-14 and BILP-15 are (83/63) and (56/49), respectively. The selectivity is higher for BILP-15 when compared to BILP-14, which is most likely because of the narrower pores of BILP-15 (5.6 Å). These values are among the highest for purely organic polymers that show considerable CO_2 uptake at low pressure. In contrast, the selectivity for CO_2/CH_4 was much lower and falls in a narrower range (8-9) that does not seem to change significantly upon temperature change. This low selectivity originates from the fact that methane is more strongly adsorbed than N_2 because of the higher polarizability of CH_4 (26.0×10^{-25} cm^3) vs. N_2 (17.6×10^{-25} cm^3); the polarizability of CO_2 (26.3×10^{-25} cm^3) makes CO_2 removal from natural gas very challenging. The initial slope values for BILP-14 and BILP-15 are summarized in Table. 2.3.

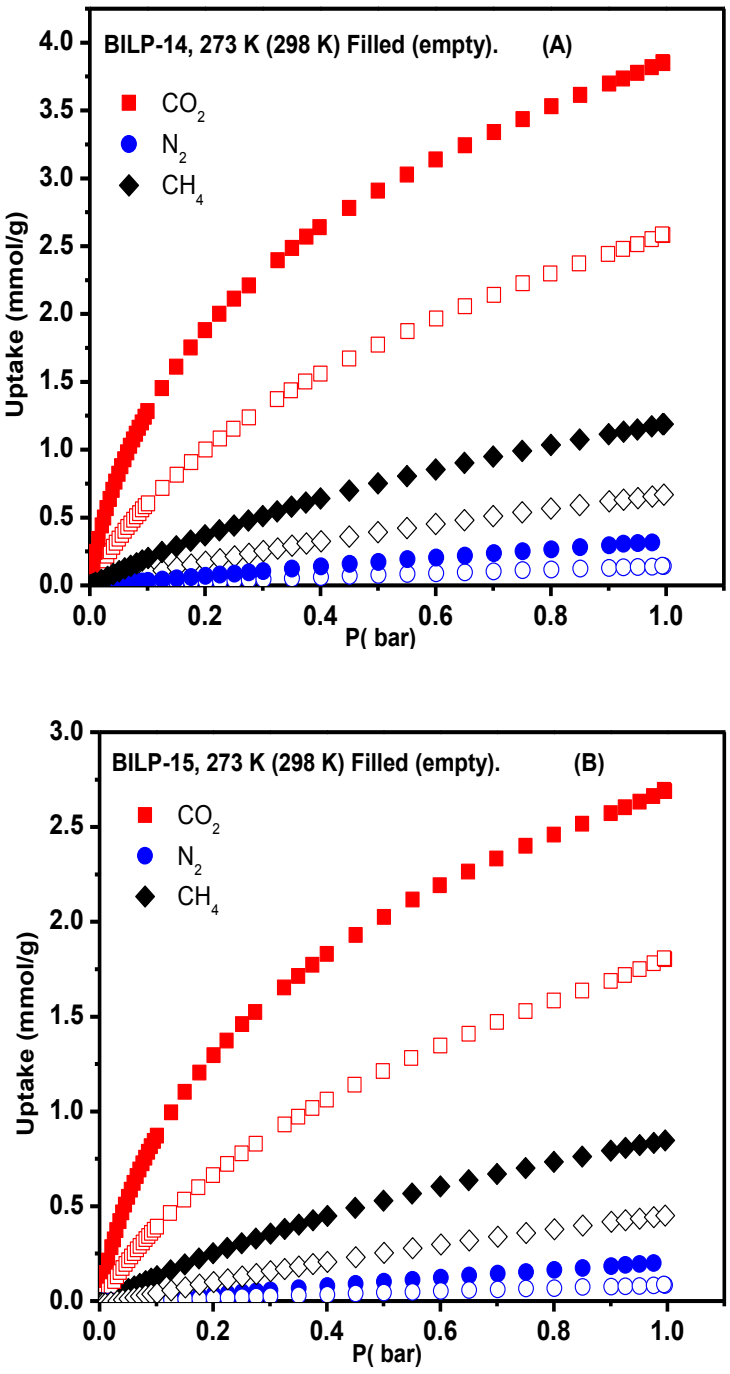

Figure 2.11: Gas sorption capacities for BILP-14 and BILP-15 at 273 K and 298 K.

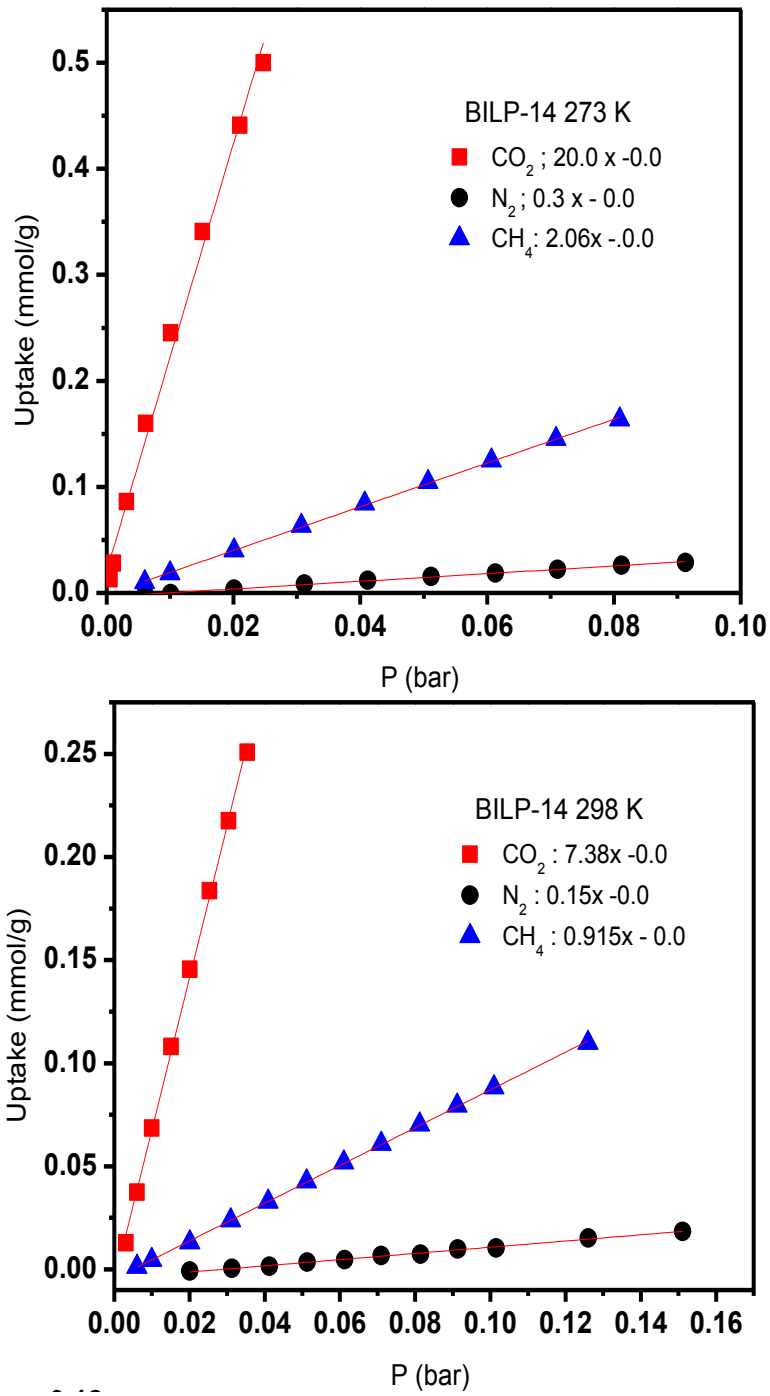

Figure.2.12A: The initial slope calculations for BILP-14 at 273 K and 298 K.

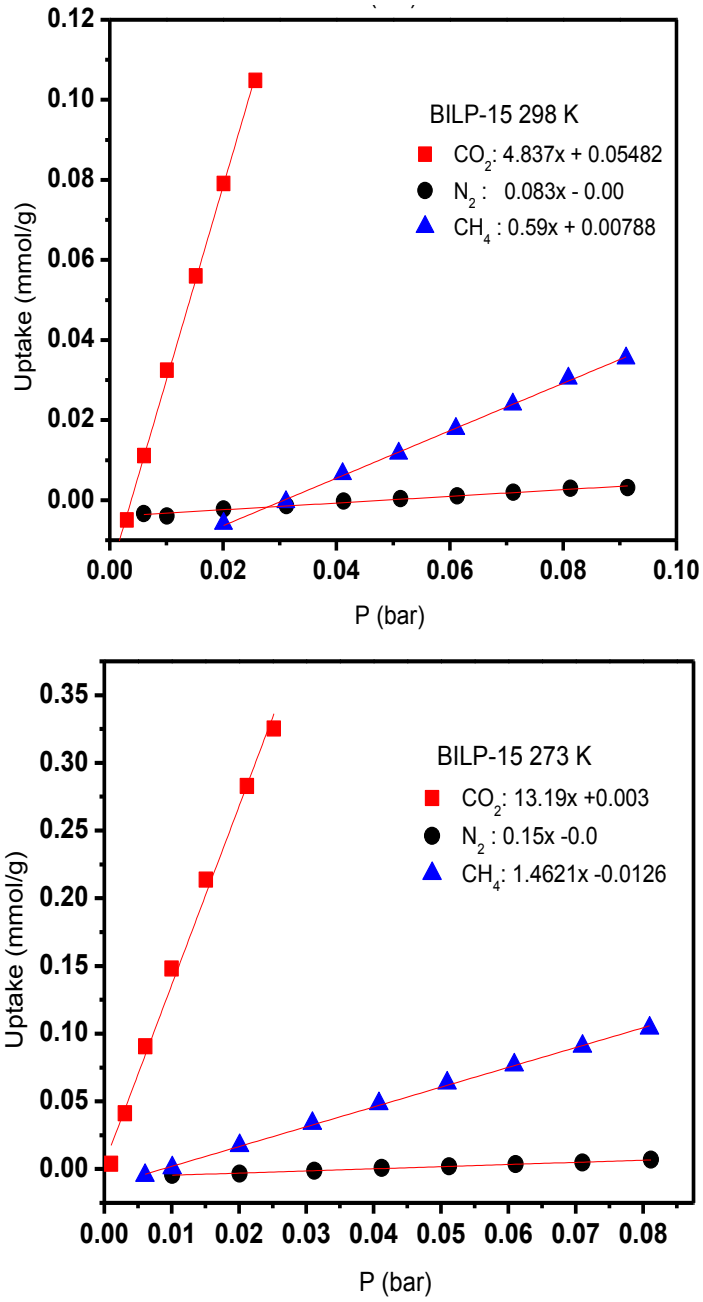

Figure.2.12B: The initial slope calculations for BILP-15 at 273 K and 298 K.

2. Ideal adsorbed solution theory (IAST)

The initial slope calculations method has been used widely for organic and inorganic hybrid materials including COFs, MOFs, ZIFs, porous carbons and cage molecules. In spite of its common use, this method which employs single-component isotherms cannot give the actual gas selectivity because selectivity factors do not take into consideration other factors such as competition of the gas molecules for adsorption sites.[69c] However, the selectivity calculations form single-component isotherms are useful and convenient to compare the performance of different porous materials in selective adsorption. On the other hand, the ideal adsorption theory (IAST) was applied to overcome the limitations of the initial slope calculations and predict the selectivity in gas mixtures, taking in consideration the competition between gas molecules. In The IAST method, the pure component isotherms of CO_2 measured at 273 and 298 K were fitted with the dual-site Langmuir (DSL) model

$$\boldsymbol{q = q_A + q_B = q_{sat,A}\frac{b_A p}{1+b_A p} + q_{sat,B}\frac{b_B p}{1+b_B p}} \qquad \text{(Eq.2.1)}$$

with T-dependent parameters b_A and b_B

$$\boldsymbol{b_A = b_{A0}\, exp\left(\frac{E_A}{RT}\right),\ b_B = b_{B0}\, exp\left(\frac{E_B}{RT}\right)} \qquad \text{(Eq.2.2)}$$

where, $\boldsymbol{q}$ is molar loading of adsorbate (mol kg^{-1}), $\boldsymbol{q_{sat}}$ is saturation loading (mol kg^{-1}) , $\boldsymbol{b}$ is parameter in the pure component Langmuir isotherm (Pa^{-1}), $\boldsymbol{p}$ is bulk gas phase pressure (Pa), $-E$ is heat of adsorption (J mol^{-1}), R is ideal gas constant (8.314 J mol^{-1} K^{-1}), T is absolute

temperature (K), subscripts A and B refers to site A and site B, respectively. Since the pure component isotherms of CH_4 and N_2 do not show any inflection characteristic they were fitted with the single-site Langmuir (SSL) model

$$\boldsymbol{q = q_{sat,A}\frac{b_A p}{1+b_A p}} \qquad \text{(Eq.2.3)}$$

with T-dependent parameter b_A

$$\boldsymbol{b_A = b_{A0}\, exp\left(\frac{E_A}{RT}\right)} \qquad \text{(Eq.2.4)}$$

Pure-component isotherm fitting parameters were then used for calculating Ideal Adsorbed Solution Theory (IAST)[1] binary-gas adsorption selectivities, S_{ads} defined as

$$\boldsymbol{S_{ads} = \frac{q_1/q_2}{p_1/p_2}} \qquad \text{(Eq.2.5)}$$

Applying the IAST equation resulted in selectivity values which are consistent with the selectivity values reported in the initial slope calculations (Figure. 2.12 and Table 2.4).

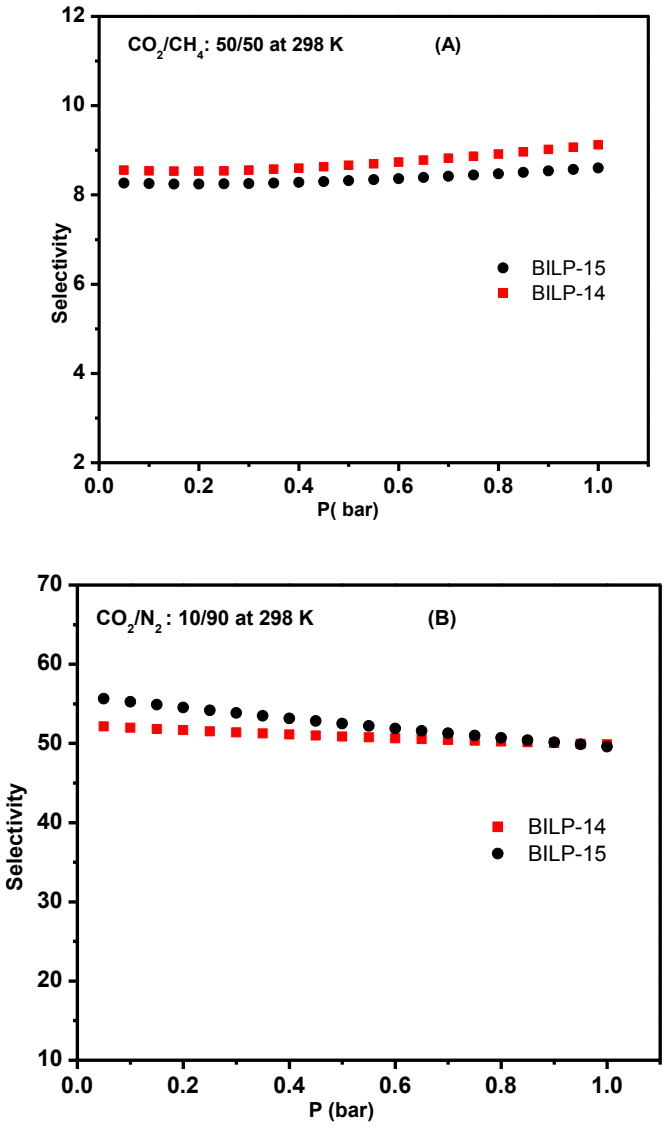

Figure 2.12C: IAST selectivities of CO_2/ CH_4 for 50/50 (A), and CO_2/ N_2 10/90 (B) binary mixtures at 298 K for BILP-14 and BILP-15.

Table 2.3: Initial slope selectivity of BILP-14 and BILP-15 at 273 K (298 K), and the IAST selectivity of BILP-14 and BILP-15 at 298 K for the binary mixtures of (CO_2/N_2: 10:90) and (CO_2/CH_4: 50:50).

BILP	Selectivity			
	Initial slope at 273 K (298 K)		IAST at 298 K	
	CO_2/N_2	CO_2/CH_4	CO_2/N_2 (10:90)	CO_2/CH_4 (50:50)
BILP-14	56 (49)	10 (9)	52	8.6
BILP-15	83 (63)	9 (8)	56	8.3

2.4. Computational Study

To gain insight into CO_2 interactions with benzimidazole-linked polymer structures and investigate the role of both heterogeneous and homogeneous moieties of BILP-14 and BILP-15 on CO_2 interaction mechanism, we carried out DFT calculations (through collaboration).[69e] Basically, the calculations have been applied with two different forms for exchange-correlation potential. These forms include the local density approximation (LDA) functional consisting of the Slater exchange and Volk-Wilk-Nusair correlation functional (SVWN)[101] and the hybrid meta exchange-correlation functional M06[102] formulated by Zhao and Truhlar. The M06 functional includes corrections for long-range dispersive forces. Since the interaction of CO_2 molecules with these units is expected to be weak (physisorption), it is necessary to go beyond the generalized gradient functionals that do not include van der Waal's terms and hence underestimate binding affinities. LDA, on the other hand, overestimates binding[103] and in cases of weak interactions it yields binding energies closer to experimental values.

It must be stated that LDA does not include dispersive forces and the agreement between theory and experiment in weakly bound systems is due to fortunate cancellation of errors. The computations have been carried out by using Gaussian 09 package[104] and 6-311+G*[105] basis sets for all our computations. The convergence in the total energy and force were set at 1×10^{-6} eV and 1×10^{-2} eV/Å, respectively. Several initial geometries were taken where the CO_2 molecules were allowed to approach different binding sites of the benzimidazole-containing units. The polymers BILP-15 and BILP-14 were modeled by their corresponding benzimidzole-containing units, biphenylimidazole (BILP-15) and benzimidazole (BILP-14), to ease the computational demand. The geometries were first optimized without symmetry constraints at the LDA level of theory, and were then used as input and re-optimized using M06 functional. All optimizations are

followed by frequency calculations to confirm that the structures represent genuine minima in the potential energy surface (PES). The atomic charges have been evaluated by applying the Natural Bonding Orbital method (NBO).[106]

2.4.1. Results and discussion of the computation study

1. In the case of BILP-15@2CO_2 and BILP-14@2CO_2, systems where two CO_2 molecules were allowed to interact with different binding sites of BILP-15 and BILP-14, the minimum energy structures were obtained when CO_2 binds to the N-sites of BILP-15 and BILP-14 at a bond length of 2.73 and 2.72 Å, respectively, on opposite sides of the aromatic system (Figure. 2.6A, B). The bond lengths between the C and O atoms of the CO_2 molecule interacting with these monomeric systems remains the same (i.e 1.16 Å) as that of the neutral CO_2, whereas its bond angle reduces to 176°. A similar angle deformation value (3.1°) was reported by Vogiatzis *et al* for imidazole-bonded CO_2.[107]

2. In the case of BILP-15@4CO_2 and BILP-14@4CO_2, the interacting sites for CO_2 are different for both systems. In BILP-15@4CO_2 (Figure. 2.13C), all CO_2 molecules preferably bind to the N-sites of BILP-15 (2.82-2.89 Å), whereas in BILP-14@4CO_2 (Figure. 2.6D), two CO_2 molecules bind to the N-sites of BILP-14 (2.72-2.74Å) and the other two bind to the C-atom of the central phenyl ring (3.06-3.15Å). The CO_2 molecules are mostly captured by the N-site of biphenylimidazole (BILP-15) and benzimidazole (BILP-14). This can be explained by the fact that the imidazole rings attached to these systems are highly polar and carry a net dipole moment. The CO_2 molecule, on the other hand, is highly symmetric and has a permanent electrical quadrupole moment that can be described as two electrical dipoles sitting back-to-back and pointing in opposite directions. The electrostatic force of interaction between the CO_2 molecules and these polymeric systems can be attributed to the dipole-quadrupole interaction.

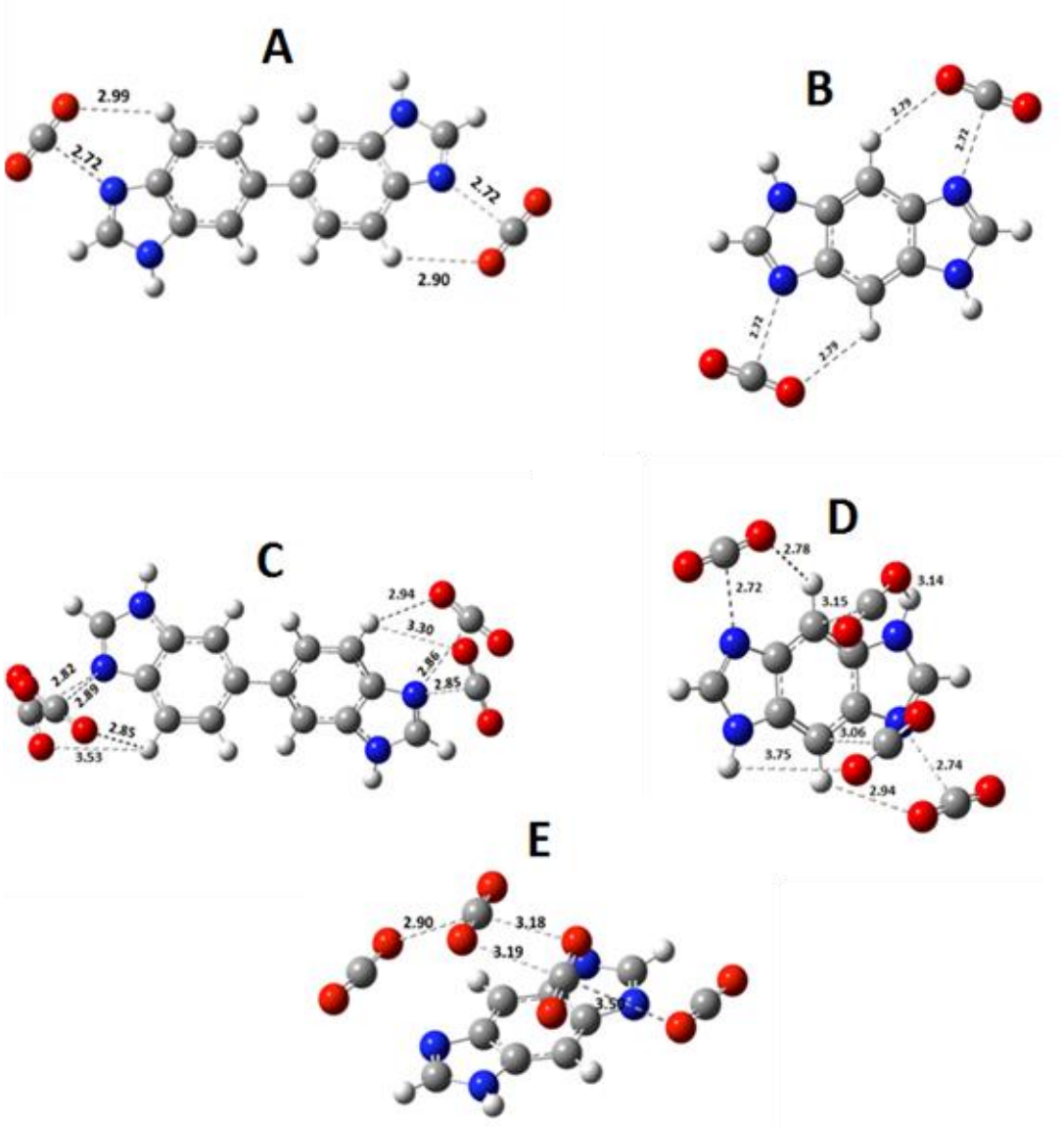

Figure 2.13: Fully optimized geometries of BILPs-CO_2 interactions calculated at M06/6-311+G* level of theory. The bond lengths are in Å. The blue, grey, white and red colors stand for N, C, H and O atoms, respectively.

The DFT study also revealed that these interactions are further stabilized by complementary interactions involving aryl C-H and CO_2 (C-H···O=C=O) with variable bond distances in the range of 2.79-2.94 Å (Figure. 2.13D).

3. Side-on intermolecular interactions between CO_2 molecules in BILPs@4CO_2 systems lead to O=C=O(δ-)…C(δ+)O_2 interactions (2.90 to 3.33 Å; Figure 2.13E). Noteworthy, similar interactions have been authenticated by both experimental and theoretical studies for CO_2 loaded NOT-300; a MOF that has a channel window diameter of ~6.5 Å similar to the PSDs of BILP-14 (7.0 Å) and for BILP-15 (5.6 Å).[99] Hence, both BILPs have high potential for efficient CO_2 capture. The bonding preference can be explained by examining the NBO charges between the BILP-15@nCO_2 and BILP-14@nCO_2 systems and NBO charges on the C-atom of CO_2 and the N-atom of BILPs as shown in Table 2.4. The NBO charges between the C-atom of CO_2 and the C-atom of central phenyl ring are +0.3e and -0.8e, respectively.

The binding affinities, Eb per CO_2 were calculated by determining the equilibrium geometries and corresponding total energies of these complexes according to the following equations.

$$\mathbf{E_b} = \frac{\mathbf{E[BILP-15@nCO_2]-E[BILP-15]-n*E[CO_2]}}{\mathbf{n}} \qquad \text{(Eq.2.6)}$$

$$\mathbf{E_b} = \frac{\mathbf{E[BILP-14@nCO_2]-E[BILP-14]-n*E[CO_2]}}{\mathbf{n}} \qquad \text{(Eq.2.7)}$$

Where n = 2 or 4, E[BILP-15@nCO_2] and E[BILP-14@nCO_2] are the total energies of BILP-15 and BILP-14 interacting with n number of CO_2 molecules. E[BILP-15], E[BILP-14] and E[CO_2] are the total energies of BILP-15, BILP-14 and the CO_2 molecule, respectively. The listed results for the LDA/6-311+G* method have shown good agreement with the experimental Q_{st} values at zero coverage.

Table 2.4: CO_2 Binding energies calculated at the LDA/6-311+G* and M06/6-311+G* and the Atomic charges on C-atom of CO_2 and N-atom of the imidazole.

Cluster	Binding Energy Eb kJ mol^{-1}		Atomic Charges by NBO Natural Charge bonding Method	
	LDA/6-311 +G*	M06/6-311 +G*	C-atom of CO_2	N-atom of the imidazole
BILP-15 2CO_2	-33.22	-19.28	+0.44e	-0.15e
BILP-15 4CO_2	-30.26	-18.29	+0.38e	-0.20e
BILP-14@2CO_2	-35.26	-20.32	+0.44e	-0.21e
BILP-14@4CO_2	-32.39	-20.30	+0.43e	-0.14e

2.5 Conclusions

In conclusion, we have synthesized two new benzimidazole-Linked Polymers (BILPs) using the reported synthesis approach of BILPs. The polymers were characterized by using several spectral and analytical techniques to predict the purity, stability, and chemical connectivity. The resulting polymers are thermally stable and exhibit amorphous and permanent microporous natures. The sorption measurements were applied to evaluate the porosity, pore volume, and pore size distribution evaluations. Moreover, the small gas isotherms were collected and used to calculate the heats of adsorption and selectivity values for the polymers. All results have shown consistent behavior of the new BILPs when compared to all reported BILPs. All numerical data are tabulated and plotted in above sections.

Herein, we have also reported for the first time the applicability of density functional theory (DFT) to predict the CO_2 sites of interaction on the BILPs backbone. DFT calculations have confirmed that the main CO_2 interaction site is the interaction with the accessible N-sites, in addition to the possibility of the CO_2 interaction with the C-H bond of the aryl moieties in the polymers. The selectivity values have shown that the new BILPs are promising materials for gas separation, while their modest surface area is very low to be used in gas storage applications. Accordingly, to address this limitation, the surface area needs to be improved by developing new synthetic strategies as discussed in the next Chapters.

Chapter 3

Acid-Catalyzed Formation of Benzimidazole-Linked Polymers: Impact on Porosity and Selective Gas Admission and Uptake

3.1. Introduction

Acid-catalyzed covalent bond formation plays an important role in organic synthesis. Generally, the rate of bond formation and catalyst (acid) amounts are not crucial for the synthesis of discrete molecules since they can be isolated and purified from the reaction mixture. However, controlling these parameters during the synthesis of porous organic polymers or frameworks is essential, as they dictate porosity levels and solid-state packing. For example, several classes of POPs were synthesized by acid-catalyzed processes that lead to C-N bond formation as in the case of imine-linked covalent organic polymers (COFs) and polybenzimidazoles (PBIs). [67a, 108] In both systems, condensation reactions are facilitated by controlling catalyst loading (acid) and the temperature of the reaction.[79, 109] Because water is generated during condensation steps, it can mediate the rate of reversible bond formation as in the case of imine-linked polymers, and hence control both porosity and crystallinity of the resulting materials.

The role of water in such reactions was clearly outlined for COFs generated from boronic acids in self-condensation reactions or co-polymerization with aryl-diols.[110] Likewise, the synthesis of PBIs was accomplished by applying acid-catalyzed polycondensation reactions

of diamine moieties with benzene carboxylic acids, aryl-aldehydes, and esters in the presence of catalytic polyphosphoric acid. [71-72, 109] However, the resulting PBIs have very modest surface area (~200 m^2 g^{-1}) because of the ill-defined synesthetic approach that does not take into consideration the role of the acid.

In this study, we seek to unravel the impact of acid concentration and ratio on the porosity level of BILPs. We have synthesized new polymers using our previously reported method wherein HCl-salts of the amine-containing building units lead to uncontrolled condensation rates and thus porosity. The resulting polymers were resynthesized using HCl-free amine building units in the presence of diluted acid concentrations and variable acid:amine ratios. The impact of the acid on the formation rate and the porosity was investigated, the new polymers were characterized using several spectral and analytical techniques, and their selectivity and binding affinity for small gas mixtures were studied and compared to other BILPs. Surprisingly, the latter synthetic route improved porosity by 47-97%, which can be very useful when high surface area materials are designed for high-pressure gas storage.

3.2 Experimental

Materials and methods

The starting materials, solvents, and characterization methods used in this study are reported in Chapter 2 unless otherwise noted. The new chemicals that were used for the first time in this study are reported in this section and used without further purification. 3,3'-Diaminobenzidine (DAB) was obtained from Acros Organics, tetrakis(4-formylphenyl)benzene (TFPB), and 1,3,5-Tris-(4-formylphenyl) benzene (TriFPB) were synthesized according to published methods.[69c, 69e]

All reactions were handled under an inert atmosphere of nitrogen using Schlenk line technique. All spectral and analytical characterization techniques including: elemental microanalyses, FT-IR spectra, liquid ^{1}H and ^{13}C-NMR spectra, Solid-state ^{13}C, thermogravimetric analysis (TGA), scanning electron microscopy imaging (SEM), and powder X-ray diffraction (XRD), were performed according to the methods reported in Chapter 2. Porosity and gas sorption experiments were collected by a Quantachrome Autosorb IQ2 volumetric analyzer using adsorbates of UHP grade and following the same activation and sample collection procedures.

Synthesis of BILPs

Synthesis of BILP-15

The synthetic procedure of BILP-15 was reported in Chapter 2, in the experimental section 2.2.2.

Synthesis of BILP-16

BILP-16 was synthesized in a similar fashion to the preparation of BILP-15 (Chapter 2) using 3,3'-Diaminobenzidine tetrahydrochloride hydrate (62 mg, 0.172 mmol) and 1,3,5-(4-formylphenyl)-benzene (48.5 mg, 0.125 mmol) in anhydrous DMF under a nitrogen atmosphere. The resulting product was filtered and dried under vacuum at 120 °C and 1.0 x 10^{-5} Torr for 20 hrs to give a fluffy brownish polymer, BILP-16 (100 mg, 75%) yield. Anal. Calcd. for $C_{90}H_{54}N_{12}.6H_2O$: C, 76.60%; H, 3.83%; N, 11.91%. Found: C, 76.36%; H, 4.51%; N, 12.42%.

Synthesis of BILP-15C

The acid-catalyzed BILP-15C was synthesized following the method mentioned above for BILP-16 with minor modifications. The new acid-catalyzed method was applied on BILP-15C using 3,3'-Diaminobenzidine (40 mg, 0.187 mmol) and HCl (1.9 mL, 0.4M, 0.75 mmol) in the first step, and 1,2,4,5-tetrakis(4-formylphenyl)benzene (46 mg, 0.093 mmol) in the next step in anhydrous DMF under a nitrogen atmosphere. The resulting product was filtered and dried under vacuum at 120 °C and 1.0 x 10^{-5} Torr for 20 hrs to give BILP-15C as a green fluffy solid (65 mg, 76%). Anal. Calcd. for $C_{58}H_{34}N_8.6H_2O$: C, 73.26%; H, 4.84%; N, 11.79%. Found: C, 72.83%; H, 4.28 %; N, 12.03.

Synthesis of BILP-16C

BILP-16C was synthesized in a fashion similar to the preparation of BILP-15C using 3,3'-Diaminobenzidine (40 mg, 0.187 mmol) and HCl (0.4 M/1.9 mL, 0.75 mmol) in the first step and 1,3,5-(4-formylphenyl)-benzene (48.5 mg, 0.125 mmol)in the next step in anhydrous DMF. The resulting product was filtered and dried under vacuum at 120 °C and 1.0 x 10^{-5} Torr for 20 hrs to give BILP-16C as a green solid (90 mg, 72%). $C_{90}H_{54}N_{12}.6H_2O$: C, 76.60%; H, 3.83%; N, 11.91% Found: C, 77.33%; H, 4.51%; N, 11.79%.

3.3. Results and discussions

The synthesis of BILPs reported in this study was carried out by following the synthetic protocol we developed recently, which is based on condensation coupling reactions between aryl-aldehydes and aryl-*o*-diamines (HCl salts) building units in DMF. [69] HCl not only catalyzes imidazole ring formation but also provides amine building units with chemical stability against

oxidation by molecular oxygen. To investigate the impact of HCl content on the porosity of BILPs we have selected 3,3'-Diaminobenzidine (DAB) and its HCl-salt; 3,3'-Diaminobenzidine tetrahydro-chloridehydrate (DABA), to construct BILPs from tetrakis(4-formylphenyl)benzene (TFPB), and 1,3,5-Tris-(4-formylphenyl) benzene (TriFPB) as depicted in Scheme 3.1. Treatment of DABA with TFPB and TriFPB afforded BILP-15 and BILP-16, respectively, in good yields. On the other hand, DAB was treated with TFPB and TriFPB under acid-controlled conditions to afford BILP-15C and BILP-16C (Scheme 3.2) having adjustable porosity levels as discussed below.

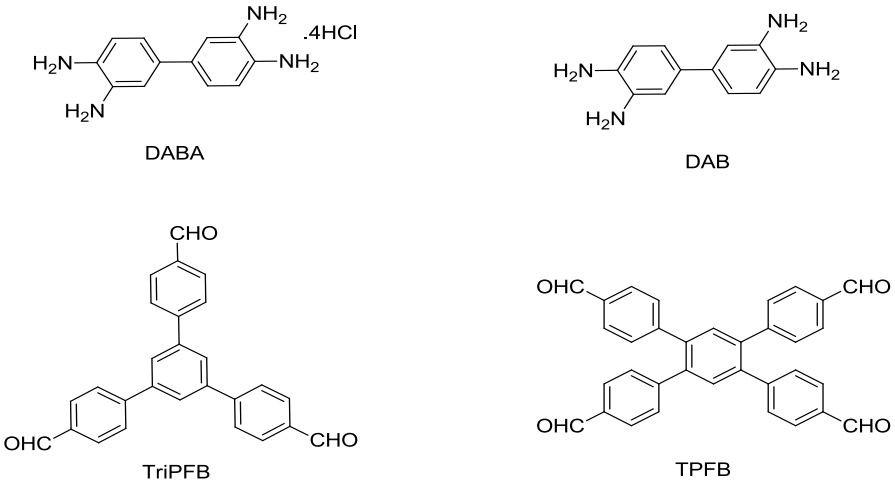

Scheme 3.1: Molecular building blocks used for the synthesis of non-catalyzed and acid-catalyzed BILPs.

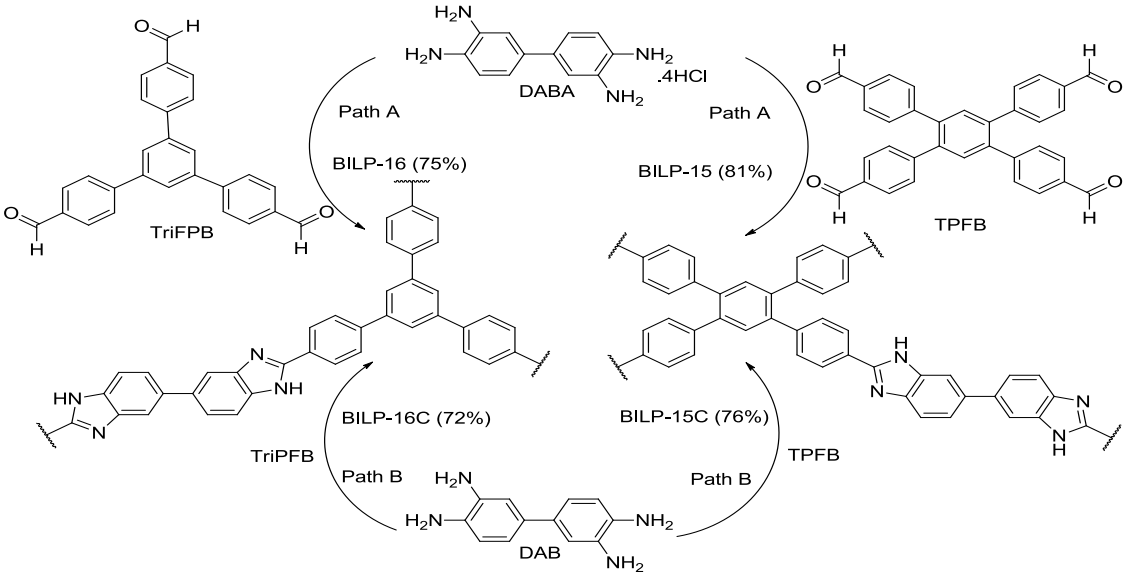

Scheme 3.2: Schematic representation of the synthesis of the non-catalyzed and acid-catalyzed BILPs.

To establish the chemical composition of BILPs and connectivity between building units of the polymers we collected elemental analysis and carried out spectral (FT-IR, ^{13}C-CP-MAS NMR) studies. Micro elemental analysis showed that BILP-15/BILP-15C and BILP-16/BILP-16C have virtually identical chemical compositions. All polymers exhibit excellent chemical stability upon treatment with aqueous HCl and NaOH (4 M) and only start to decompose at ~400 °C according to TGA studies (Figure 3.1). The FT-IR spectra confirmed imidazole ring formation and the consumption of the starting materials.

The FT-IR spectra (Figure 3.2) show N-H stretching bands around 3425 cm^{-1} (free N-H bond), 3220 cm^{-1} (hydrogen bonded N-H), while the new bands at 1620 cm^{-1} (C=N) confirmed imidazole ring formation. The skeleton vibration of imidazole ring appeared at the 1499 and 1440 cm^{-1}, respectively. The new bands around 1355 cm^{-1} can be assigned to C-N stretching and for benzimidazole ring, while the bands at 1640 cm^{-1} are due to N-H bending. The ^{13}C CP-MAS

NMR spectra of all BILPs (Figure 3.3) contain the main characteristic peak of the imidazole ring at ~152 ppm, which belongs to the carbon of the imidazole ring that originated from the aldehyde carbon. The other peaks in the aromatic range are consistent with the building units used to construct the polymers. Scanning electron microscopy (SEM) revealed aggregated particles of variable sizes (Figure 3.4), while the featureless powder XRD patterns (Figure 3.5) are consistent with expected amorphous nature of BILPs.[69]

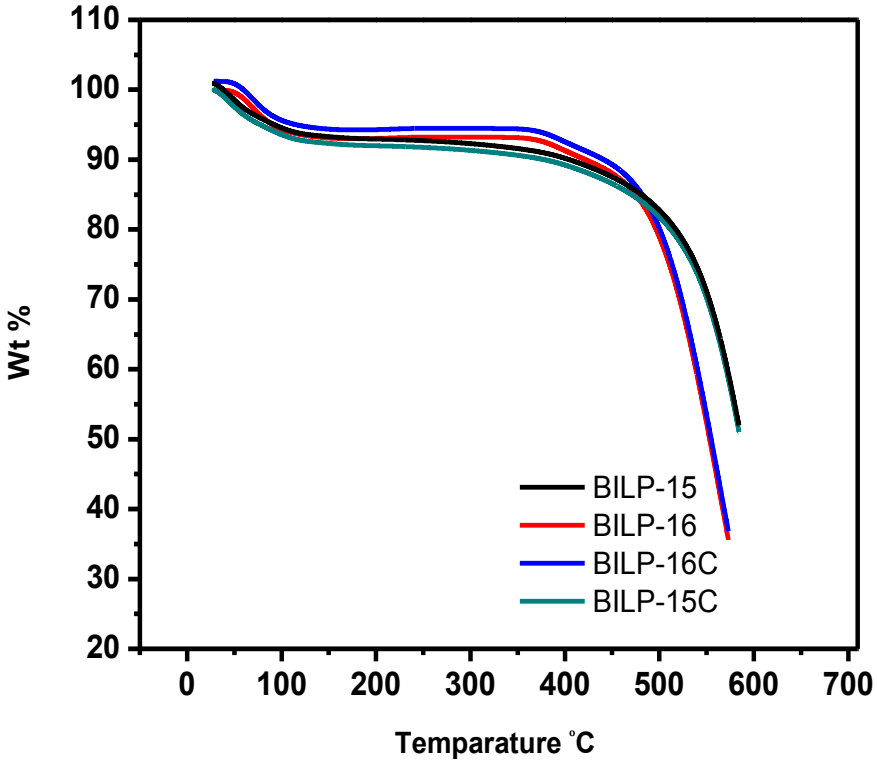

Figure 3.1: Thermogravimetric analysis (TGA) of BILP-15, BILP-16, BILP-15C, and BILP-16C

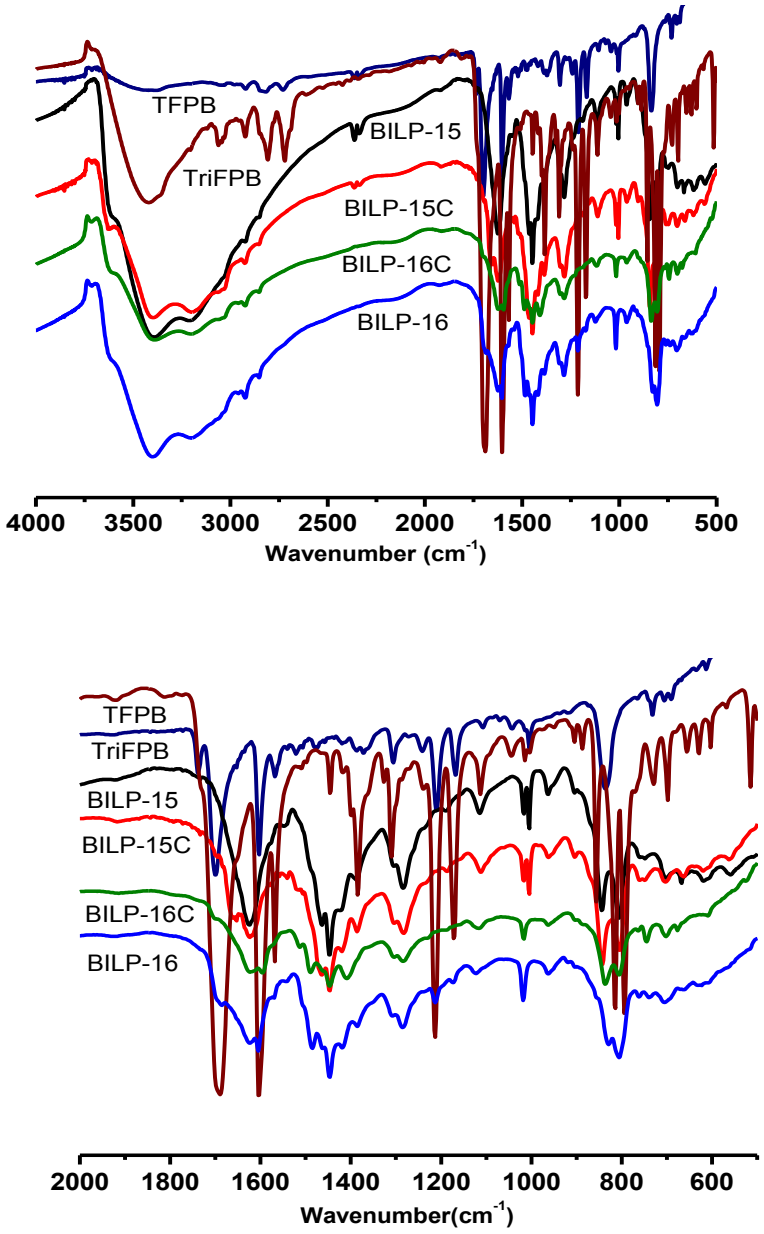

Figure 3.2: FT-IR spectra of BILP-15, BILP-16, BILP-15C and BILP-16C and their starting building units

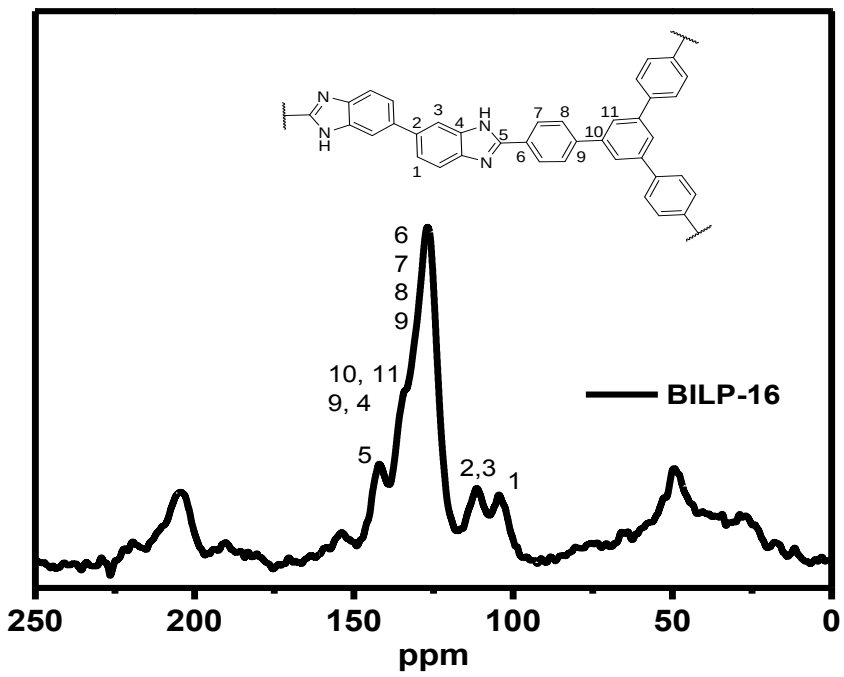

Figure 3.3: Solid state ^{13}C CP-MAS NMR spectra for BILP-16

(Note: The successful formation of BILP-15 was reported in Chapter 2, while BILP-15C and BILP-16C were confirmed by elemental analysis, FT-IR only and used for further measurements).

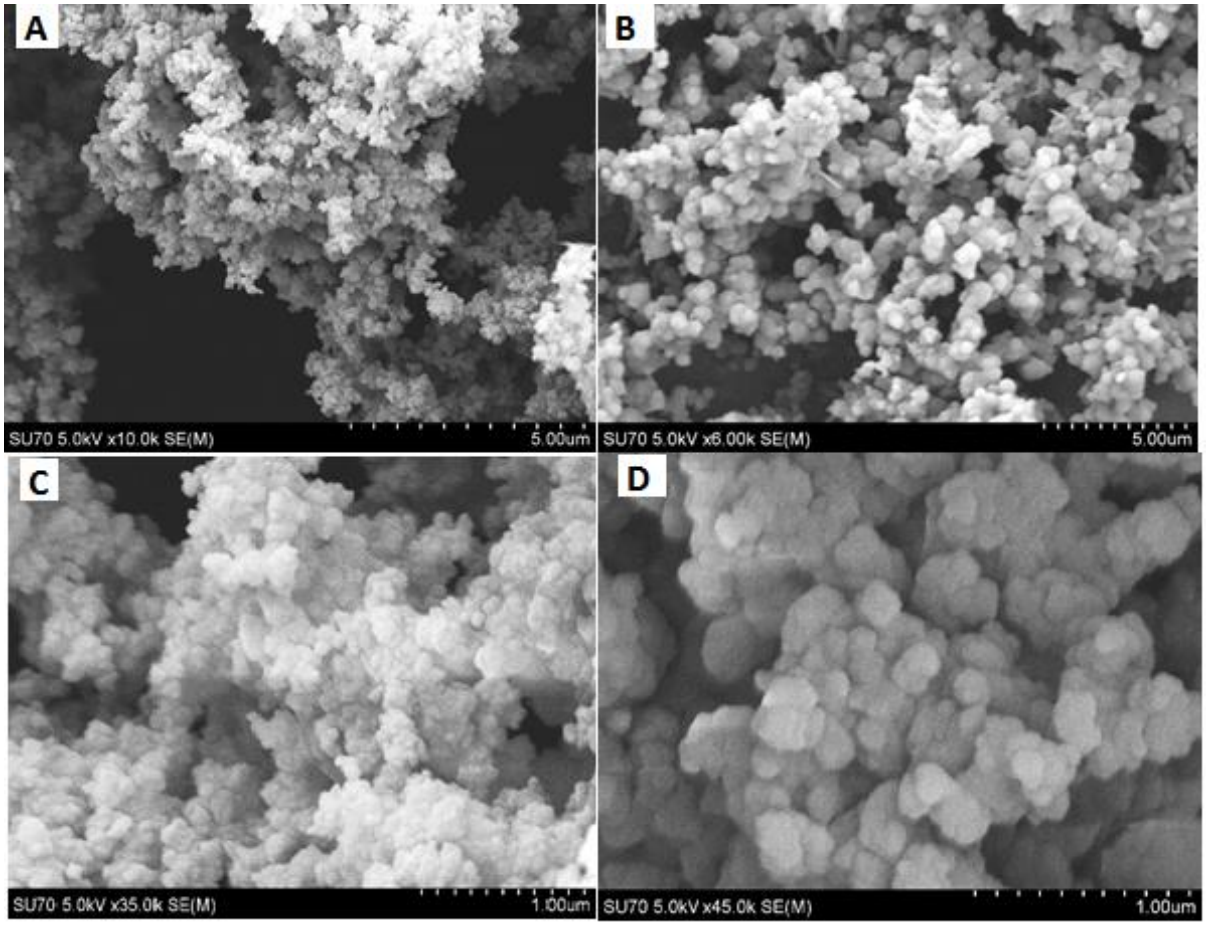

Figure 3.4: Scanning electron microscopy (SEM) images BILP-15 (A), BILP-15C (B), BILP-16 (C) and BILP-16C (D)

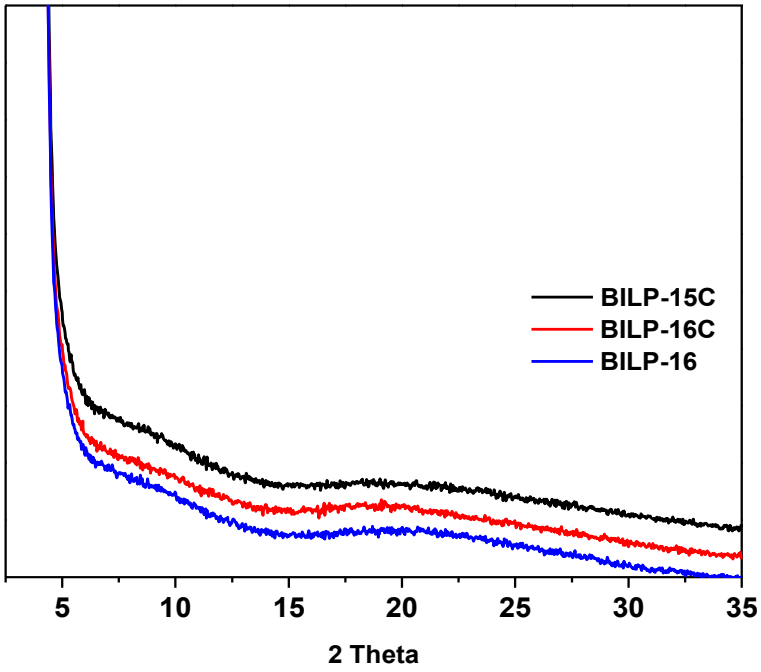

Figure 3.5: X-ray diffraction pattern (XRD) for BILP-15C, BILP-16 and BILP-16C

(Note: BILP-15 was reported in Chapter 2).

3.3.1 Impact of the acid-catalyzed process on porosity

Because high surface area and pore volume are among the desired parameters for gas storage applications, especially under high pressure conditions, the use of extended organic thrusts has been employed to attain exceptionally porous MOFs and POPs.[84b, 111] However, when this approach was used for BILPs as in the case of BILP-15, which was synthesized by condensation reactions between 1,2,4,5-tetrakis(4-formylphenyl)benzene and 3,3'-diaminobenzidine tetrahydrochloride, the resultant polymer exhibited low surface area (448 $m^2 g^{-1}$).[69e] One possible reason would be the somewhat flexible nature of the 3,3'-diaminobenzidine linker core, wherein rotation about C-C bonds provides limited control over directional network growth and hence reduces porosity (Figure 6). To improve porosity, we envisioned that controlling the formation rate of the acid-catalyzed imine-linked would enhance network expansion as in the case of imine-linked COFs.[45, 67a] In the aldehyde-amine condensation reaction, the dehydration and imine oligomers formation step is acid-catalyzed.

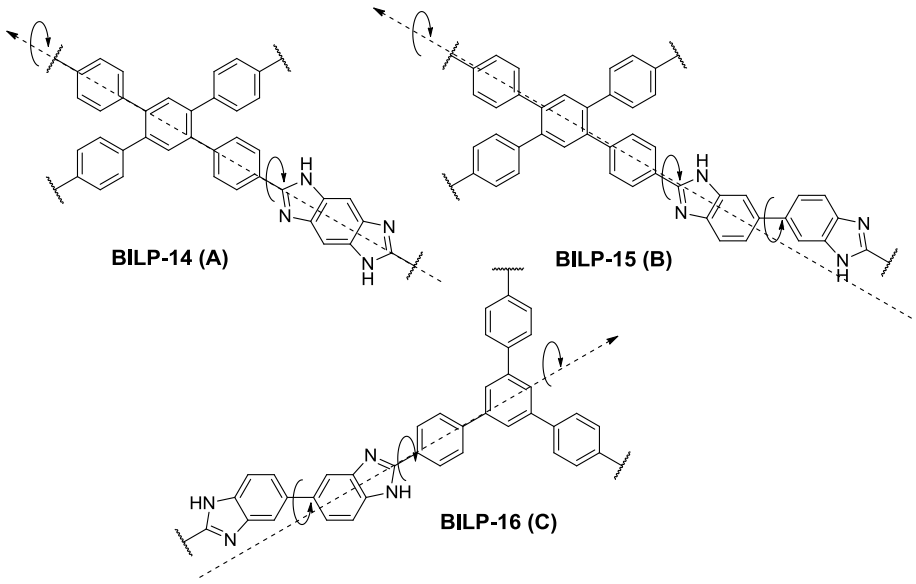

Figure 3.6: Possible rotations around the imidazole rings. (A) Rigid BILP-14 (B) Flexible BILP-15 and (C) BILP-16

Accordingly, the proposed mechanism for the BILPs formation depends on the liberation of hydrochloric acid from the aryl-*o*-diamine salts into the solution. The acid protonates the carbonyl group and catalyzes imine-bond formation, which is then followed by molecular oxygen assisted dehydration and cyclization of the imidazole moiety as shown in Scheme 3.2.[79] Because of the reversible nature of the imine bond, which is the first step in framework expansion, we sought after controlling the rate of condensation to improve the porosity of BILPs. We have selected DAB, which is acid-free and commercially available, in the presence of controlled catalytic amounts of HCl. We have noted that according to porosity measurements, the surface area of BILP-15 and BILP-16 can be increased significantly by 92% and 47%, respectively, when HCl amounts are optimized.

The influence that hydrochloric acid has over the porosity of BILP-15 and BILP-16 was studied by scanning the effect of different acid concentrations and mole ratios (with respect to amine building units) required for polymer formation. In our first approach, we determined the optimal acid concentration at two sets of constant mole ratios for HCl/DAB (1:1) and (2:1). At 1:1 mole ratio and different acid concentrations (0.1- 2.0 M), the BET surface area was around 120 $m^2 g^{-1}$ in all cases (Figure 7A and Table 3.1). Moreover, the color of the resulting polymers was black-gray after exposure to air for 2 hours. It is assumed that incomplete polymerization processes leave behind unreacted amine sites that undergo oxidation in the presence of air.

Table 3.1: The impact of different acid concentrations on the porosity of BILP-16C at 1:1 HCl/DAB

[HCl] mol L^{-1}	Vol[a] HCl (mL)	Vol H_2O (mL)	SA^{b}_{BET} (m^2 g^{-1})
2.0	0.09	-	56
1.5	0.12	0.03	87
1.0	0.19	0.1	102
0.6	0.32	0.23	113
0.5	0.75	0.66	120
0.4	0.37	0.28	120
0.3	0.62	0.53	93
0.1	1.87	1.78	28

[a] Volume of HCl calculated at 1:1 HCl/ DBA and 0.187 mmol DBA. [b] SA surface area (BET).

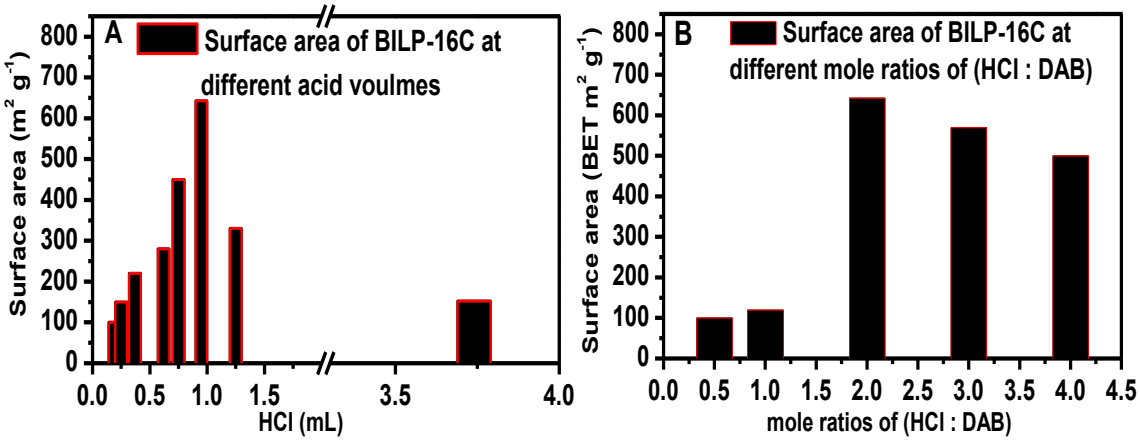

Figure 3.7: (A) Porosity of BILP-16C at different acid concentrations and 2:1 HCl/DAB; (B) Porosity of BILP-16C at different HCl: DAB mole ratios at constant acid concentration.

On the other hand, when 2:1 mole ratio was used the resulting BET surface area reached high values that range from 100 to 643 m^2 g^{-1} as shown in Figure 7B and summarized in Table 3.2.

Table 3.2: The impact of different acid concentrations on the porosity of BILP-16C at 2:1 of HCl/DAB

[HCl] mol L^{-1}	**Vol[a] HCl (mL)**	**Vol H_2O (mL)**	**SA_{BET} (m^2 g^{-1})**	**SA %[b]**
2.0	0.19	-	100	-77.0
1.5	0.25	0.06	150	-66.0
1.0	0.37	0.18	220	-49.0
0.6	0.62	0.43	280	-43.0
0.5	0.75	0.56	450	+3.3
0.4	0.95	0.76	643	+48.0
0.3	1.25	1.06	330	-24.0
0.1	3.74	3.28	152	-65.0

[a] Volume of HCl calculated at 2:1 of HCl/ DBA and 0.187 mmol DBA. [b] SA %: The change percentage of the surface area BILP-16C(s) compared to the surface area of the non-catalyzed BILP-16 (435 m^2 g^{-1})

A gradual increase in surface area was noted as acid concentrations decreased to 0.4 M. At low acid concentration the amount of water content will increase in the solution, which will lead to slower imine-oligomer formation. In contrast, at higher acid concentrations (above 0.6 M) the rate of polymerization increases leading to "uncontrolled" network growth and much lower porosity levels. The lower porosity at very low acid concentrations (0.1 and 0.3 M) could be related to the enhanced reversible nature of the polycondensation as the water content increases and shifts the reaction toward the starting materials. The optimum porosity of BILP-16C (C: catalyzed); was obtained at 0.4 M (643 m^2 g^{-1}) which corresponds to an increase of 47% compared to non-catalyzed BILP-16 (435 m^2 g^{-1}).

When 1.5 and 2 M were used, the resulting BILP-16C materials were consistent with the materials obtained from the 1:1 mole ratio experiments. These experiments were performed twice for each acid concentration and the resulting polymers have the same chemical stability and surface area. In the second set of experiments, the study was aimed at varying the mole ratio of (HCl:DAB) at the optimal acid concentration (0.4M) identified from the above studies. The optimal surface area was recorded when 2:1 mole ratio was used (Table 3.2), while a slightly lower porosity was recorded for the higher mole ratios 3:1 and 4:1 as shown in Figure 7B and Table 3.3.

Table 3.3: Impact of different HCl: DBA mole ratios on the porosity of BILP-16C at constant acid concentration

HCl:DAB	**[HCl] mmol L^{-1}**	**Vol[a] HCl (mL)**	**SA_{BET} (m^2 g^{-1})**	**SA %[b]**
5:1	0.4	0.23	100	-77.0
1:1	0.4	0.46	120	-72.0
2:1	0.4	0.93	643	+48.0
3:1	0.4	1.4	570	+31.0
4:1	0.4	1.87	500	+15.0

[a] Volume of HCl calculated at different HCl:DBA and 0.187 mmol DBA.[b] SA %: The change percentage of the surface area of BILP-16C(s) compared to the surface area of the non-catalyzed BILP-16 (435 m^2 g^{-1})

These results suggest that 2 equiv. of 0.4M HCl are needed to optimize porosity while excess acid amounts tend to lower porosity. In a similar fashion, we used these synthetic routes to optimize the porosity of BILP-15 (448 m^2 g^{-1}) and have found that the surface area of BILP-15C

(862 $m^2 g^{-1}$) increases by 92%. Because porosity is vital for gas separation, we have assessed all polymers in regard to CO_2 capture and separation from N_2 and CH_4 as outlined below.

3.3.2 Porosity Measurements and Gas Uptakes

The impact of the acid-catalyzed processes on the porosity of BILP-16C and BILP-15C has been investigated and compared to the non-catalyzed BILP-15 and BILP-16. To study porosity, argon isotherms were collected at 87 K and 1.0 bar (Figure 3.8A) and used to determine surface area, pore volume, and pore size distribution of all polymers. The rapid Ar uptakes at low pressure (0-0.1 bar) are consistent with the microporous nature of the polymers, while the minor hysteresis observed for BILPs is consistent with the flexible nature of the networks. Pore size distribution (PSD) curves were derived from the Ar adsorption branch using nonlocal density functional theory (NLDFT) and were found to be centered around 5.6-7.0 Å as shown in Figure 3.8B.

The random distribution domain of PSD in the rage of ~10 to 20 Å may arise from the lack of uniform pore growth and network expansion. Pore volume was calculated from single point measurements at P/P_o = 0.95 and found to be 0.27, 0.27, 0.42 and 0.47 cc g^{-1} for BILP-15, BILP-16, BILP-15C and BILP-16C, respectively. The overall pore volumes of BILP-15C and BILP-16C were improved by 36% and 43%, respectively, compared to the non-catalyzed BILPs. Applying the Brunauer-Emmett-Teller (BET) model within the pressure range of P/P_o = 0.05-0.15 resulted in SA_{BET} of 448 $m^2 g^{-1}$ (BILP-15), 862 $m^2 g^{-1}$ (BILP-15C), 435 $m^2 g^{-1}$ (BILP-16) and 643 $m^2 g^{-1}$ (BILP-16C) as shown in Figure 3.9 and Table 3.4. It should be noted that the surface areas of BILP-15 and BILP-16 are much lower than those of reported BILPs most likely as a result of the flexible nature of the amine-based linker. Poor network growth also leads to narrow pore channels making these polymers very promising for gas separation.

To take advantage of the microporous nature of BILPs and their chemical heterogeneity, preferential binding of small gases has been studied for N_2, CO_2, and CH_4. Therefore, pure gas uptake isotherms were collected to evaluate gas uptake and selectivity as well as the binding affinity for CO_2 and CH_4 as summarized in Table 3.5. At 273 K, all CO_2 isotherms (Figure 3.10A) are fully reversible and exhibit a steep rise at low pressure, which is in agreement with the behavior of previously reported BILPs. The uptake by BILP-15 and BILP-16 (~119 mg g^{-1}) is low compared to all reported BILPs (values range 235-118 mg g^{-1}). A noticeable increase in the CO_2 uptake was recorded for BILP-15C and BILP-16C (~152 mg g^{-1}). The uptake drops to ~102 mg g^{-1} at 298 K (Figure 3.10B). The hydrogen uptake for BILPs at 77 K falls in the range of 0.85-1.7 wt% (Figure. 3.11C-D), while the CH_4 uptake was in the range of 1.4-1.7 wt%, (Figure 3.10 E-F).

The Q_{st} values for CO_2 (27.4-33.0 kJ mol^{-1}, Figure 3.11A) are within the range reported for BILPs and nitrogen-rich porous networks. The higher Q_{st} values of BILP-15 and BILP-16 could be attributed to the narrow pores, which provide stronger interactions for CO_2. The Q_{st} for H_2 was calculated from adsorption data collected at 77 and 87 K (Figure. 3.12B). The zero-coverage range of Q_{st} values for BILPs is 7.4-8.3 kJ mol^{-1}. Similarly, low-pressure CH_4 isotherms were collected at 273 and 298 K and used to calculate the Q_{st} for CH_4. At zero coverage the Q_{st} is 21.5-26.5 kJ mol^{-1} (Figure. 3.11C).

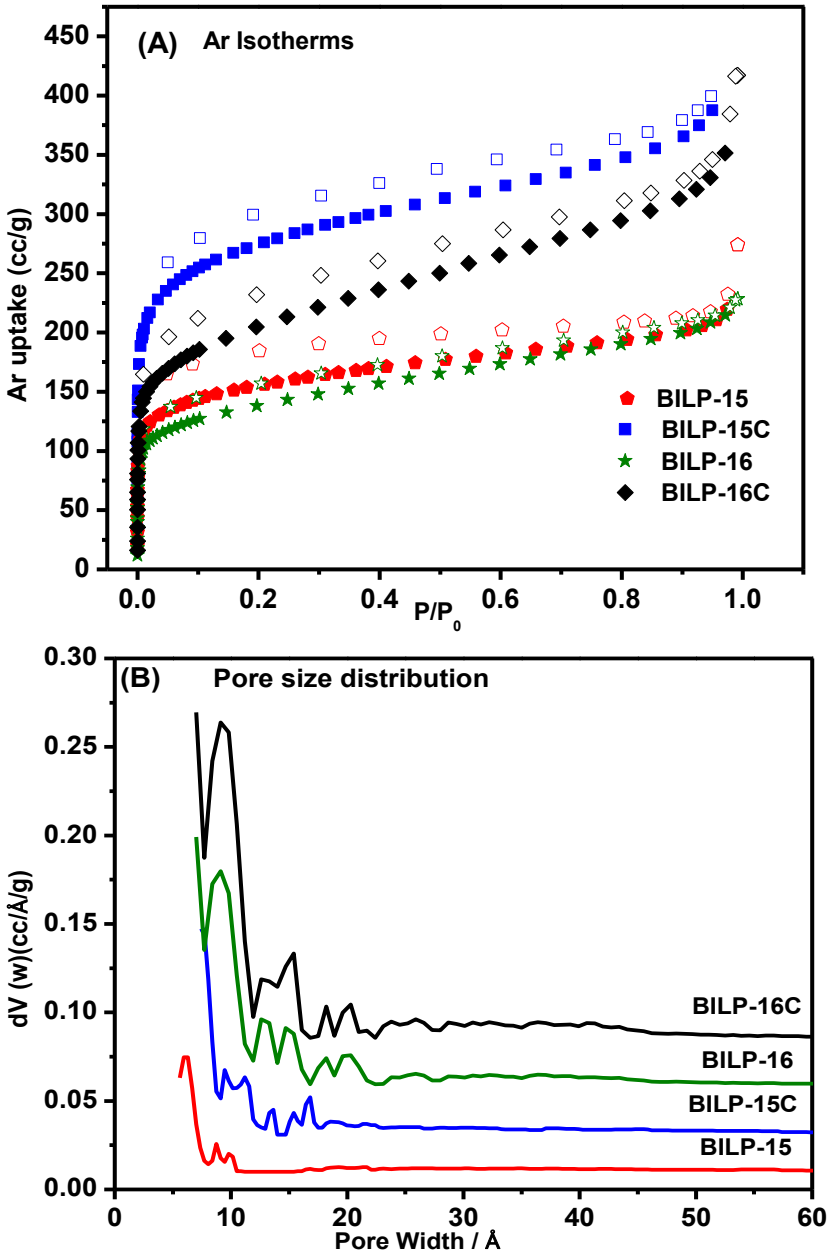

Figure 3.8: (A) Argon isotherms (B) Pore size distribution of acid-catalyzed and non-catalyzed BILPs.

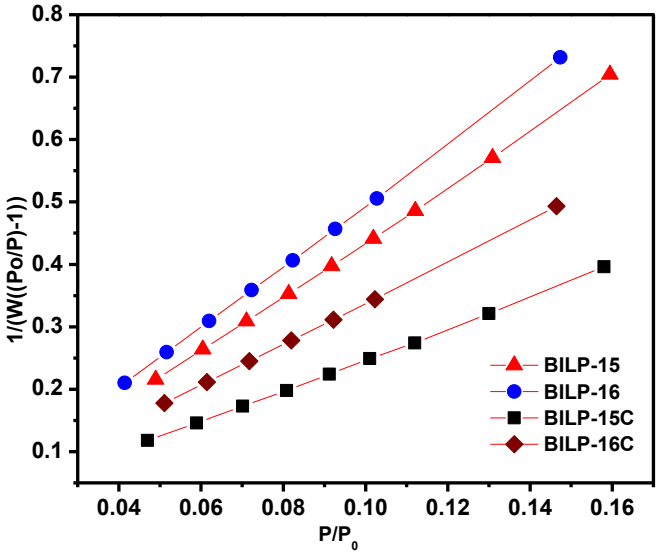

Figure 3.9: BET surface area plots for non-catalyzed and acid-catalyzed BILPs were calculated from the Ar adsorption isotherm at 87 K. The model was applied from P/Po = 0.05-0.16. (W = Weight of gas absorbed at a relative pressure P/Po).

Table 3.4: BET and Langmuir values for non-catalyzed and acid-catalyzed BILPs were calculated from Ar adsorption isotherms at 87 K

BILP	**Surface area (BET)** $m^2 g^{-1}$	**Langmuir Surface area** $m^2 g^{-1}$
BILP-15	448	568
BILP-16	435	520
BILP-15C	862	995
BILP-16C	643	680

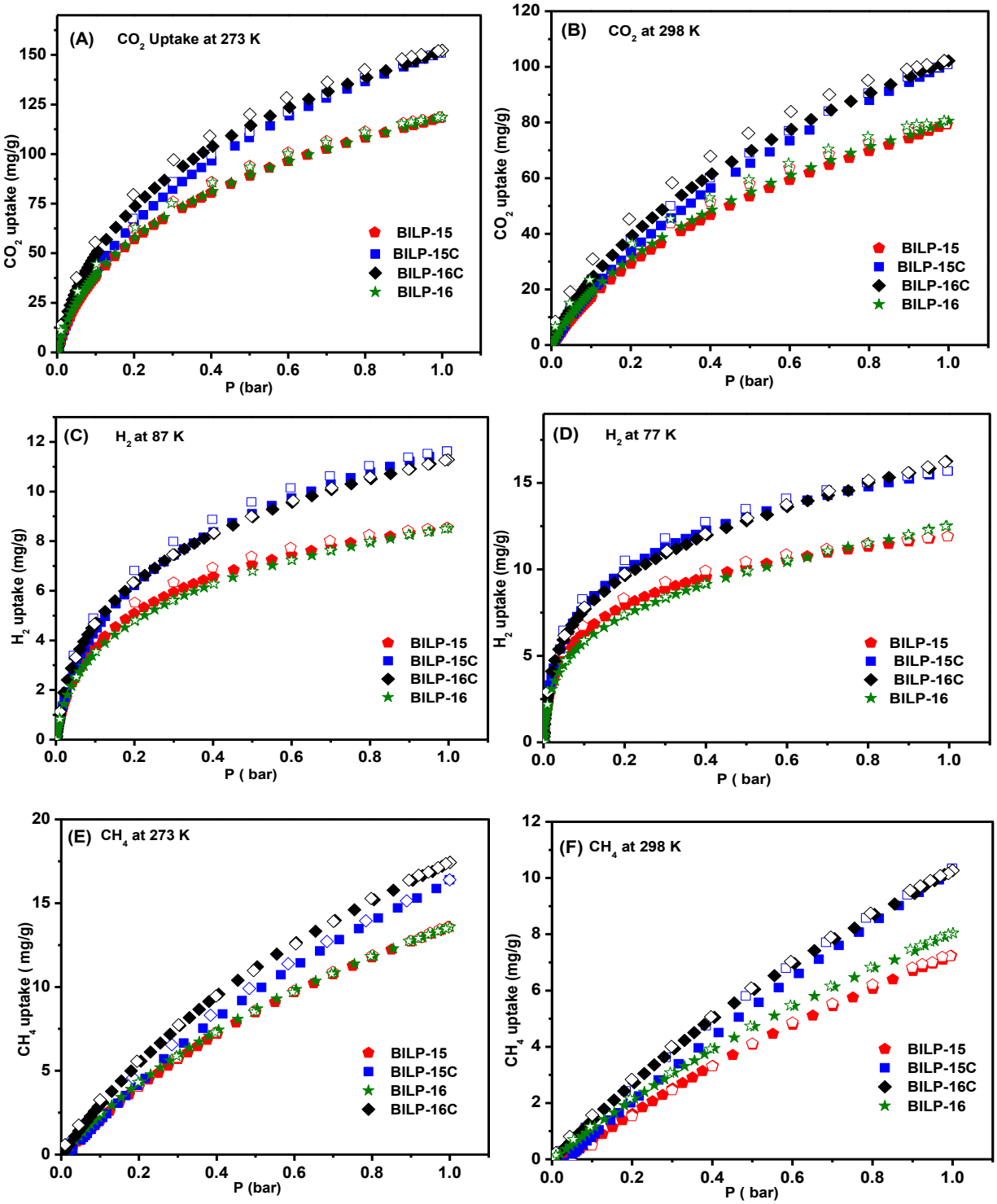

Figure 3.10: Gas uptake isotherms (A-B) CO_2 at 273/298 K, (C-D) H_2 at 87/77 K, and (E-F) CH_4 at 273/298 K

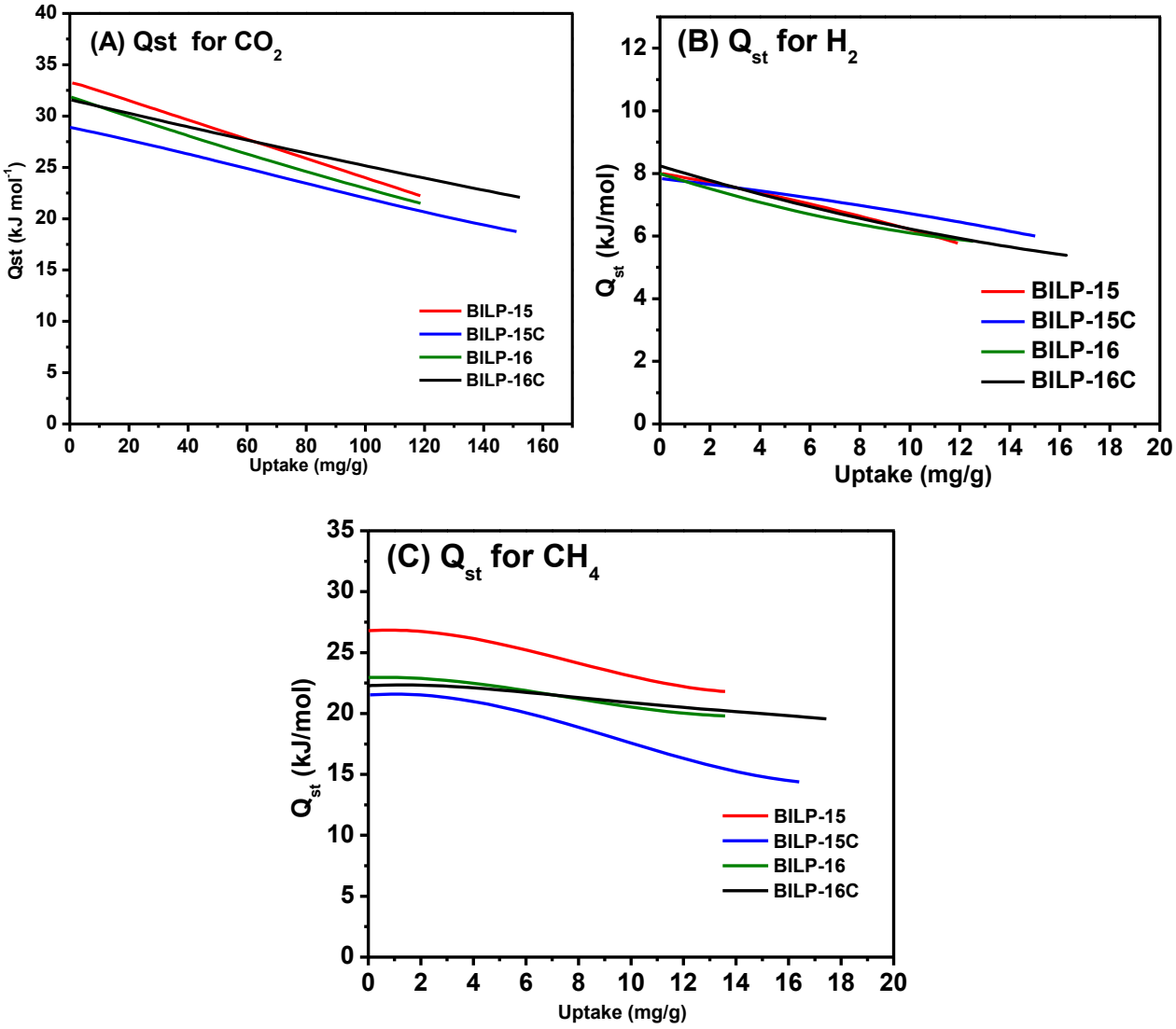

Figure 3.11: Heats of adsorption of acid-catalyzed and non-catalyzed BILPs

Table 3. 5: Gas uptake and Heats of adsorptions of acid-catalyzed and non-catalyzed BILPs

polymer	SA_{BET}[a]	Pore volume[b]	H_2 at 1 bar[c]			CO_2 at 1 bar[c]			CH_4 at 1 bar[c]			N_2 at 1 bar[c]	
			77 K	87 K	Q_{st}	273 K	298 K	Q_{st}	273 K	298 K	Q_{st}	273 K	298 K
BILP-15	448	0.27	11.9	8.5	8.0	118	80.0	33.0	13.5	7.2	26.5	5.7	2.4
BILP-16	435	0.27	12.5	8.5	8.0	118.7	80.7	32.0	13.5	8.0	23	3.0	6.5
BILP-15C	862	0.42	15.7	11.6	7.8	151.0	101.0	28.9	16.4	10.3	21.5	7.2	3.1
BILP-16C	643	0.47	16.2	11.3	8.2	152.3	102.2	31.6	17.4	10.3	22.3	8.0	3.1

[a]Surface area ($m^2\ g^{-1}$) was calculated from Ar isotherm. [c]Pore volume (cc g^{-1}) was calculated from single point measurements (P/P_0 =0.95). [c]Gas uptake in mg g^{-1} and the isosteric enthalpies of adsorption (Q_{st}) in kJ mol^{-1}).

3.4 Gas Selectivity Studies

The preferential binding of non-catalyzed BILP-15 and BILP-16 and acid-catalyzed BILP-15C and BILP-16C, for CO_2 over CH_4 and N_2, was evaluated using the initial slope calculations and ideal adsorbed solution theory (IAST). The pure gas isotherms for CO_2, CH_4 and N_2 were collected at 273 and 298 K up to 1 bar (Figure 3.12). The initial slope ratios were estimated from Henry's law constants from single-component adsorption isotherms collected at the same temperature (Figure 3.13). Furthermore, IAST method was applied at 298 K to predict the adsorption selectivity for gas mixtures based on pure components gas isotherms. The selectivities from IAST were calculated for gas mixture composition of CO_2:N_2 (10:90) and CO_2:CH_4 (50:50) at 298 K and were in good agreement with the initial slope calculations as shown in Table 3.1 and Figure 3.14.

Accordingly, these calculations were performed to evaluate the impact of the acid-catalyzed synthesis strategy on the selectivity of BILP-15C and BILP-16C. From the initial slope calculations at 273 K/298 K, a notable change in CO_2/N_2 selectivity values was observed for BILP-15C (61/50) compared to BILP-15 (83/63). The significant decrease in selectivity can be attributed to the much higher porosity and slightly larger pore size of BILP-15C, which makes them accessible to nitrogen molecules as well. In contrast, only slight changes were noted for BILP-16 and BILP-16C, which can be attributed to the low porosity and similar pore size distribution (7.0 Å) of both polymers. These selectivity values indicate that the impact of the acid-catalyzed strategy on BILP-15 is more pronounced compared to BILP-16, which can be seen from the improved surface area of BILP-15 (92%) compared to BILP-16 (47%). The selectivity values calculated by IAST at 298 K were consistent with initial slope calculations. Moreover, CO_2/CH_4 selectivity values for all polymers fall in the range 6-10. Selectivity studies

revealed that the tradeoff between CO_2 selectivity and uptake is more pronounced for BILP-15C due to its much higher porosity.

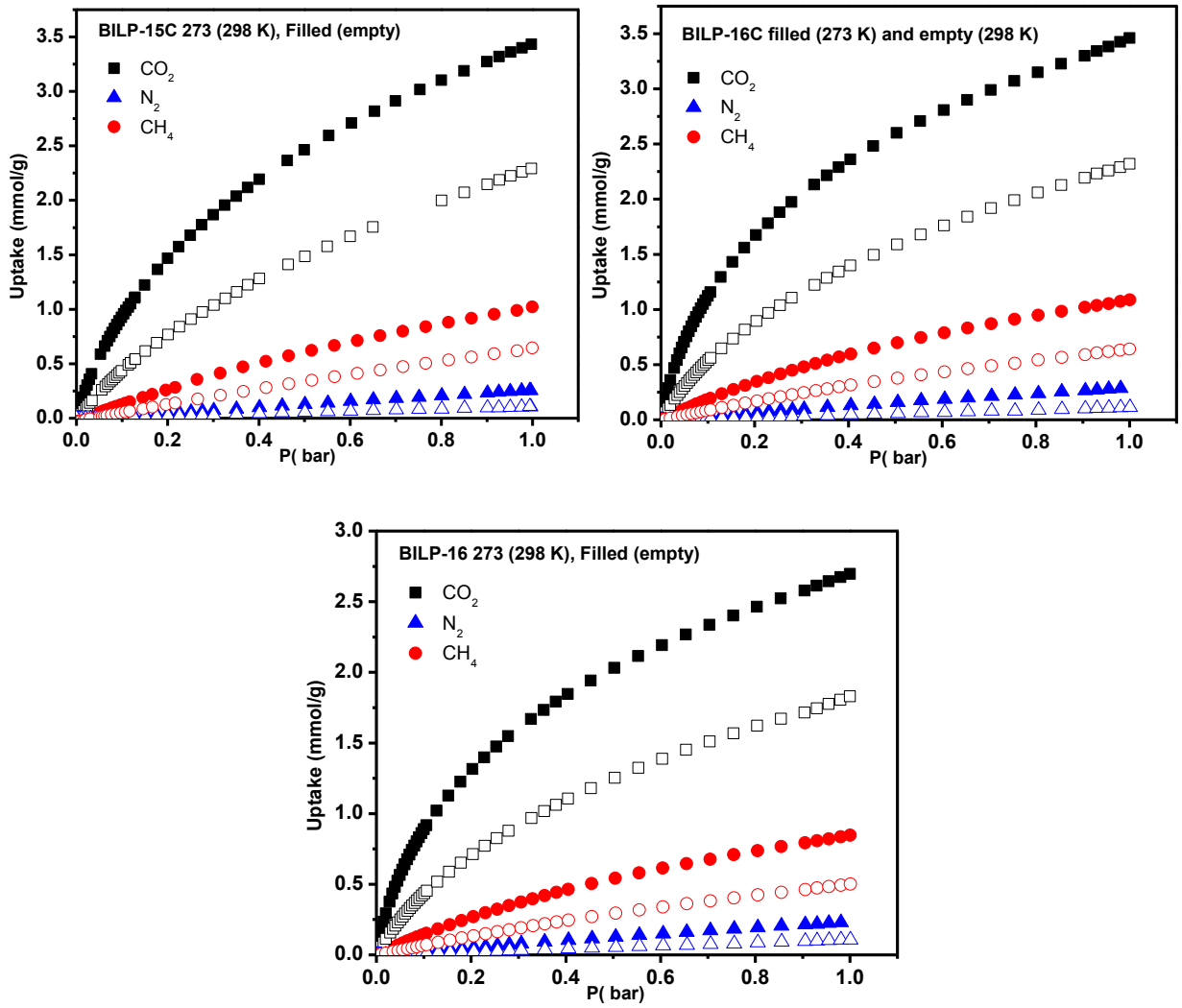

Figure 3.12: Gas sorption capacities for BILP-15C, BILP-16C, and BILP-16 at 273 K (filled) and 298 K (empty). (The gas sorption isotherms of BILP-15 was reported in Chapter 2).

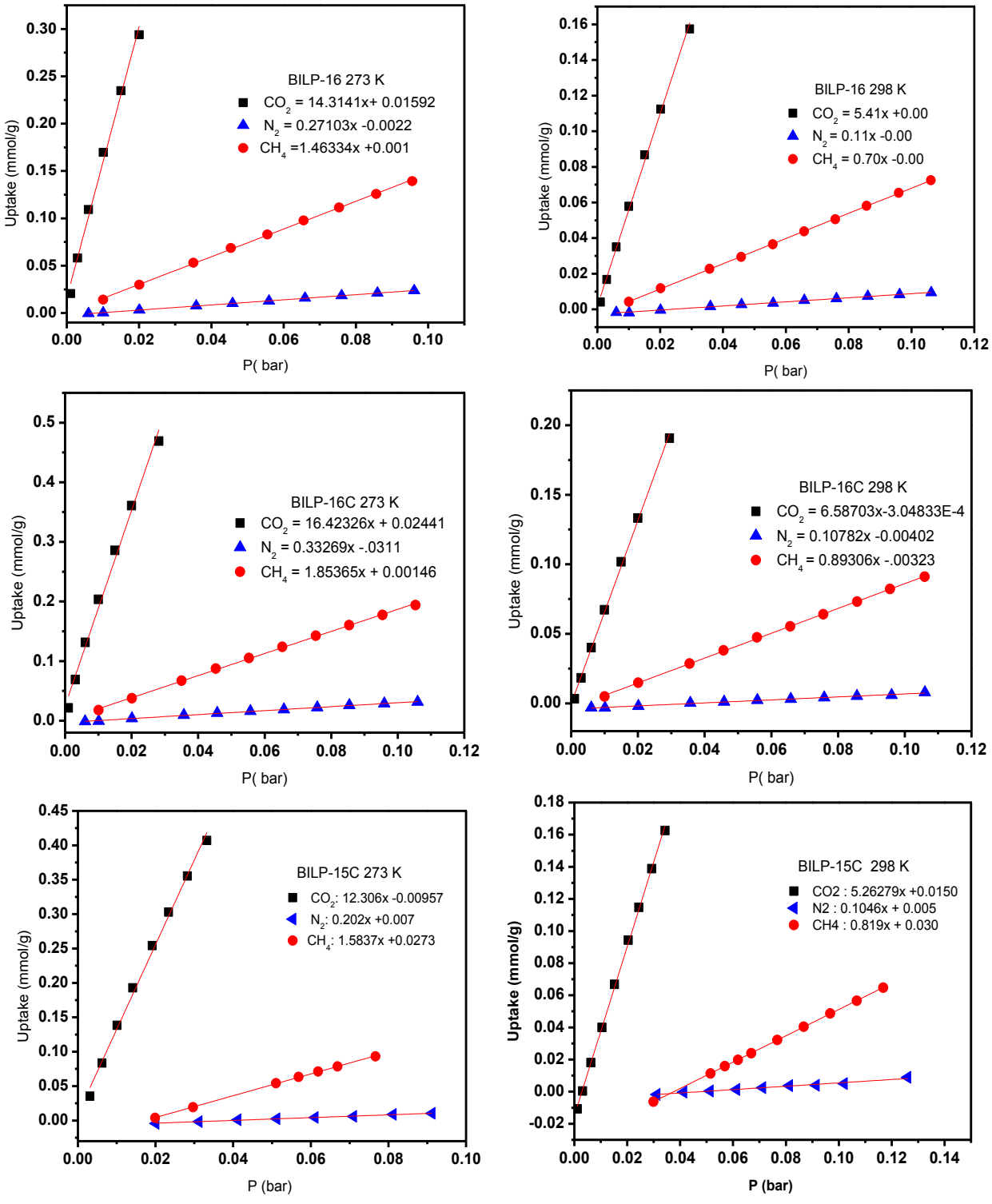

Figure 3.13: Adsorption selectivity of CO_2 over N_2 and CH_4 for BILPs from initial slope calculations for BILP-15C, BILP-16C, and BILP-16 (BILP-15 was reported in Chapter 2).

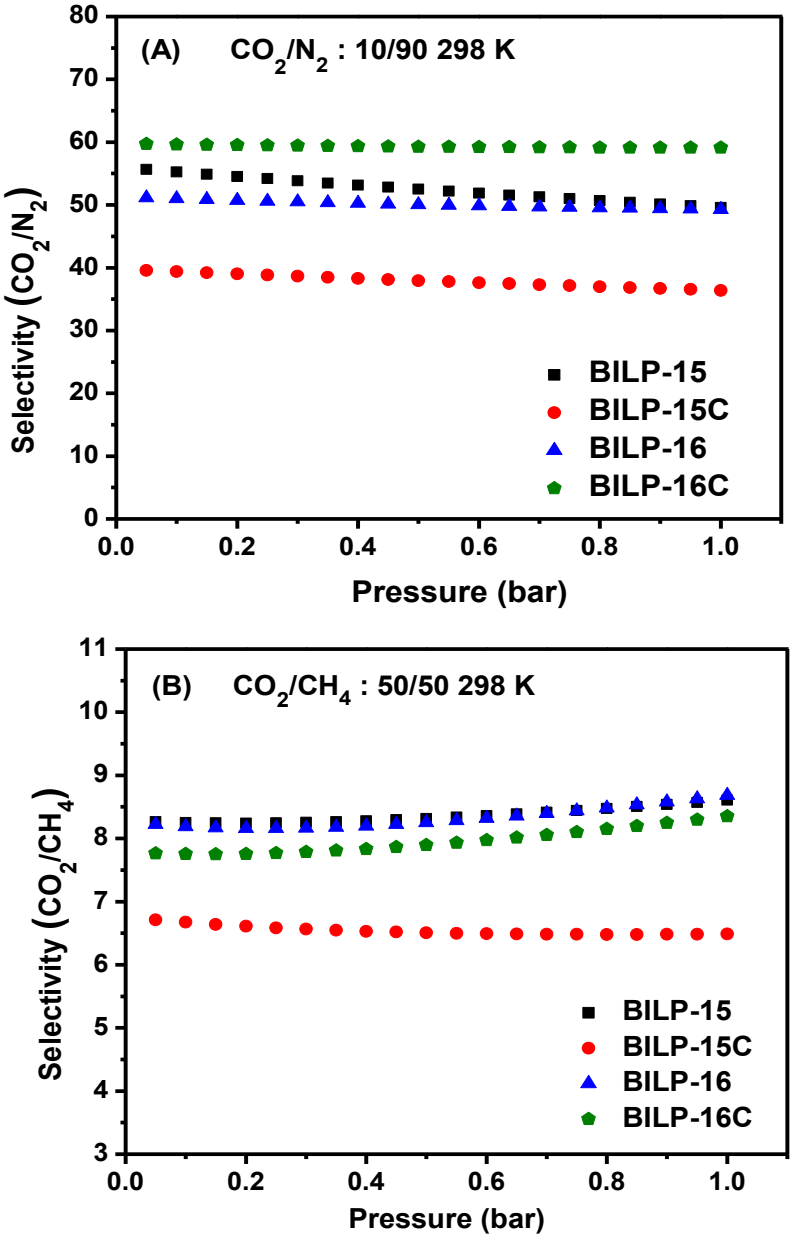

Figure 3.14: IAST selectivity data for CO_2/N_2 and CO_2/CH_4 at different binary mixture ratios for BILP-15, BILP-15C, BILP-16, BILP-16C.

3.5 Conclusions

In conclusion, we have investigated the impact of acid-catalyzed formation rates of the imidazole units on the porosity levels of BILPs and subsequent effects on CO_2 and CH_4 binding affinities and selective uptake over N_2. The resulting polymers were characterized via spectral and analytical characterization methods and the impact of the acid-catalyzed method was evaluated by studying the porosity of all polymers. BILP-15C and BILP-16C showed improved porosity and pore volume (862 m^2 g^{-1}, 0.69 cc g^{-1}) and (643 m^2 g^{-1}, 0.69 cc g^{-1}). In contrast, the CO_2 binding affinity (Q_{st}) dropped from 33.0 to 27.4 kJ mol^{-1} for BILP-15 and from 32.0 to 31.2 for BILP-16. According to adsorption measurements, the porosity of the acid-catalyzed BILPs was improved significantly for BILP-15C (92%) and BILP-16C (47%). However, both polymers exhibited lower selectivity towards CO_2/CH_4 when compared to non-catalyzed polymers as a result of their higher porosity and larger pores.

Chapter 4

Highly Porous and Photoluminescent Pyrazine-Derived Benzimidazole-Linked Polymers

4.1. Introduction

Conjugated microporous polymers (CMPs) are a subclass of hypercrosslinked polymers (HCPs) that have a broad range of applications. However, the most significant difference between CMPs and HCPs is the formation of the multiple carbon-carbon bonds and aromatic rings that form extended-conjugated networks in CMPs.[53] CMPs have potential applications in electronics and optoelectronics, especially in the materials containing N-heterocyclic building units, which are known ~~as~~ to be promising candidates for n-type semiconductors.[112] Furthermore, embodiment of N-heterocyclic building units into π-electron rich molecules or conjugated polymers is a well-known strategy for optical structure manipulation. Therefore, integrating novel optical properties into POPs in general and BILPs in particular, without compromising porosity would be vital for their future multifaceted applications.

In this chapter we illustrate the synthesis of highly conjugated BILPs using pyrazine-containing building units that allow for N-enrichment and electronic structure modification of BILPs. As a result, these polymers possess novel gas uptake and optical properties.

4.2. Experimental

Materials and Methods

The solvents and characterization methods used in this study are reported in the previous Chapters unless otherwise noted. Concentrated hydrochloric and sulfuric acids are purchased from Sigma-Aldrich and Acros Organics and used without further purification. All reactions were handled under an inert atmosphere of nitrogen using Schlenk line technique. 6,7,15,16-tetraamine-quinoxalino[2'-3': 9,10]phenanthro[4,5-abc]phenazine (TQPP-NH_2), 1,3,5,7-tetrakis-4-formylphenyladamantane (AdmFPB), 1,2,4,5-Tetrakis(4-formylphenyl)benzene (TFPB), 1,3,5-Tris-(4-formylphenyl) benzene (TriFPB), and Tetrakis-4-formylphenylmethane (TFPM), were synthesized according to published methods.[69c-e, 113] All spectral and analytical characterization techniques including: elemental microanalyses, FT-IR spectra, ^{1}H-NMR, ^{13}C CP-MAS Solid-state NMR, thermogravimetric analysis (TGA), scanning electron microscopy imaging (SEM), and powder X-ray diffraction (XRD), were performed according to the methods reported in Chapter 2. Porosity and gas sorption experiments were collected by a Quantachrome Autosorb IQ2 volumetric analyzer using adsorbates of UHP grade and following the same activation and sample collection procedures.

Experimental Procedures

Synthesis of BILP-17

A 100 mL Schlenk flask was charged with 6,7,15,16-tetraamine-quinoxalino[2'-3': 9,10]phenanthro[4,5-abc]phenazine (TQPP-NH_2) (60 mg, 0.104 mmol) and 30 mL of anhydrous DMF. The solution was cooled to -30 ^{o}C and HCl (0.04 M, 2 mL) was added to the solution and stirred for 1 hr. 1,3,5,7-tetrakis(4-formylphenyl) Adamantane (29.0 mg, 0.052 mmol) in 25 mL

anhydrous DMF was added dropwise to the pervious charged solution. Temperature was maintained around -30 ^{o}C until the brown solid product formation completed and then increased to RT and kept stirring overnight. The flask containing the reaction mixture was bubbled with air for 15 min and capped. The reaction mixture was then heated in an oven at 130 ^{o}C (0.5 ^{o}C/min) for 3 days to afford a brownish polymer, which was isolated by filtration over a medium glass frit. The product was immersed in DMF (20 mL overnight) and then in (20 mL) acetone. The product was dried under vacuum at 120 ^{o}C and 1.0 x 10^{-5} Torr for 20 hrs to give BILP-17 as a brown solid (41.0 mg, 79%). Anal. Calcd for $C_{55}H_{44}N_8.6H_2O$: C, 65.6%; H, 4.97%; N, 11.13%. Found: C, 66.73%; H, 5.29 %; N, 10.39%.

Synthesis of BILP-18

BILP-18 was synthesized in a similar fashion to the preparation of BILP-17 using (TQPP-NH_2) (60 mg, 0.104 mmol) and 1,2,4,5-tetrakis(4-formylphenyl)benzene (25 mg, 0.051 mmol), in presence of HCl (0.4 M, 2 mL). The resulting polymer was isolated, dried and activated to afford BILP-18 as a yellowish solid (37.0 mg, 74.0%). Anal. Calcd for $C_{45}H_{22}N_8.3H_2O$: C, 65.17%; H, 4.5 %; N, 11.48 %. Found: C, 66.7%; H, 4.49 %; N, 10.76%.

Synthesis of BILP-19

BILP-19 was synthesized in a similar fashion to the preparation of BILP-17 using (TQPP-NH_2) (60 mg, 0.104 mmol) and 1,3,5-tris(4-formylphenyl)benzene (27 mg, 0.069 mmol) in presence of HCl (0.4 M, 2 mL). The resulting polymer was isolated, dried and activated to afford BILP-19 as a yellowish solid (50.0 mg, 78%). Anal. Calcd for $C_{81}H_{60}N_{12}.3H_2O$: C, 69.93%; H, 4.74 %; N, 12.09 %. Found: C, 68.14%; H, 4.32 %; N, 10.91%.

Synthesis of BILP-20

BILP-20 was synthesized in a similar fashion to the preparation of BILP-17 using (TQPP-NH_2) (60 mg, 0.104 mmol) and tetrakis(4-formylphenyl)methane (22.4 mg, 0.052 mmol) in presence of HCl (0.4 M, 2 mL). The resulting polymer was isolated, dried and activated to afford BILP-20 as a yellowish solid (30.0 mg, 74%). Anal. Calcd for $C_{52}H_{38}N_8.2H_2O$: C, 77.30%; H, 5.10 %; N, 14.28 %. Found: C, 76.72%; H, 5.13 %; N, 12.92%.

4.3. Results and discussions

The synthesis of Pyrazine-derived BILPs was demonstrated using the acid-catalyzed strategy, which was applied in the preparation of the acid-catalyzed BILPs in Chapter 3. The new polymers were synthesized using 6,7,15,16-tetraamine-quinoxalino[2'-3': 9,10]phenanthro[4,5-abc]phenazine (TQPP-NH_2) (A) and different aryl-aldehydes (B-E) (Scheme 4.1) to afford the new pyrazine-derived BILPs, as mentioned in the experimental details. The combinations between (A, B), (A, C), (A, D), and (A, E) (Scheme 4.1) resulted in BILP-17, BILP-18, BILP-19, and BILP-20, respectively.

The new pyrazine-derived BILPs were synthesized by applying the acid-catalyzed strategy, which is used due to the presence of the neutral (TQPP-NH_2). This neutral amine needs to be protonated to assist the polycondensation reaction. After applying the general synthetic method, the isolation and successive washing of the polymers by aqueous, acidic and basic solutions has resulted in the desired polymers. The new pyrazine-derived BILPs were activated at 120 °C and 1.0 x 10^{-5} Torr for 20 hrs before characterization.

The successful polycondensation reaction and the imidazole ring formation were confirmed by spectral and analytical techniques. The impact of the extended-conjugated system on the electronic properties, porosity, and gas adsorption properties were investigated.

Pyrazine-derived BILPs have shown good agreement with all BILPs regarding their physiochemical stability. The chemically robust BILPs remained intact upon treatment with aqueous HCl and NaOH (4 M). The thermal stability, measured by thermogravimetric analysis (TGA), showed initial weight losses around 100 ºC, followed by sharp decomposition around 400 ºC (Figure 4.2 A). This high thermal stability is due to the formation of the imidazole ring beside the presence of the pyrazine core, as a nitrogen-containing heterocyclic compound, which has been proven as a valuable building unit for thermally stable polymers and electron-accepting π-conjugated polymers.[113a, 114] All pyrazine-derived BILPs are amorphous as illustrated from powder X-ray diffraction studies (Figure 4.2B). Scanning electron microscopy (SEM) of the polymers was used to establish the phase purity of the polymers. It has revealed agglomerated particles *ca*. 0.5-0.3 μm in size (Figure 4.3). The chemical composition of pyrazine-derived BILPs was determined by microelemental analysis, which showed the successful incorporation of the extended–conjugated core and the imidazole ring formation. Moreover, it showed that nitrogen atoms of the imidazole ring are involved in hydrogen bonding with water molecules, which is consistent with other BILPs and TGA results.

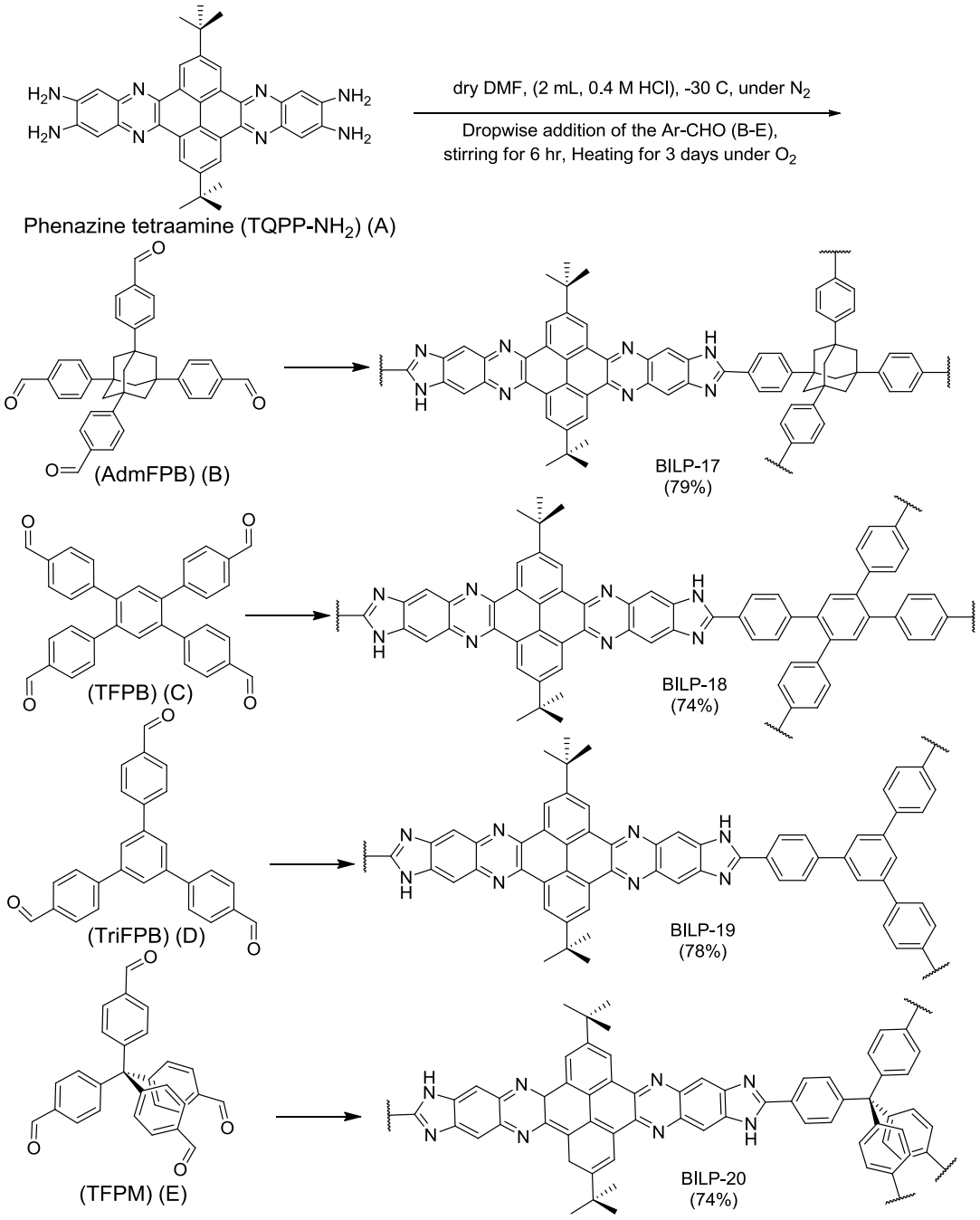

Scheme 4.1: Synthesis of pyrazine-derived BILPs

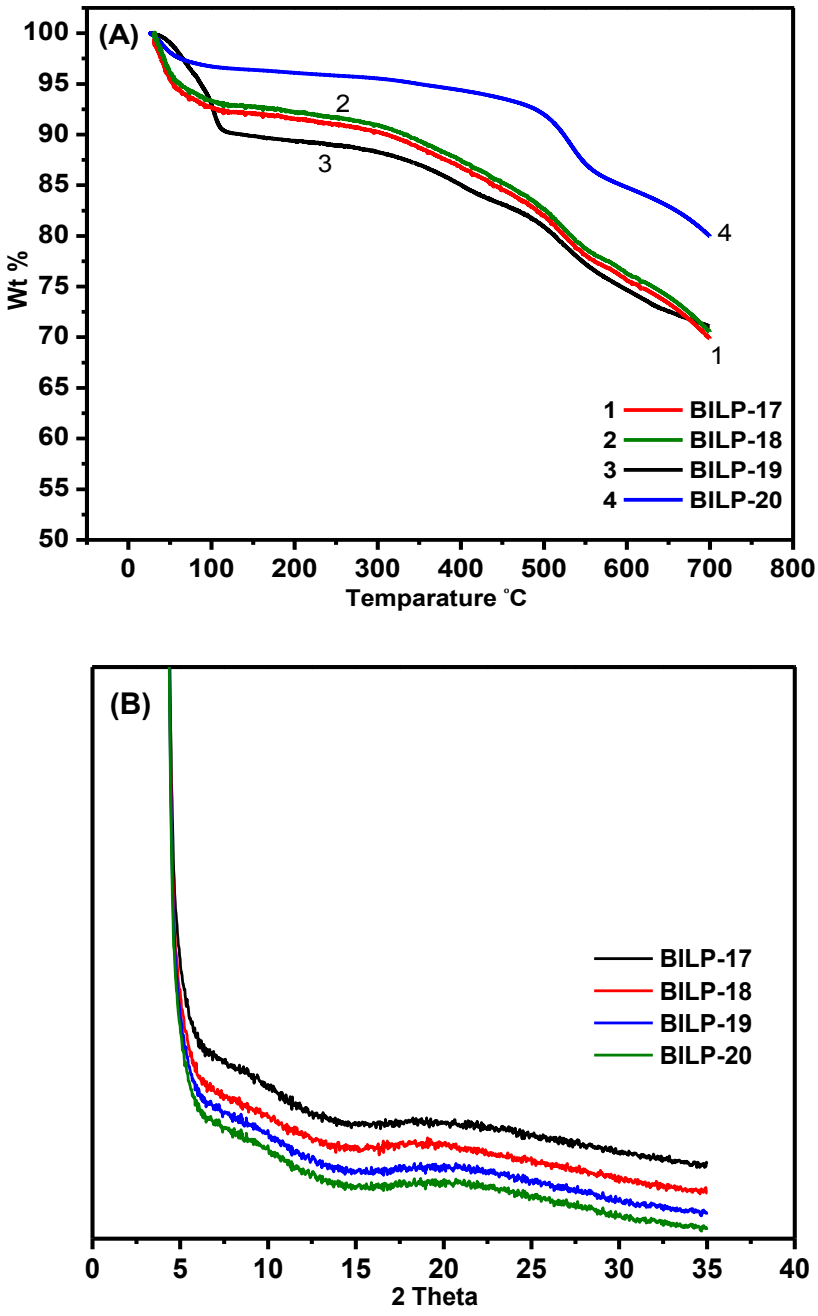

Figure 4.2: (A) Thermal gravimetric profiles of pyrazine-derived BILPs measured under N_2. (B) Pattern X-ray diffraction of pyrazine-derived BILPs.

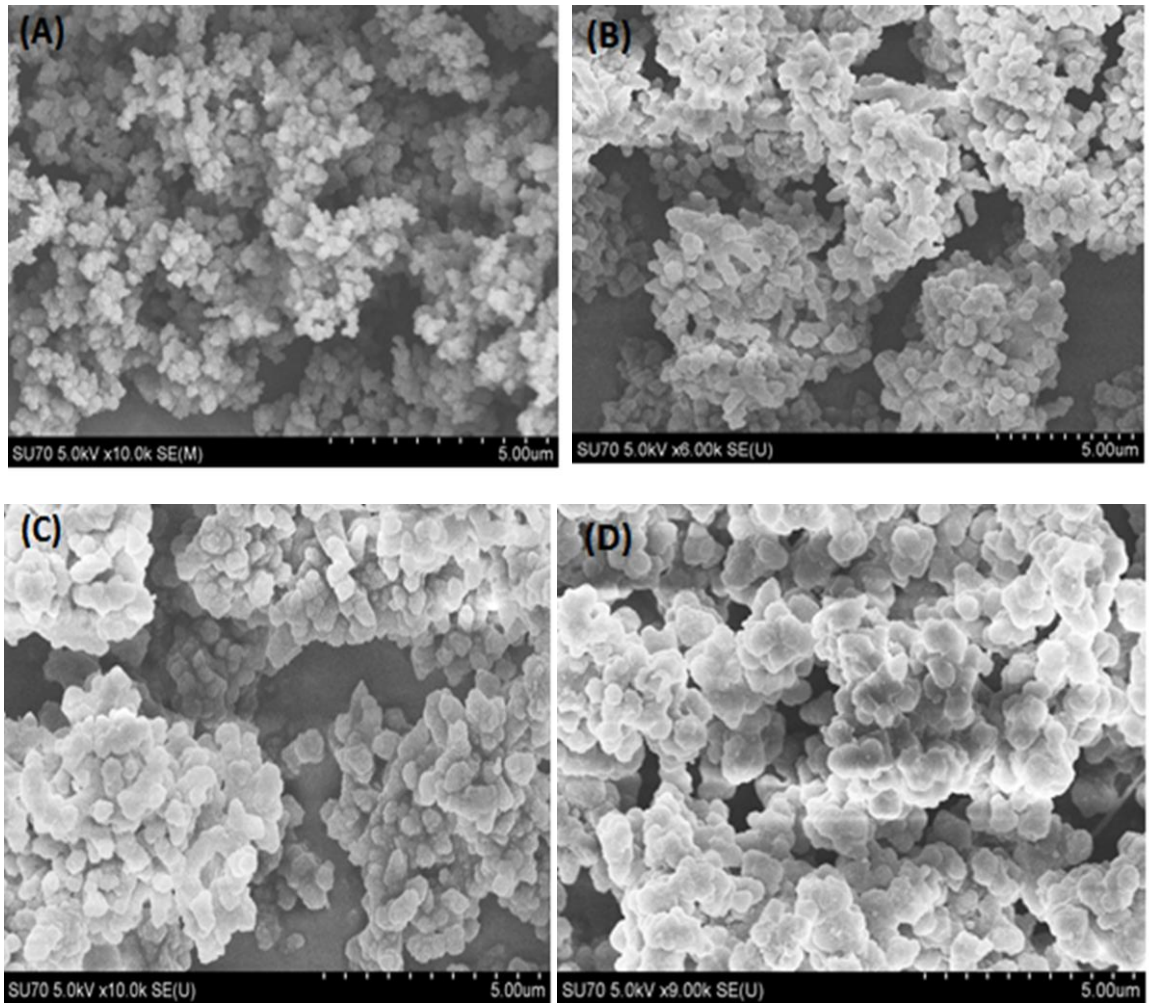

Figure 4.3: SEM images of (A) BILP-17, (B) BILP-18, (C) BILP-19, and (D) BILP-20.

The chemical connectivity of the pyrazine-derived BILPs was verified using FT-IR and ^{13}C-NMR. FT-IR spectra, for aryl-aldehyde starting materials and the corresponding BILPs, confirmed the successful incorporation of the conjugated core upon BILP synthesis. Moreover, it has shown ~~a~~ new significant vibration bands for imidazole ring skeleton and the consummation of the vibration band corresponding to aldehyde-carbon, confirming polymer formation. The vibrations at 1620, 1480, 1435, 1370, and 1275 cm^{-1} confirmed imidazole ring formation, while the substantial attenuated peak at 1700 cm^{-1} suggested the full consummation of aryl-aldehydes in the polymerization. The other stretching vibrations around 3425 cm^{-1} and 3220 cm^{-1} are assigned to free N-H, while the bands in the rang 2750-3030 cm^{-1} belong to C-H aromatic carbons. The strong bands' intensity in the range 2880-2970 cm^{-1} corresponds to C-H bond of the alkyl substituent, (t-butyl), the expanded region from 2000-500 cm^{-1} shows the characteristic vibrations in that range (Figure 4.4-4.7).

The ^{13}C CP-MAS NMR spectra showed successful formation of the new BILPs and the incorporation of the extended conjugated cores. The peaks that belong to the t-butyl group carbons appear around 22-25 ppm. The aliphatic secondary carbon of the adamantane core and the tert-carbon of tetraphenyl methane core appear around 25 and 31 ppm. The resonance peaks around 100, 127, 130 and 133 ppm belong to the aromatic C-H bonds and the peak at around 150 ppm corresponds to imidazole ring carbon. The carbon of the carbonyl group in the aryl-aldehydes was down shifted from 200 to 151 ppm due to the imidazole ring formation (Figure 4.8).

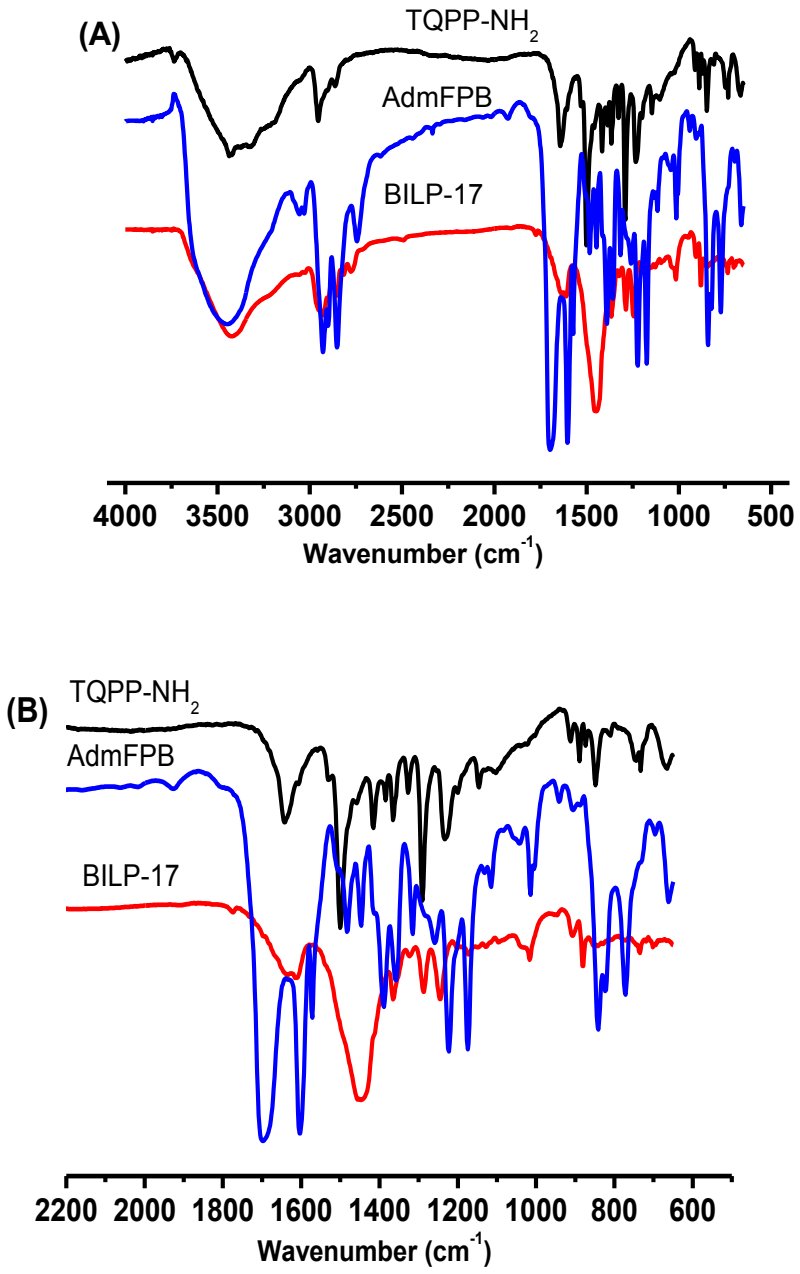

Figure 4.4: FT-IR spectra of BILP-17 and its corresponding starting materials in the range (A) (4100-500 cm^{-1}) and (B) (2200-500 cm^{-1}).

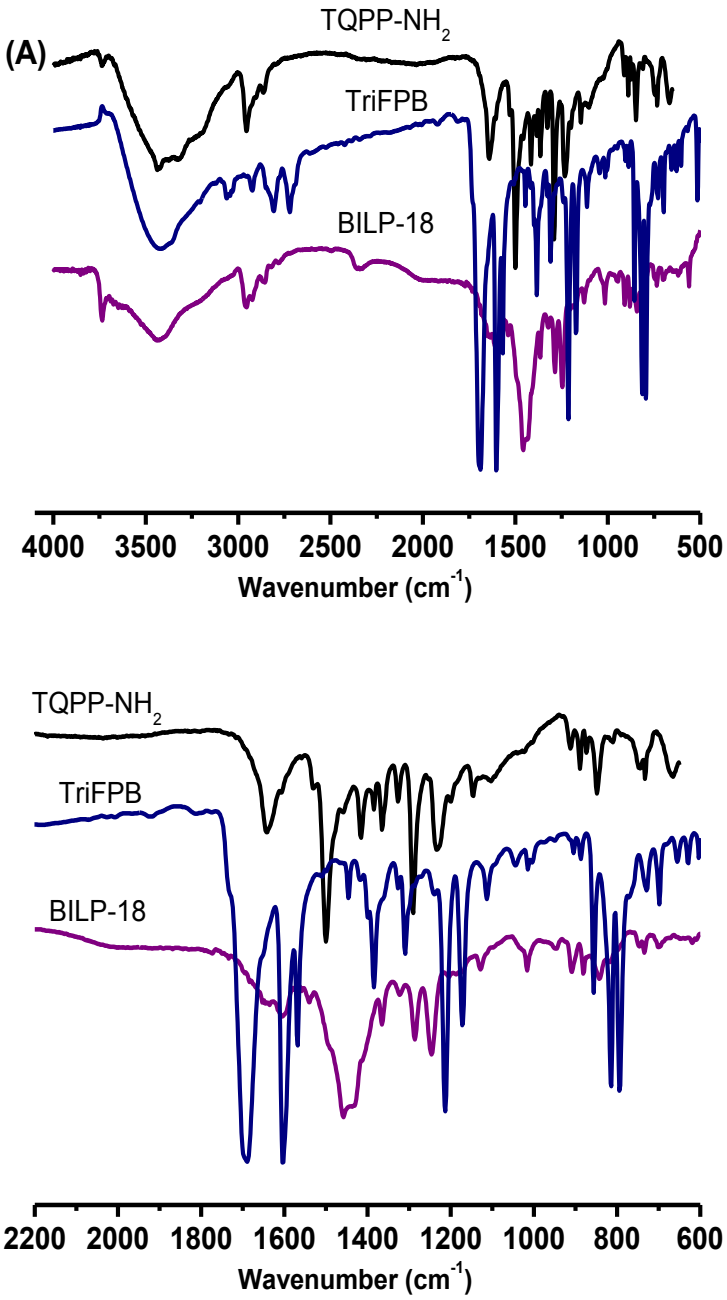

Figure 4.5: FT-IR spectra of BILP-18 and its corresponding starting materials in the range (A) (4100-500 cm^{-1}) and (B) (2200-500 cm^{-1}).

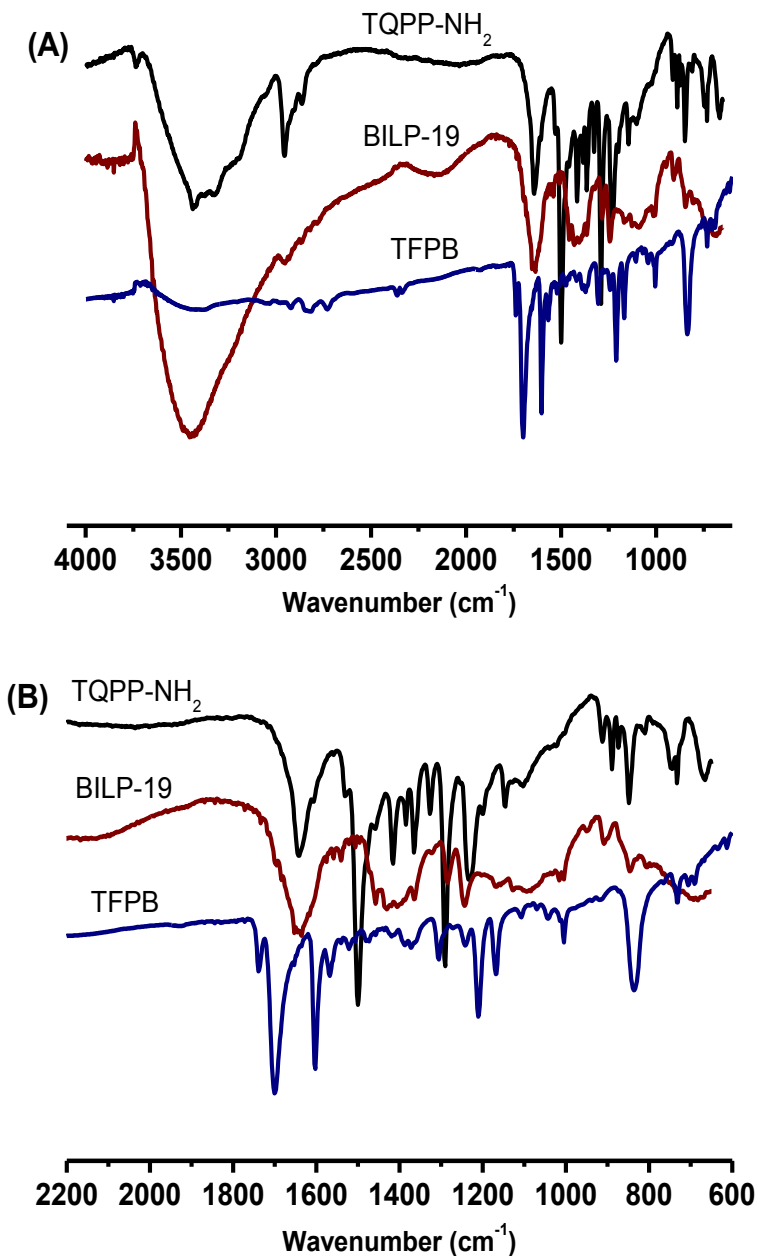

Figure 4.6: FT-IR spectra of BILP-19 and its corresponding starting materials in the range (A) (4100-500 cm^{-1}) and (B) (2200-500 cm^{-1}).

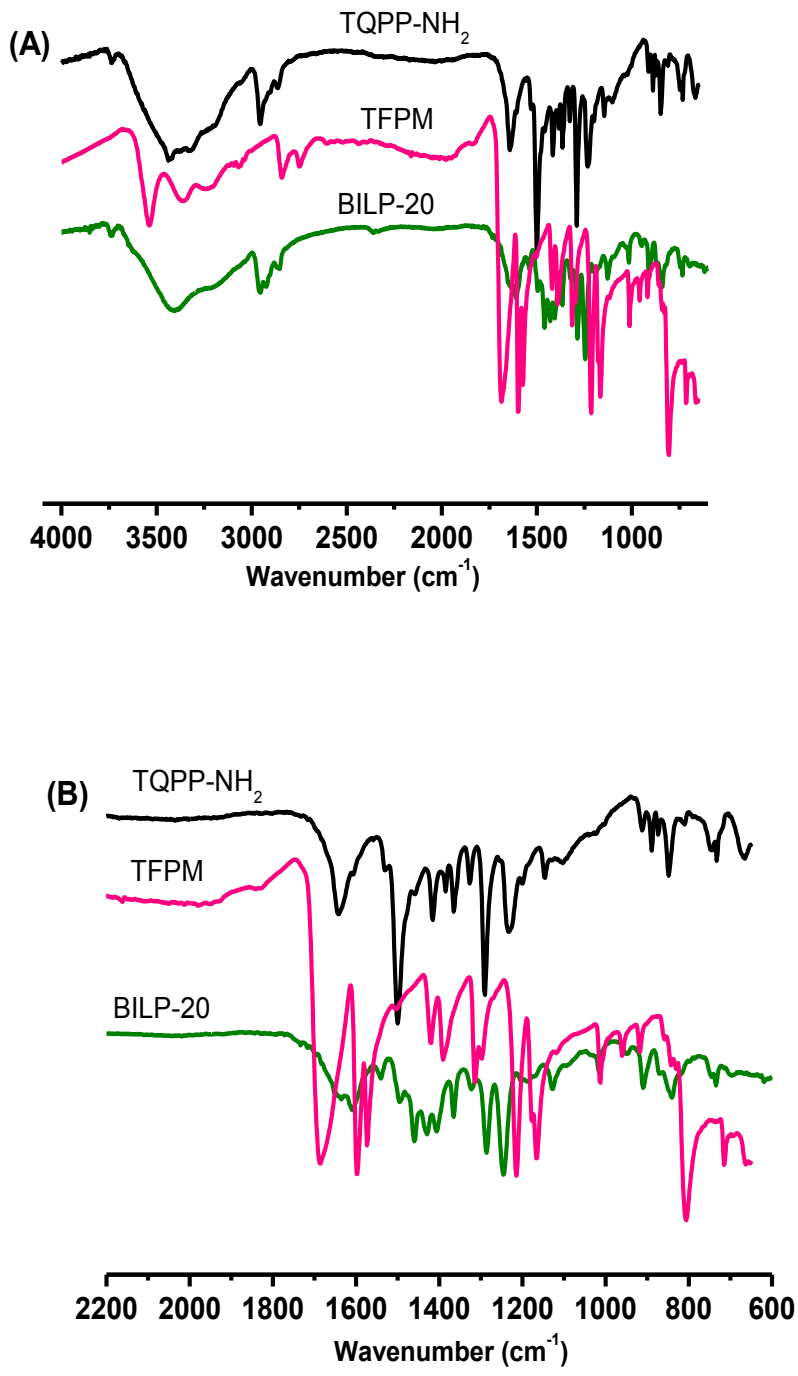

Figure 4.7: FT-IR spectra of BILP-20 and its corresponding starting materials in the range (A) (4100-500 cm^{-1}) and (B) (2200-500 cm^{-1}).

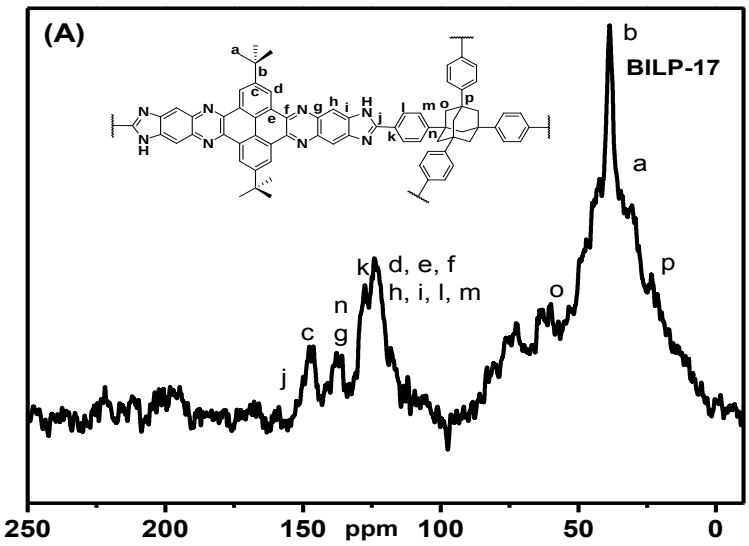
(A)
BILP-17
b
a
p
o
k
d, e, f
h, i, l, m
n
g
c
j
250
200
150
ppm
100
50
0

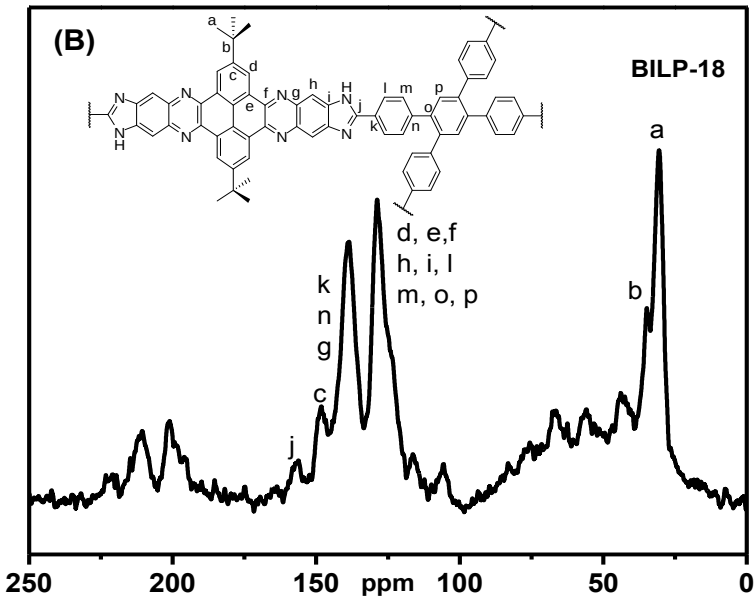
(B)
BILP-18
a
b
d, e,f
h, i, l
m, o, p
k
n
g
c
j
250
200
150
ppm
100
50
0

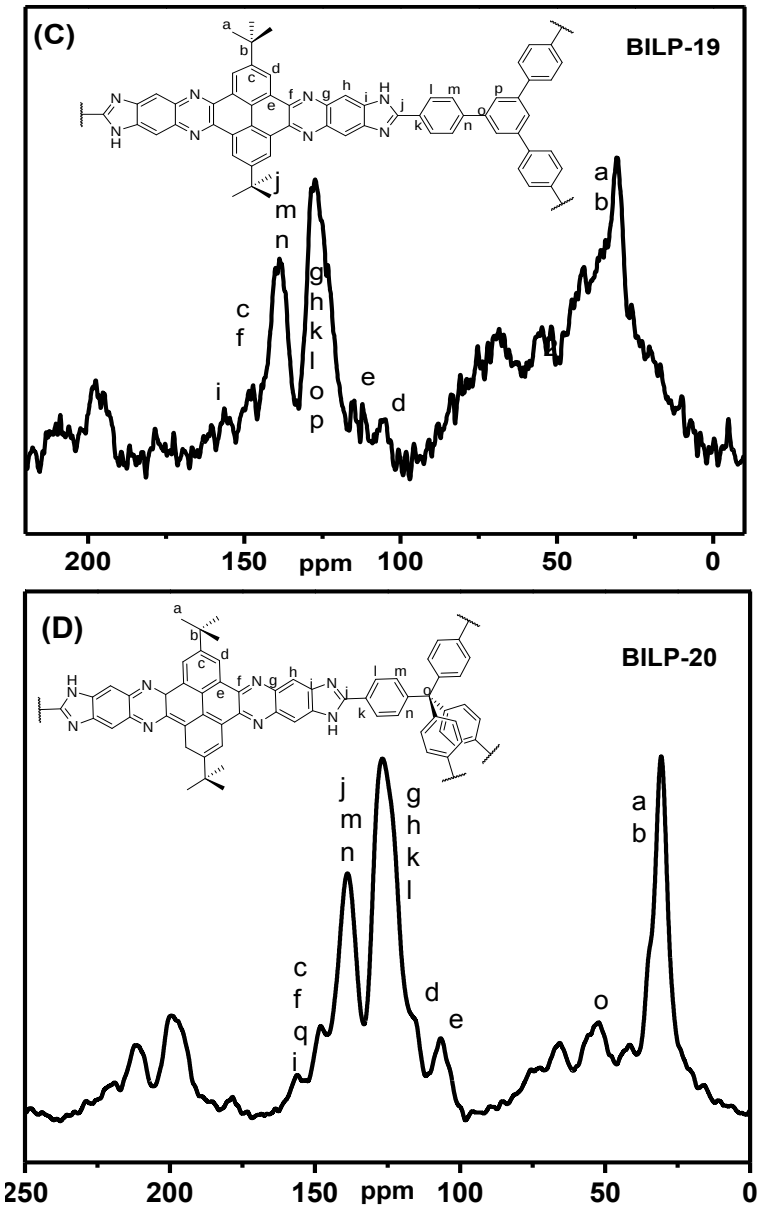

Figure 4.8B: Solid state ^{13}C CP-MAS NMR spectra of (A) BILP-17, (B) BILP-18, (C) BILP-19, and (D) BILP-20.

4.3.1 Porosity and Low Pressure Gas Uptake Measurements

The porosity of pyrazine-derived BILPs was investigated by argon sorption-desorption measurements. Prior to sorption measurements, the polymers were activated at 120 °C and 1.0 x 10^{-5} Torr for 20 hrs. The isotherms were collected at 87 K, which resulted in fully reversible behavior and indicated the microporosity. The gradual uptake of Ar with increased pressure leads to Type III isotherms, which was observed from the rapid Ar uptake at low pressure (0-0.1 bar) as illustrated in Figure 4.9. This trend is expected because of the long nature of the organic linkers that tend to form flexible frameworks. The hysteresis observed for all materials is consistent with the powdery and the flexible nature of BILPs. Applying the BET model to the sorption branch within the pressure range of P/P_o= 0.05-0.15 resulted in moderate surface areas 952, 947, 623, and 975 $m^2 g^{-1}$ for BILP-17, BILP-18, BILP-19, and BILP-20, respectively (Table 4.1 and Figure 4.10). The surface areas of pyrazine-derived BILPs are within the range of the surface areas of all reported BILPs, especially the 2D polymers. It is well documented that the presence of the (t-butyl) group on the pyrene core plays a significant role in enhancing the solubility when used in small molecules because it suppresses strong pi-stacking and thus molecular aggregation.[112]

Pore size distribution (PSD) curves were estimated from the argon isotherms by nonlocal density functional theory (NLDFT) on the adsorption branch with a cylindrical/sphere pore model on the argon isotherms. PSD was found to be centered at 10.0 Å (BILP-17), 9.7 Å (BILP-18) and ~8.99 Å (BILP-19 and BILP-20) as shown in Figure 4.11. Pore volume was calculated from single point measurements (P/P_o= 0.95) and found to be 0.76, 0.69, 0.37, and 0.57, cc g^{-1} for BILP-17, BILP-18, BILP-19, and BILP-20, respectively. The large pore volume of BILP-17 most likely is due to the presence of the adamantane core, which also leads to the highest

porosity and largest PSD. It is worth mentioning that the 3D networks reveal higher porosity and greater pore volume than 2D networks.

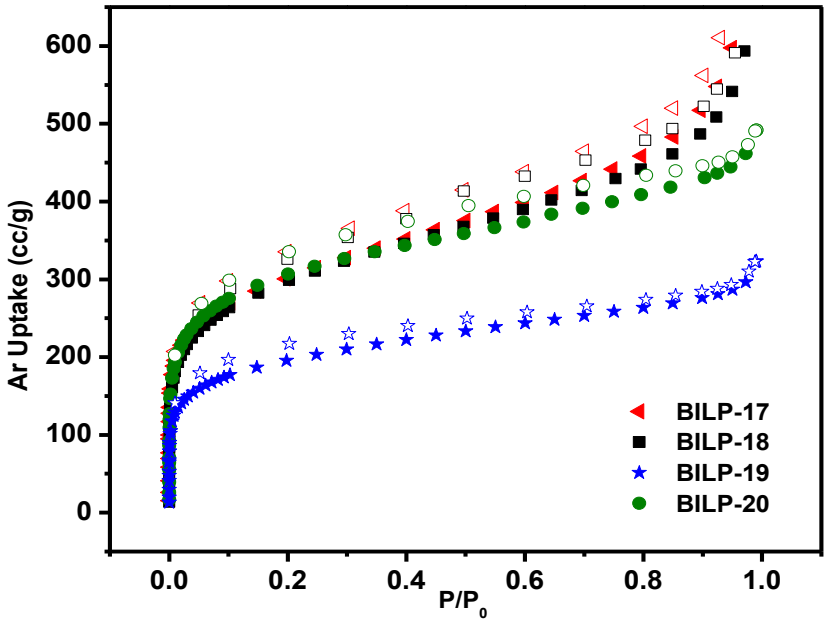

Figure 4.9: Ar adsorption isotherms for pyrazine-derived BILPs were measured at 87 K. The filled symbols are adsorption points and the empty symbols are desorption points.

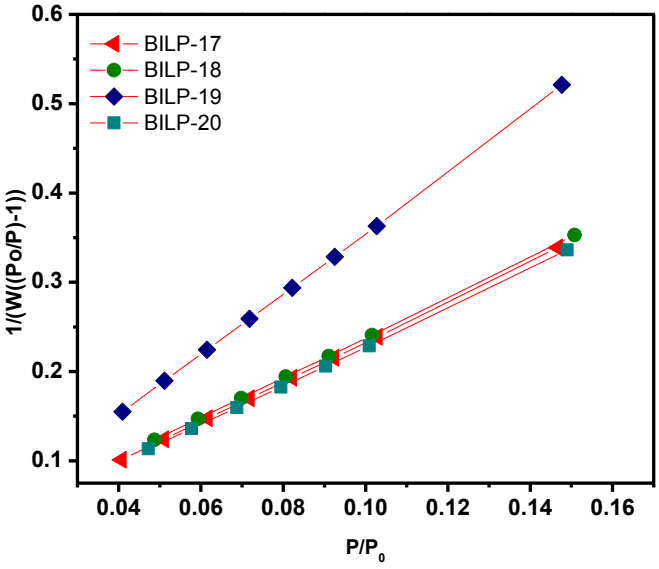

Figure 4.10: BET surface area plots for pyrazine-derived BILPs were calculated from the Ar adsorption isotherm at 87 K. The model was applied from P/Po = 0.05-0.16. (W = Weight of gas absorbed at a relative pressure P/Po).

Table 4.1: BET and Langmuir values pyrazine-derived BILPs were calculated from Ar adsorption isotherms at 87 K

BILP	**Surface area (BET)** $m^2 g^{-1}$	**Langmuir Surface area** $m^2 g^{-1}$
BILP-17	952	1181
BILP-18	947	1202
BILP-19	623	775
BILP-20	975	1227

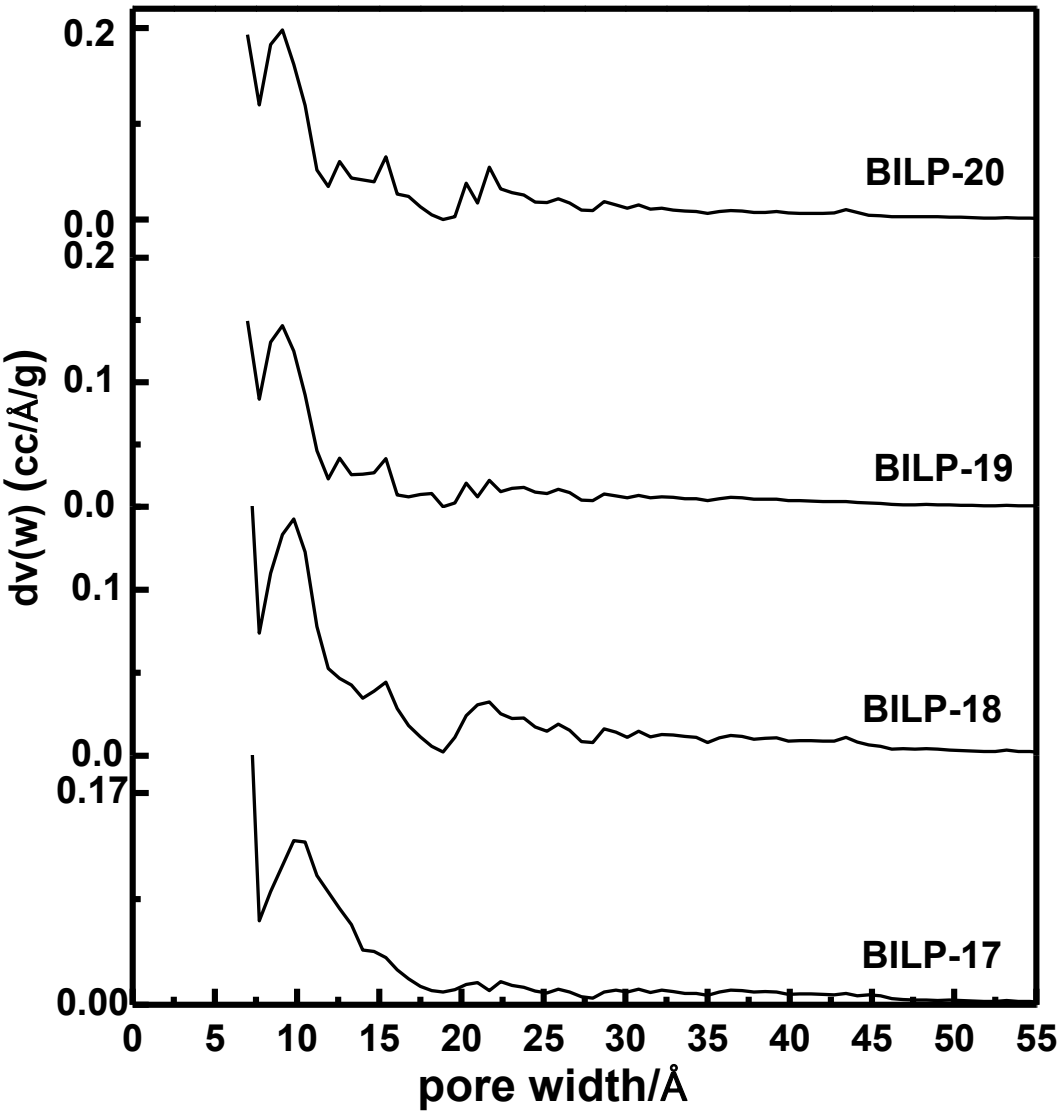

Figure 4.11: Pore Size Distribution of pyrazine-derived BILPs was calculated from the Ar adsorption isotherms.

In addition to the heterogeneity and sub-nanometer porosity of pyrazine-derived BILPs, tailoring the microporosity and altering the pore dimensions and environment are believed to have a significant impact on selective gas uptake and binding affinities. Moreover, the "elastic" nature of the polymers can be beneficial for admitting gas molecules or ions into the pores for storage and sensing applications. Accordingly, the impact of the imidazole moiety and the chemical nature of the pyrazine core on the uptake of small gas molecules CH_4, CO_2 and H_2, and the preferential binding of CO_2 over N_2 and CH_4, were investigated. CO_2, H_2 and CH_4 gas isotherms were collected and their respective isosteric heats of adsorption (Q_{st}) calculated and summarized in Table 4.2.

The CO_2 isotherms of the polymers are fully reversible with very minor hysteresis and exhibit a steep rise at low pressure. BILP-17 has the highest CO_2 uptake 141 mg g^{-1} at (273 K / 1 bar) among the polymers, which can be attributed to the largest pore volume. The uptakes for BILP-18, BILP-19, and BILP-20 are 127, 97, and 124 mg g^{-1}, respectively (Figure 4.12 A, B). The CO_2 uptake values are within the uptake ranges of other BILPs. The high CO_2 uptakes are expected to arise from strong interactions of the polarizable CO_2 molecules through dipole-quadrupole interactions that utilize the imine-nitrogen sites of imidazole rings and the presence of the extended conjugated system.

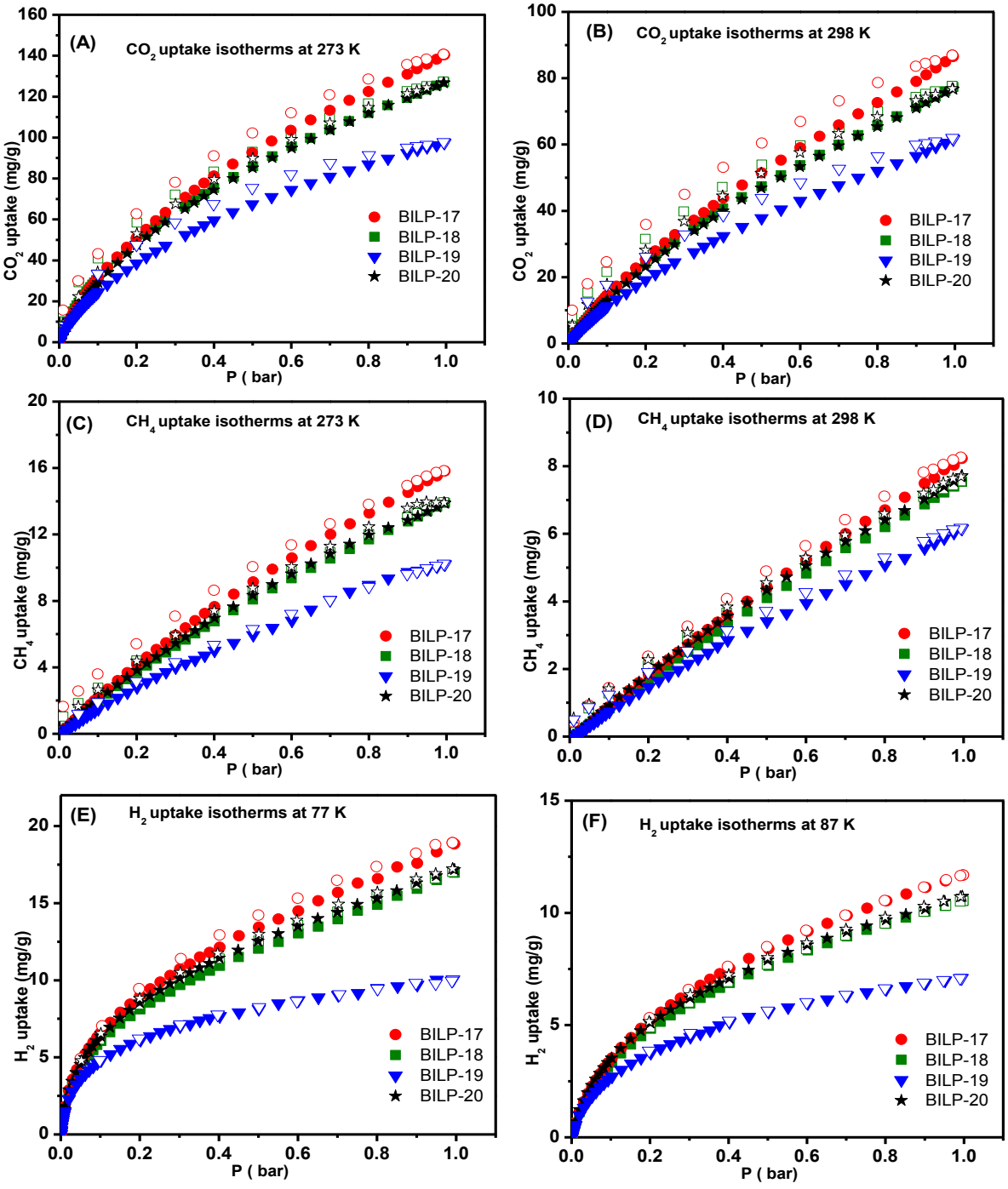

Figure 4.12: CO_2, CH_4, and H_2 gas uptake isotherms for pyrazine-derived BILPs.

The binding affinity for CO_2 was determined by calculating the isosteric heats of adsorption Q_{st} using the adsorption data collected at 273 K and 298 K and compared to the Q_{st} of other BILPs. Heats of adsorption were calculated using the virial method, which revealed that the Q_{st} values at zero coverage fall relatively in a range 39-29 kJ mol^{-1} (Figure 4.13 A). BILP-18 has the highest Q_{st} (39 kJ mol^{-1}) among all BILPs, which can be related to the small pore size and the chemical nature of the polymer. The presence of the high extended-conjugated environment beside the pyrazines' free-nitrogen sites are believed to introduce more CO_2 interaction sites than other polymers. This Q_{st} value is consistent with the reported value for BILP-10 (38 kJ mol^{-1}), which was expected to arise from strong interactions of the polarizable CO_2 molecules through hydrogen bonding and/or dipole-quadrupole interactions. [69a] Accordingly, by comparing the heats of adsorption for BILP-10, BILP-18, and other pyrazine-derived BILPs, it is notable that there is some correlation between the Q_{st} value and the formation of large pores and the presence of extended-conjugated system. However, the presence of the adamantane and tetraphenylmethane cores in BILP-17 and BILP-20 can limit the conjugation and lower CO_2 interaction.

We also considered pyrazine-derived BILPs for hydrogen and methane storage studies because both gases are highly attractive candidates for use in automotive applications as a result of their abundance and clean nature. Moreover, CO_2 removal from flue gas or methane-rich gases (natural gas and landfill gas) is needed to mitigate climate change and enhance the quality, and energy density of methane-rich fuels.[3, 7] Accordingly, methane and hydrogen pure gas isotherms were collected at low pressure conditions, and their heats of adsorption were calculated. Methane isotherms are completely reversible and exhibit maximum uptake of 16.0 mg g^{-1} at 273 K for BILP-17, and the uptake range is (12-14 mg g^{-1}) for other polymers (Figure 4.12 C, D). These

values are within the range reported for all BILPs. The Q_{st} for CH_4 was calculated using the adsorption data, and resulted in the highest value for BILP-17 (23.6 kJ mol^{-1}), which drops slightly with loading (Figure 4.13 B). On the other hand, BILP-19 has the lowest CH_4 uptake and Q_{st} compared to other polymers, which is attributed to being the lowest surface area polymer. BILP-18 and BILP-20 have almost the same values, which can be related to their similar porosity properties.

To evaluate pyrazine-derived BILPs toward hydrogen uptake and binding affinity, pure hydrogen isotherms were collected at 77 K and 87 K at 1 bar. The hydrogen uptake of the polymers was within the range of all BILPs (1.0-1.9 wt%) (Figure 4.12 E, F). The H_2 Q_{st} values for pyrazine-derived BILPs are consistent with Q_{st} values of all BILPs and in the range 7.6-8.0 kJ mol^{-1} (Figure 4.13C). The H_2 uptake remains modest and far below the DOE target for 2015.

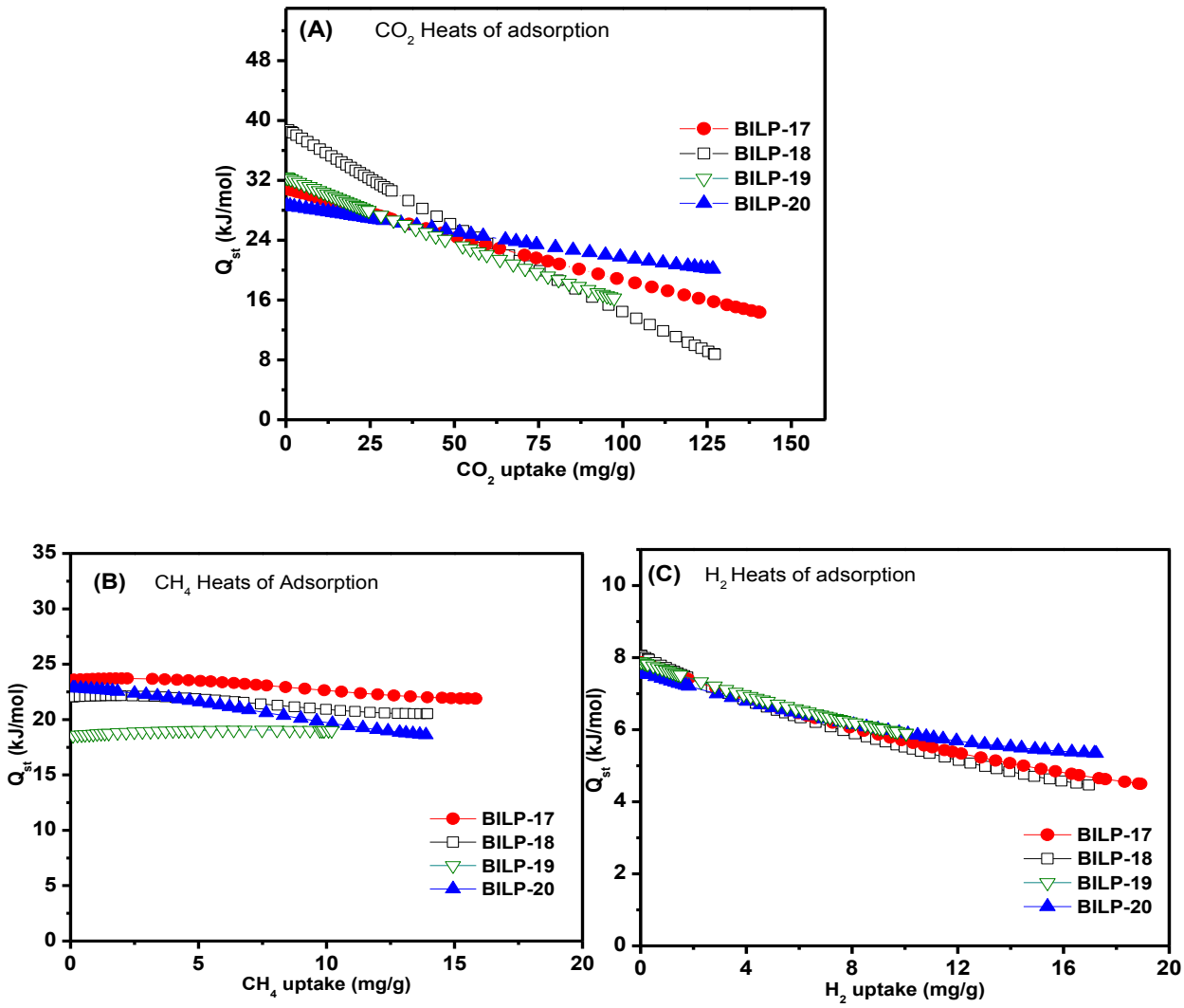

Figure 4.13: Isosteric heats of adsorption (Q_{st}) for pyrazine-derived BILPs (A) CO_2, (B) CH_4, (C) and H_2.

Table 4.2: Gas Uptake and heats of adsorption data of pyrazine-derived BILPs

polymer	SA[a] BET	Pore volume[b]	H_2 at 1 bar[c]			CO_2 at 1 bar[c]			CH_4 at 1 bar[c]			N_2 at 1 bar[c]	
			77 K	87 K	Q_{st}	273 K	298 K	Q_{st}	273 K	298 K	Q_{st}	273 K	298 K
BILP-17	**952**	0.76	19	12	7.8	141	87	31	16	8	23.6	6.4	1.9
BILP-18	**947**	0.69	17	11	8.0	127	78	39	13.9	7.6	22	6.1	2.6
BILP-19	**623**	0.37	10	7	7.9	97	62	32	10	6	18.6	3.9	1.4
BILP-20	**975**	0.57	17	11	7.6	124	77	29	14	7.7	21	6.3	1.9

[a]Surface area ($m^2\ g^{-1}$) was calculated from Ar isotherm. [c]Pore volume (cc g^{-1}) was calculated from single point measurements (P/P_0 =0.95). [c]Gas uptake in mg g^{-1} and the isosteric enthalpies of adsorption (Q_{st}) in kJ mol^{-1}).

4.3.2 Gas Selectivity Studies

The preferential binding of pyrazine-derived BILPs to CO_2 over CH_4 and N_2 was calculated using the initial slope calculations of pure gas isotherms, which was collected at 273 K (Figure 4.14). These calculations were performed to evaluate the impact of the extended and limited-conjugated natures on the selectivity of the new polymers. The resulting selectivity data from initial slope are summarized in Table 4.3 and Figure 4.15. From the initial slope calculations and at 273 K, CO_2/N_2 selectivity values for the extended-conjugated BILP-18, and BILP-19 are 60 and 86, respectively. On the other hand, the selectivity of BILP-17 and BILP-20 was calculated at 273 K and resulted in 61 and 46, respectively. Overall, the IAST data were collected at 273 K (Figure 4.16) and seem to be consistent with the results obtained from initial slope calculations.

Table 4.3: Initial slope selectivity of pyrazine-derived BILPs at 273 K (298 K)

BILP	Selectivity			
	Initial Slope data 273 K(298 K)		IAST 273 K	
	CO_2/N_2	CO_2/CH_4	CO_2/N_2	CO_2/CH_4
BILP-17	61	6	63	8
BILP-18	60	9	104	13
BILP-19	86	10	81	10
BILP-20	46	7	47	7

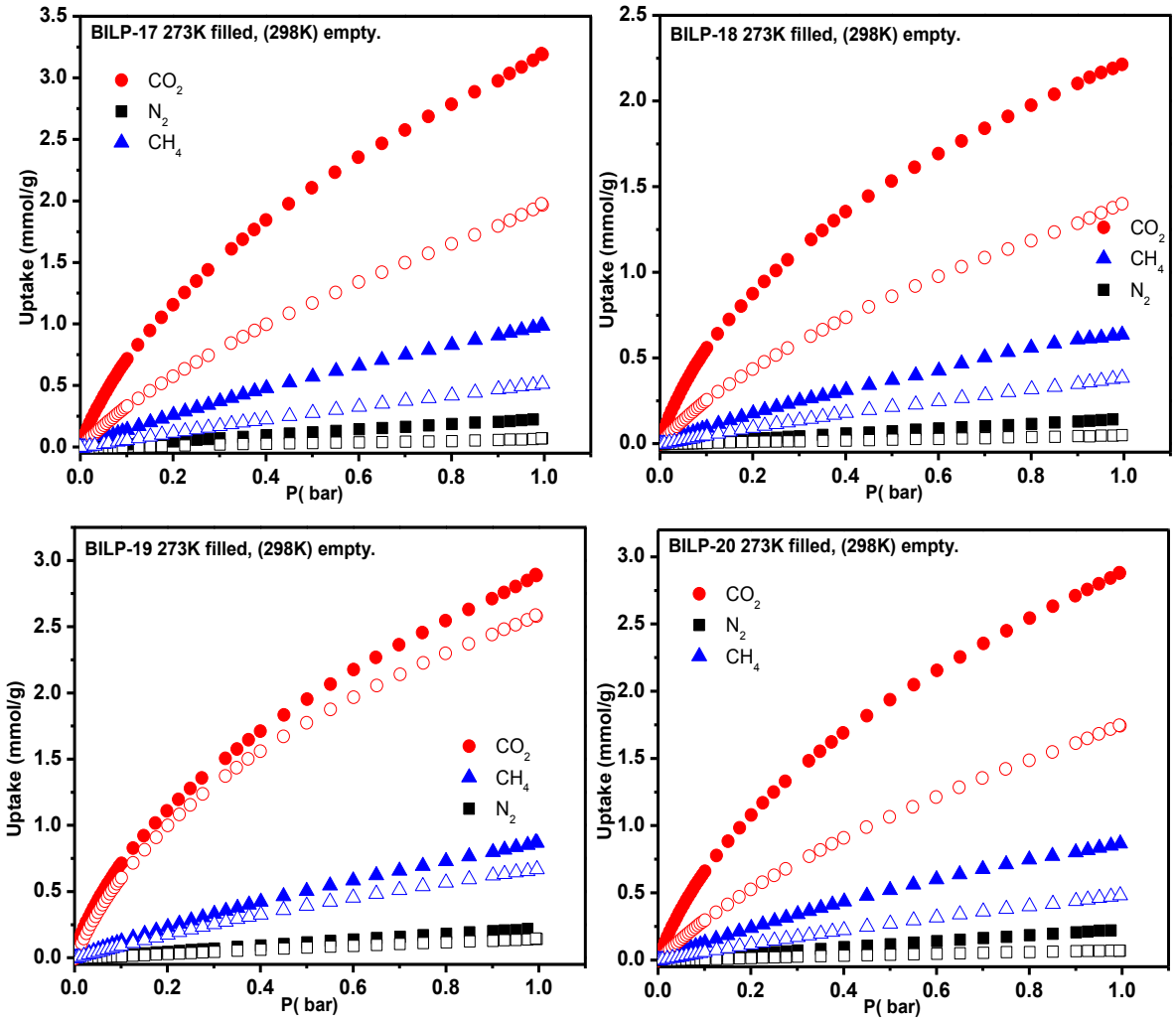

Figure 4.14: Gas sorption capacities of pyrazine-derived BILPs

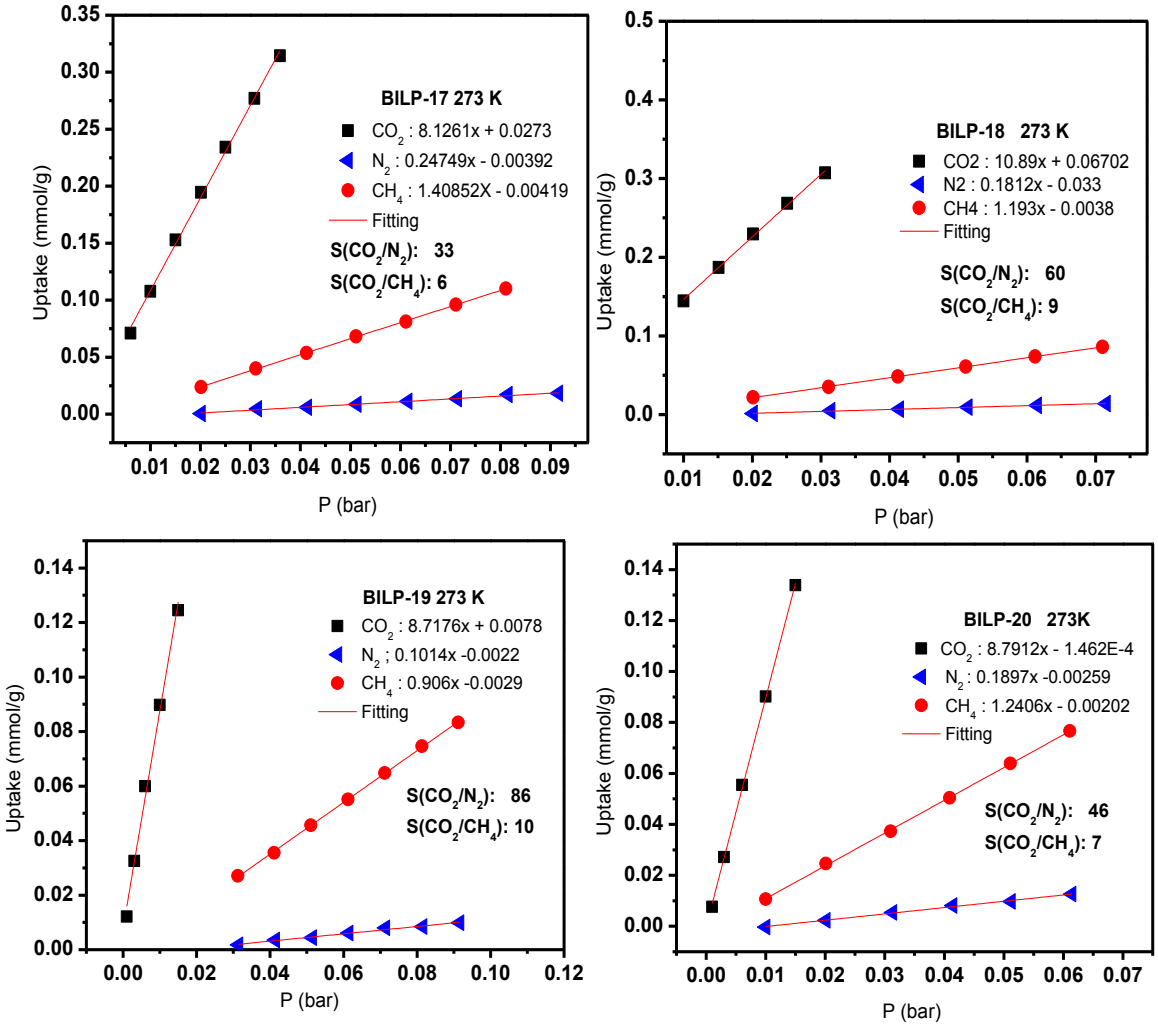

Figure 4.15: Initial slope calculations of pyrazine-derived BILPs and the adsorption selectivity of CO_2 over N_2 and CH_4 at 273 K.

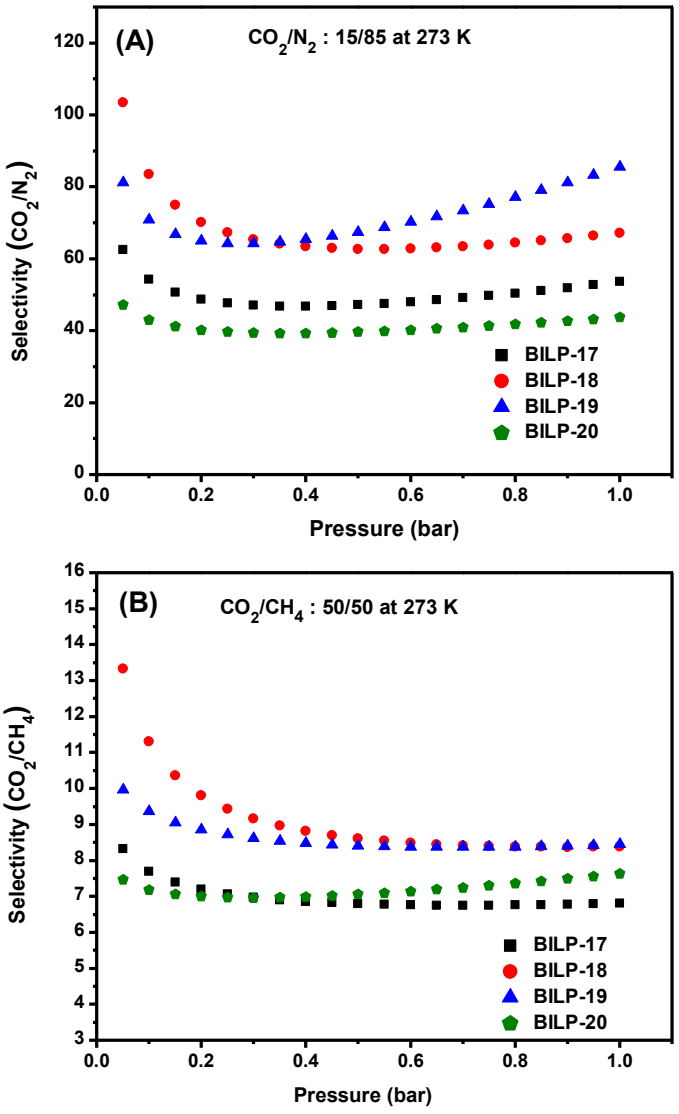

Figure 4.16: Ideal Adsorption Solution Theory selectivity data for CO_2/N_2 and CO_2/CH_4 at 273 K and different binary mixture ratios for BILP-17, BILP-18, BILP-19, and BILP-20.

4.4. Photoluminescence Study

To investigate the electronic structure of BILPs we have recorded the UV-Visible absorption, photoluminescence (PL), and photoluminescence excitation spectra of BILP-17 and BILP-18 and the corresponding tetra-amine monomers (Figure 4.17).

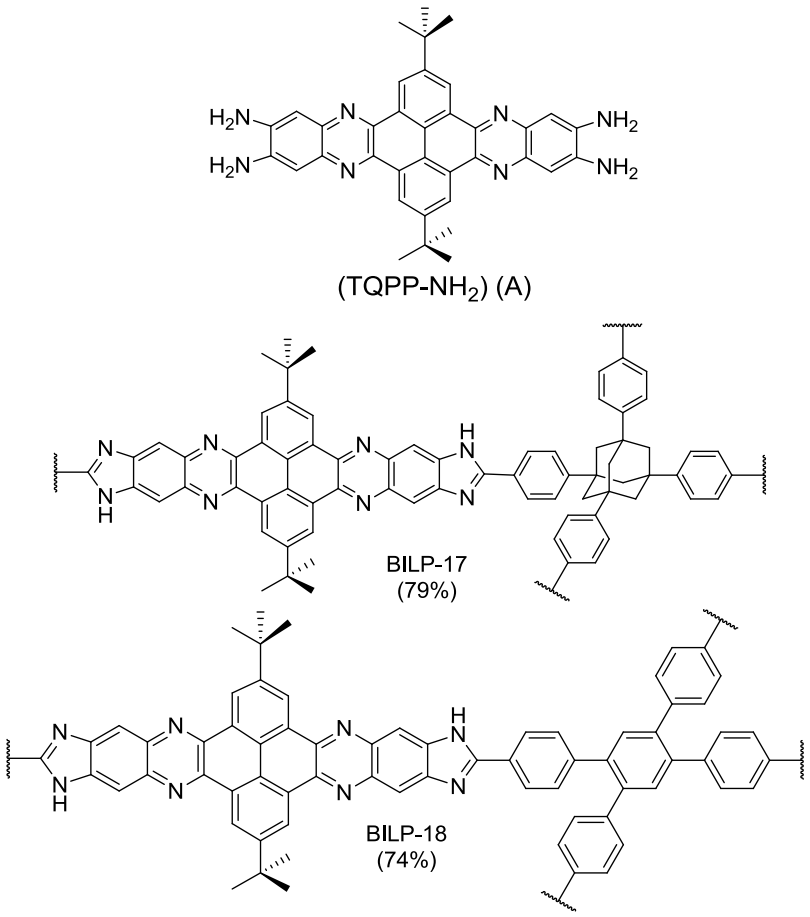

Figure 4.17: The structures of TQPP-NH_2, BILP-17 and BILP-18.

4.4.1. Experimental Methods and Measurements

UV-visible absorption spectra were recorded using a Cary 6000i UV-Vis-NIR spectrophotometer (Agilent Technologies) by using 10 mm quartz cuvettes. For the solution UV-visible absorption and emission spectra, ~0.0035g polymers were dispersed in DMF and sonicated for 2-3 min, and the solution was allowed to settle for couple of minutes. Supernatant of the solution was used to carry out the UV-vis measurements.

Absorption spectra of the powdered polymers were acquired by Diffuse reflectance (DRA) utilizing an integrating sphere attached in the Cary 6000i UV-visible spectrophotometer. The powdered polymer was pressed on top of a barium sulfate (as background) surface to perform the band gap measurements. The data obtained from DRA was converted to absorption utilizing the Kubelka-Munk function.[115]

Solution photoluminescence of the polymers was done in a Cary Eclipse Fluorescence spectrophotometer (Agilent Technologies) with 10 nm excitation and emission slit in a 10 mm quartz optical cell. Same technique was adapted for preparing solution as UV-vis to obtain solution PL. Emission measurements of the powdered polymers were carried out at liquid N_2 temperature where the polymer samples were taken inside an NMR tube and placed into transparent glass N_2 dewar (already filled with liquid N_2) and excited at exciton wavelengths to get the emission spectra.

4.4.2. Results and Discussions

Both BILP-17 and BILP-18 exhibit well-defined absorption spectra when dispersed in dimethylformamide (DMF) via sonication. The absorption spectrum of BILP-17 exhibits sharp excitonic features at 304, 340 and 451 nm along with a low intensity absorption hump at 428 nm whereas that of BILP-18 exhibits similar excitonic features at 297, 344, and 461 nm and a low intensity shoulder at 433 nm (Figure 4.18A).

In contrast, the corresponding monomer units dispersed in DMF display well-defined excitonic peaks at 315, 337, and 468 nm with a low intensity shoulder at 440 nm. Based on the literature reports on pyrene-fused Azaacenes the absorption humps observed at 428, 433, and 440 nm for BILP-17, BILP-18, and the corresponding tetra-amine monomers can be assigned to n-π* electronic transitions, respectivly.[17,18] Likewise, the sharp excitonic maxima observed at 340, 344, and 337 nm for BILP-17, BILP-18, and the monomers are likely to arise from π-π* optical transitions.[17,18] The relatively smaller changes in the solution absorption spectra of polymers in comparison to monomer units suggest minimum or no change in the electronic structure upon polymerization.

The solid state diffuse reflectance (converted to absorption) spectra of both polymers exhibit well-defined bandgaps, which are 1.74 and 1.99 for BILP-17 and BILP-18. The bandgap onsets in the visible spectrum that are significantly red shifted compared to the tetra-amine monomer units (2.21 eV). The lower bandgaps observed in polymers in comparison to precursor monomers can be attributed to increased charge delocalization of the excitonic states, which can potentially create low energy electronic transitions upon polymerization.[19]

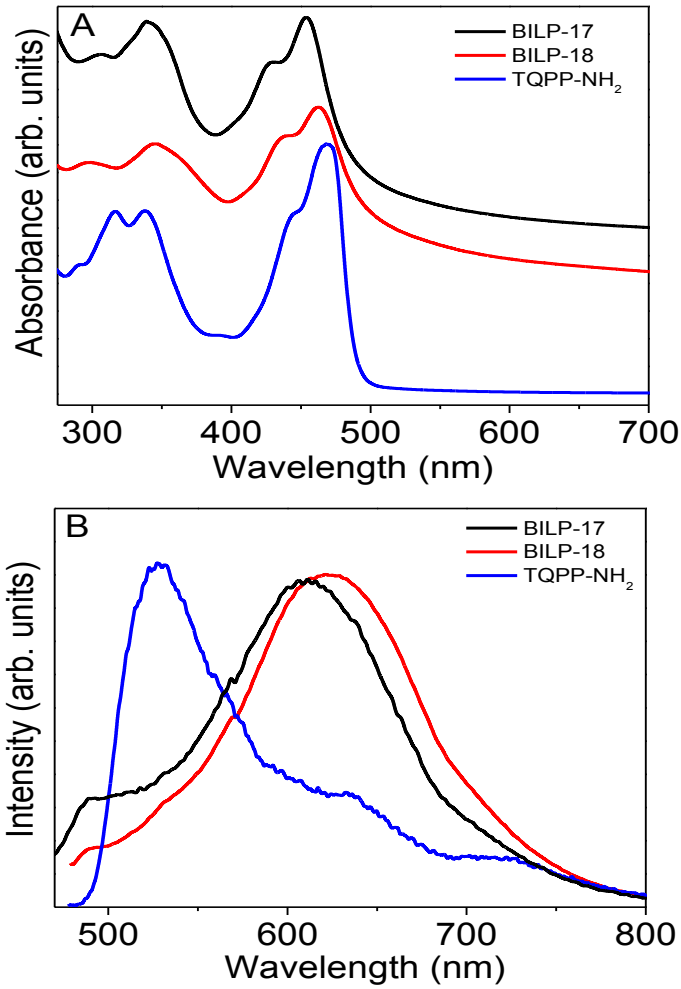

Figure 4.18: UV-visible (A) absorption, and (B) emission, spectra of the BILP-17 (black) BILP-18 (red) and the corresponding monomer units (blue).

When a solution of BILP-17 is excited at 340 nm (π-π*) or 428 nm (n-π*) electronic transitions, low intensity orange-red color emission was observed (π_{max} ~608 nm, PLE = 463 nm). Similarly, the luminescence spectrum of BILP-18 in DMF exhibits intense red fluorescence with an emission maximum at ~630 nm (PLE = 448 nm). In contrast, the corresponding tetra-amine units dispersed in DMF exhibit green fluorescence with an emission maximum at 528 nm (PLE = 395 nm) along with a well-defined vibronic pattern (Figure 4.18B) suggesting the inherent molecular structure.[20] The Stokes shift of ~160-167 nm was observed for both polymers revealing significant changes in the exciton prior to radiative relaxation. Consistent with the bandgap measurements, the emission energy of BILP-17 is found to be intermediate of those of the tetra-amine monomer and BILP-18 likely due to the disruption of conjugation at the adamantane center. Nevertheless, the vibronic structure inherent in the monomer units was not observed in the emission spectra of both polymers, suggesting the absence of molecular structure. This observation is consistent with the increased pi-conjugation in both polymers as a result of benzimidazole moiety formation.

Quantum yield measurements were carried out relative to Rhodamine 101 in ethanol and showed values in range of <0.1% and 9% for BILP-17 and BILP-18, respectively. The improved quantum efficiencies of BILP-18 in comparison to BILP-17 can be attributed to the increased charge delocalization in BILP-18, which can potentially increase the probability of radiative recombination of the exciton.

4. 5 Conclusions

In conclusion, we have synthesized new pyrazine-derived BILPs as examples of extended-conjugated benzimidazole-linked polymers. The new polymers were synthesized via polycondensation reaction between aryl-aldehydes and (TQPP-NH_2) building units. The successful incorporation of the phenazine core and the imidazole moiety into the polymer backbone were confirmed by spectral and analytical characterization methods. All pyrazine-derived polymers are porous with modest surface areas around ~950 m^2 g^{-1}, while BILP-19 has the lowest surface area, 623 m^2 g^{-1}. The heats of adsorption were calculated from the virial method for CO_2, CH_4 and H_2 for all polymers, and have shown values within the range of all reported BILPs. The preferential selectivity of CO_2/N_2 and CO_2/CH_4 were evaluated for the polymers at 273 K from the initial slope calculations and IAST. BILP-18 has shown the highest selectivity value from IAST, which confirmed the high CO_2 uptake due to the presence of the extended-conjugated surface. In addition to their gas uptake, BLP-17 and BILP-18 are semiconducting with bandgap of (1.74-1.99). Such properties make both polymers interesting for sensing applications.

Chapter 5

Alkoxy-Functionalized Benzimidazole-Linked Polymers

5.1. Introduction

The inclusion of new functionality on the surface and the pores of POPs was believed to have a significant impact on the binding affinity and gas separation applications. The synthetic methods for achieving this target include post-synthetic and pre-synthetic modification strategies.[44a, 59b, 64] Several examples of each method have been discussed in Chapter 1 and it has been shown that tuning the affinity of the framework functionalities toward CO_2 is an essential step in optimizing the adsorptive properties.[24, 60, 62] For instance, tailoring accessible nitrogen or amine functionalities into the framework of POPs or MOFs can significantly enhance CO_2 binding and uptake. BILPs are nitrogen-decorated POPs wherein the nitrogen sites are incorporated into the structure upon imidazole ring formation.[69] The accessible nitrogen sites are typically responsible for the enhanced CO_2 adsorption. However, their low surface areas compromise the high binding affinity and CO_2 capture, limiting their applications to only low pressure settings. Thus, introducing new functional groups, which would provide more interaction sites and enhance CO_2 uptake and porosity, is an important target to overcome these limitations.

In this Chapter we describe the synthesis of a series of alkoxy-functionalized BILPs using a multi-functional strategy called "Rational Ligand Design". This strategy depends on introducing different functional groups to the organic building units, which allows for tailoring of gas uptake properties, binding affinity, and porosity of the polymers. This approach was used to explore the impact of different pendant and freely rotating alkoxy groups to enhance the porosity of BILPs and study their impact on the gas sorption. The synthesis, characterization and the impact of the rational design process on the porosity is discussed in this Chapter.

5.2. Experimental

Materials and Methods

The starting materials, solvents, and characterization methods used in this study are reported in Chapter 2 and used without other purifications unless otherwise noted. The new chemicals in this study, used for the first time, are reported in this section. Tetrabromohydroquinone, anhydrous potassium carbonate, potassium hydroxide, dimethylsulfate, bromoethane, 1-bromobutane, isobutyl iodide and methanol are obtained from Sigma-Aldrich and Acros Organics and used without further purification. All reactions were handled under an inert atmosphere of nitrogen using Schlenk line technique. All aldehydes were purified according to the purification procedure reported for tetraphenyl formyl benzene (TFPB)[69e] in Chapter 2. All spectral and analytical characterization techniques including: elemental microanalyses, FT-IR spectra, liquid ^{1}H and ^{13}C-NMR spectra, Solid-state ^{13}C, thermogravimetric analysis (TGA), scanning electron microscopy imaging (SEM), and powder X-ray diffraction (XRD), were performed according to the methods reported in Chapter 2. Porosity and gas sorption experiments were collected by a

Quantachrome Autosorb IQ2 volumetric analyzer using adsorbates of UHP grade and following the same activation and sample collection procedures.

Synthesis and Characterization of BILPs and their starting materials

Synthesis of the Dialkoxyhydroquinones

The introduction of alkoxy functional groups to tetrakis(phenylformyl)benzene (TFPB) aldehyde, was accomplished by substitution reaction between tertabromohydroquinine (TBHQ) and different alkyl reagents (e.g. dimethylsulfate, bromoethane, 1-bromobutane and isobutyl iodide).The synthesis protocol of alkoxy-substituted derivatives was demonstrated according to the reported methods[116] and displayed in Scheme 5.1.

Synthesis of dimethoxy-tetrabrombenzene

A suspension of (TBHQ) and potassium carbonate in dry acetone was treated with dimethoxysulfate (methylating agent) over 1 hr. The mixture was stirred at RT for 24 hrs. The resulting orange suspension was filtered, the solvent was removed, and the final product was treated with portions of ammonium hydroxide, filtered, and recrystallized from methanol to obtain crystals in favorable yields. The ^{1}H-NMR and ^{13}C-NMR results are consistent with the reported values.[116a]

Synthesis of diethoxy-, dibutoxy- and di-isobutoxy tetrabromobenzene derivatives

A solution of (TBHQ) and potassium hydroxide in methanol was treated with alkyl halides (e.g. ethyl bromide, n-butyl bromide, and isobutyl iodide). The resulting dialkoxy tetrabromobenzene derivatives solution was heated at reflux for 48 hrs. The solvent was removed, and the residue was extracted with diethyl ether, washed with sodium hydroxide (0.5 M) and hydrochloric acid (0.1 M). After solvent removal, the products were recrystallized from methanol to afford 2,3,5,6-

Tetrakis-(4-bromo)dialkoxybenzene derivatives $(OR)_2TBB$ as fluffy white products. The ^1H-NMR and ^{13}C-NMR results are consistent with the reported values.[116a]

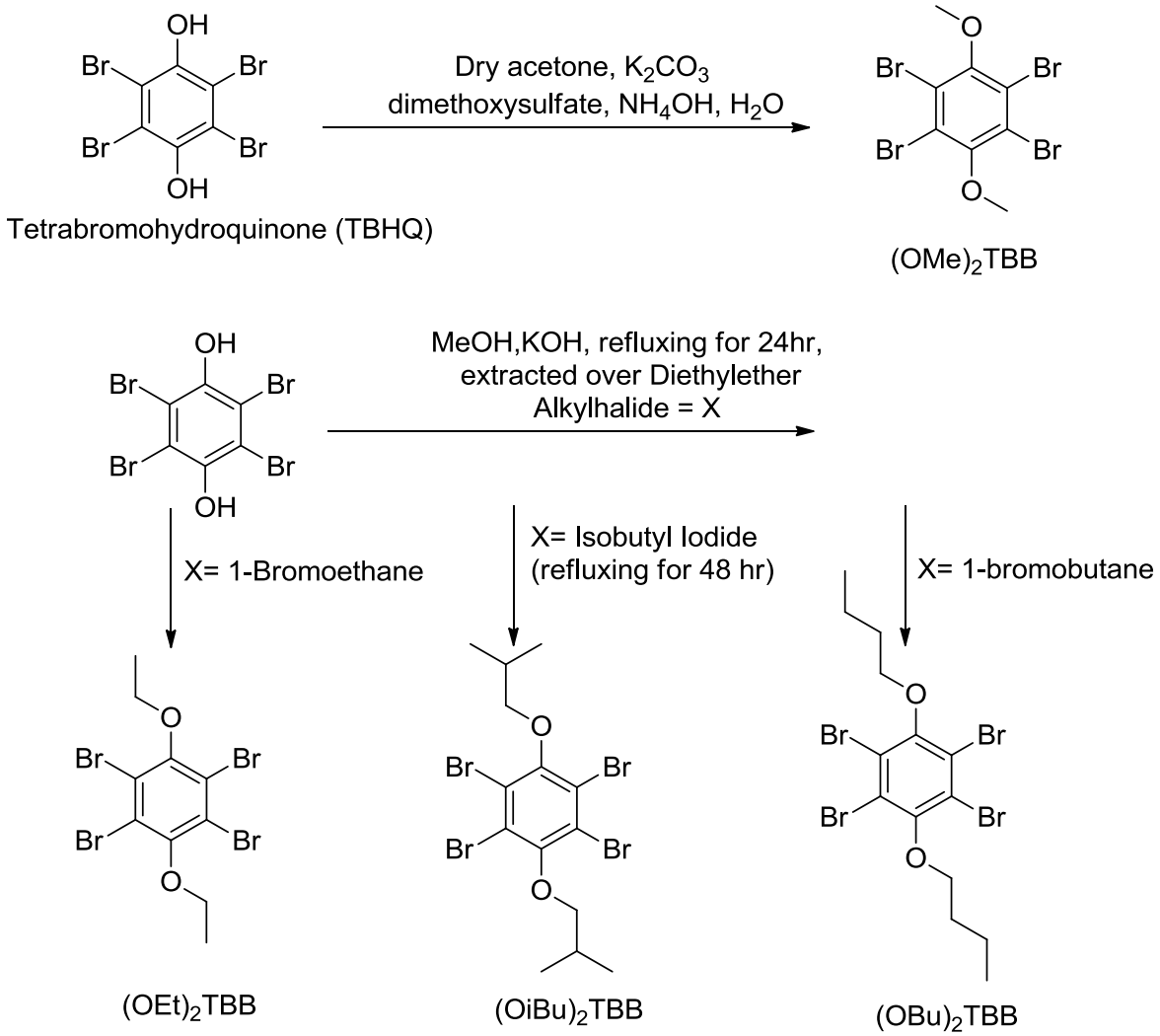

Scheme 5.1: Synthesis of dialkoxy substituted tetrabromobenzene derivatives.

Synthesis of the Functionalized Aryl-aldehydes

After the successful incorporation of dialkoxy substituents to tertabromohydroquinine, their corresponding dialkoxy tetraphenylformyl benzene derivatives were synthesized by Suzuki-coupling reactions (Scheme 5.2). The new alkoxy aryl-aldehydes were synthesized by using the synthetic approach of TFPB[69e] with minor modifications.

Synthesis of Tetrakis-(4-formylphenyl)-1,4-dimethoxybenzene $(OMe)_2$TFPB

2,3,5,6-Tetrakis-(4-formylphenyl)-1,4-dimethoxybenzene $(OMe)_2$TPFB was synthesized by following the synthetic protocol of TFPB.[69e] A mixture consisting of 2,3,5,6-Tetrabromo-1,4-dimethoxybenzene (1.2 g, 2.67 mmol), 4-formylphenylboronic acid (2.4 g, 16.0 mmol), palladium tetrakis(triphenylphosphine) (0.12 g, 0.10 mmol, 5.2 mol%), and potassium carbonate (4.2 g, 30.43 mmol) was stirred and refluxed in dry 1,4-Dioxane (50 mL) under inert conditions for 3 days. The resulting milky suspension was poured into ice slurry and stirred for 30 min. The product was filtered and extracted with chloroform then recrystallized from hot ethylacetate to afford $(OMe)_2$TFPB as a white powder (1.1 g, 73%). Anal. Calcd for $C_{36}H_{26}O_6$: C, 77.97%; H, 4.73%; O, 17.31% Found: C, 77.73%; H, 4.95%; O, 17.38%. ^{1}H NMR (300 MHz, $CDCl_3$, δ (ppm)): 9.96 (s, 4H, formyl H) 2.86 (s, 6H, Methoxy- H), 7.38 (d, 8H, Ar H) and 7.73 (d, 8H, Ar H).^{13}C NMR ($CDCl_3$, 75 MHz) δ (ppm) 191.0, 152.0, 142.0, 136.0, 135.0, 131.0, 129.0 and 61 (Methoxy-C) (Figure 5.1A).

Synthesis of 2,3,5,6-Tetrakis-(4-formylphenyl)-1,4-diethoxybenzene $(OEt)_2$TFPB

2,3,5,6-Tetrakis-(4-formylphenyl)-1,4-diethoxybenzene $(OEt)_2$TFPB was synthesized by following the synthetic protocol of (TFPB).[69e] A mixture consisting of 2,3,5,6-Tetrabromo-1,4-diethoxybenzene (1.2 g, 2.51 mmol), 4-formylphenylboronic acid (2.4 g, 16.0 mmol), palladium tetrakis(triphenylphosphine) (0.12 g, 0.10 mmol, 5.2 mol%), and potassium carbonate (4.2 g, 30.43 mmol) in dry 1,4-Dioxane (50 mL) under N_2 for 3 days. The resulting mixture was treated with an ice slurry (200 mL) and 70 mL concentrated hydrochloric acid then extracted with chloroform. The crude yellowish product was purified by silica gel column using chloroform to afford $(OEt)_2$TFPB as a pale yellow powder (1.0 g, 67%). Anal. Calcd for $C_{38}H_{30}O_6$: C, 78.33%; H, 5.19%; O, 16.48% Found: C, 78.94%; H, 5.0 %; O, 16.06 %. ^{1}H NMR (300 MHz, $CDCl_3$, δ (ppm)): 9.95 (s, 4H, formyl H), 0.5 (t, 6H, -CH_3), 3.0 (q, 4H, -CH_2), 7.39 (d, 8H, Ar H) and 7.75 (d, 8H, Ar H).^{13}C NMR ($CDCl_3$, 75 MHz) δ (ppm) 192.0, 151.0, 143.0, 135.0, 134.0, 131.0, 128.0 , 69 (-CH_2) and 15 (terminal –CH_3) (Figure 5.1B).

Synthesis of 2,3,5,6-Tetrakis-(4-formylphenyl)-1,4-dibutoxybenzene $(OBu)_2$TFPB

2,3,5,6-Tetrakis-(4-formylphenyl)-1,4-diethoxybenzene $(OBu)_2$TFPB was synthesized according to the reported synthesis of TFPB with minor modification.[69e] A mixture consisting of 2,3,5,6-Tetrabromo-1,4-dibutoxybenzene (1.2 g, 2.25 mmol), 4-formylphenylboronic acid (2.4 g, 16.0 mmol), palladium tetrakis(triphenyl-phosphine) (0.12 g, 0.10 mmol, 5.2 mol%), and potassium carbonate (4.2 g, 30.43 mmol) and degassed water (2 mL) in dry DMF (50 mL) under N_2 for 3 days. The resulting mixture was treated with an ice slurry (200 mL) and 70 mL concentrated hydrochloric acid then extracted with chloroform. The crude yellow product was purified by silica gel column using chloroform to afford $(OBu)_2$TFPB as a pale yellow powder (1.2 g, 84.0%). Anal. Calcd for $C_{42}H_{38}O_6$: C, 78.97%; H, 6.0%; O, 15.03% Found: C, 79.27%; H,

6.12%; O, 14.61%. ^{1}H NMR (300 MHz, $CDCl_3$, δ (ppm)): 10.0 (s, 4H, formyl H), 7.40 (d, 8H, Ar H), 7.75 (d, 8H, Ar H) 2.94 (t, 4H, -OCH_2), 0.85 (m, 4H, -CH_2), 0.73 (m, 4H, -CH_2), 0.45 (t, 6H, -CH_3),.^{13}C NMR ($CDCl_3$, 75 MHz) δ (ppm) 191.0 (-CHO) , 150.0, 143.0, 136.0, 135.0, 131.0, 128.0 (Ar–C), 72, 31, 18 and 13 (Butoxy carbons) (Figur 5.1C).

Synthesis of 2,3,5,6-Tetrakis-(4-formylphenyl)-1,4-di-isobutoxybenzene $(OiBu)_2$TFPB

2,3,5,6-Tetrakis-(4-formylphenyl)-1,4-diethoxybenzene $(OiBu)_2$TFPB was synthesized by following the synthetic protocol of (TFPB) with minor modification.[69e] A mixture consisting of 2,3,5,6-Tetrabromo-1,4-diisobutoxybenzene (1.3 g, 2.44 mmol), 4-formylphenylboronic acid (2.4 g, 16.0 mmol), palladium tetrakis(triphenylphosphine) (0.12 g, 0.10 mmol, 5.2 mol%), and potassium carbonate (4.2 g, 30.43 mmol) in dry 1,4-Dioxane (50 ml) under N_2 for 3 days. The resulting mixture was treated with a slurry consisting of 200 mL ice and70 mL concentrated hydrochloric acid then extracted with chloroform. The crude yellowish product was purified by silica gel column using chloroform to afford $(OiBu)_2$TFPB as white powder (1.25 g, 78.0%). Anal. Calcd for $C_{42}H_{38}O_6$: C, 78.97%; H, 6.0%; O, 15.03% Found: C, 77.0%; H, 5.98%; O, 16.61%. ^{1}H NMR (300 MHz, $CDCl_3$, δ (ppm)): 10.0 (s, 4H, formyl H), 7.40 (d, 8H, Ar H), 7.75 (d, 8H, Ar H) 2.73 (d, 4H, -CH_2), 1.10 (m, 2H, -CH), 0.26 (d, 12H, -CH_3),^{13}C NMR ($CDCl_3$, 75 MHz) δ (ppm) 191.0 (-CHO) , 150.0, 143.0, 136.0, 135.0, 131.0, 128.0 (Ar–C), 80.0 (-OC), 29 (sec-C), 18 (-CH_3) (Figure 5.1D).

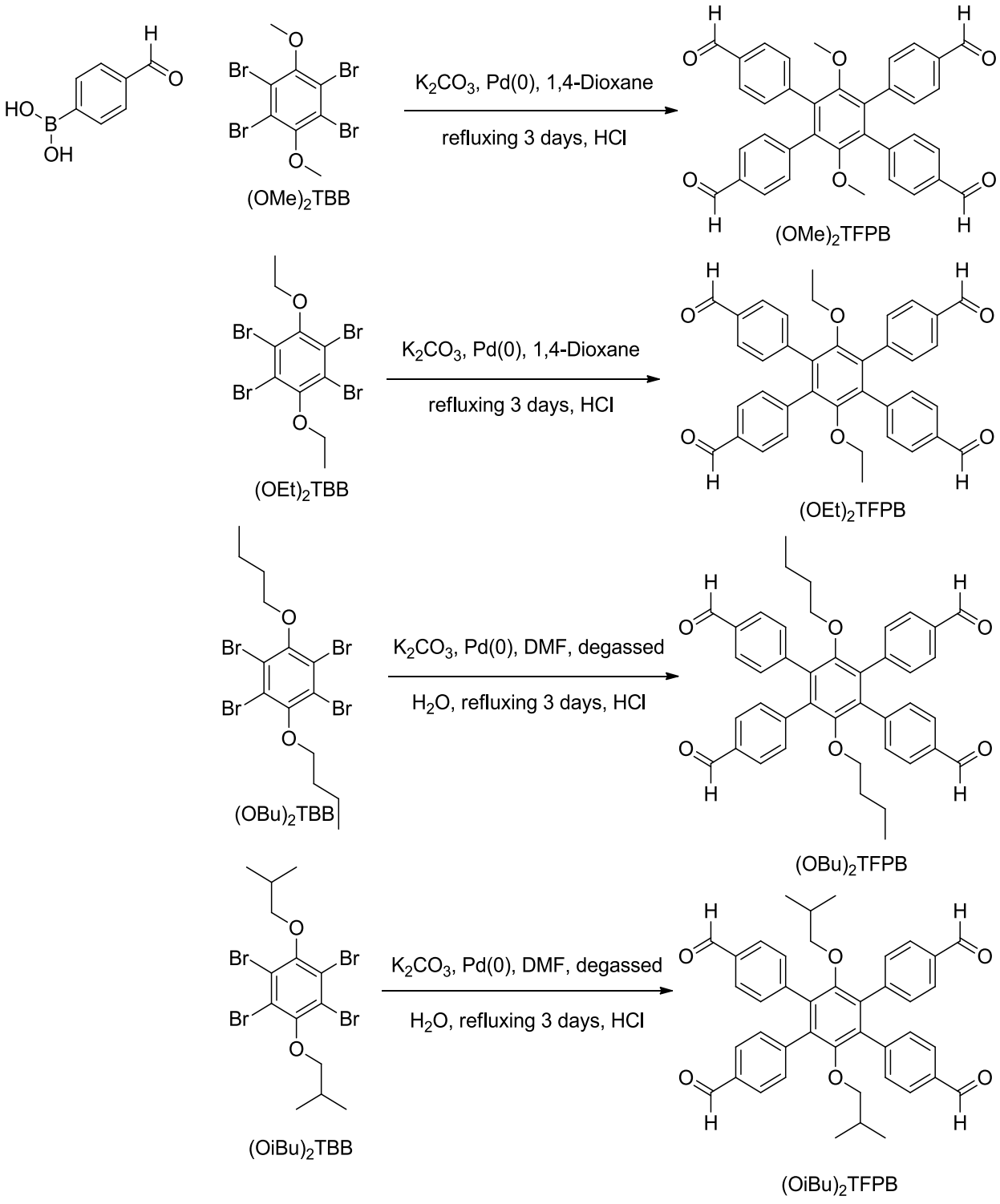

Scheme 5.2: Synthesis of dialkoxy aryl-aldehyde derivatives

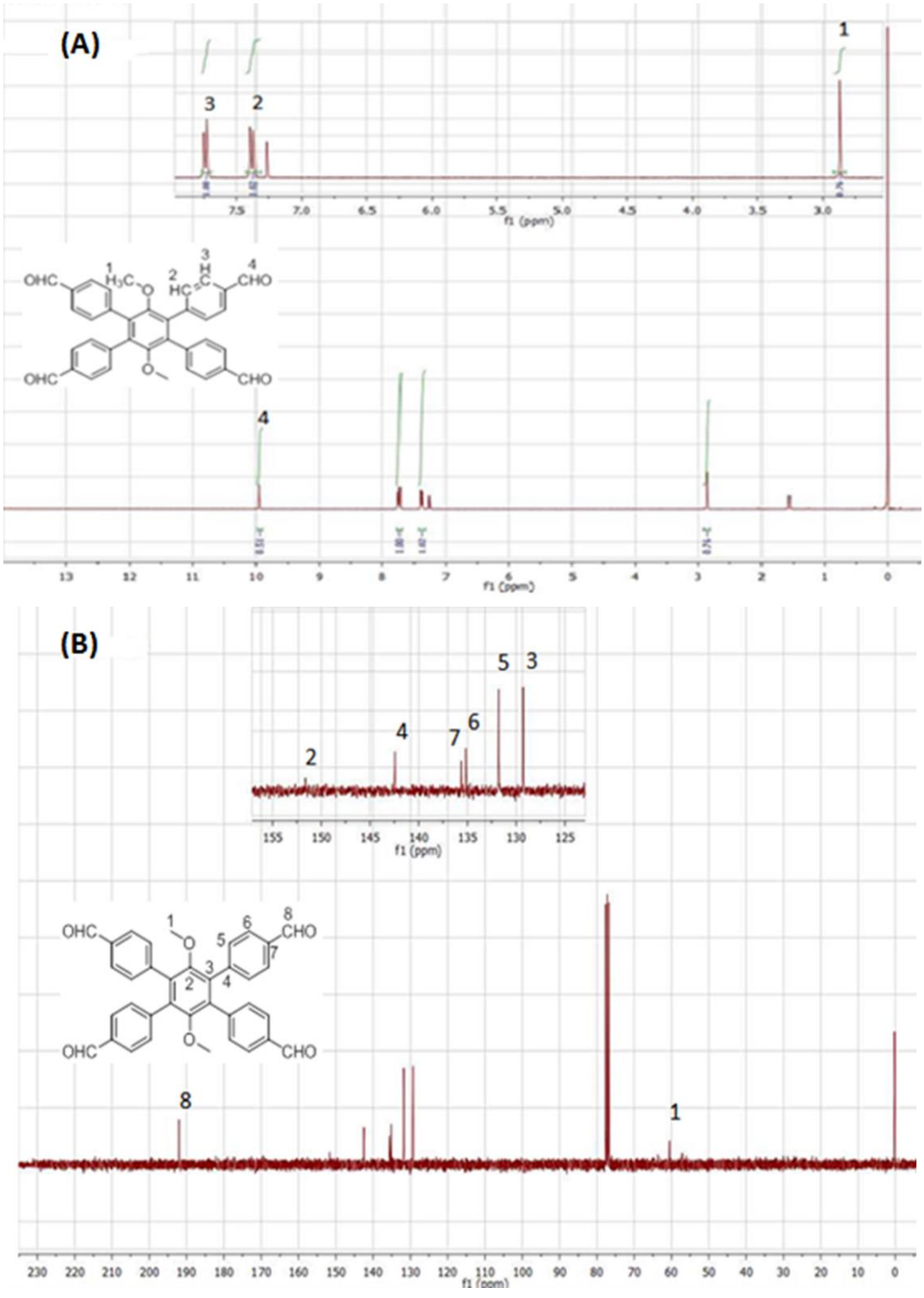

Figure 5.1A: (A) ^{1}H-NMR and (B) ^{13}C-NMR of $(OMe)_2$TFPB

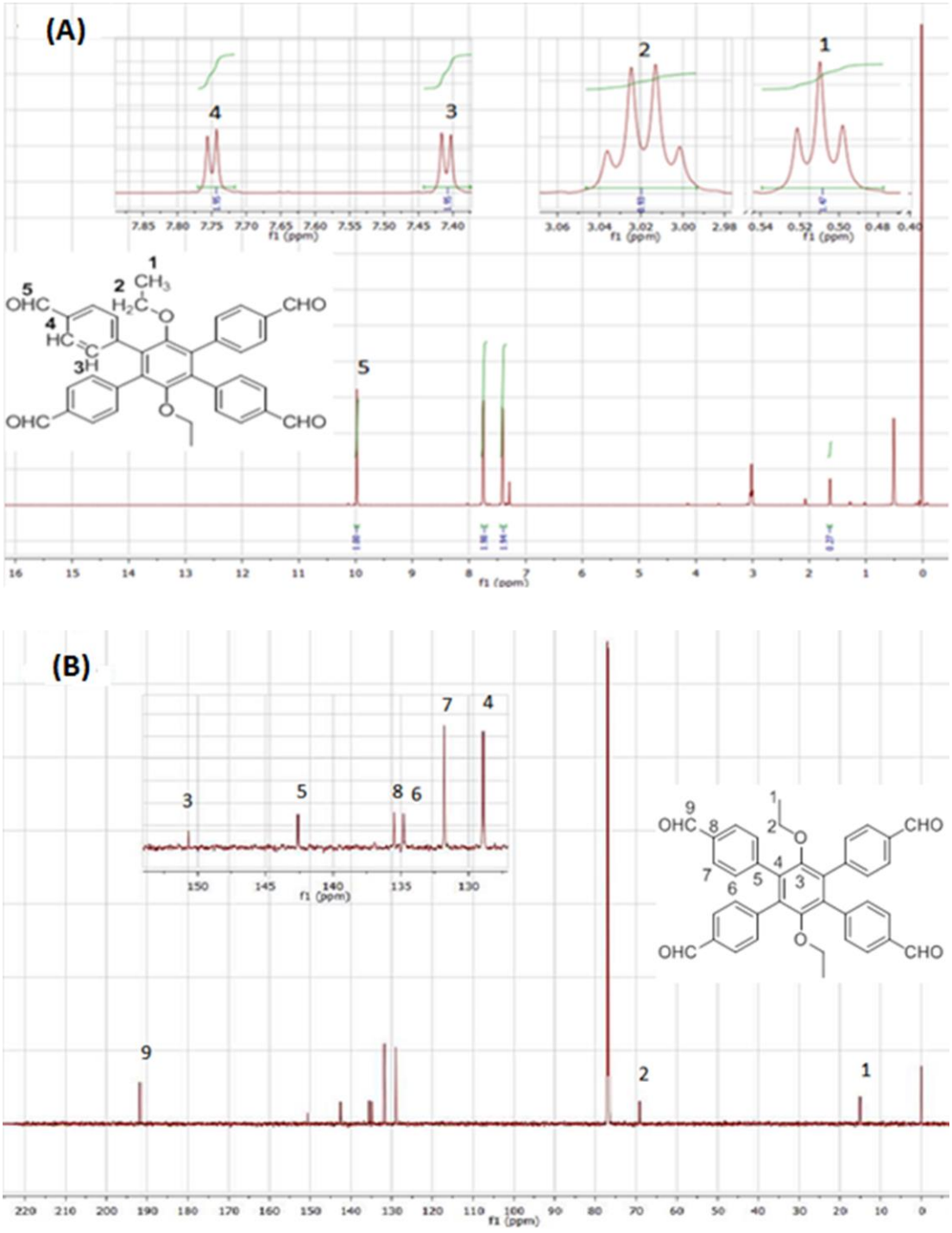

Figure 5.1B: (A) ^{1}H-NMR and (B) ^{13}C-NMR of $(OEt)_2TFPB$

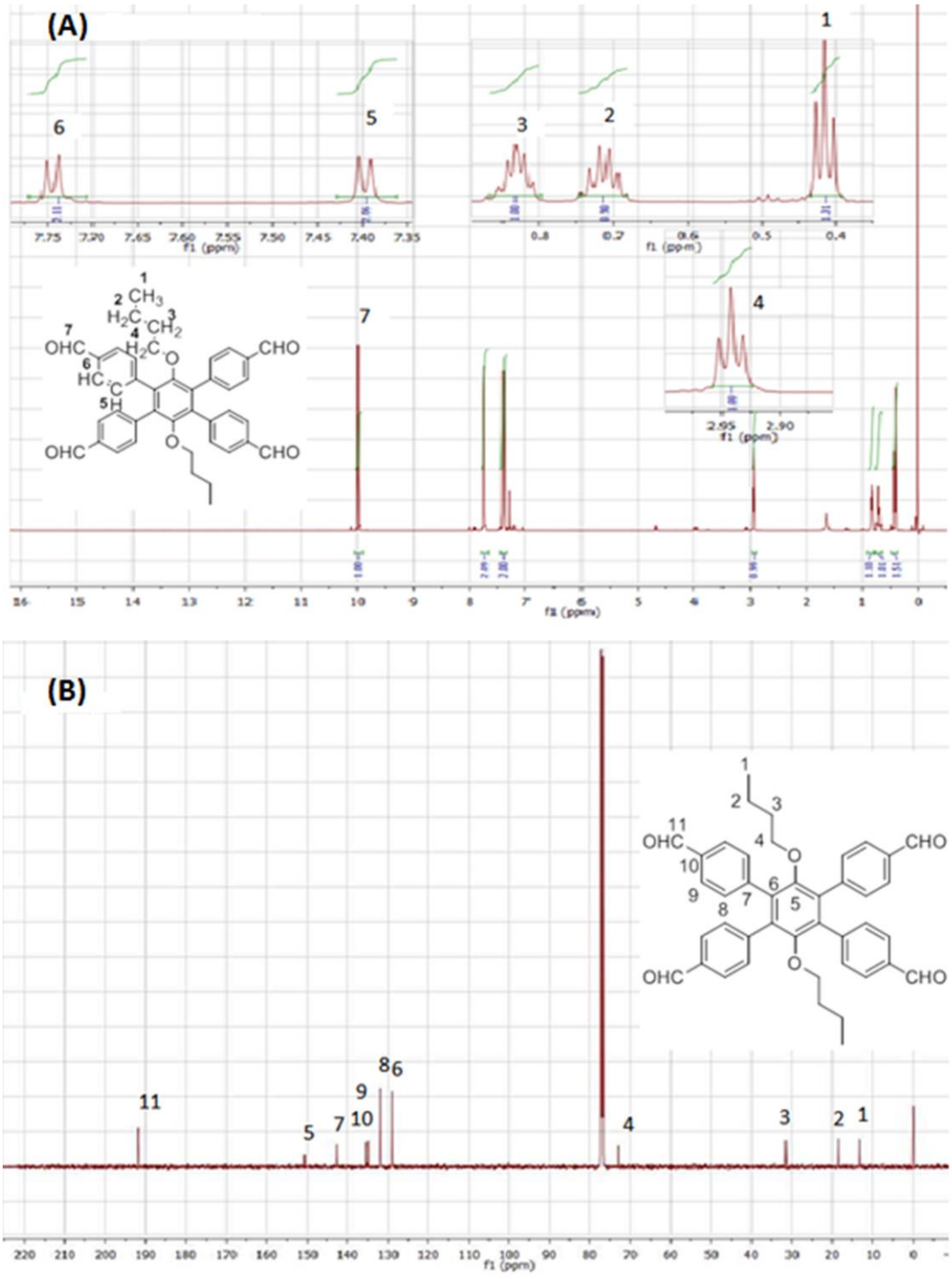

Figure 5.1C: (A) ^{1}H-NMR and (B) ^{13}C-NMR of $(OBu)_2TFPB$

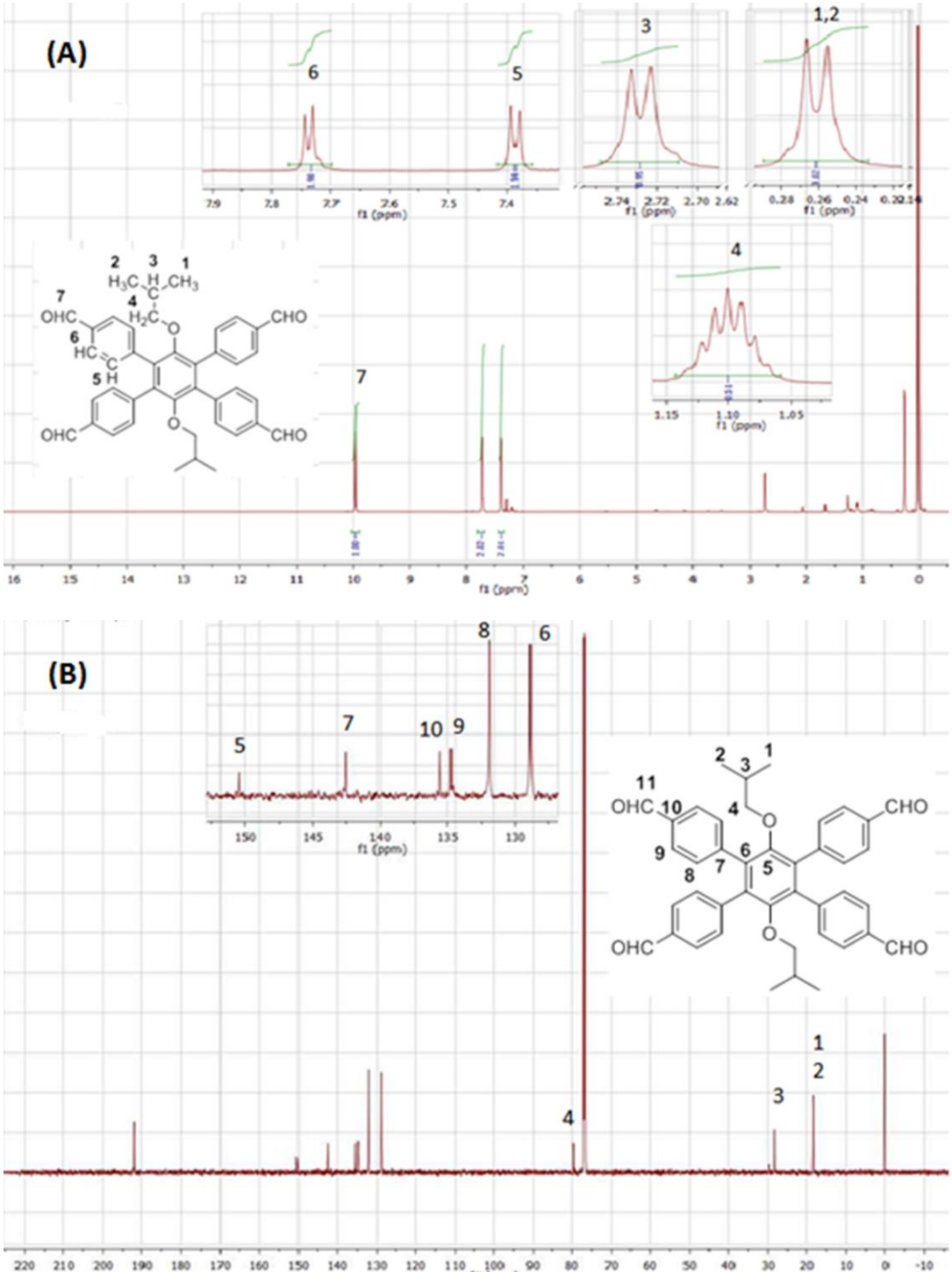

Figure 5.1D: (A)^{1}H-NMR and (B) ^{13}C-NMR of $(OiBu)_2TFPB$

5.3. Synthesis of Alkoxy-Functionalized BILPs

The synthesis of dialkoxy-functionalized BILP-14 and BILP-15 derivatives was accomplished by applying the reported synthetic approach of BILPs.[69] The new BILP-14 and BILP-15 derivatives were prepared by polycondensation reaction between alkoxy-functionalized aryl-aldehydes and aryl-o-diamine building BTA and DABA respectively (Figure 5.2).

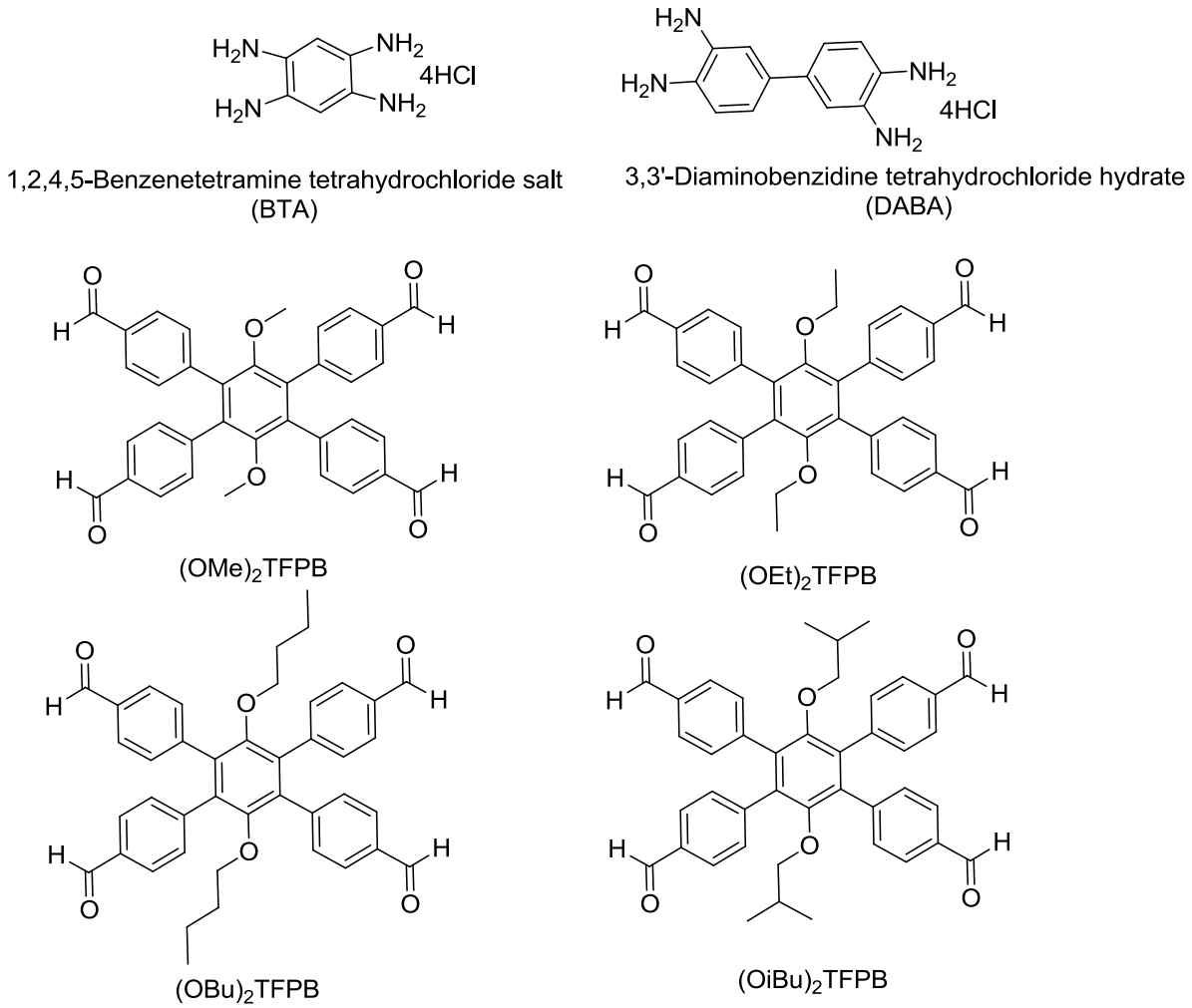

Figure 5.2: Molecular building unit blocks used for the synthesis of alkoxy-functionalized BILPs

The synthetic protocols, spectral and analytical characterizations, and adsorption measurements of alkoxy-functionalized BILP-14 and BILP-15 derivatives are discussed in two separate sections. The first section includes BILP-14-OR derivatives, which are demonstrated as: BILP-14-OMe, BILP-14-OEt, BILP-14-OBu and BILP-14-OiBu, while the second section includes BILP-15-OR derivatives, displayed as: BILP-15-OMe, BILP-15-OEt, BILP-15-OBu and BILP-15iOBu.

5.4 Alkoxy-Functionalized BILP-14-OR Derivatives

Synthesis of Dialkoxy-Functionalized BILP-14-OR Derivatives

Synthesis of BILP-14-OMe

BILP-OMe was synthesized in a fashion similar to the preparation of BILP-14.[69e] A 100 mL Schlenk flask was charged with 1,2,4,5-Benzenetetramine tetrahydrochloride salt (BTA) (52 mg, 0.183 mmol) and 30 mL of anhydrous DMF under a nitrogen atmosphere. The solution was cooled to around -30 °C and a solution of 2,3,5,6-Tetrakis-(4-formylphenyl)-1,4-dimethoxybenzene $(OMe)_2$TFPB) (50 mg, 0.09 mmol) in 25 mL anhydrous DMF was added dropwise to the pervious charged solution over 3 hrs. Temperature was maintained around -30 °C until a yellowish brown solid product formation completed and was then increased to RT and kept overnight. The flask containing the reaction mixture was flashed with air for 15 min and capped. The reaction mixture was then heated in an oven at 130 °C (0.5 °C/min) for 3 days to afford a fluffy brownish polymer, which was isolated by filtration over a glass frit. The resulting product was immersed in DMF (20 mL overnight) and then in acetone (20 mL). The product was filtered and dried under vacuum at 120 °C and 1.0 x 10^{-5} Torr for 20 hrs to give BILP-14-OMe

as a brown fluffy solid (60 mg, 81%). Anal. Calcd for $C_{48}H_{30}N_8O_2.4H_2O$: C, 70.07%; H, 4.62%; N, 13.62%. Found: C, 68.98%; H, 4.05%; N, 12.27%.

Synthesis of BILP-14-OEt

BILP-14-OEt was synthesized in a fashion similar to the preparation of BILP-14 using (BTA) (52 mg, 0.183 mmol) and 2,3,5,6-Tetrakis-(4-formylphenyl)-1,4-diethoxybenzene $(OEt)_2$TFPB) (53 mg, 0.092 mmol) in anhydrous DMF under a nitrogen atmosphere. The resulting product was filtered and dried under vacuum at 120 °C and 1.0 x 10^{-5} Torr for 20 hrs to give BILP-14-OMe as a pale brown fluffy solid (62.0 mg, 80%). Anal. Calcd for $C_{50}H_{34}N_4O_2.4H_2O$: C, 70.52%; H, 4.93%; N, 13.16%. Found: C, 69%; H, 4.72%; N, 12.49%.

Synthesis of BILP-14-OBu

BILP-14-OBu was synthesized in a fashion similar to the preparation of BILP-14 using (BTA) (52 mg, 0.183 mmol) and 2,3,5,6-Tetrakis-(4-formylphenyl)-1,4-dibutoxybenzene $(OBu)_2$TFPB) (58.45 mg, 0.092 mmol) in anhydrous DMF under a nitrogen atmosphere. The resulting product was filtered and dried under vacuum at 120 °C and 1.0 x 10^{-5} Torr for 20 hrs to give BILP-14-OBu as a brown fluffy solid (65 mg, 79%). Anal. Calcd for $C_{54}H_{42}N_8O_2.4H_2O$: C, 71.44%; H, 5.51%; N, 12.35%. Found: C, 69.74%; H, 4.72%; N, 10.50%.

Synthesis of BILP-14-OiBu

BILP-14-OiBu was synthesized in a fashion similar to the preparation of BILP-14 using (BTA) (52 mg, 0.183 mmol) and 2,3,5,6-Tetrakis-(4-formylphenyl)-1,4-diibutoxybenzene $(OiBu)_2$TFPB) (58.45 mg, 0.092 mmol) in anhydrous DMF under a nitrogen atmosphere. The resulting product was filtered and dried under vacuum at 120 °C and 1.0 x 10^{-5} Torr for 20 hrs to

give BILP-14-OiBu as a brown fluffy solid (60 mg, 72%). Anal. Calcd for $C_{54}H_{42}N_8O_2.4H_2O$: C, 71.44%; H, 5.51%; N, 12.35%. Found: C, 72.14%; H, 5.18%; N, 12.07%.

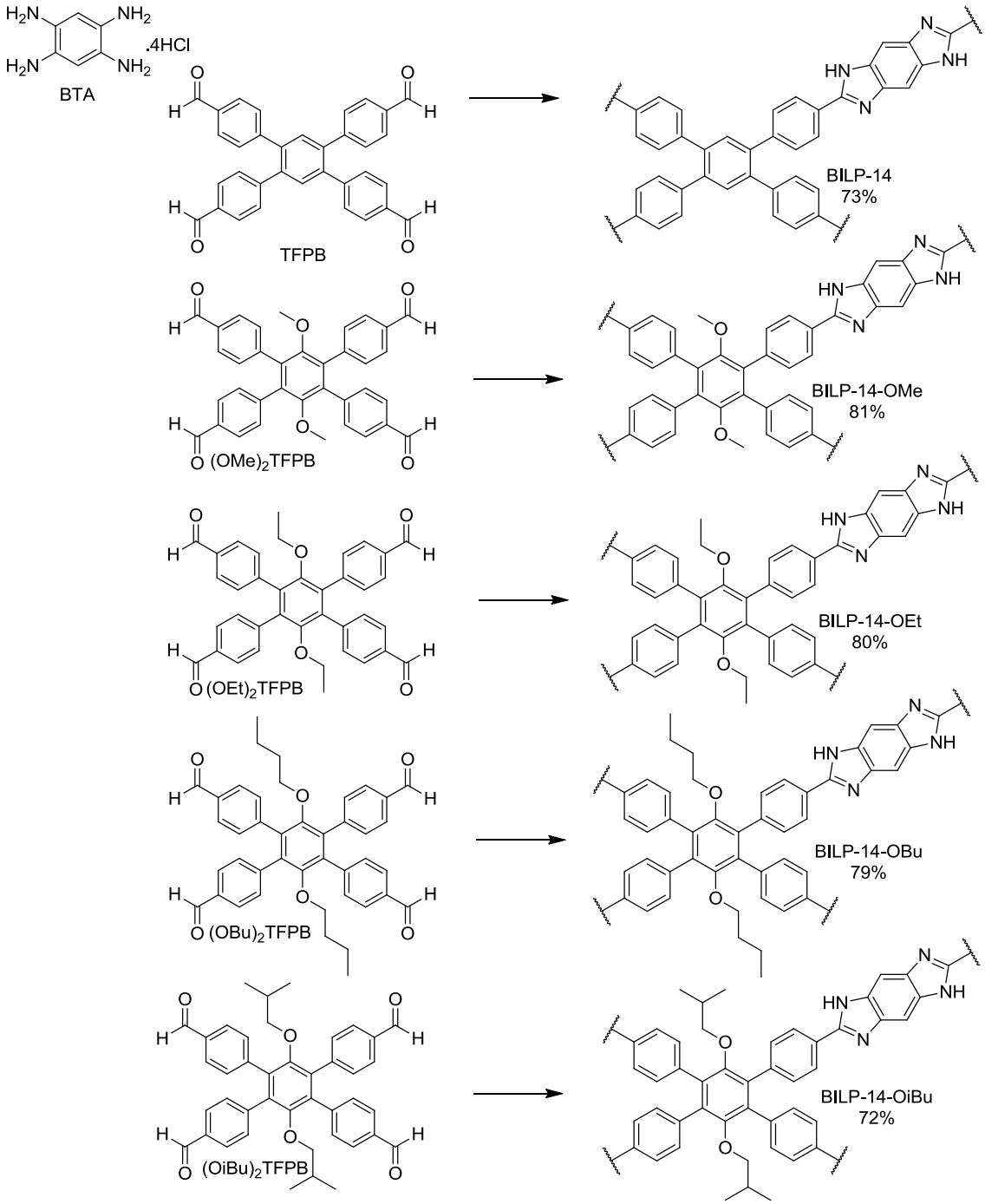

Scheme 5.3: Synthesis of BILP-14 and BILP-14-OR derivatives

5.4.1 Results and Discussions

In this Chapter the synthesis of new alkoxy-functionalized BILP-14-OR derivatives and their spectral and analytical characterizations, and gas adsorption properties were studied. The new polymers were synthesized by polycondensation reaction between alkoxy aryl-aldehydes (-OMe, -OEt, -OBu and -OiBu) and aryl-o-diamines (BTA) (Figure.5.2). Alkoxy aryl-aldehydes were accomplished by incorporation of alkyl groups to tetrabromhydroquinone (TBHQ), followed by Suzuki-coupling reaction between alkoxy-substituent of (TBHQ) and boronic acid aldehyde. The synthesis of BILP-14-OR derivatives, and their corresponding alkoxy aryl-aldehydes, is described above.

The experimental protocol of the synthesis of BILP-14-OR derivatives was demonstrated following a similar fashion to the synthesis of all BILPs. The isolation, and successive washing of the polymers by aqueous, acidic, and basic solutions, has resulted in a new series of BILP-14-OR including: BILP-14-OMe, BILP-14-OEt, BILP-14-OBu, and BILP-14-OiBu. The new polymers were activated at 120 °C and 1.0 x 10^{-5} Torr for 20 hrs before characterization.

The successful incorporation of alkoxy-groups into the polymers was confirmed by spectral and analytical techniques, and compared to the parent materials. The impact of the new functionality on the porosity and gas adsorption properties was investigated and compared to BILP-14.

BILP-14-OR polymers have shown good agreement with all BILPs regarding their physiochemical stability upon exposure to low acid or base concentrations (~0.5M). However, at higher acid concentrations (> 2 M), a notable permanent change was observed in the color of the polymers compared to BILP-14. This observation can be attributed to the cleavage of the alkoxy groups, which was assisted by high HCl concentration.[117] The resulting product was tested by

FT-IR, TGA, and ^{13}C-NMR after soaking in (2 M) acid and confirmed the formation of a hydroxyl-functionalized polymer. Further studies and characterizations of hydroxyl-derivatives of BILP-14 polymers (BILP-14OH) are beyond the scope of this research.

The thermal stability of BILP-14-OR was supported by thermogravimetric analysis (TGA) (Figure 5.3), which showed initial weight losses around 100 ºC, followed by sharp decomposition around 300 ºC. This decrease in the stability was expected to occur due to the presence of flexible linkers (-OEt, -OBu, and -OiBu), which allow more disruptive movement in the polymers' structure and allow decomposition to begin at an earlier stage when compared to BILP-14. Also, this behavior was observed in a recent study of alkoxy-functionalized MOFs, which showed that the incorporation of pendant hydrophobic groups played a significant role in tuning the materials stability.[118] In this study, a series of copper-dialkoxy substituted MOFs were synthesized, by incorporation of pendant alkoxy groups (e.g. -OMe, -OEt, -O^{n}Pr (propyl), and -O^{n}Hex (hexyl), and the impact of these groups on moisture and thermal stability of the materials was investigated. Thermal stability was studied by TGA, while the moisture stability was measured by PXRD.

PXRD has shown that the -OMe functionalized MOF is the least stable polymer, when compared to the other groups, while the -O^{n}Hex functionalized MOF is the most stable framework of them all. This observation was confirmed by adding drops of water to the powder samples; the drops of water were absorbed by -OEt and -O^{n}Pr, while no interaction or change in the shape of the water droplets occurred in the case of the -O^{n}Hex substituted MOF. Interestingly, the thermal stability trend of MOFs is consistent with the stability of BILP-14-OR derivatives. This result confirmed that the early decomposition around 300 ºC is due to the presence of alkoxy groups.

The introduction of extended hydrophobic alkoxy-chains (e.g. -O^{n}Hex) was believed to play a significant role in increasing the moisture stability of MOF materials by increasing the hydrophobicity, while at the same time decreasing the thermal stability and assisting with the framework collapse.[118] On the other hand, the incorporation of alkylated groups, (-Me, -Et and –^{n}Pr) groups to generate a series of alkylated-COFs, has shown that the alkyl groups did not alter the thermal stability of the parent COF, which suggests that these alkyl groups are not thermally cleaved prior to network decomposition.[119] All BILP-14-OR derivatives are amorphous as illustrated from powder X-ray diffraction studies. Scanning electron microscopy (SEM) images of BILP-14-OR derivatives were used to establish the phase purity of the polymers. They have revealed different morphologies and variable particle size for BILP-14 and BILP-14-OR derivatives. For example, BILP-14 has formed agglomerated particles *ca*. 0.5-0.3 μm, while BILP-14-OR derivatives have aggregated spherical particles *ca*. 0.3-0.1μm (Figure 5.4).

The chemical composition of the BILP-14-OR derivatives was determined by microelemental analysis, which showed the successful incorporation of alkoxy functional groups to aryl-aldehydes and the polymers' networks. Moreover, it showed that nitrogen atoms of the imidazole ring are involved in hydrogen bonding with water molecules, which is consistent with other BILPs and TGA results.

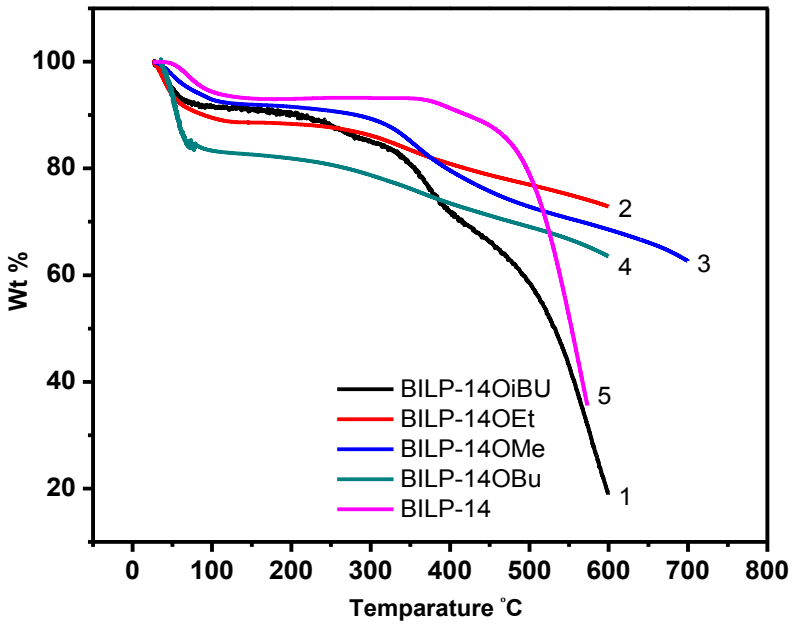

Figure 5.3: Thermal gravimetric profiles of BILP-14 and BILP-14-OR derivatives measured under N_2.

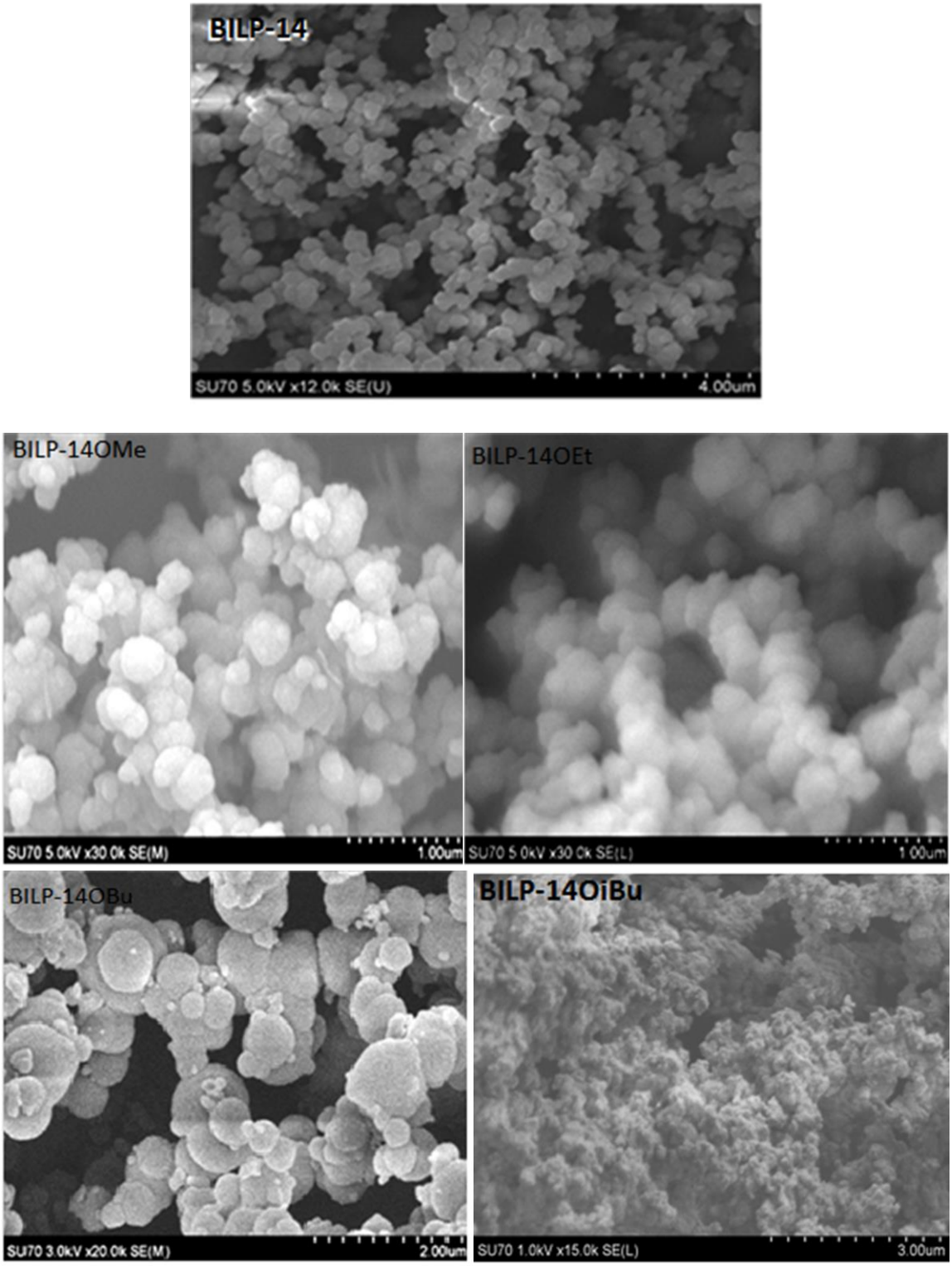

Figure 5.4: SEM images of BILP-14 and BILP-14-OR derivatives.

The chemical connectivity of the BILP-14-OR derivatives was verified using FT-IR and ^{13}C NMR. FT-IR spectra, for alkoxy aryl-aldehyde starting materials and the corresponding BILP-14-OR derivatives, confirmed the successful incorporation of alkoxy groups and the formation of BILP-14-OR derivatives through polycondensation reaction between alkoxy aryl-aldehydes and BTA. The appearance of new significant vibration bands, of the imidazole ring skeleton and the consummation of the vibration band corresponding to aldehyde-carbon, confirmed the polymer formation. The vibrations at 1620, 1480, 1435, 1370, and 1275 cm^{-1} confirmed imidazole ring formation, while the substantial attenuated peak at 1700 cm^{-1} suggested the full consummation of aryl-aldehydes in the polymerization. The other stretching vibrations around 3425 cm^{-1} and 3220 cm^{-1} are assigned to free N-H, while the bands in the range 2750-3030 cm^{-1} belong to C-H aromatic carbons. The new vibrations at 1450, 1378, 1246, 1205, 1030, and 943 cm^{-1} belong to the new incorporated alkoxy groups. The strong band intensity in the range 2880-2970 cm^{-1} corresponds to C-H bond of the alkyl substituent (Figure 5.5).[119-120] The expanded region from 2000-500 cm^{-1} shows clearly the characteristic vibrations of BILP-14-OR derivatives (Figure.5.5).

The ^{13}C CP-MAS NMR spectra showed the successful formation of the new BILPs and the incorporation of the dialkoxy functional groups. The peaks belonging to the alkoxy carbon (C-O) of (-OMe, -OEt,-OBu and -OiBu) appear around 80, 72, 69 and 61 ppm respectively.[121] The aliphatic secondary carbons in -OBu and -OiBu appear around 31, 29 and 18 ppm. The terminal -CH_3 group appears around 15 ppm. The aromatic C-O carbon appears around 148 ppm, while the resonance peaks around 100, 127, 130 and 133 ppm belong to the aromatic C-H bonds. The peak around 150 ppm corresponds to carbon of the imidazole ring. ^{13}C-NMR results, for the solid state BILP-14-OR derivatives and aryl aldehydes, are consistent and appeared in similar ranges. The

only difference noticed was for the carbonyl aldehyde, which down shifted from 200 to 151 ppm due to the imidazole ring formation. The peaks below100 and above 175 ppm are spinning side, while the resonance of alkoxy groups overlaps with the region below 100 ppm.

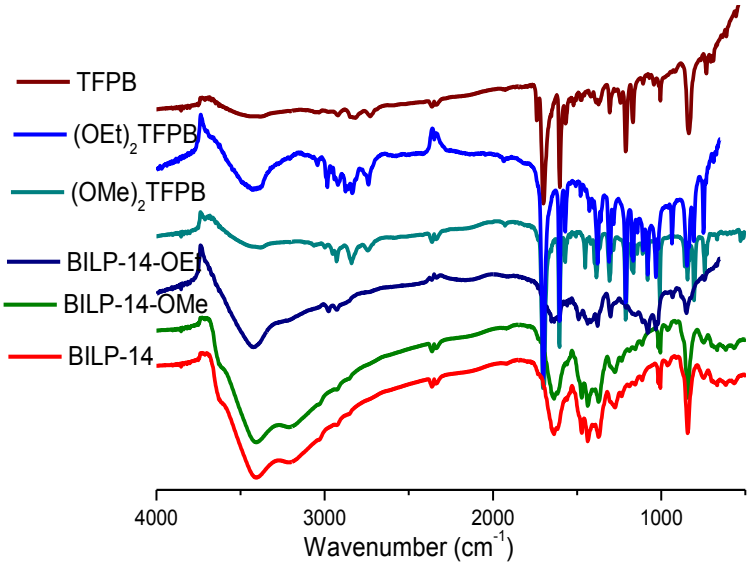

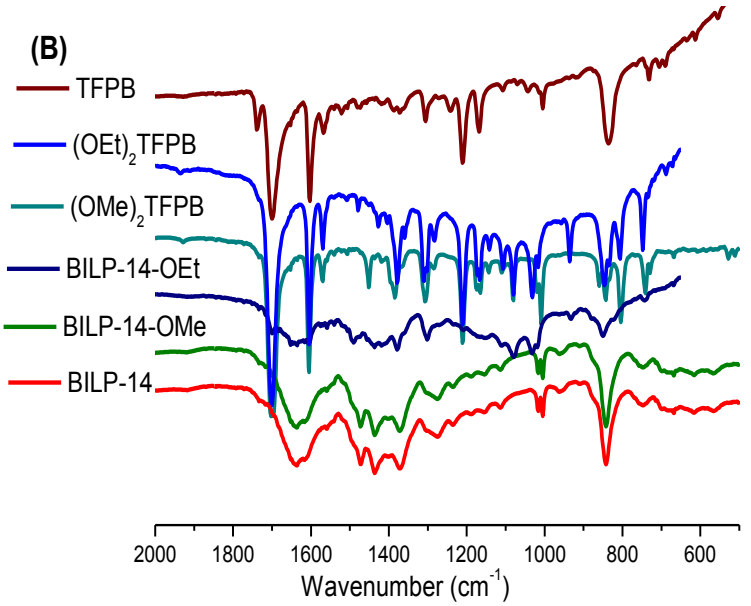

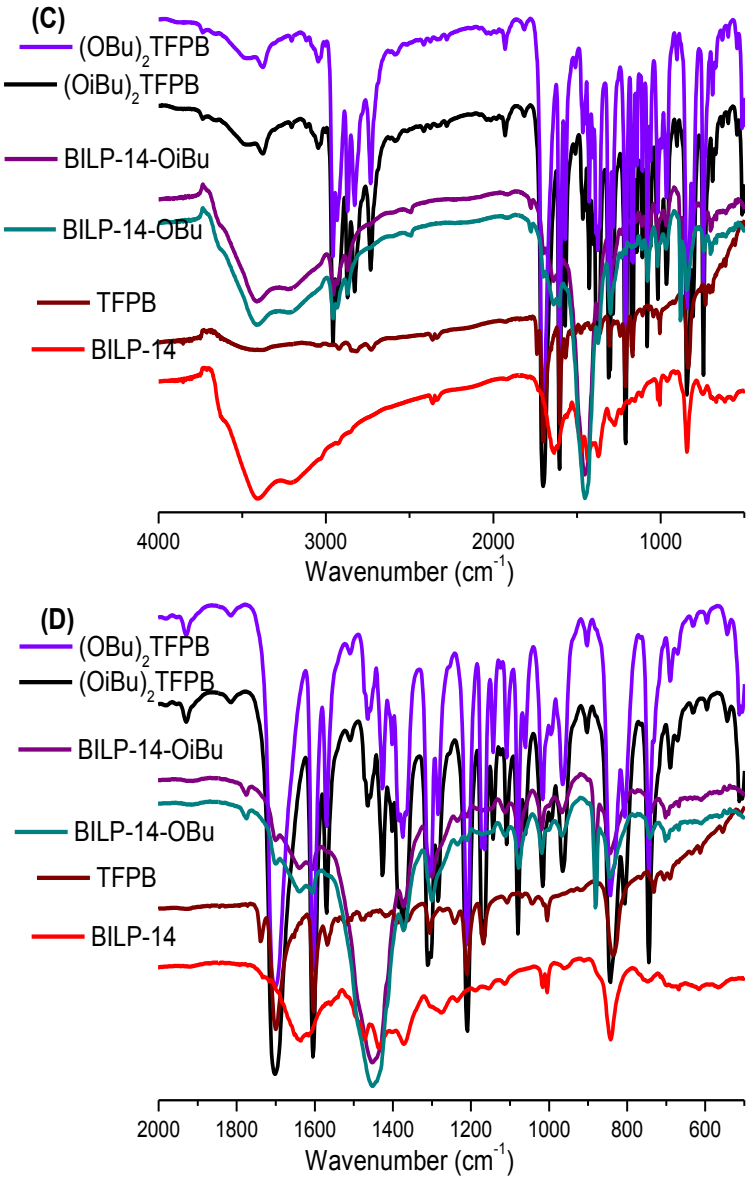

Figure 5.5: FT-IR spectra of BILP-14 and BILP-14-OR derivatives and their aryl-aldehydes starting building units in the ranges (A, C) 4000-500 and (B, D) 2000-500 cm^{-1}.

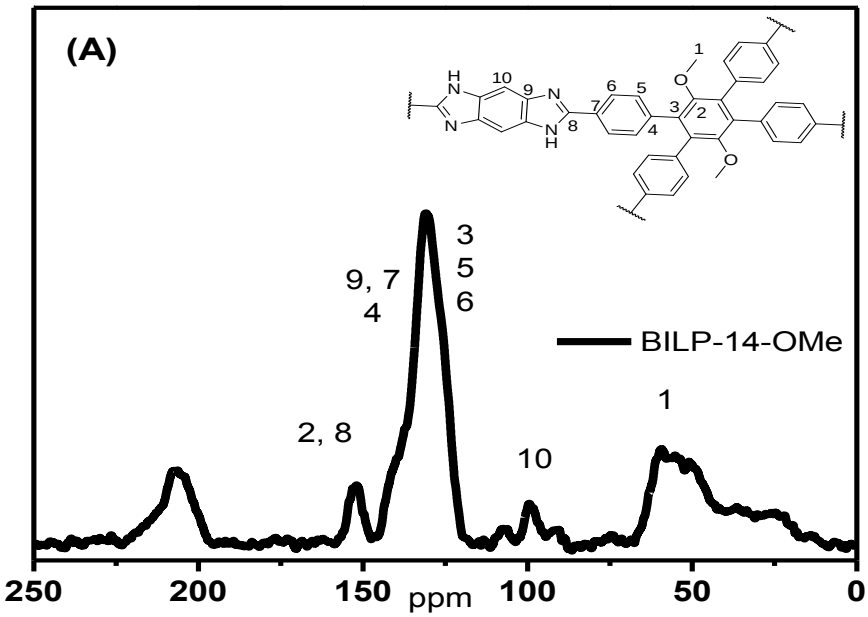
(A)
BILP-14-OMe
9, 7
4
3
5
6
2, 8
10
1
250
200
150
ppm
100
50
0

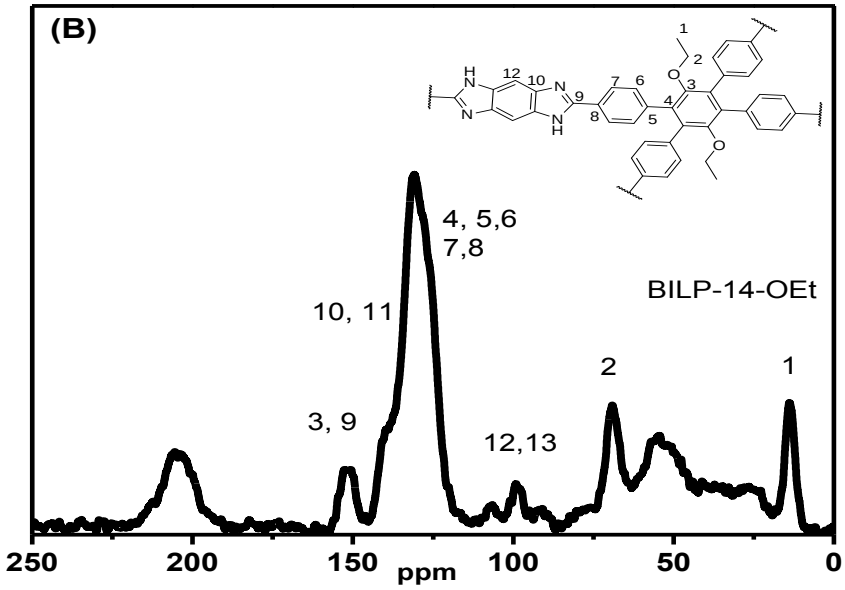
(B)
BILP-14-OEt
4, 5,6
7,8
10, 11
3, 9
12,13
2
1
250
200
150
ppm
100
50
0

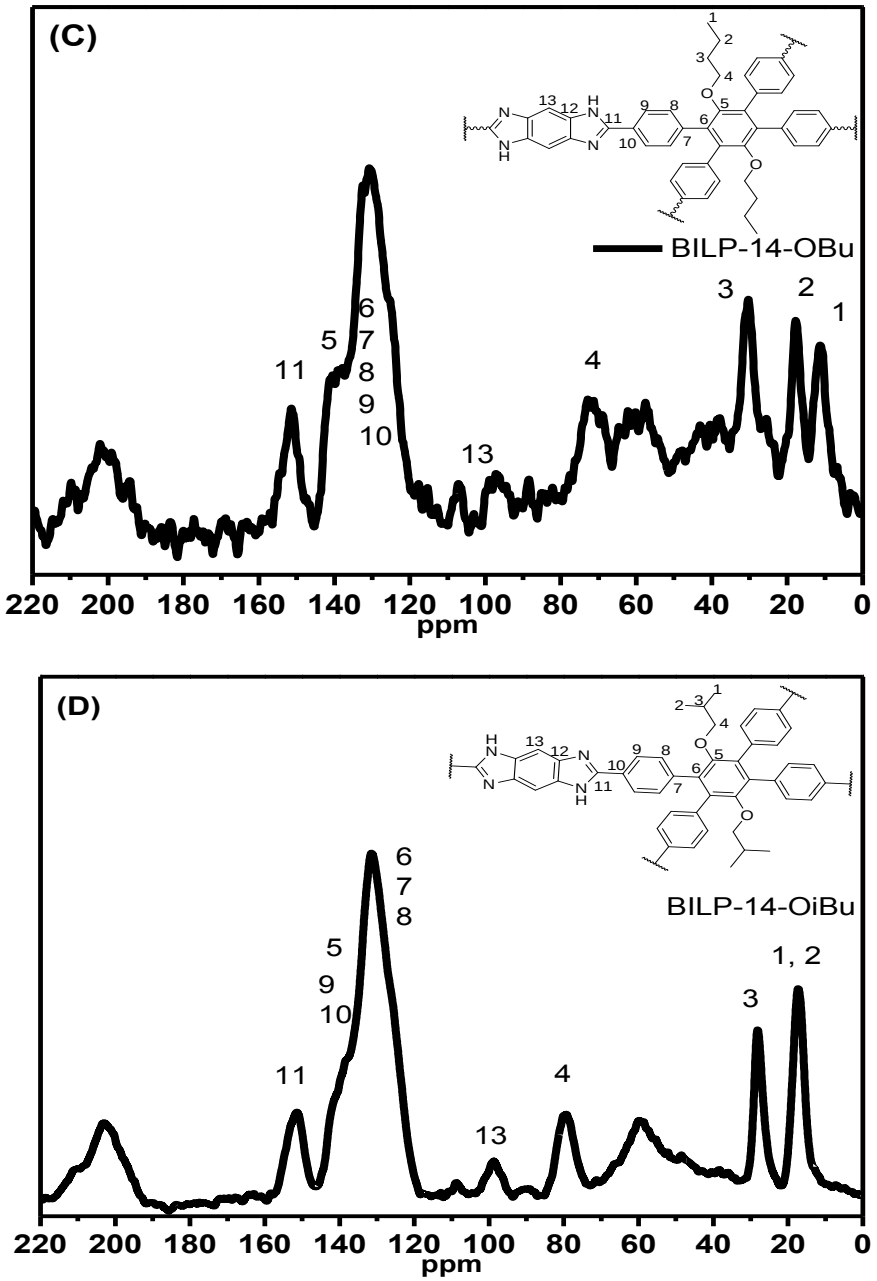

Figure 5.6: (A-D) Solid state ^{13}C CP-MAS NMR spectra of BILP-14-OR derivatives.

5.4.2 Porosity and Low Pressure Gas Uptake Measurements

The porosity of BILP-14-OR derivatives was investigated by argon sorption-desorption measurements. Prior to sorption measurements, the polymers were activated at 120 °C and 1.0 x 10^{-5} Torr for 20 hrs. The isotherms were collected at 87 K, which resulted in fully reversible behavior and indicated microporosity (Type-I-Type II) from the rapid Ar uptake at low pressure (0-0.1 bar) as illustrated in Figure 5.7. The minor hysteresis observed for all materials is consistent with the powdery and flexible nature of BILPs. Applying the BET model to the sorption branch within the pressure range of P/P_o= 0.05-0.15 resulted in moderate surface areas of 685, 1163, 1108, and 921 $m^2 g^{-1}$ for BILP-14-OMe, BILP-14-OEt, BILP-14-OBu and BILP-14-OiBu, respectively (Figure 5.8). This trend was somewhat unpredicted when compared to (1005 $m^2 g^{-1}$) for BILP-14 due to the fact that the incorporation of longer alkoxy chains on the monomer should occupy the free void space in the pores and consequently, decrease the argon uptake and the apparent surface area of the polymers.[118-119]

This hypothesis has a good agreement with the trend, which was observed between BILP-14 and BILP-14-OMe and BILP-14-OiBu, but not BILP-14-OEt and BILP-14-OBu. The unexpected higher porosity with the longer linkers (-OEt and -OBu), is suggested to arise from the presence of pendent alkoxy groups, which effectively reduce the pore size to be close to the kinetic diameter of argon and enhance the interaction between the host network and guest argon molecules. Interestingly, this trend of porosity is consistent with what has been observed in the porosity changes for copper-dialkoxy substituted MOFs, which was discussed above.[118] The higher surface area for BILP-14-OEt and BILP-14Bu compared to BILP-14-OMe is due to flexible rotation of the –OEt and -OBu groups. This rotation can provide a larger surface area for argon to adsorb onto, whereas -OMe group cannot facilitate this larger surface area. This

behavior was observed with the alkyl-functionalized COFs (e.g. methyl-COF-16 Å (753 m^2 g^{-1}) and ethyl-COF-14 Å(805 m^2 g^{-1}).[119] The notable decrease in the surface area for BILP-14-OiBu can be attributed to the presence of the branched bulky isobutoxy group, which would fill the pore, reducing the pore size and the overall surface area. Thus, the introduction of branched substituents has a small influence on the porosity of BILP-14 and this result has been observed in isopropoxy pillared-Layered MOF when compared to linear alkoxy-substituted MOF.[120a] The improved porosity of BILP-14-OEt compared to BILP-14, is due to the incorporation of the -OEt group, which is believed to introduce a little control over the network interpenetration, suppress the impact of favorable π-π stacking, and increase the surface area.

Pore size distribution (PSD) curves were estimated from the argon isotherms by nonlocal density functional theory (NLDFT) on the adsorption branch with a cylindrical/sphere pore model. PSD was found to be centered at 7.0 Å for BILP-14, while it is around 8.5 Å, 6.8Å, 8.5 Å, and 6.8 Å for BILP-14-OMe, BILP-14-OEt, BILP-14-OBu, and BILP-14-OiBu, respectively (Figure 5.9). BILP-14-OiBu also contains certain pores with a relatively small distribution between 11 to 15 Å. The pore volume was calculated from single point measurements (P/P_o= 0.95) and found to be 0.55, 0.39, 0.66, 0.56, and 0.51 cc g^{-1} for BILP-14, BILP-14-OMe, BILP-14-OEt, BILP-14-OBu and BILP-14-OiBu, respectively.

In general, pore volumes of the polymers slightly increase with the bulkiness of the substituents. For example, the highest surface area BILP-14-OEt has the largest specific pore volume (0.66 cc g^{-1}) among all BILP-14-OR derivatives. This can be attributed to the presence of the flexible ethoxy substituent, which introduces more pore space and suppresses the network contraction. It has been documented that the presence of the flexible groups prevents the packing of the substituents inside the pores, while the branched groups assist network packing and lower the

pore volume.[120a] For example, the pore volume of BILP-14-OiBu is slightly lower than BILP-14-OBu, which believed to be due to the branched isobutoxy group. The smallest pore volume is observed for BILP-14-OMe, which also has the lowest surface area.

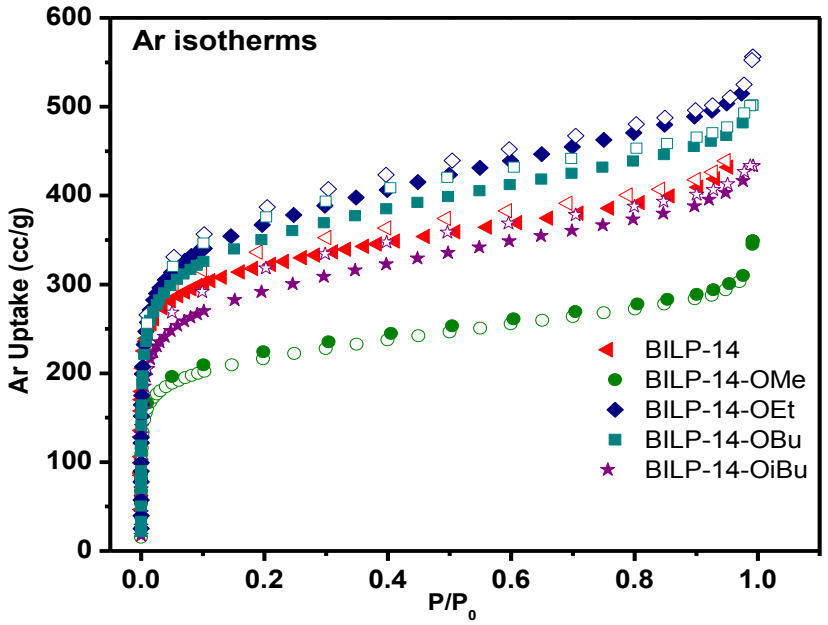

Figure 5.7: Ar adsorption isotherms for BILP-14 and BILP-14-OR derivatives measured at 87 K. The filled symbols are adsorption points and the empty symbols are desorption points.

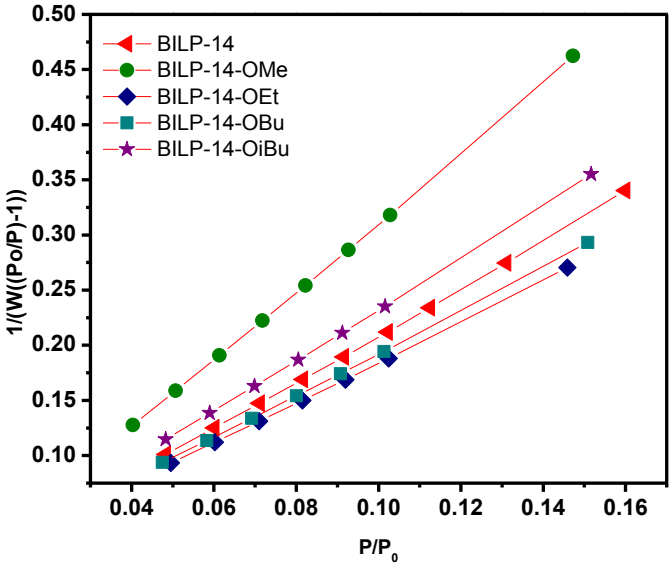

Figure 5.8: BET surface area plots for BILP-14 and BILP-14-OR derivatives calculated from the Ar adsorption isotherm at 87 K. The model was applied from P/Po = 0.05-0.16. (W = Weight of gas absorbed at a relative pressure P/Po).

Table 5.1: BET values for BILP-14 and BILP-14-OR derivatives calculated from Ar adsorption isotherms at 87 K.

BILP	**Surface area (BET)** $m^2 g^{-1}$	**Langmuir Surface area** $m^2 g^{-1}$
BILP-14	1105	1212
BILP-14-OMe	685	842
BILP-14-OEt	1164	1450
BILP-14-OBu	1108	1388
BILP-14-OiBu	921	1155

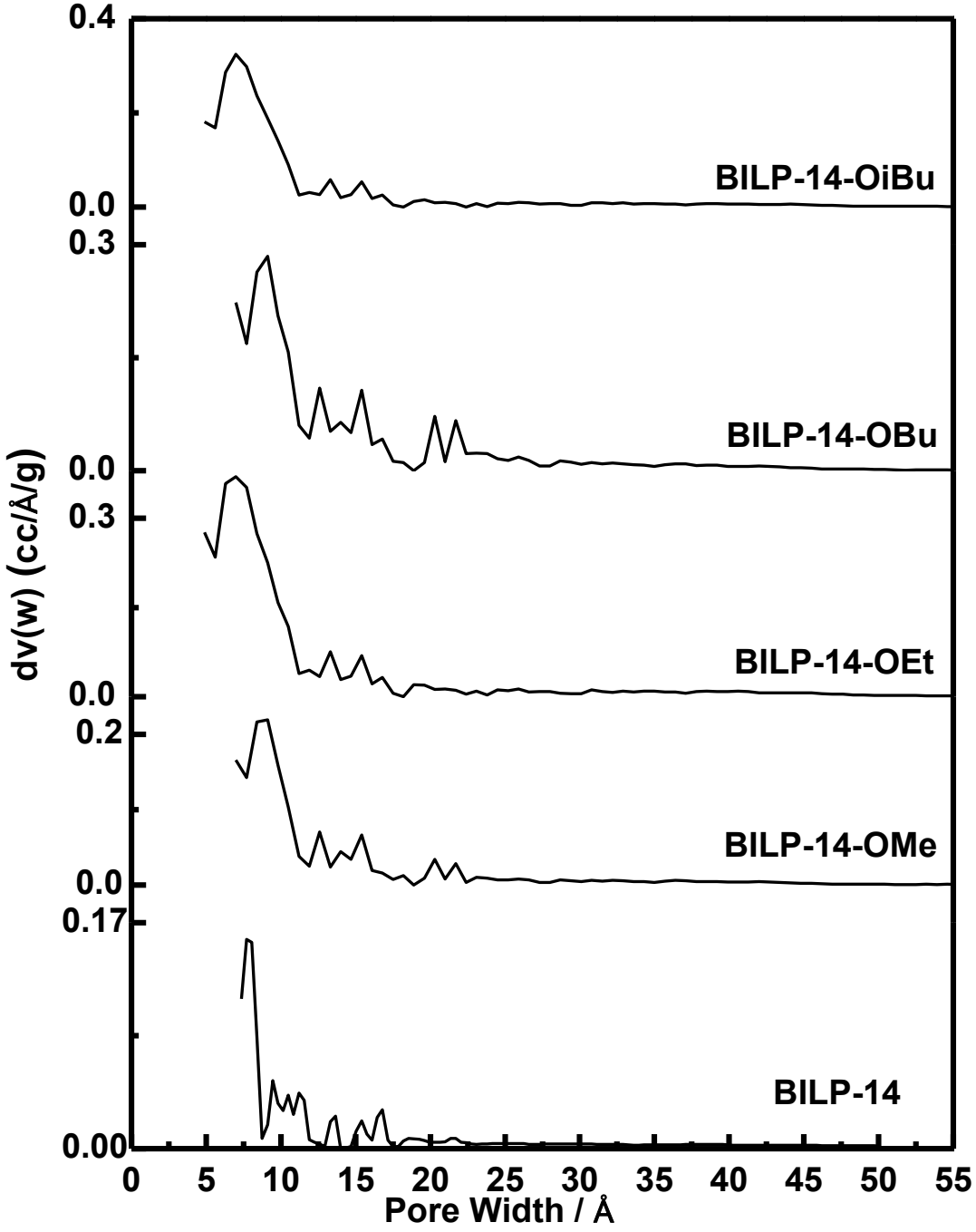

Figure 5.9: Pore Size Distribution of BILP-14 and BILP-14-OR derivatives were calculated from the Ar adsorption isotherms.

In addition to the heterogeneity and subnanometer porosity of BILP-14-OR derivatives, tailoring the microporosity and altering the pore dimensions and environment are believed to significantly impact the selective gas uptake and enhance binding affinities. Accordingly, the impact of the imidazole moiety and the chemical nature of the new incorporated alkoxy groups on the uptake of small gas molecules CO_2 and H_2, and the preferential binding of CO_2 over N_2 and CH_4, was investigated. CO_2, H_2 and CH_4 gas isotherms were collected and their respective isosteric heats of adsorption (Q_{st}) calculated and summarized in Table 5.1.

The CO_2 isotherms of BILP-14-OR derivatives are fully reversible with very minor hysteresis and exhibit a steep rise at low pressure. It is worth mentioning that BILP-14-OEt has the highest CO_2 uptake among the polymers, 203 mg g^{-1} at (273 K / 1 bar). The uptakes for BILP-14-OMe, BILP-14-OBu and BILP-14-OiBu are 142, 177, and 158 mg g^{-1}, respectively (Figure 5.10A). The CO_2 uptake values are within the uptake ranges of other BILPs, especially those which were constructed from 2D building units. The high CO_2 uptakes are expected to arise from strong interactions of the polarizable CO_2 molecules through dipole-quadrupole interactions that utilize the imine-nitrogen sites of imidazole rings. More recently, we have shown from DFT calculations that the non-functionalized backbone (e.g. aryl C-H bonds) of BILPs also provides interaction sites for CO_2.

Thus, the higher surface area polymers exhibit a higher number of these interaction sites and higher CO_2 uptake. The incorporation of alkoxy pendant groups (e.g. -OEt, and -OBu) has resulted in higher surface area BILP-14-OR derivatives and hence, introduced more CO_2 interaction sites. However, there is no notable direct impact of the chemical nature of these groups on the behavior of CO_2 isotherms and the overall uptake. We suggest that DFT calculations would be useful for investigating the possible role of the pendant groups in

enhancing CO_2 uptake. Other alkoxy groups; -OMe and -OiBu have lowered the porosity of BILPs and hence the CO_2 uptake.

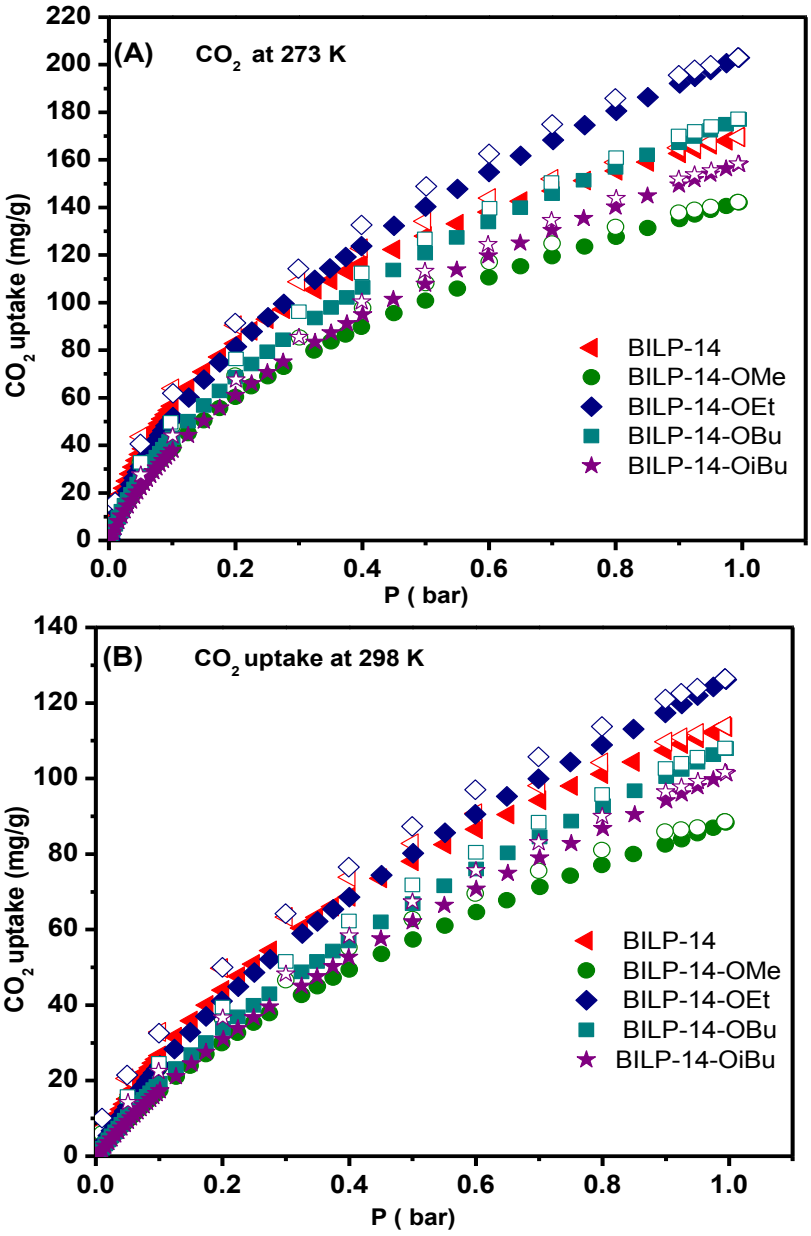

Figure 5.10A: CO_2 uptake isotherms of uptake isotherms of BILP-14 and BILP-14-OR derivatives at 273 K (A) and 298 K (B).

The binding affinity for CO_2 was determined by calculating the isosteric heats of adsorption Q_{st} using the adsorption data, which was collected at 273 K and 298 K for BILP-14-OR and compared to the Q_{st} of BILP-14. Heats of adsorption were calculated using the virial method, which revealed that the Q_{st} values at zero coverage fall relatively in a range of (29-32.9 kJ mol^{-1}) for BILP-14-OR derivatives (Figure 5.11A) and 33.5 kJ mol^{-1} for BILP-14. These values are within the range of Q_{st} values for other BILPs and indicate that CO_2 interactions after the incorporation of alkoxy groups are still weak enough to allow for materials regeneration without applying heat. BILP-14-OMe and BILP-14-OBu have the highest Q_{st} value among all BILP-14-OR derivatives due to the possible formation of multiple interaction sites between CO_2 and the pore walls, especially at low pressure, which can be related to the larger pore size and small pore volume of the polymers. This result has been supported by the recent report of MIL-47(V^{III}), which has shown that the decrease in effective pore size due to the attached -OMe group might result in stronger CO_2 adsorption.[122] In contrast, the lower Q_{st} values for BILP-14-OEt and BILP-14OiBu, are due to their larger pore volume and higher surface area, which requires higher pressure settings to force multiple interaction sites for CO_2 compared to other BILP-14-OR derivatives. [59a, 64, 111]

We also considered BILP-14-OR polymers for hydrogen and methane storage studies because both gases are highly attractive candidates for use in automotive applications as a result of their abundance and clean nature. Moreover, CO_2 removal from flue gas or methane-rich gases (natural gas and landfill gas) is needed to mitigate climate change and enhance the quality, and energy density of methane-rich fuels.[3, 7] Accordingly, methane and hydrogen pure gas isotherms were collected at low pressure conditions, and their heats of adsorption were calculated. Methane isotherms are completely reversible and exhibit a maximum uptake of 20.4 mg g^{-1} at 273 K for

BILP-14-OEt, and the uptake range is (15.5-19 mg g^{-1}) for other BILP-14-OR derivatives (Figure 5.10B). These values are within the range reported for all BILPs. The Q_{st} for CH_4 was calculated using the adsorption data, and resulted in high values for BILP-14-OMe and BILP-14-OEt, which can be attributed to the small pore volume, higher surface area, and greater number of interaction sites for CH_4. On the other hand, the Q_{st} values for BILP-14-OBu and BILP-14-OiBu are lower than other BILP-14-OR and within the range of reported BILPs. These lower Q_{st} values might be attributed to the weak interaction between CH_4 and the hydrophobic butoxy substituents (Figure 5.11B).

To evaluate BILP-14-OR derivatives with regard to hydrogen uptake and binding affinity, pure hydrogen isotherms were collected at 77 K and 87 K at 1 bar. The hydrogen uptake for the BILP-14-OR derivatives was within the range of all BILPs (1.3-2.3 wt%) (Figure 5.10C). The highest surface area polymer, BILP-14-OEt, has the highest uptake value (2.38 wt%), while the other polymers are in the range of (1.59- 2.16 wt%). The H_2 Q_{st} values for BILP-14-OR derivatives are also consistent with Q_{st} values of all BILPs and higher than the value for BILP-14. The increased Q_{st} value of BILP-14-OR (7.9-8.3 kJ mol^{-1}) (Figure 5.11C) compared to BILP-14 (7.1 kJ mol^{-1}) may be partially attributed to a reduction in the pore size for BILP-14-OMe and the introduction of bulky alkoxy groups for the other BILP-14-OR derivatives. It is believed that the introduction of electron-donating groups or atoms on the aromatic structures improves hydrogen uptake and binding affinity. This result has been observed in methoxy-modified MOF-5 where the presence of methoxy groups appears to have a favorable effect on the low pressure H_2 uptake capability.[120b]

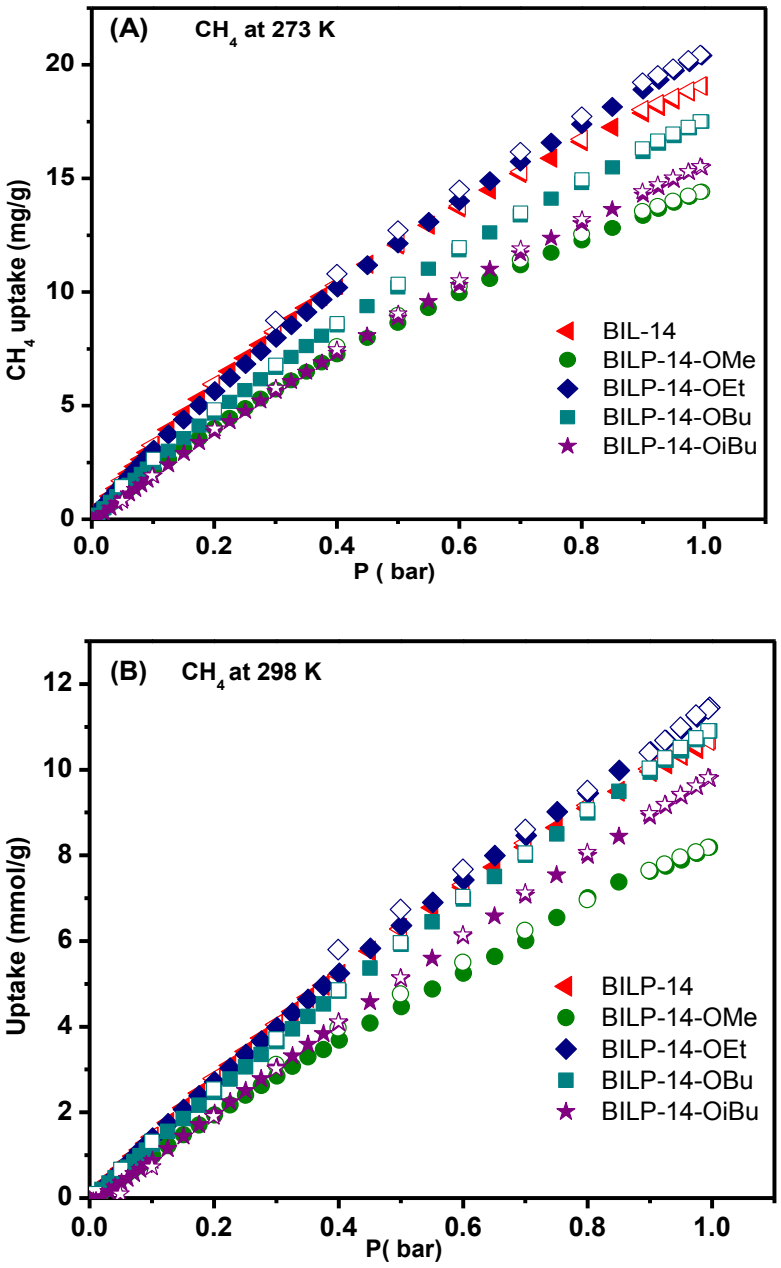

Figure 5.10B: CH_4 uptake isotherms of BILP-14 and BILP-14-OR derivatives at 273 K (A) and 298 K (B).

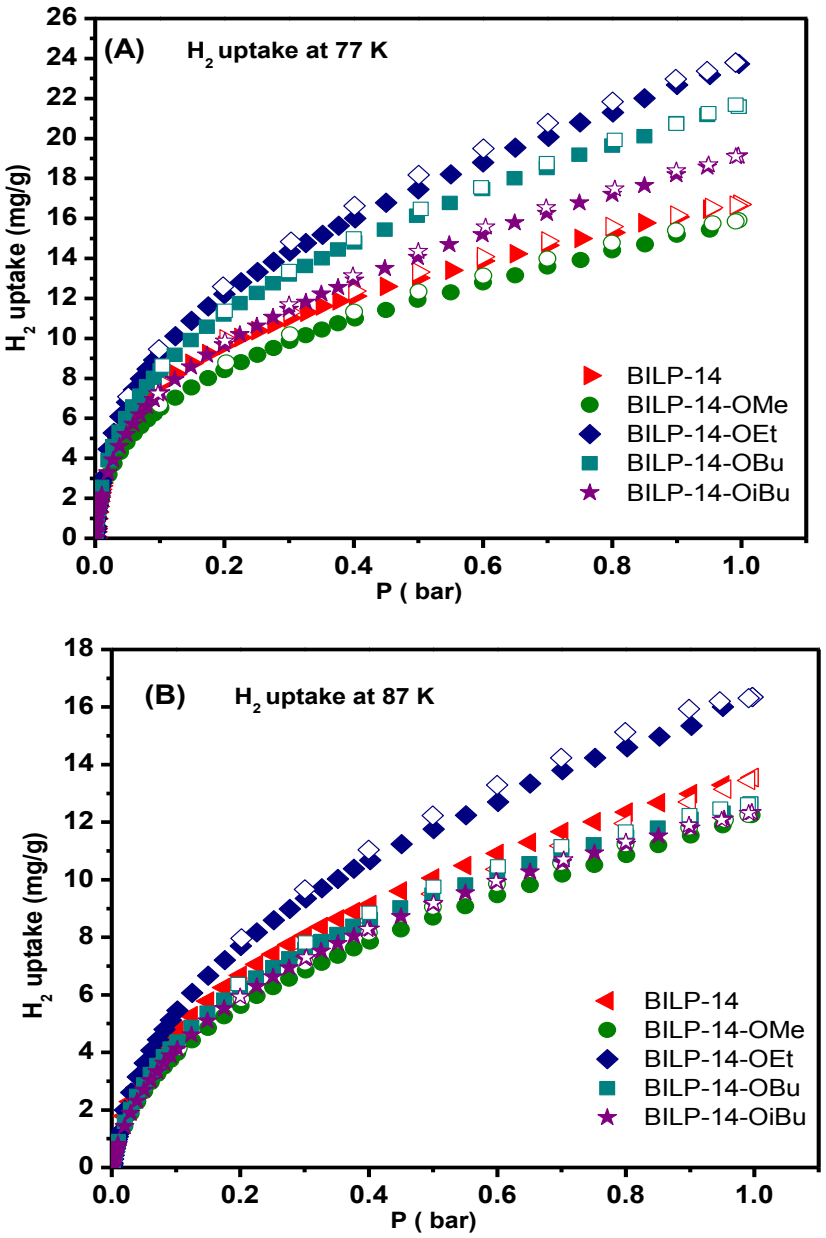

Figure 5.10C: H_2 uptake isotherms of BILP-14 and BILP-14-OR derivatives at 77 K (A) and 87 K (B).

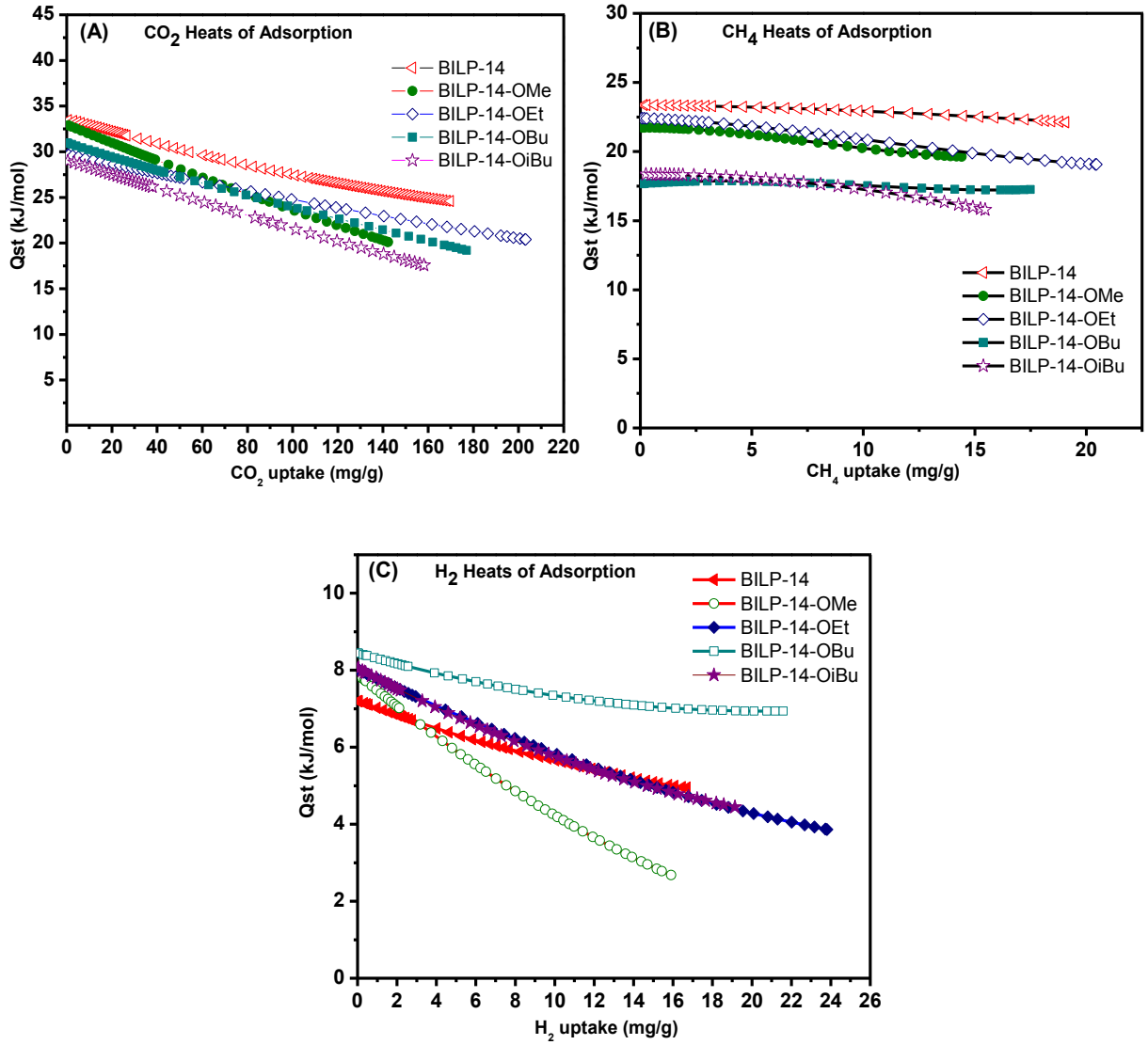

Figure 5.11: CO_2, CH_4 and H_2 isosteric heats of adsorption (Q_{st}) for BILP-14 and BILP-14-OR derivatives.

5.4.3 Gas Selectivity Studies

The preferential binding of BILP-14 to CO_2 over CH_4 and N_2 was calculated using the initial slope calculations of pure gas isotherms, which were collected at 273 K and 298 K. The CO_2/N_2 and CO_2/CH_4 selectivities for BILP-14 at (273 K/298 K) are (56/49) and (10/9), respectively. Furthermore, the selectivity results at 298 K were validated by the ideal adsorbed solution theory (IAST), which predicts the adsorption selectivity for gas mixtures based on pure components gas isotherms.[97] The selectivities from IAST were calculated for gas mixture composition CO_2:N_2 (10:90) and CO_2:CH_4 (50:50) and resulted in selectivity values of 52 and 9 at 298 K, respectively, which are consistent with the initial slope results. Accordingly, these calculations were performed to evaluate the impact of the new incorporated alkoxy groups on the selectivity of BILP-14-OR derivatives and compared to BILP-14.

The selectivity data from both initial slope and IAST are summarized in Table 5.1. From the initial slope calculations at 273 K, notable changes in CO_2/N_2 selectivity values were observed for BILP-14-OEt (64) and BILP-14-OiBu (81), which reveals small pore size distribution (6.8 Å) compared to BILP-14. The highest selectivity value was recorded for BILP-14-OiBu and that indicates a significant impact of the -OiBu group on gas separation processes. This high performance can be attributed to the presence of the branched substituent, the small pore size, and the moderate surface area of BILP-14-OiBu. The higher selectivity of BILP-14-OEt compared to BILP-14-OBu, which has a similar range of porosity can be attributed to the small pore size of BILP-14-OEt, which makes the material more effective for gas separation. On the other hand, the larger pore size BILP-14-OMe and BILP-14-OBu (8.5Å) have shown consistent selectivity values with BILP-14 and indicated almost no impact of the alkoxy groups on the selectivity (Figure 5.12). The selectivity values for all polymers at 298 K were consistent

for both methods and indicate that the alkoxy groups do not alter gas selectivity at 298 K (Figure 5.13). In contrast, the selectivity for CO_2/CH_4 is lower than BILP-14 and falls in the range of 9-6. The low selectivity indicates that the CO_2/CH_4 separation process is more challenging than CO_2/N_2, which can be explained due to the fact that the polarizability and adsorption potential of CH_4 is higher than N_2.

Table 5.2: Initial slope selectivity of BILP-14 and BILP-14-OR derivatives at 273 K (298 K), and the IAST selectivity of BILP-14 and BILP-14-OR derivatives at 298 K for the binary mixtures of (CO_2/N_2: 10:90) and (CO_2/CH_4: 50:50).

BILP	**Selectivity**			
	Initial slope at 273 K (298)		**IAST at 298 K**	
	CO_2/N_2	**CO_2/CH_4**	**CO_2/N_2 (10:90)**	**CO_2/CH_4 (50:50)**
BILP-14	56 (49)	10 (9)	52	9
BILP-14-OMe	57(39)	10 (7)	45	7
BILP-14-OEt	64(36)	10(6)	41	7
BILP-14-OBu	48(25)	9(6)	25	6
BILP-14-OiBu	81(34)	9(7)	22	6

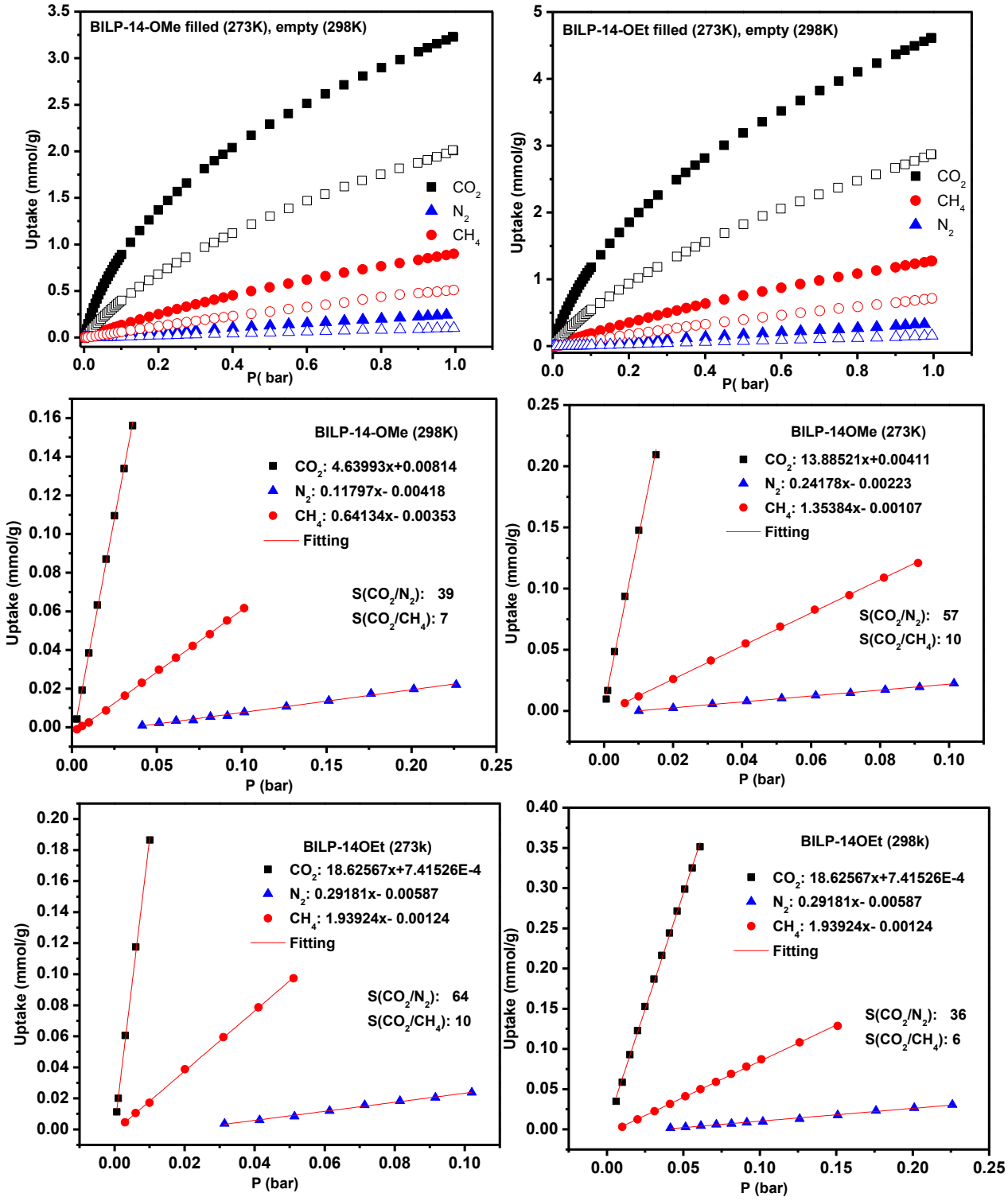

Figure 5.12A: Gas sorption capacities for BILP-14-OMe and BILP-14-OEt derivatives and the adsorption selectivity of CO_2 over N_2 and CH_4 from initial slope calculations.

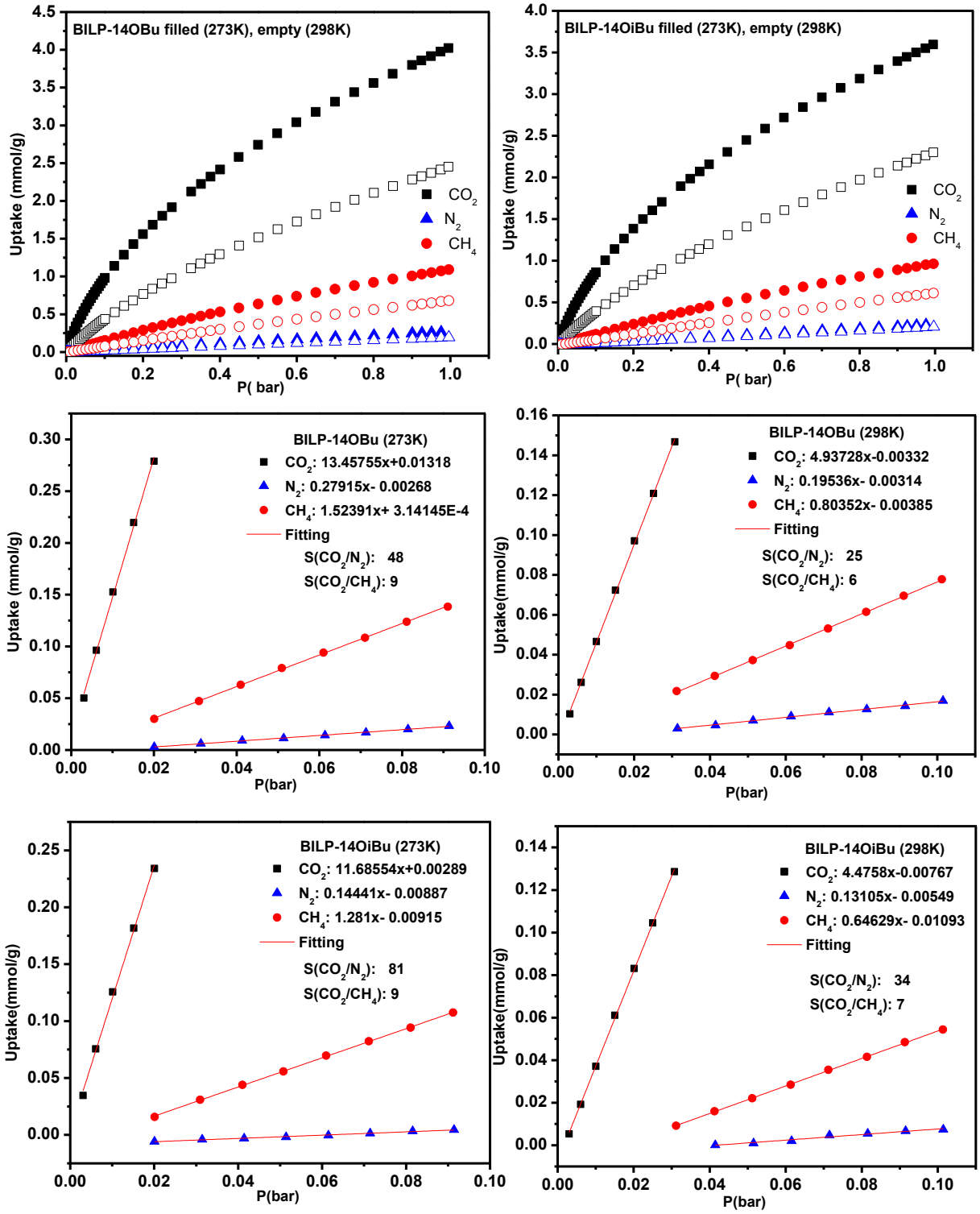

Figure 5.12B: Gas sorption capacities for BILP-14-OBu and BILP-14-OiBu derivatives and the adsorption selectivity of CO_2 over N_2 and CH_4 from initial slope calculations.

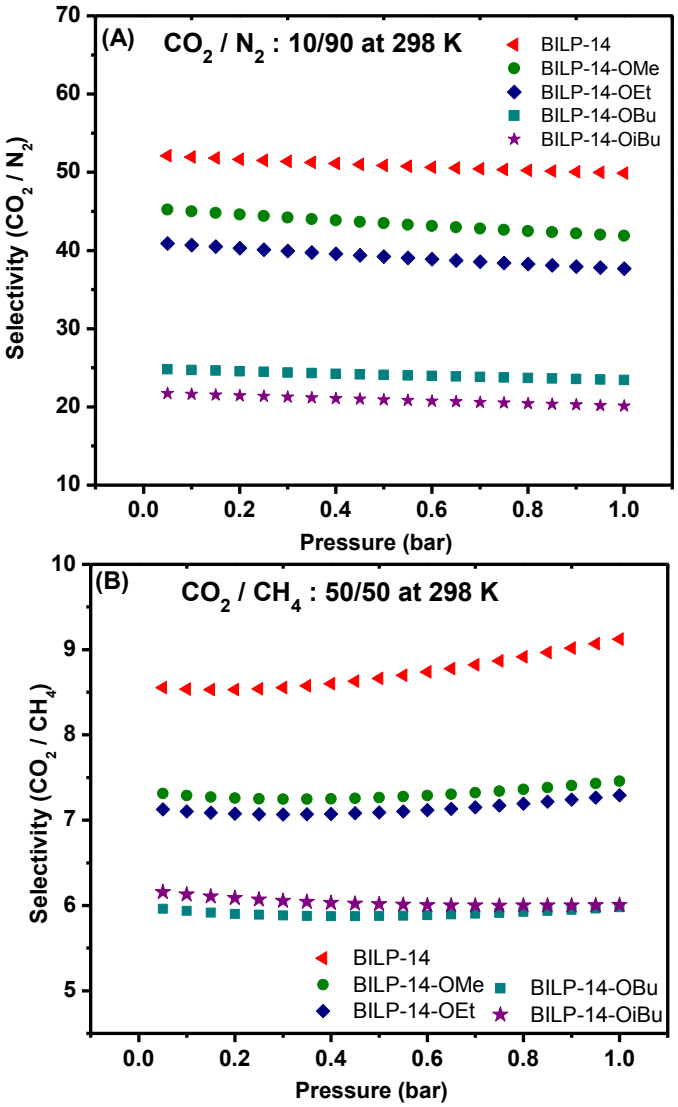

Figure 5.13: IAST selectivities of CO_2/ N_2 10/90 and CO_2/ CH_4 for 50/50 binary mixtures at 298 K for BILP-14 and BILP-14-OR derivatives.

Table 5.3: Gas Uptake and heats of asorption data of BILP-14 and BILP-14-OR derivatives

polymer	SA_{BET}[a]	Pore volume[b]	H_2 at 1 bar[c]			CO_2 at 1 bar[c]			CH_4 at 1 bar[c]			N_2 at 1 bar[c]	
			77 K	87 K	Q_{st}	273 K	298 K	Q_{st}	273 K	298 K	Q_{st}	273 K	298 K
BILP-14	**1005**	0.55	17	14	7.1	170	114	33.5	19	11	23.3	9.0	4.0
BILP-14-OMe	**685**	0.39	15.9	12.2	7.9	142	87	32.9	14.4	8.2	21.8	6.9	2.8
BILP-14-OEt	**1163**	0.66	23.8	16.3	8.0	203	126	29.6	20.4	11.4	23.6	9.5	4.4
BILP-14-OBu	**1108**	0.56	21.6	12.6	8.4	177	108	30.9	17.5	11	17.4	7.4	5.4
BILP-14-OiBu	**921**	0.51	19.0	12.0	8.0	158	101	29.0	15.5	9.7	18.0	6.6	5.7

[a]Surface area ($m^2\ g^{-1}$) was calculated from Ar isotherm. [c]Pore volume (cc g^{-1}) was calculated from single point measurements (P/P_0 =0.95). [c]Gas uptake in mg g^{-1} and the isosteric enthalpies of adsorption (Q_{st}) in kJ mol^{-1}).

5.5 Alkoxy-Functionalized BILP-15-OR Derivatives

In this section we have mentioned a new series of alkoxy-functionalized BILP-15-OR derivatives and discussed their synthesis, spectral and analytical characterizations, and gas adsorption properties. The synthetic protocol of BILP-15-OR derivatives was demonstrated in a fashion similar to the preparation of BILP-15, using 3,3'-Diaminobenzidine tetrahydrochloride hydrate salt (DABA) and alkoxy-aryl aldehydes (Figure 5.1). The polycondensation reaction between DABA, and alkoxy aryl-aldehydes $(OMe)_2$TFPB, $(OEt)_2$TFPB, $(OBu)_2$TFPB and $(OiBu)_2$TFPB, resulted in BILP-15-OMe, BILP-15-OEt, BILP-15-OBu, and BILP-15-iOBu, respectively. The synthesis of alkoxy aryl-aldehydes and their starting materials were displayed in section 1 of this Chapter.

Synthesis of Dialkoxy-Functionalized BILP-15-OR Derivatives

Synthesis of BILP-15-OMe

BILP-15-OMe was synthesized in a fashion similar to the preparation of BILP-15.[69e] A 100 mL Schlenk flask was charged with 3,3'-Diaminobenzidine tetrahydrochloride hydrate salt (DABA) (65 mg, 0.181 mmol) and 30 mL of anhydrous DMF under a nitrogen atmosphere. The solution was cooled to around -30 °C, and a solution of 2,3,5,6-Tetrakis-(4-formylphenyl)-1,4-dimethoxybenzene ($(OMe)_2$TFPB) (50 mg, 0.091 mmol) in 25 mL anhydrous DMF, was added dropwise to the pervious charged solution over 3 hrs. Temperature was maintained around -30 °C until yellowish brown solid product formation completed and was then increased to RT and kept overnight. The flask, containing the reaction mixture, was flashed with air for 15 min and capped. The reaction mixture was then heated in an oven at 130 °C (0.5 °C/min) for 3 days to afford a fluffy brownish polymer, which was isolated by filtration over a glass frit. The product

was immersed in DMF (20 mL overnight) and then in (20 mL) acetone. The product was filtered and dried under vacuum at 120 °C and 1.0 x 10^{-5} Torr for 20 hrs to give BILP-15-OMe as a brown fluffy solid (75 mg, 85%). Anal. Calcd for $C_{60}H_{38}N_8O_2.4H_2O$: C, 73.92%; H, 4.72%; N, 11.50%. Found: C, 71.98%; H, 4.06%; N, 10.0%.

Synthesis of BILP-15-OEt

BILP-15-OEt was synthesized in a similar fashion to the preparation of BILP-15, using (DABA) (65 mg, 0.181 mmol) and 2,3,5,6-Tetrakis-(4-formylphenyl)-1,4-diethoxybenzene ($(OEt)_2$TFPB) (53.0 mg, 0.091 mmol) in anhydrous DMF under a nitrogen atmosphere. The resulting product was filtered and dried under vacuum at 120 °C and 1.0 x 10^{-5} Torr for 20 hrs to give BILP-15-OEt as a brown fluffy solid (77 mg, 82%). Anal. Calcd for $C_{62}H_{42}N_8O_2.6H_2O$: C, 71.25%; H, 4.54%; N, 10.64%. Found: C, 71.68%; H, 5.20%; N, 10.79%.

Synthesis of BILP-15-OBu

BILP-15-OBu was synthesized in a similar fashion to the preparation of BILP-15 using (DABA) (65 mg, 0.181 mmol) and 2,3,5,6-Tetrakis-(4-formylphenyl)-1,4-dibutoxybenzene ($(OBu)_2$TFPB) (58 mg, 0.09 mmol) in anhydrous DMF under a nitrogen atmosphere. The resulting product was filtered and dried under vacuum at 120 °C and 1.0 x 10^{-5} Torr for 20 hrs to give BILP-15-OBu as a brown fluffy solid (83 mg, 84%). Anal. Calcd for $C_{66}H_{50}N_8O_2.6H_2O$: C, 72.32%; H, 5.67%; N, 10.23%. Found: C, 70.34%; H, 4.58%; N, 9.0%.

Synthesis of BILP-15-iOBu

BILP-15-iOBu was synthesized in a similar fashion to the preparation of BILP-15 using (DABA) (65 mg, 0.181 mmol) and 2,3,5,6-Tetrakis-(4-formylphenyl)-1,4-dibutoxybenzene ($(OiBu)_2$TFPB) (58 mg, 0.09 mmol) in anhydrous DMF under a nitrogen atmosphere. The

resulting product was filtered and dried under vacuum at 120 °C and 1.0 x 10^{-5} Torr for 20 hr to give BILP-15-iOBu as a brown fluffy solid (83 mg, 84%). Anal. Calcd for $C_{66}H_{50}N_8O_2.4H_2O$: C, 74.77%; H, 5.48%; N, 10.75%. Found: C, 75.29%; H, 5.28%; N, 10.87%.

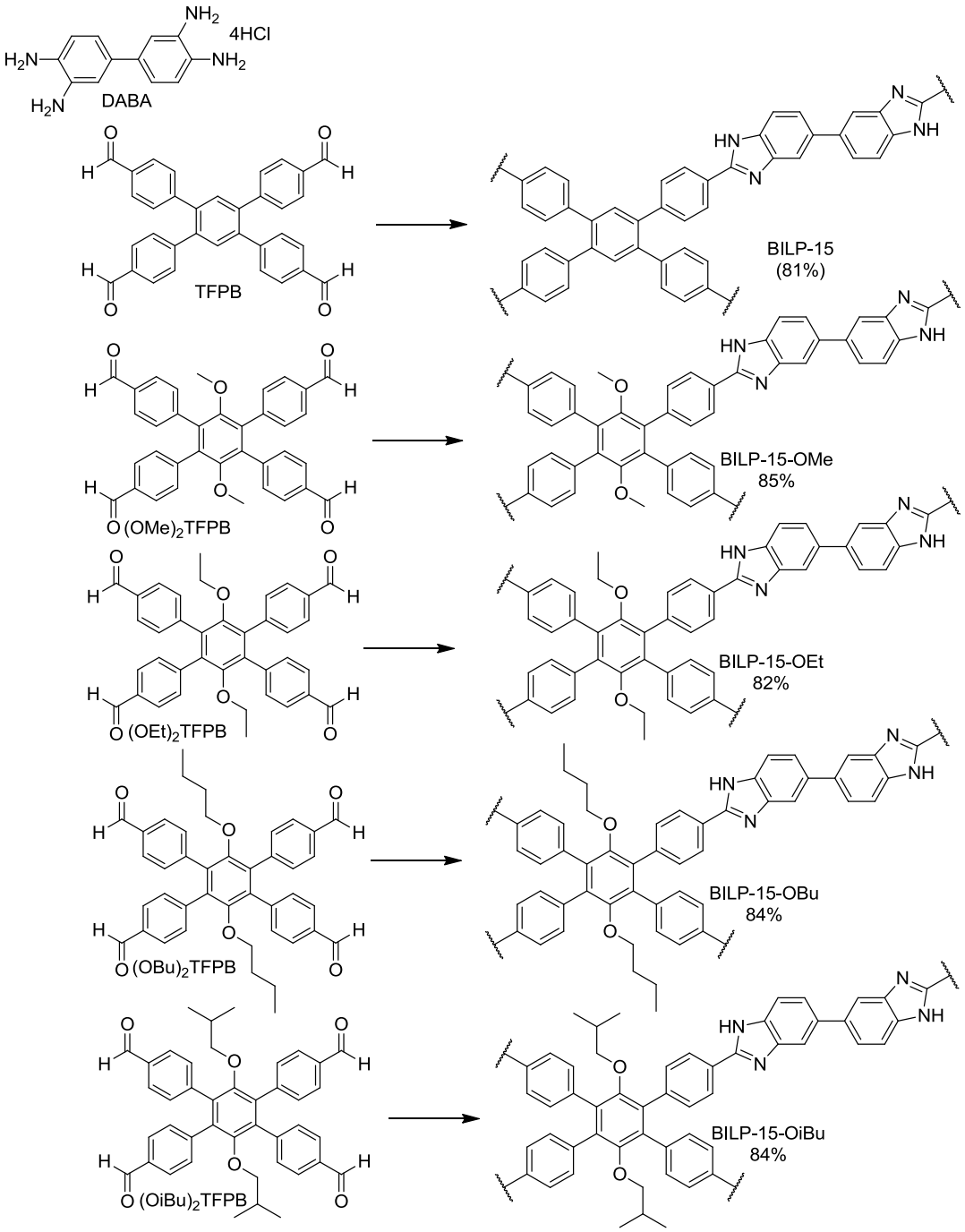

Scheme 5.4: Synthesis of BILP-15 and BILP-15-OR derivatives.

5.5.1 Results and discussions

The synthesis, spectral and analytical characterizations, and adsorption measurements of BILP-15-OR derivatives were demonstrated in this section and compared to BILP-15. After polymerization and isolation, the new synthesized BILP-15-OR derivatives, BILP-15-OMe, BILP-15-OEt, BILP-15-OBu, and BILP-15-iOBu, were dried and activated at 120 °C and 1.0 x 10^{-5} Torr for 20 hrs before any further characterizations. The successful incorporation of alkoxy-groups to the polymers' backbone was confirmed by spectral and analytical techniques such as: elemental analysis, ^{13}C-NMR, and IR. The impact of the new functionality on the porosity and gas adsorption properties was investigated by gas sorption measurements and compared to BILP-15.

BILP-15-OR derivatives have shown similar physiochemical stability to BILP-14-OR upon exposure to high acid concentrations (> 2 M), wherein the permanent color change after soaking in acid is attributed to the cleavage of the alkoxy groups.[117] TGA has also shown consistent thermal stability of BILP-15-OR when compared to BILP-14-OR derivatives.

The first weight loss at 100 ºC is attributed to the removal of water molecules, while the weight loss in the range of 300-350 ºC is attributed to the presence of alkoxy flexible linkers (-OMe, -OEt, -OBu, and -OiBu). On the other hand, the main pronounced weight loss for BILP-15 is around 400 ºC, which is consistent with the behavior of all BILPs. Thus, these linkers were believed to introduce more disruptive movement in the polymer structure, and assist the network collapse at an earlier stage compared to BILP-15.[118, 120b, 122-123]

In a recent study on MOFs, it has been proven that the incorporation of functionalized linkers featuring pendent flexible substituents to MOFs produces thermo-mechanical responsive materials. This unique behavior is suggested to originate from the increased thermal motions

(vibrations and rotation) of the linear side chains with increasing temperature, and assist the early decomposition.[123] Thus, the presence of alkoxy linkers in BILP-15-OR could enhance these vibration-rotation motions, and assist the material decomposition in the range of 250-300 ºC.

All BILP-15-OR derivatives are amorphous as illustrated from powder X-ray diffraction studies. Scanning electron microscopy (SEM) images of BILP-15-OR derivatives established phase purity of the polymers and revealed different morphologies and variable particle size. BILP-15 has agglomerated particles *ca*. 0.5-0.3 μm, while BILP-15-OR derivatives revealed more uniform aggregated spherical particles *ca*. 0.3-0.1μm (Figure 5.15).

The chemical composition of BILP-15-OR derivatives and their corresponding alkoxy aryl-aldehydes were determined by microelemental analysis, which showed the successful incorporation of alkoxy functional groups to aryl-aldehydes and polymers' networks. Moreover, it showed that nitrogen atoms of imidazole rings are involved in hydrogen bonding with water molecules, which is consistent with other BILPs and TGA results.

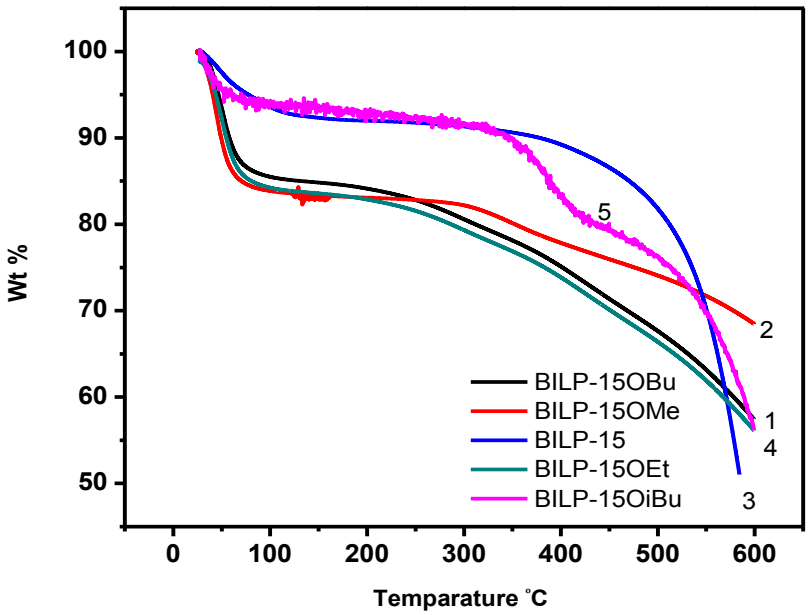

Figure 5.14: (A) Thermal gravimetric profiles of BILP-15 and BILP-15-OR derivatives measured under N_2.

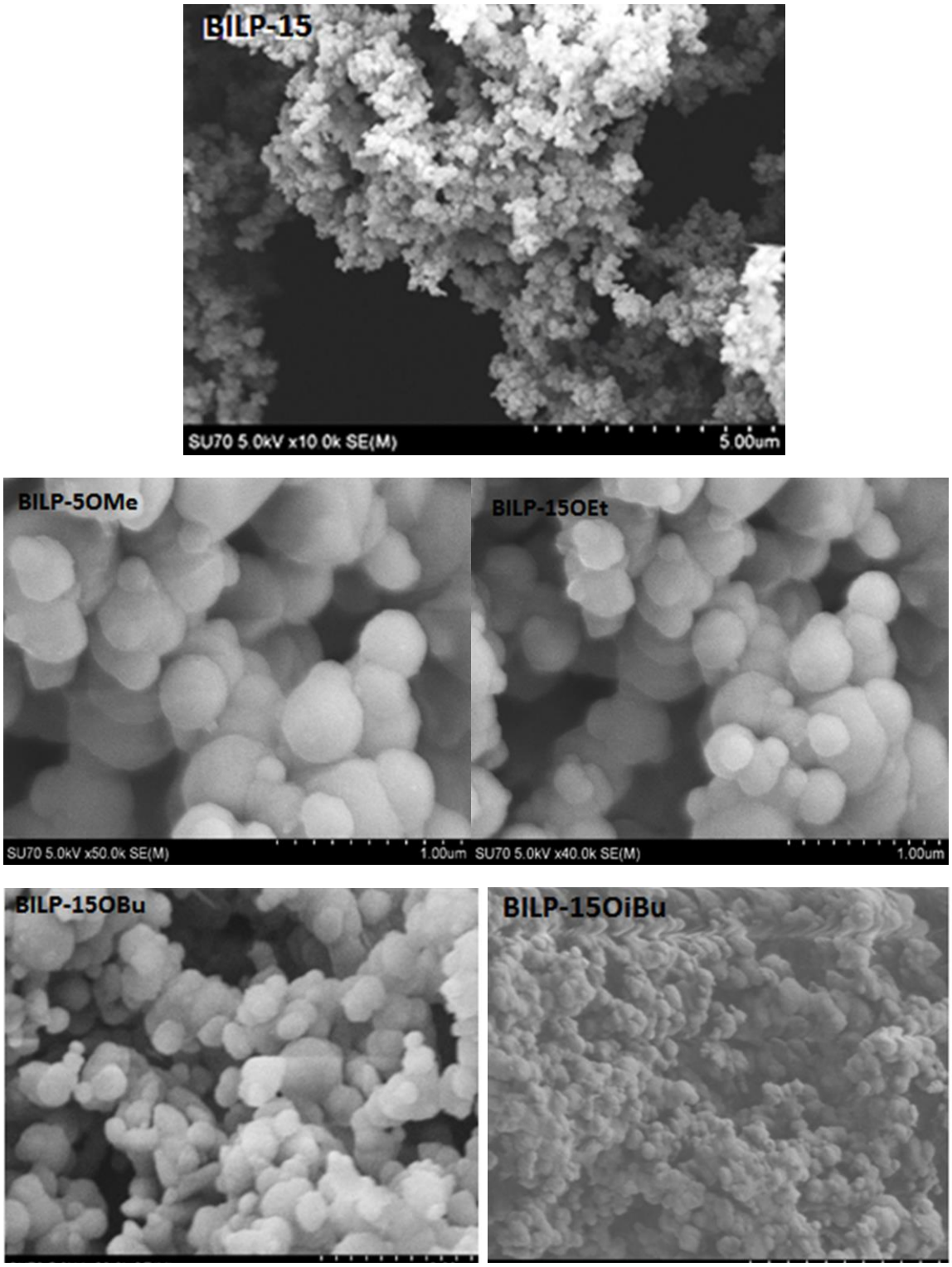

Figure 5.15: SEM images of BILP-15 and BILP-15-OR derivatives.

The chemical connectivity of BILP-15-OR derivatives was verified using FT-IR and ^{13}C NMR. FT-IR spectra, for alkoxy aryl-aldehyde starting materials and the corresponding BILP-15-OR derivatives, confirmed the successful formation of BILP-15-OR derivatives. The new significant vibrations at 1620, 1480, 1435, 1370, and 1275 cm^{-1} and the substantial attenuated peak at 1700 cm^{-1} confirmed the successful polycondensation reaction. The other stretching vibrations around 3425 cm^{-1} and 3220 cm^{-1} are assigned to free N-H, while the bands in the range of 2750-3030 cm^{-1} belong to C-H aromatic carbons. The vibrations at 1450, 1378, 1246, 1205, 1030, and 943 cm^{-1} belong to the alkoxy groups. The strong band intensity in the range of 2880-2970 cm^{-1} corresponds to C-H bonds of the alkyl substituent.[119-120] The expanded region shows the bands in the range 2000-500 cm^{-1} (Figure 5.16).

The ^{13}C CP-MAS NMR spectra show the successful formation of the new BILPs and the incorporation of the dialkoxy functional groups. The peaks belonging to the alkoxy carbons (C-O) of (-OMe, -OEt,-OBu and -OiBu) appear around 80, 72, 69, and 61 ppm, respectively.[121] The aliphatic secondary carbons in -OBu and -OiBu appear around 31, 29, and 18 ppm. The terminal -CH_3 group appears at around 15 ppm. The aromatic C-O carbon appears around 148 ppm, while the resonance peaks around 100, 127, 130, and 133 ppm belong to the aromatic C-H bonds. The peak around140 ppm belongs to the carbon of the biphenyl moiety in BILP-15-OR derivatives. The peak at around 150 ppm corresponds to the imidazole ring carbon. These results are consistent with BILP-14-OR derivatives and appeared in similar ranges. The different peak shape in the aromatic range of 100-160 ppm is due to the presence of the biphenyl group.

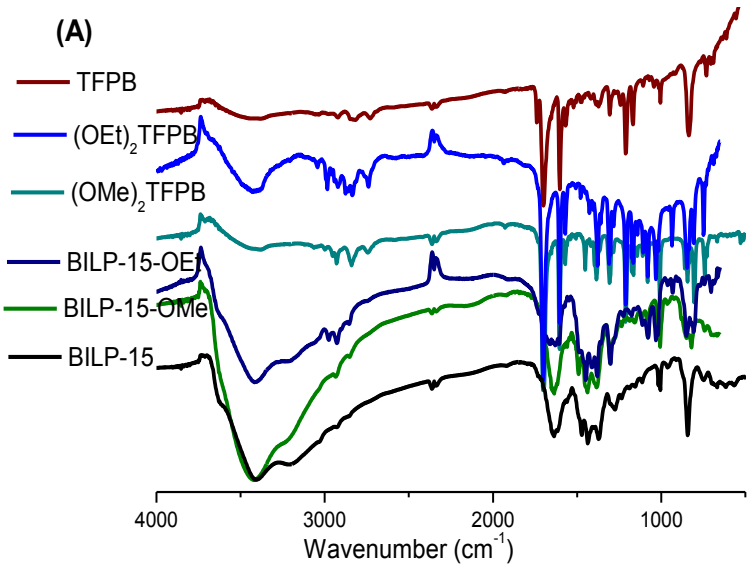
(A)
TFPB
(OEt)2TFPB
(OMe)2TFPB
BILP-15-OEt
BILP-15-OMe
BILP-15
4000
3000
2000
1000
Wavenumber (cm-1)

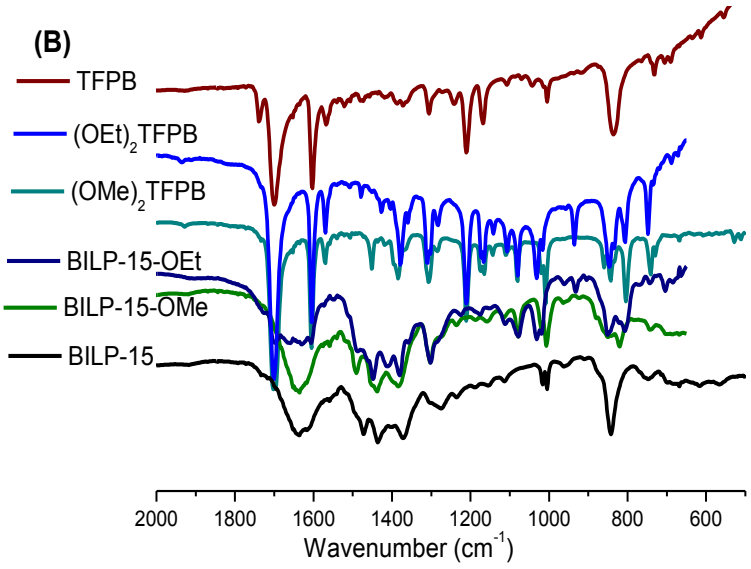
(B)
TFPB
(OEt)2TFPB
(OMe)2TFPB
BILP-15-OEt
BILP-15-OMe
BILP-15
2000
1800
1600
1400
1200
1000
800
600
Wavenumber (cm-1)

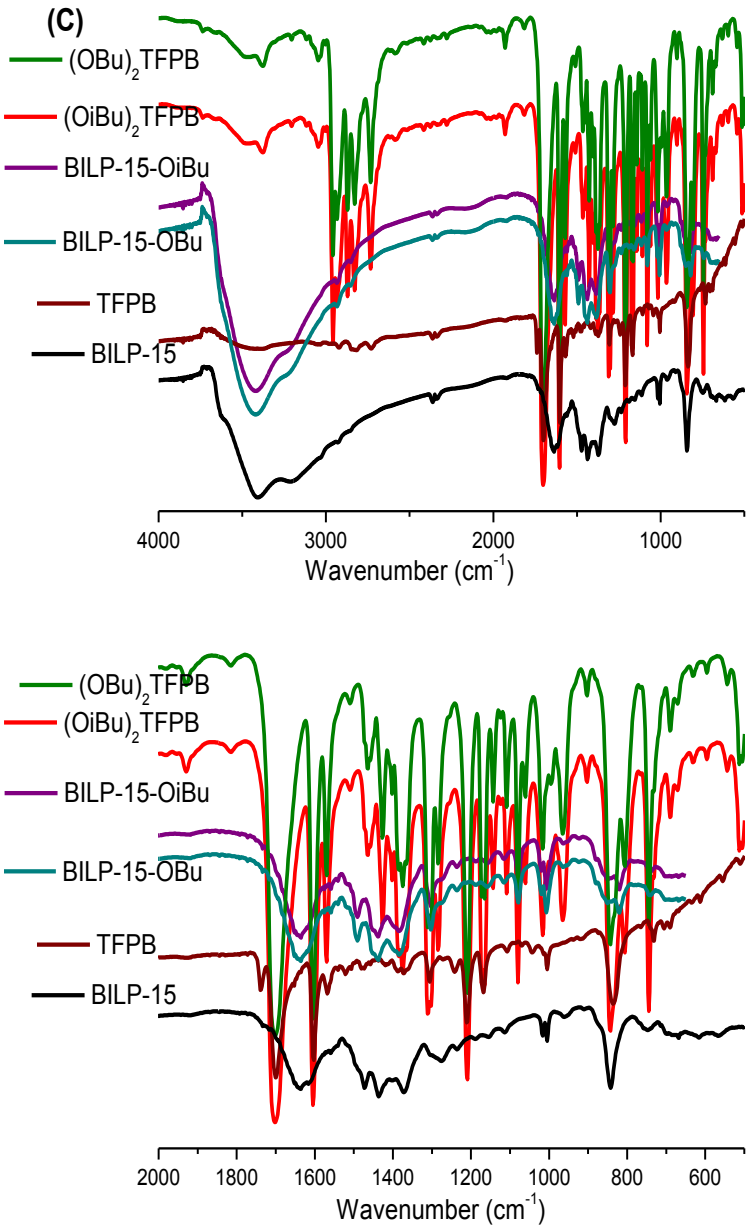

Figure 5.16: FT-IR spectra of BILP-15 and BILP-15-OR derivatives and their aryl-aldehydes starting building units in the ranges 4000-500 and 2000-500 cm^{-1}.

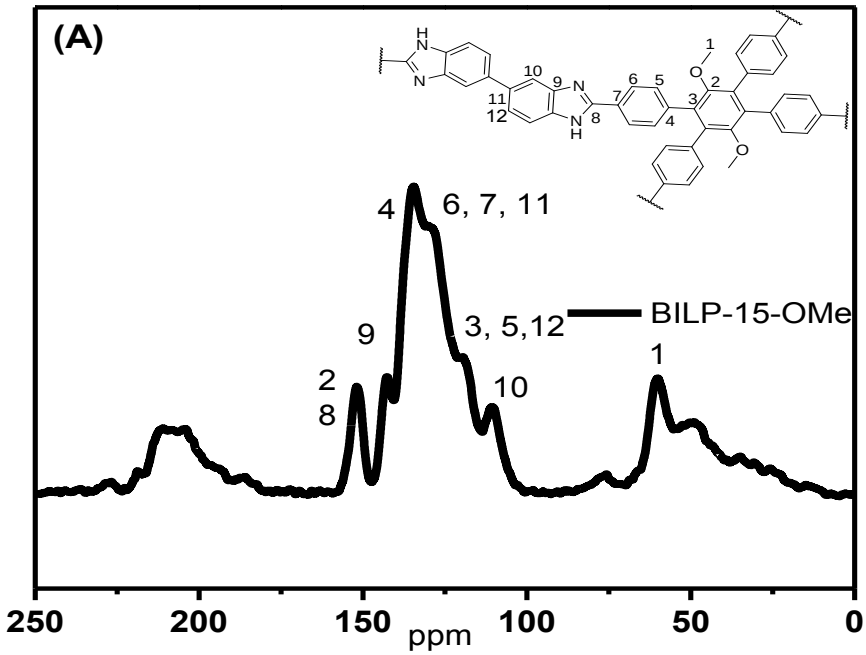
(A)
4
6, 7, 11
9
3, 5,12
BILP-15-OMe
2
8
10
1
250
200
150
ppm
100
50
0

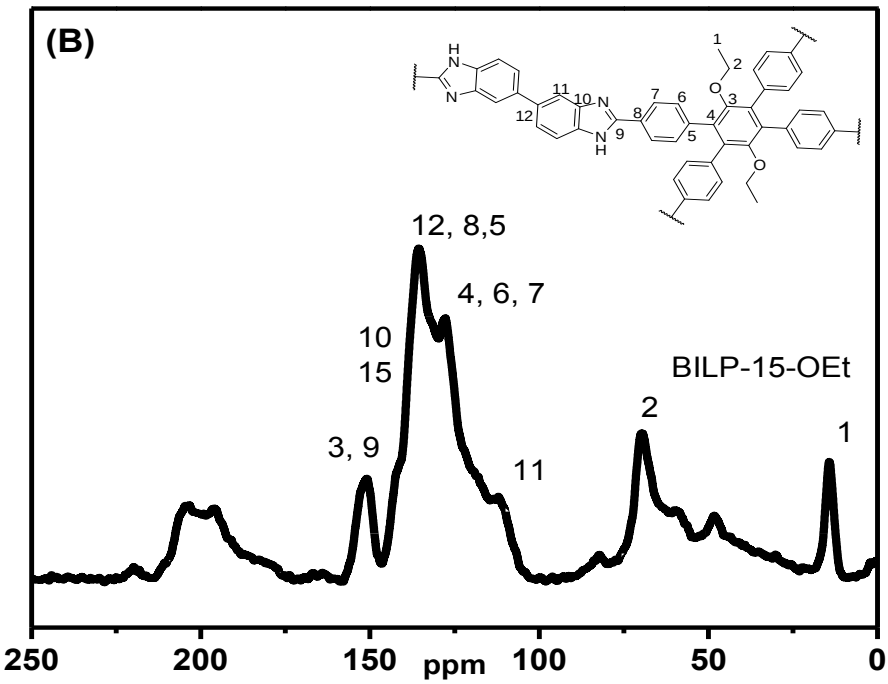
(B)
12, 8,5
4, 6, 7
10
15
BILP-15-OEt
2
1
3, 9
11
250
200
150
ppm
100
50
0

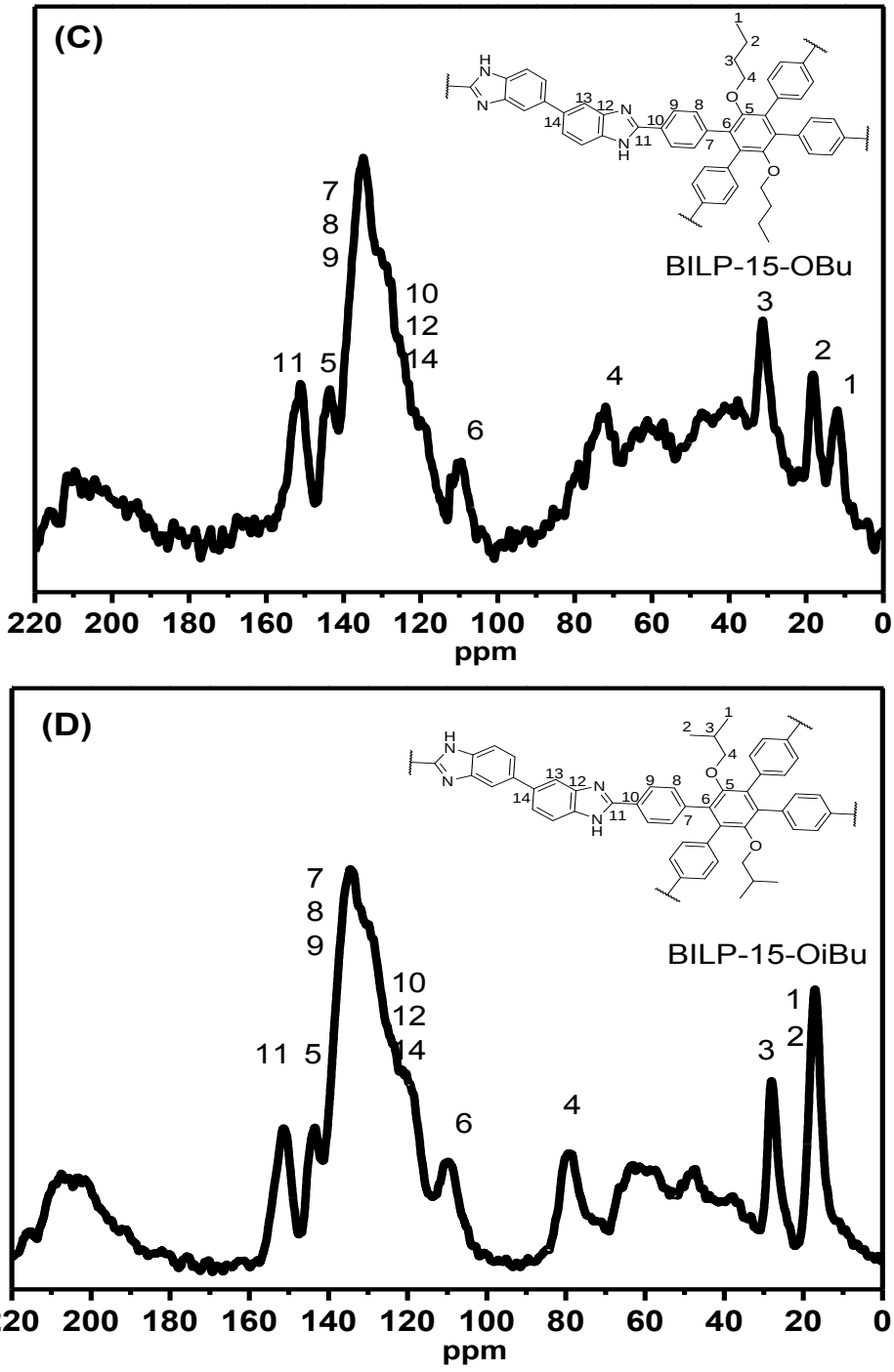

Figure 5.17: Solid state ^{13}C CP-MAS NMR spectra of BILP-15-OR derivatives.

5.5.2 Porosity and Low Pressure Gas Uptake Measurements

The porosity of BILP-15-OR derivatives was investigated by argon sorption-desorption measurements. Prior to sorption measurements, the polymers were activated at 120 °C and 1.0 x 10^{-5} Torr for 20 hrs. The isotherms were collected at 87 K, which resulted in fully reversible behavior and indicated microporosity (Type-I-Type II) from the rapid Ar uptake at low pressure (0-0.1 bar) as illustrated in Figure 5.18. The minor hysteresis observed for all materials is consistent with the powdery and flexible nature of BILPs. Applying the BET model to the sorption branch within the pressure range of P/P_o= 0.05-0.15 resulted in moderate surface areas; BILP-15-OMe (614 $m^2 g^{-1}$), BILP-15-OEt (861 $m^2 g^{-1}$), BILP-15-OBu (1311 $m^2 g^{-1}$) and BILP-15-iOBu (853 $m^2 g^{-1}$) (Figure 5.19). Interestingly, these surface areas are higher than the surface area of BILP-15 by 37%, 92%, 192%, and 90%, respectively. Thus, the pre-introduction of alkoxy groups on BILP-15, which was targeted to improve the CO_2 uptake and binding affinity, is believed to have a positive effect on the porosity of BILP-15.

We mentioned earlier that the lower surface area of BILP-15 was attributed to the presence of the flexible 3,3'-diaminobenzidine building unit, which enhances the network interpenetration. However, further investigations have shown that the rational design of the elongated building units with bulky groups introduces a control over the formation of the interpenetrated networks and assists in the formation of non-interpenetrated structures. Examples of this strategy, as discussed in Chapter1, include: the incorporation of naphthalene substituents or azolium moieties to the dicarboxylate linker, the pre-introduction of (aryl-Br) to benzene-tetraryl-tetrabenzoic acid and the ligand-elaboration method, wherein (-CH_3, -Br and –CH_2OH) have been incorporated on a series of 4,4'-ethylenedibenzoic acids.[80b, 85, 87a, 90-92, 124] The common conclusion after applying each of these modifications is that the selective design of the organic linker with pendent groups

differing in size and/or length is the leading step to achieve a non-interpenetrated network and gain more control over network formation.

Thus, by varying the length and size of the pendant incorporated groups in BILP-15-OR derivatives; we have confirmed that this strategy is applicable and it resulted in improved polymer porosity compared to BILP-15. The linear -OMe, -OEt, and -OBu groups have resulted in a systematic increase in the porosity of the corresponding BILP-15-OR derivatives, while a significant decrease was noticed in the case of the branched -OiBu group. These results can be attributed to the fact that the linear groups can rotate freely and provide more interaction sites for argon to adsorb (-OBu > -OEt > -OMe). In contrast, -OiBu introduces more bulkiness, which would fill the pores thereby reduces the size and the available surface area for argon adsorption. This observation is consistent with the porosity of isopropoxy pillared-Layered MOF, when compared to linear alkoxy-substituted MOF.[120a]

It is noteworthy that the porosity of BILP-15 was increased by up to 192 % in the case of BILP-15-OBu by applying this strategy, while it was increased by only 92 % when applying the acid-catalysis strategy discussed in Chapter 3.

Pore size distribution (PSD) curves were estimated from the argon isotherms by nonlocal density functional theory (NLDFT) on the adsorption branch with a cylindrical/sphere pore model on the argon isotherms. PSD was found to be centered at 5.6.0 Å for BILP-15, while it is around 7.0 Å, for BILP-15-OMe, and BILP-15-OBu and around 4.9 Å for BILP-15-OEt, and BILP-15-iOBu (Figure 5.9). BILP-15-OBu also contains pores with relatively small distribution from 11 to 15 Å. The pore volume was calculated from single point measurements (P/P_o= 0.95) and found to be 0.27, 0.36, 0.49, 0.70, and 0.45 cc g^{-1} for BILP-15, BILP-15-OMe, BILP-15-OEt, BILP-15-OBu, and BILP-15-iOBu, respectively.

In general the pore volumes of the polymers slightly increase with the length of the pendant substituents and decrease with the bulkiness. For example, the highest surface area BILP-15-OBu has the largest specific pore volume (0.70 cc g^{-1}) among all BILP-15-OR derivatives. This can be attributed to the presence of the longer flexible substituent compared to -OMe and -OEt groups. This longer group introduces more pore space and suppresses the network contraction. These results are consistent with the results that we have observed for BILP-14-OR derivatives. Moreover, It shows that the presence of the flexible -OMe, -OEt, and -OBu groups prevents the packing of the substituents inside the pores, while the branched -OiBu group assists the network packing, and lowers the pore volume.[120a]

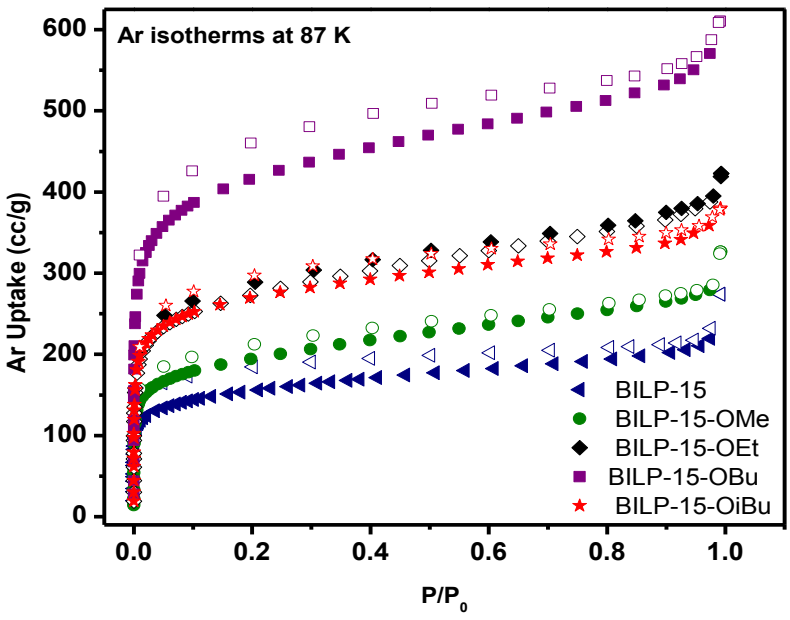

Figure 5.18: Ar adsorption isotherm for BILP-15 and BILP-15-OR derivatives measured at 87 K. The filled symbols are adsorption points and the empty symbols are desorption points

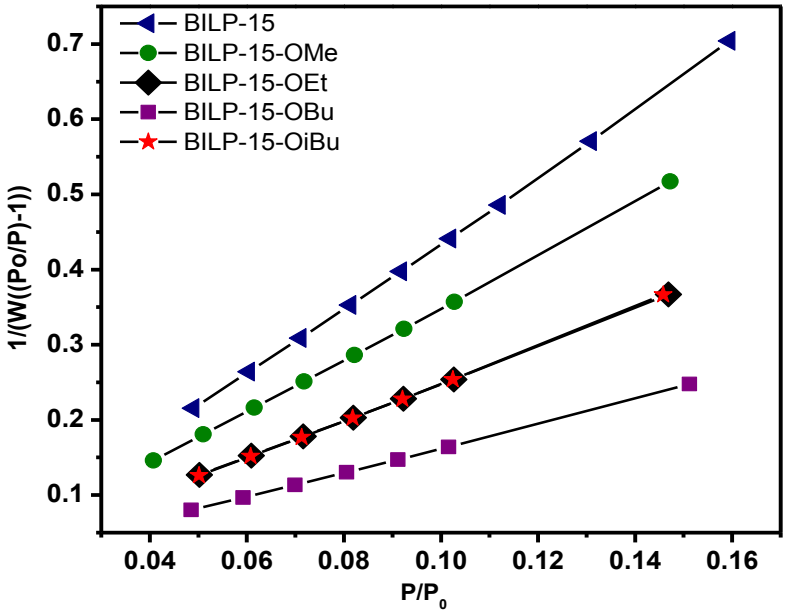

Figure 5.19: BET plots for BILP-15 and BILP-15-OR derivatives calculated from the Ar adsorption isotherm at 87 K. The model was applied from P/Po = 0.05-0.16. (W = Weight of gas absorbed at a relative pressure P/Po).

Table 5.4: BET and Langmuir surface areas for BILP-15 and BILP-15-OR derivatives calculated from the Ar adsorption isotherm at 87 K.

BILP	Surface area (BET) $m^2 g^{-1}$	Langmuir Surface area $m^2 g^{-1}$
BILP-15	448	568
BILP-15-OMe	614	758
BILP-15-OEt	861	1075
BILP-15-OBu	1311	1643
BILP-15-iOBu	853	1061

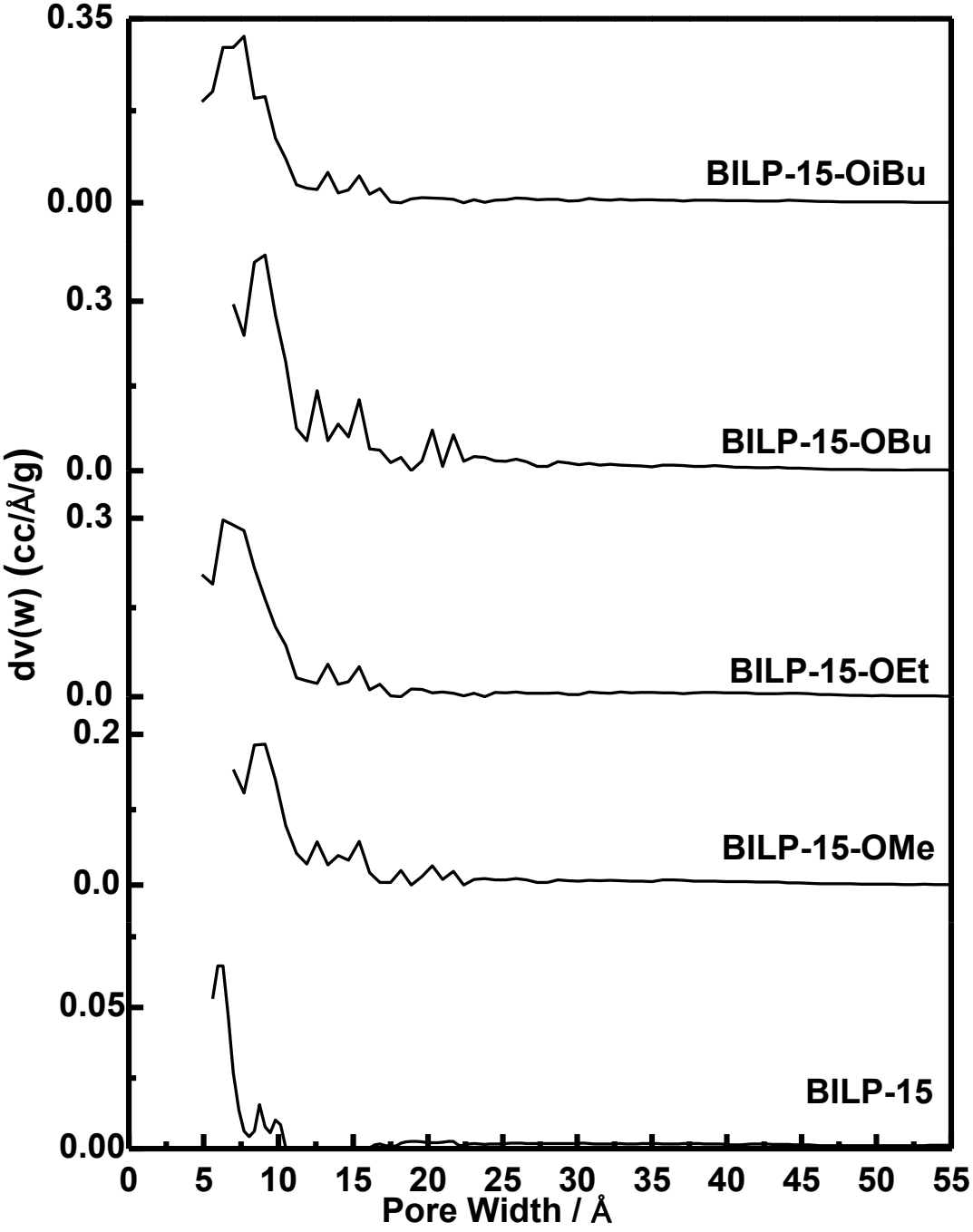

Figure 5.20: The Pore Size Distribution of BILP-15 and BILP-15-OR derivatives

In addition to the heterogeneity and subnanometer porosity of BILP-15-OR derivatives, tailoring the microporosity and altering the pore dimensions and environment are believed to have a significant impact on the selective gas uptake and enhance the binding affinities. Accordingly, the impact of the imidazole moiety, the chemical nature of the new incorporated alkoxy groups on the uptake of small gas molecules CO_2 and H_2, and the preferential binding of CO_2 over N_2 and CH_4 were investigated. CO_2, H_2 and CH_4 gas isotherms were collected and their respective isosteric heats of adsorption (Q_{st}) were calculated and summarized in Table 5.6.

The CO_2 isotherms of BILP-15-OR derivatives are fully reversible with very minor hysteresis and exhibit a steep rise at low pressure. It is worth mentioning that BILP-15-OBu has the highest CO_2 uptake at 218 mg g^{-1} at (273 K/ 1 bar). The uptakes for BILP-15-OMe, BILP-15-OEt, and BILP-15-iOBu are 138, 157, and 147 mg g^{-1}, respectively. The CO_2 uptake values are within the uptake range of other BILPs, especially those which were constructed from 2D building units.

The high CO_2 uptakes are expected to arise from strong interactions between the polarizable CO_2 molecules through dipole-quadrupole interactions that utilize imine-nitrogen sites of imidazole rings. Thus, the higher surface area polymers exhibit a higher number of these interaction sites and higher CO_2 uptake. The incorporation of alkoxy pendant groups (e.g. -OEt, and -OBu) has resulted in higher surface area BILP-15-OR derivatives and, hence introduced more CO_2 interaction sites. However, there is no notable direct impact of the chemical nature of these groups on the behavior of CO_2 isotherms and the overall uptake; we suggest that DFT calculations would be useful for investigating the possible role the pendant groups play in enhancing CO_2 uptake.

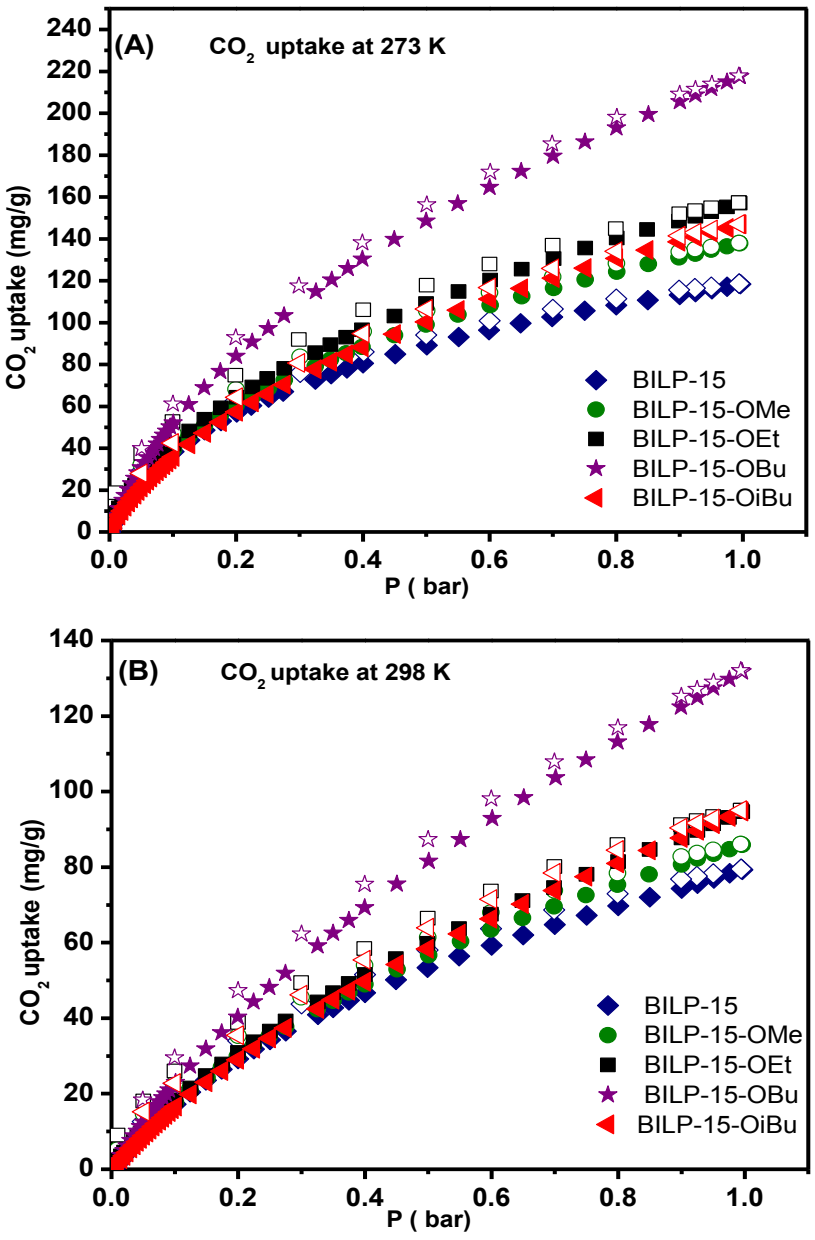

Figure 5.21A: CO_2 uptake isotherms of BILP-15 and BILP-15-OR derivatives at 273 K (A) and 298 K (B).

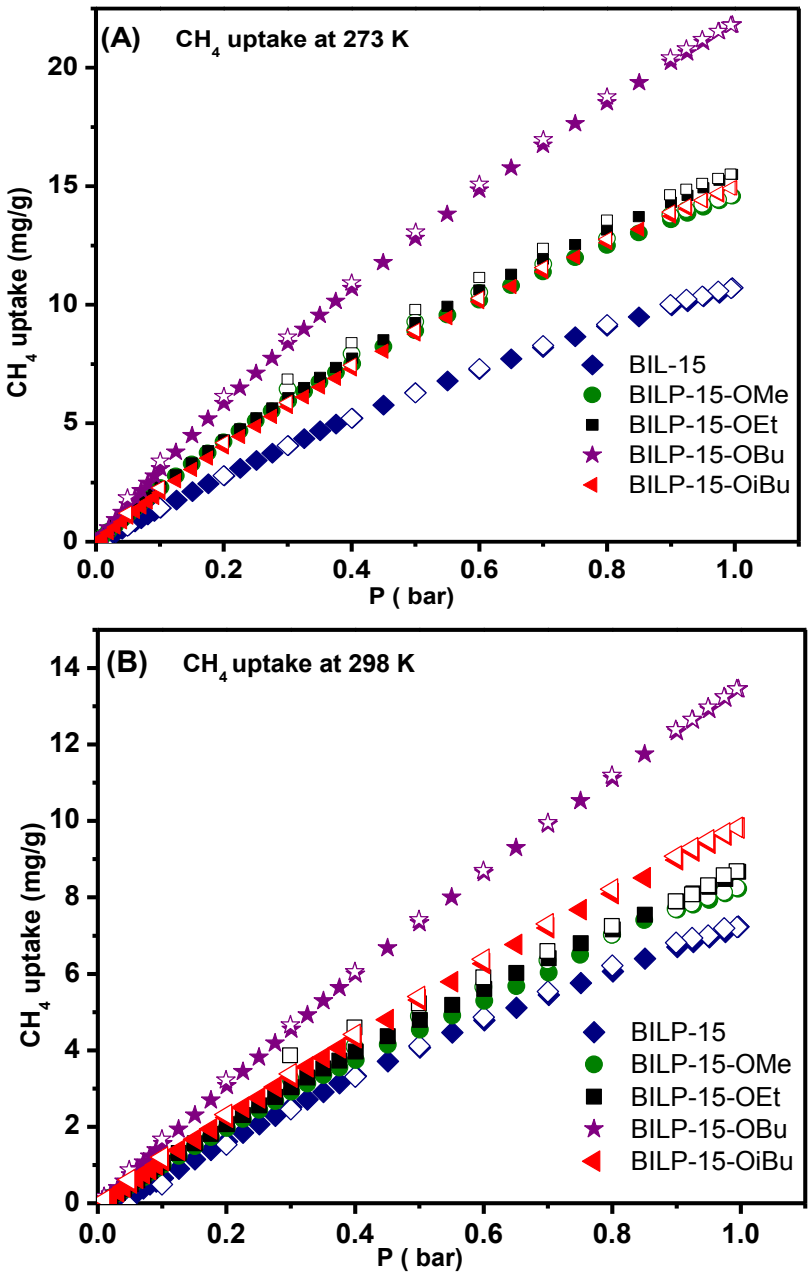

Figure 5.21B: CH_4 uptake isotherms of BILP-15 and BILP-15-OR derivatives (A) at 273 K and (B).298 K.

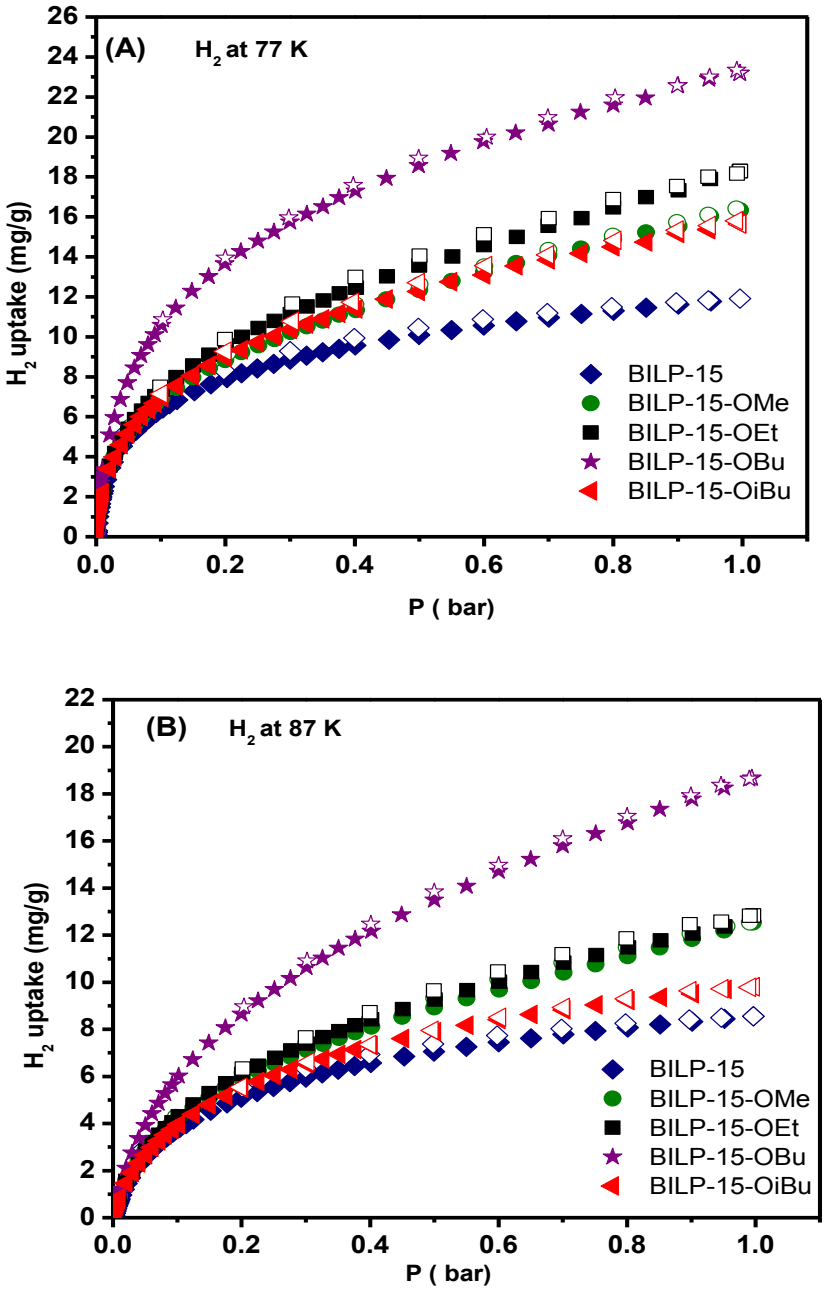

Figure 5.21C: H_2 uptake isotherms of BILP-15 and BILP-15-OR derivatives at 77 K (A) and 87 K (B).

The binding affinity for CO_2 was determined by calculating the isosteric heats of adsorption Q_{st} using the adsorption data collected at 273 K and 298 K for BILP-15-OR and compared to the Q_{st} of BILP-15. Heats of adsorption were calculated using the virial method, which revealed that the Q_{st} values at zero coverage fall relatively in a range of (29-33.5 kJ mol^{-1}) for BILP-15 and BILP-15-OMe, BILP-15-OBu, and BILP-15-iOBu. However, BILP-15-OEt has the highest Q_{st} value (37 kJ mol^{-1}) compared to the other polymers. The moderate Q_{st} value for BILP-15-OBu (31.0 kJ mol^{-1}) is expected to arise due to the high surface area and large pore size, which provides more accessible nitrogen sites in comparison with the other polymers. Moreover, the larger pore volume and higher surface area of BILP-15-OBu requires higher pressure settings to force the formation of multiple interaction sites for CO_2 compared to other BILP-15-OR derivatives. [59a, 64, 111]

The highest Q_{st} (37 kJ mol^{-1}) for BILP-15-OEt can be attributed to the high surface coverage and smallest pore size (4.9 Å). In contrast, BILP-15-iOBu has an unexpected Q_{st} value of (29.0 kJ mol^{-1}). This value does not correlate to the low surface area and small pore size of this polymer. It has been stated above that the presence of the branched -OiBu substituent is expected to fill the pores, reduce the number of the accessible nitrogen sites and reduce the surface area. Thus, the amount of CO_2 is limited to the surface coverage, which indicates that CO_2 evacuation from the surface can be performed rapidly, and simply at low pressure settings and without applying heat. In general, all Q_{st} values still indicate that CO_2 interactions after the incorporation of alkoxy groups are weak enough to allow for materials regeneration without applying heat.

Similar to BILP-14-OR derivatives, we also considered BILP-15-OR polymers for hydrogen and methane storage studies. Both gases are highly attractive candidates for use in automotive applications as a result of their abundance and clean nature. Moreover, CO_2 removal from flue

gas or methane-rich gases (e.g. natural gas and landfill gas) is needed to mitigate climate change and enhance the quality and energy density of methane-rich fuels.[3, 7] Accordingly, methane and hydrogen pure gas isotherms were collected under low pressure conditions and their heats of adsorption were calculated. Methane isotherms are completely reversible and exhibit a maximum uptake of 21.8 mg g^{-1} at 273 K for BILP-15-OBu, and the uptake range is (14.0-15.5 mg g^{-1}) for other BILP-15-OR derivatives. These values are within the range reported for BILPs. The Q_{st} for CH_4 was calculated using the adsorption data and resulted in high values for BILP-15-OMe and BILP-15-OEt, which can be attributed to the small pore volume and greater number of interaction sites for CH_4. On the other hand, the low Q_{st} value for BILP-15-OBu is related to the large pore volume and size, which provide more CH_4 interaction sites. The lowest Q_{st} value, belonging to BILP-15-iOBu, can be attributed to the presence of the branched -OiBu group, as stated above for the Q_{st} of CO_2.

To evaluate BILP-15-OR derivatives with regard to their hydrogen uptake and binding affinity, pure hydrogen isotherms were collected at 77 K and 87 K at 1 bar. The hydrogen uptake of the BILP-15-OR derivatives was within the range of all BILPs (1.5-2.3 wt%). The highest surface area polymer, BILP-15-OBu, has the highest uptake value (2.30 wt%), while the other polymers are in the range of (1.56- 1.82 wt%). The H_2 *Q*st values for BILP-15-OR derivatives are also consistent with Q_{st} values of all BILPs and higher than the value for BILP-15. The Q_{st} value for BILP-15 and BILP-15-OR is in the range of (7.9-8.7 kJ mol^{-1}). The highest Q_{st} value (7.8 kJ mol^{-1}) for BILP-15-OBu is due to the multiple interaction sites and high surface area. It is believed that the introduction of electron-donating groups or atoms on the aromatic structures improves hydrogen uptake and binding affinity. This result was observed in methoxy-modified

MOF-5, where the presence of methoxy groups appears to have a favorable effect on the low pressure H_2 uptake capability.[120b]

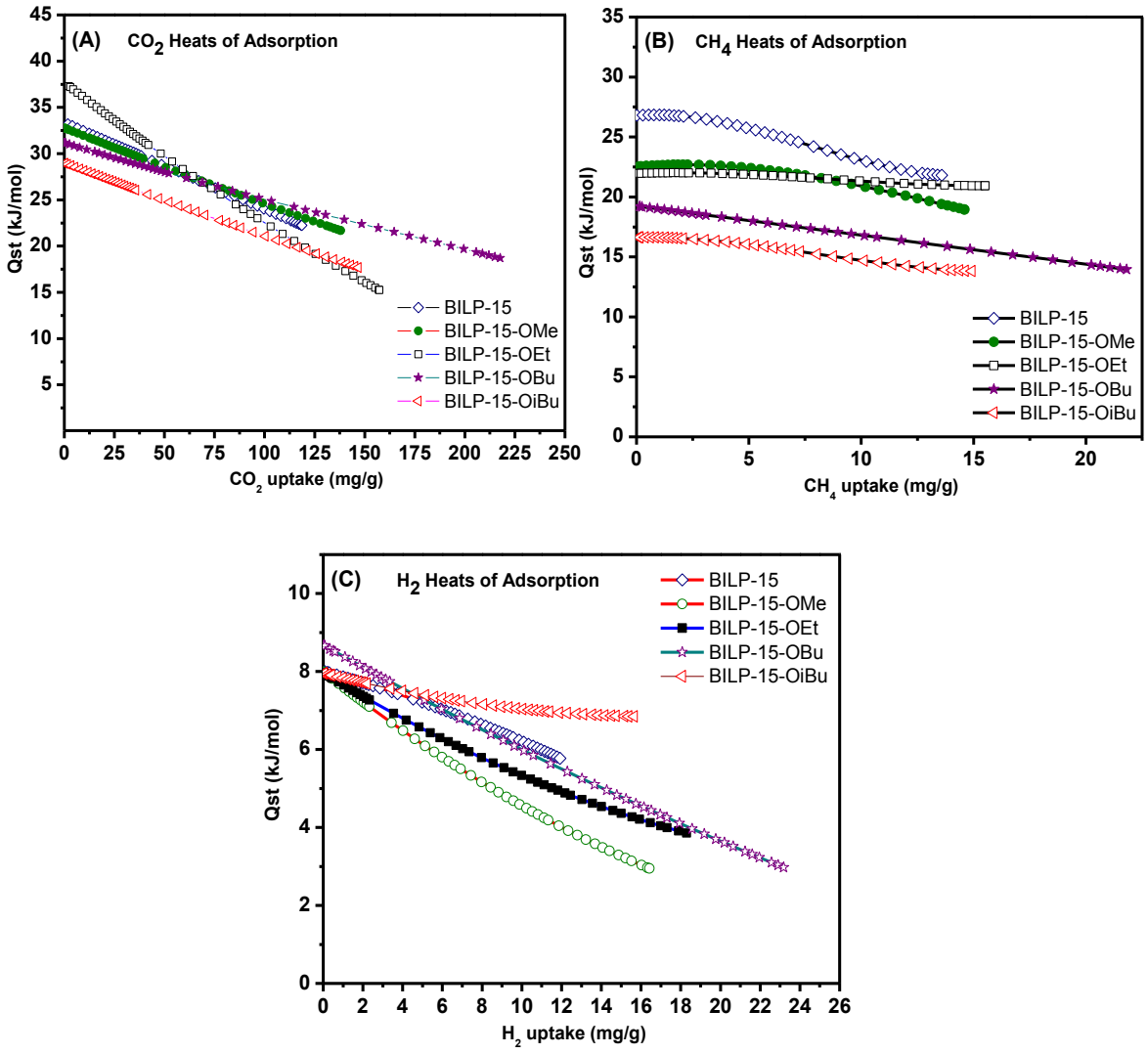

Figure 5.22: CO_2, CH_4 and H_2 isosteric heats of adsorption (Q_{st}) for BILP-15 and BILP-15-OR derivatives.

5.5.3 Gas Selectivity Studies

The preferential binding of BILP-15 to CO_2 over CH_4 and N_2 was calculated by using the initial slope calculations of pure gas isotherms collected at 273 K and 298 K. The CO_2/N_2 and CO_2/CH_4 selectivities at (273 K/298 K) were (83/63) and (10/9), respectively. Furthermore, the selectivity results at 298 K were validated by the ideal adsorbed solution theory (IAST), which predicts the adsorption selectivity for gas mixtures based on pure components gas isotherms.[97] The selectivities from IAST were calculated for gas mixture composition CO_2:N_2 (10:90) and CO_2:CH_4 (50:50) and resulted in selectivity values of 52, and 9 at 298 K, respectively, which are consistent with the initial slope results. Accordingly, these calculations were performed to evaluate the impact of the new incorporated alkoxy groups on the selectivity of BILP-15-OR derivatives and compared to BILP-15.

The selectivity data from both initial slope and IAST are summarized in Table 5.5. From the initial slope calculations at 273 K, notable changes in CO_2/N_2 selectivity values were observed for all polymers compared to BILP-15. The initial slope selectivities of CO_2/N_2 at 273 K for BILP-15, BILP-15-OMe, BILP-15-OEt, BILP-15-OBu, and BILP-15-iOBu are 83, 50, 39, 40, and 52, respectively. The dramatic decrease in the selectivity of these polymers when compared to BILP-15 is due to the improved surface area of BILP-15-OR derivatives. For example, the surface area of BILP-15-OBu has improved by 192 % and its selectivity decreased by 50% compared to BILP-15. This result shows that the incorporation of the -OBu group to BILP-15 has increased the porosity and compromised the selectivity. The selectivity of all other BILP-15-OR derivatives has decreased by 40-50% compared to BILP-15 due to the surface area improvement.

On the other hand, a significant decrease in the selectivity of CO_2/N_2 at 298 K was observed for BILP-15-OBu and BILP-15-iOBu, which can be attributed to the higher nitrogen uptake for these polymers at 298 K. The selectivity values for all polymers at 298 K are consistent for both methods and indicate that the alkoxy groups have significantly altered the gas selectivity at 298 K. In contrast, the selectivity for CO_2/CH_4 is lower than BILP-15 and falls in the range of 8-6. The low selectivity indicates that the CO_2/CH_4 separation process is more challenging than CO_2/N_2, which can be explained by the fact that the polarizability and adsorption potential of CH_4 is higher than N_2.

Table 5.5: Initial slope selectivity of BILP-15 and BILP-15-OR derivatives at 273 K (298 K), and the IAST selectivity of BILP-15 and BILP-15-OR derivatives at 298 K for the binary mixtures of (CO_2/N_2: 10:90) and (CO_2/CH_4: 50:50).

BILP	Selectivity			
	Initial slope at 273 K (298 K)		IAST at 298 K	
	CO_2/N_2	CO_2/CH_4	CO_2/N_2 (10:90)	CO_2/CH_4 (50:50)
BILP-15	83 (63)	10 (9)	55	9
BILP-15-OMe	50(50)	9 (7)	53	7
BILP-15-OEt	39(47)	7(7)	53	8
BILP-15-OBu	40(24)	7(6)	25	6
BILP-15-iOBu	52(20)	7(6)	20	6

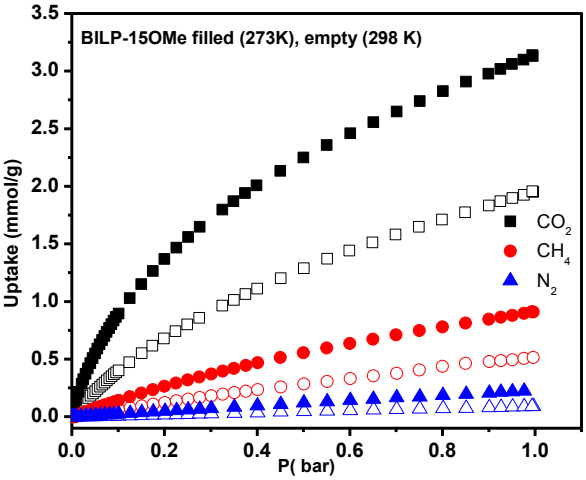
BILP-15OMe filled (273K), empty (298 K)
Uptake (mmol/g)
P(bar)
CO2
CH4
N2

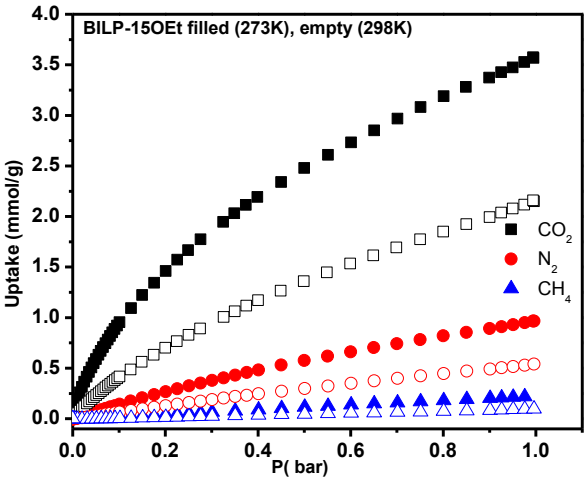
BILP-15OEt filled (273K), empty (298K)
Uptake (mmol/g)
P(bar)
CO2
N2
CH4

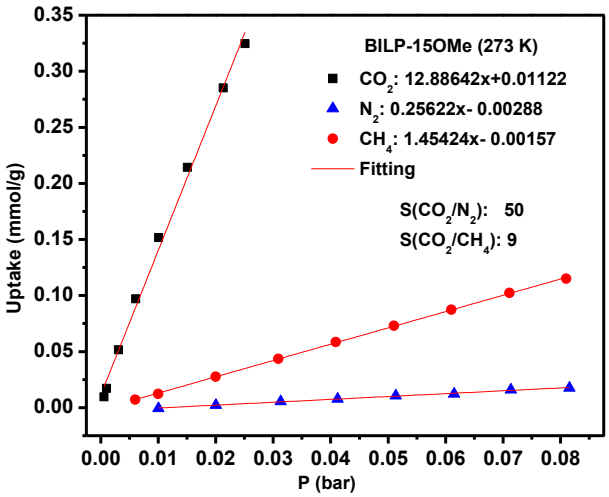
BILP-15OMe (273 K)
CO2: 12.88642x+0.01122
N2: 0.25622x- 0.00288
CH4: 1.45424x- 0.00157
Fitting
S(CO2/N2): 50
S(CO2/CH4): 9
Uptake (mmol/g)
P (bar)

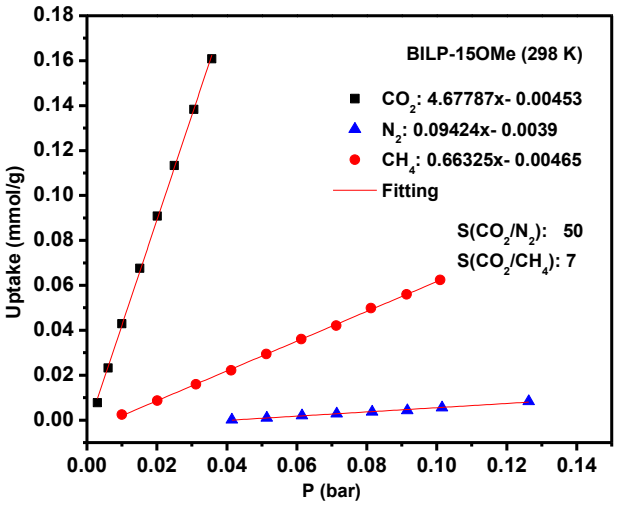
BILP-15OMe (298 K)
CO2: 4.67787x- 0.00453
N2: 0.09424x- 0.0039
CH4: 0.66325x- 0.00465
Fitting
S(CO2/N2): 50
S(CO2/CH4): 7
Uptake (mmol/g)
P (bar)

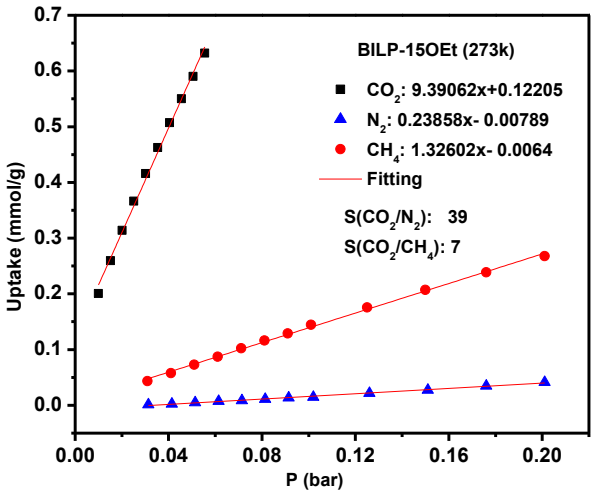
BILP-15OEt (273k)
CO2: 9.39062x+0.12205
N2: 0.23858x- 0.00789
CH4: 1.32602x- 0.0064
Fitting
S(CO2/N2): 39
S(CO2/CH4): 7
Uptake (mmol/g)
P (bar)

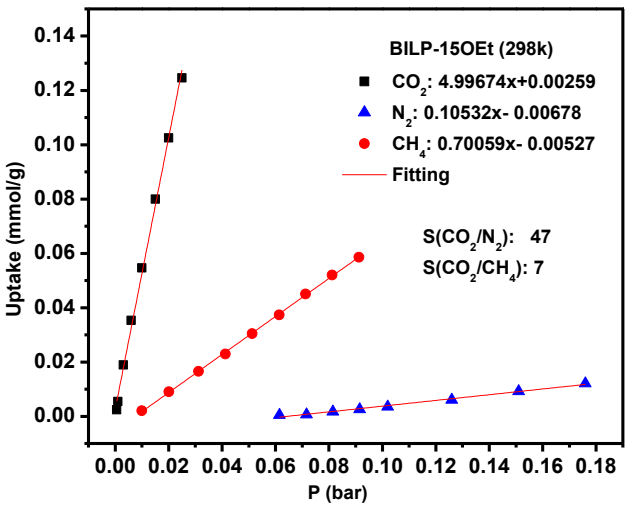
BILP-15OEt (298k)
CO2: 4.99674x+0.00259
N2: 0.10532x- 0.00678
CH4: 0.70059x- 0.00527
Fitting
S(CO2/N2): 47
S(CO2/CH4): 7
Uptake (mmol/g)
P (bar)

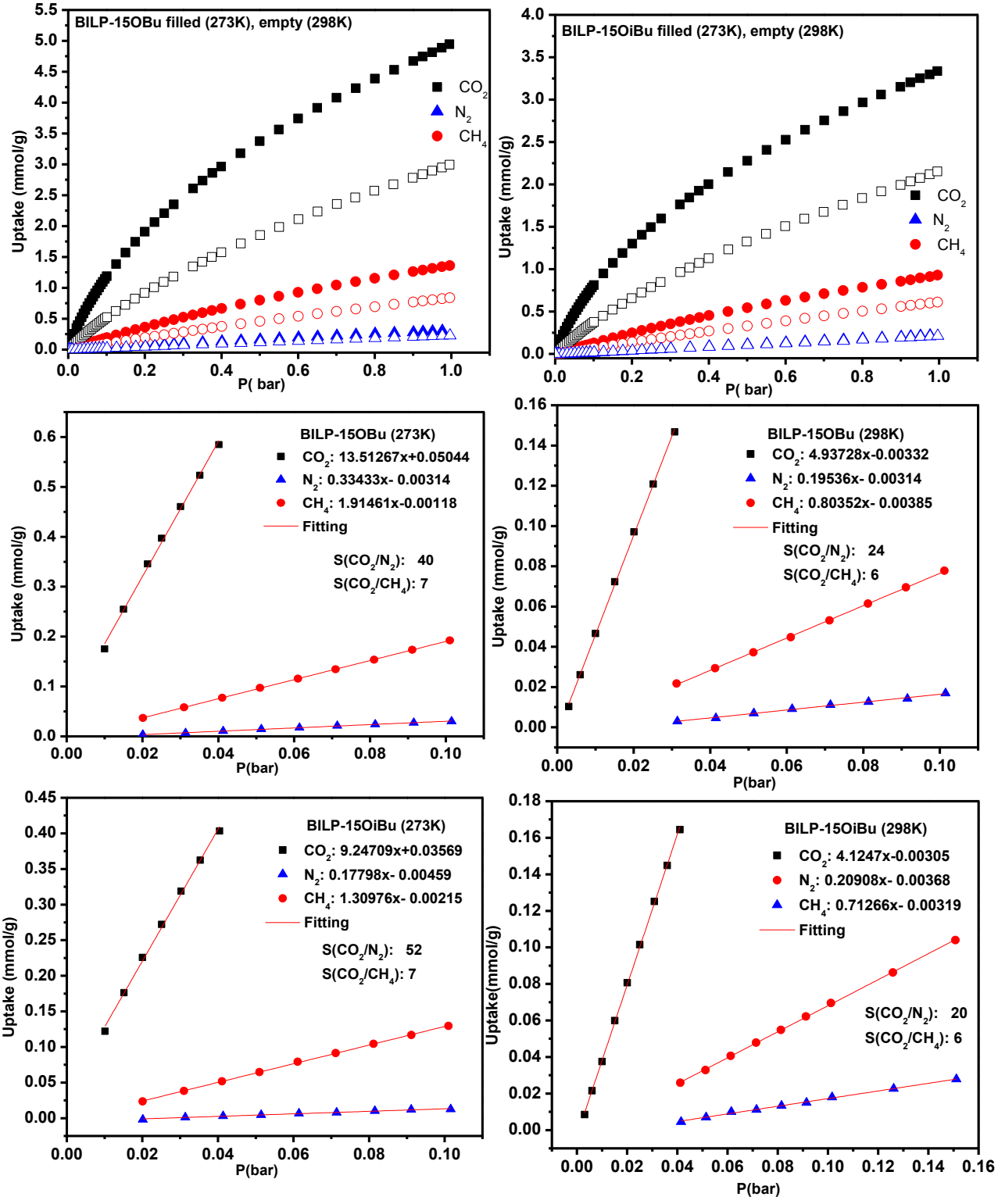

Figure 5.23: Gas sorption capacities for BILP-15 and BILP-15-OR derivatives and the adsorption selectivity of CO_2 over N_2 and CH_4 for from initial slope calculations.

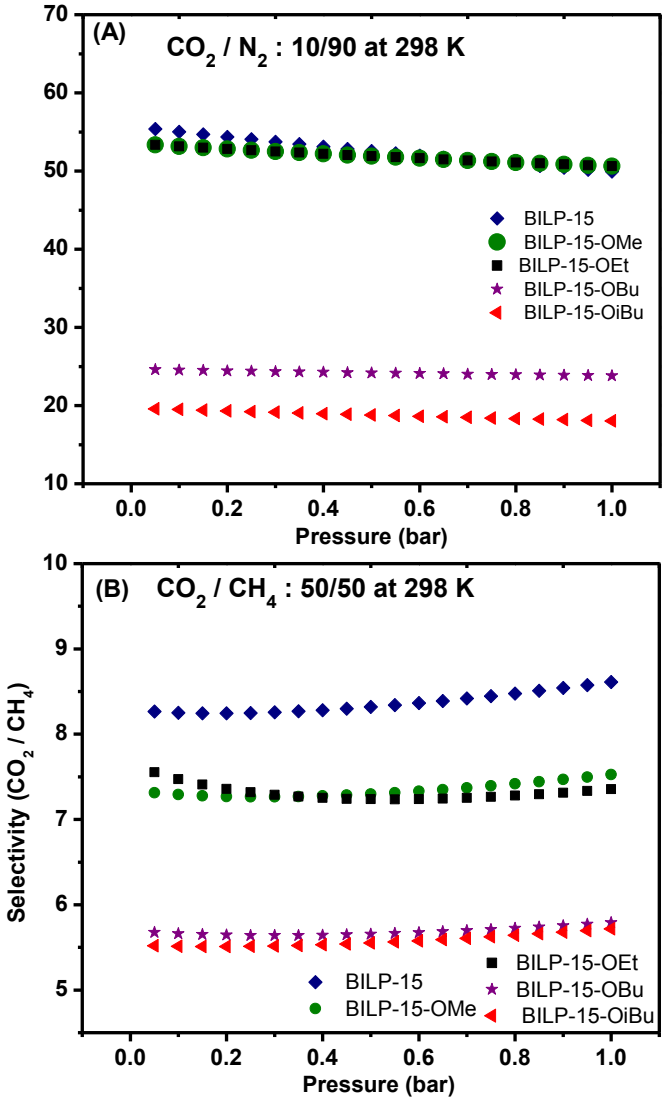

Figure 5.24: IAST selectivities of CO_2/ N_2 10/90 and CO_2/ CH_4 for 50/50 binary mixtures at 298 K for BILP-15 and BILP-15-OR derivatives.

Table 5.6: Gas Uptake and heats of adsorption data of BILP-15 and ILP-15OC derivatives

polymer	SA_{BET}[a]	Pore volume[b]	H_2 at 1 bar[c]			CO_2 at 1 bar[c]			CH_4 at 1 bar[c]			N_2 at 1 bar[c]	
			77 K	87 K	Q_{st}	273 K	298 K	Q_{st}	273 K	298 K	Q_{st}	273 K	298 k
BILP-15	**448**	0.27	12	8.5	8.0	118	80	33.5	11	7.2	26.5	5.7	2.4
BILP-15-OMe	**614**	0.36	16.4	12.5	8.0	138	86	33.0	14.6	8.2	23.0	6.3	2.4
BILP-15-OEt	**861**	0.49	18.2	12.8	7.9	157	95	37.0	15.5	8.7	22.0	6.3	2.7
BILP-15-OBu	**1311**	0.70	23.0	18.6	8.7	218	132	31.0	21.8	13.5	19.0	8.6	6.3
BILP-15-iOBu	**853**	0.45	15.6	9.8	7.9	147	95	29.0	14.9	9.8	17.0	6.0	6.0

[a]Surface area ($m^2\ g^{-1}$) was calculated from Ar isotherm. [b]Pore volume (cc g^{-1}) was calculated from single point measurements (P/P_0 = 0.95). [c]Gas uptake in mg g^{-1} and the isosteric enthalpies of adsorption (Q_{st}) in kJ mol^{-1}).

5.6 Conclusions

In conclusion, we have synthesized a series of alkoxy-functionalized BILPs and investigated their porosity and selective gas uptake. These polymers were synthesized by incorporating different pendant alkoxy-groups (-OMe, -OEt, -OBu and -OiBu) into BILP-14 and BILP-15. In BILP-14 derivatives, the alkoxy groups led to irregular surface area trends that varied according to the bulkiness and length of the alkyl substituent. In contrast, functionalization of BILP-15 with the same alkoxy-groups resulted in a systematic increase in surface area. This remarkable increase in the porosity is related to the presence of the bulky groups inside the pores, which most likely limits network interpenetration as a result of the flexible diamine linker. This was clearly observed for BILP-15-OBu that has a surface area double that of BILP-15.

According to gas uptake studies, the higher surface area polymers provide more interaction sites for gas molecules and increase the overall gas uptake. The highest CO_2/N_2 selectivity at 273 K and CO_2 binding affinity were reported for BILP-14-OEt. This polymer featured higher surface area and pore volume compared to BILP-14. Compared to all derivatives, BILP-14-OiBu and BILP-15-iOBu have shown low porosity and different thermal stability. However, all sorption measurements and selectivity calculations have shown that the inclusion of the pendant alkoxy functionalities plays a significant role in enhancing porosity.

Chapter 6: Conclusions

Carbon capture and sequestration (CCS) is the most widely used method for CO_2 separation from N_2, H_2, and CH_4 and includes both post-combustion and pre-combustion processes. The use of porous organic polymers (POPs) is one of the most promising proposed solutions for CO_2 capture due to their high porosity, thermal and mechanical stability, and heterogeneous functionality. Among POPs are benzimidazole-linked polymers (BILPs), which are promising candidates for CO_2 capture and separation applications due to their porosity, and nitrogen-containing functionality. To gain a greater understanding of the factors that affect the porosity, gas uptake and selectivity of BILPs, we have synthesized new BILPs that contain flexible, longer tetraamine building units. The use of the flexible linker was targeted at developing high porosity BILPs. However, the resulting BILPs have revealed the lowest porosity when compared to all reported BILPs. This result can be attributed to the flexible nature of the linkers, which enhances network interpenetration and lowers porosity. Thus, the main target of this study was to develop new synthetic strategies that can control network formation, improve the porosity, and enhance the sorption properties of new BILPs.

Our first strategy involved the synthesis of two new benzimidazole-linked polymers; BILP-14 and BILP-15. These polymers have shown that the use of long and flexible linkers in BILPs leads to low porosity as in the case of BILP-15. Accordingly, the first proposed solution to control the formation of the BILP-15 network was performed by re-synthesizing the polymer under the control of an acid-catalyzed process, wherein the acid plays the role of “catalyst” leading to controlled network growth. Interestingly, the acid-catalyzed BILP-15 has shown an

improved porosity (92%) compared to BILP-15. This result demonstrates the effectiveness of this synthetic approach in enhancing the porosity of organic polymers, which has many implications on their use in gas storage and separation applications. Moreover, we carried out a theoretical study by applying DFT calculations to explore the accessible CO_2 interaction sites with BILP-15 and BILP-14. The outcome of this study indicated that CO_2 binds to the imine-N of BILPs and that this binding is supplemented by another interaction with the C-H of the phenyl group. The binding affinities for CO_2 according to DFT calculations were very similar to those obtained from experimental studies.

Another adapted strategy was the use of "rational ligand design". This method enables the integration of new chemical functionality such as (-OR) into the pores of BILPs by modifying the organic linkers of BILP-14 and BILP-15 to alter their porosity and affinity for small gas molecules. The new functionalized polymers were synthesized by modifying the aryl-aldehyde building unit (TFPB) through the incorporation of pendant linear and branched alkoxy functional groups to generate BILP-14-OR and BILP-15-OR polymers. The impact of the substituent length on the porosity of the polymers was clearly observed in BILP-15-OR derivatives. For example, the incorporation of the butyl group (BILP-15-OBu) improved the porosity of BILP-15 by 192%. However, a random trend in porosity was noticed in the case of alkoxy-functionalized BILP-14 when compared to BILP-14. By applying this strategy, we have synthesized a series of BILP-14-OR and BILP-15-OR derivatives and studied the impact of the functionality on the gas uptake of the polymers. In all polymers, the acid-catalyzed and the functionalized polymers, we have investigated the preferential uptake of CO_2 over N_2 and CH_4 by applying selectivity calculations using the initial slope and IAST methods. Moreover, we have calculated the change in heats of adsorption for CO_2, H_2, and CH_4 upon pore decoration using the

virial method. Heats of adsorption are important for both gas storage and separation. We have found that BILPs have moderate CO_2 Qst values (28.0-35.0 kJ mol^{-1}), which are within the desired range for CO_2 capture from flue gas and methane-rich gases. Overall, the impact of the improved porosity of the acid-catalyzed BILPs, BILP-14-OR, and BILP-15-OR derivatives, on selectivity and heats of adsorption was very pronounced. In general, high surface area polymers exhibited lower selectivity and heats of adsorption.

To improve the porosity and binding affinity of BILPs for CO_2, we have synthesized new pyrazine-derived BILPs that feature π-conjugated cores. In addition to their porous nature, these polymers have novel electronic structures making them interesting for optical applications. The electronic properties of BILP-17 and BILP-18 were studied by photoluminescence studies, which have shown that BILP-17 and BILP-18 are semiconducting with bandgaps of (1.74-1.99 eV). As such, the high surface area, chemical nature, and semiconducting properties of pyrazine-derived BILPs make this class of polymers very promising for optoelectronics and sensing applications.

Overall, we have developed new and versatile synthetic strategies that enable new BILPs synthesis to improve gas uptake and separation properties. Future work in this area should focus on post-synthetic modification of alkoxy-functionalized BILPs to generate more hydrophobic pores (functionalization with -OH) to improve CO_2 capture. Initial attempts by –OR cleavage of BILP-14-OR and BILP-15-OR seem to be promising. However, the ability to prevent pore contraction/collapse is necessary to attain sufficient porosity levels that are essential for the use of BILPs in the areas and applications mentioned.

References

1. (a) Sumida, K.; Rogow, D. L.; Mason, J. A.; McDonald, T. M.; Bloch, E. D.; Herm, Z. R.; Bae, T. H.; Long, J. R., Carbon dioxide capture in metal-organic frameworks. *Chem. Rev.* **2012,** *112* (2), 724-81; (b) D'Alessandro, D. M.; Smit, B.; Long, J. R., Carbon dioxide capture: prospects for new materials. *Angew. Chem.* **2010,** *49* (35), 6058-82.

2. Li, J.-R.; Ma, Y.-G.; McCarthy, M. C.; Sculley, J.; Yu, J.-M.; Jeong, H.-K.; Balbuena, P. B.; Zhou, H.-C., Carbon dioxide capture-related gas adsorption and separation in metal-organic frameworks. *Coord. Chem. Rev.* **2011,** *255* (15-16), 1791-1823.

3. Makal, T. A.; Li, J.-R.; Lu, W.; Zhou, H.-C., Methane storage in advanced porous materials. *Chem. Soc. Rev.* **2012,** *41* (23), 7761-7779.

4. Dinca, M.; Dailly, A.; Tsay, C.; Long, J. R., Expanded sodalite-type metal-organic frameworks: increased stability and H(2) adsorption through ligand-directed catenation. *Inorg. chem.* **2008,** *47* (1), 11-3.

5. Dawson, R.; Cooper, A. I.; Adams, D. J., Nanoporous organic polymer networks. *Prog. Polym. Sci.* **2012,** *37* (4), 530-563.

6. Murray, L. J.; Dinca, M.; Long, J. R., Hydrogen storage in metal-organic frameworks. *Chem. Soc. Rev.* **2009,** *38* (5), 1294-1314.

7. Furukawa, H.; Yaghi, O. M., Storage of Hydrogen, Methane, and Carbon Dioxide in Highly Porous Covalent Organic Frameworks for Clean Energy Applications. *J. Am. Chem. Soc.* **2009,** *131* (25), 8875-8883.

8. Dinca, M.; Long, J. R., Strong H_2 Binding and Selective Gas Adsorption within the Microporous Coordination Solid $Mg_3(O_2C\text{-}C_{10}H_6\text{-}CO_2)_3$. *J. Am. Chem. Soc.* **2005,** *127* (26), 9376-9377.

9. Kustov, L. M.; Tarasov, A. L.; Sung, J.; Godovsky, D. Y., Hydrogen storage materials. *Mendeleev Commun.* **2014,** *24* (1), 1-8.

10. Yang, H.; Xu, Z.; Fan, M.; Gupta, R.; Slimane, R. B.; Bland, A. E.; Wright, I., Progress in carbon dioxide separation and capture: A review. *J. Environ. Sci.* **2008,** *20* (1), 14-27.

11. Drage, T. C.; Snape, C. E.; Stevens, L. A.; Wood, J.; Wang, J.; Cooper, A. I.; Dawson, R.; Guo, X.; Satterley, C.; Irons, R., Materials challenges for the development of solid sorbents for post-combustion carbon capture. *J. Mater. Chem.* **2012,** *22* (7), 2815-2823.

12. Dawson, R.; Stockel, E.; Holst, J. R.; Adams, D. J.; Cooper, A. I., Microporous organic polymers for carbon dioxide capture. *En. Environ.. Sci.* **2011,** *4* (10), 4239-4245.

13. (a) D'Alessandro, D. M.; Smit, B.; Long, J. R., Carbon Dioxide Capture: Prospects for New Materials. *Angew. Chem.-Int. Edit* **2010,** *49* (35), 6058-6082; (b) Drage, T. C.; Snape, C. E.; Stevens, L. A.; Wood, J.; Wang, J.; Cooper, A. I.; Dawson, R.; Guo, X.; Satterley, C.; Irons, R., Materials challenges for the development of solid sorbents for post-combustion carbon capture. *J. Mater. Chem.* **2012,** *22* (7), 2815-2823.

14. Álvarez, G.; Alcaide, F.; Miguel, O.; Cabot, P. L.; Martínez-Huerta, M. V.; Fierro, J. L. G., Electrochemical stability of carbon nanofibers in proton exchange membrane fuel cells. *Electrochimica Acta* **2011,** *56* (25), 9370-9377.

15. (a) Thomas, A., Functional Materials: from Hard to Soft Porous Frameworks. *Angew. Chem.-Int. Edit.* **2010,** *49* (45), 8328-8344; (b) Britt, D.; Furukawa, H.; Wang, B.; Glover, T. G.; Yaghi, O. M., Highly efficient separation of carbon dioxide by a metal-organic framework

replete with open metal sites. *Proc. Natl. Acad. Sci. U. S. A.* **2009,** *106* (49), 20637-20640; (c) Chen, L.; Lin, Y.; Kong, C. Carbon dioxide capture material, its preparation method and use. CN103285827A, 2013.

16. Dubois, L.; Thomas, D., CO_2 Absorption into Aqueous Solutions of Monoethanolamine, Methyldiethanolamine, Piperazine and their Blends. *Chem. Eng. Tech.* **2009,** *32* (5), 710-718.

17. Schroder, M.; Yang, S. Metal-organic frameworks (MOF) for gas capture. WO2013144628A1, 2013.

18. Liu, Y.; Wang, Z. U.; Zhou, H.-C., Recent advances in carbon dioxide capture with metal-organic frameworks. *Greenhouse Gases: Sci. Technol.* **2012,** *2* (4), 239-259.

19. Rochelle, G. T., Amine Scrubbing for CO_2 Capture. *Science (New York, N.Y.)* **2009,** *325* (5948), 1652-1654.

20. Sumida, K.; Rogow, D. L.; Mason, J. A.; McDonald, T. M.; Bloch, E. D.; Herm, Z. R.; Bae, T.-H.; Long, J. R., Carbon Dioxide Capture in Metal–Organic Frameworks. *Chem. rev.* **2011,** *112* (2), 724-781.

21. Cui, G.; Wang, C.; Zheng, J.; Guo, Y.; Luo, X.; Li, H., Highly efficient SO_2 capture by dual functionalized ionic liquids through a combination of chemical and physical absorption. *Chem. Commun. (Cambridge, U. K.)* **2012,** *48* (20), 2633-2635.

22. Cadena, C.; Anthony, J. L.; Shah, J. K.; Morrow, T. I.; Brennecke, J. F.; Maginn, E. J., Why is CO_2 so soluble in imidazolium-based ionic liquids? *J. Am. Chem. Soc.* **2004,** *126* (16), 5300-5308.

23. Cui, Y.; Cheng, Q.-Y.; Wu, H.; Wei, Z.; Han, B.-H., Graphene oxide-based benzimidazole-crosslinked networks for high-performance supercapacitors. *Nanoscale* **2013,** *5* (18), 8367-8374.

24. Figueroa, J. D.; Fout, T.; Plasynski, S.; McIlvried, H.; Srivastava, R. D., Advances in CO2 capture technology—The U.S. Department of Energy's Carbon Sequestration Program. *International Journal of Greenhouse Gas Control* **2008,** *2* (1), 9-20.

25. Berger, A. H.; Bhown, A. S., Comparing physisorption and chemisorption solid sorbents for use separating CO_2 from flue gas using temperature swing adsorption. *Energy Procedia* **2011,** *4* (0), 562-567.

26. Soboleva, T.; Zhao, X.; Malek, K.; Xie, Z.; Navessin, T.; Holdcroft, S., On the micro-, meso-, and macroporous structures of polymer electrolyte membrane fuel cell catalyst layers. *ACS applied materials & interfaces* **2010,** *2* (2), 375-84.

27. Jeromenok, J.; Weber, J., Restricted Access: On the Nature of Adsorption/Desorption Hysteresis in Amorphous, Microporous Polymeric Materials. *Langmuir : the ACS journal of surfaces and colloids* **2013,** *29* (42), 12982-12989.

28. Wang, S.; Peng, Y., Natural zeolites as effective adsorbents in water and wastewater treatment. *Chem. Eng. J. (Amsterdam, Neth.)* **2010,** *156* (1), 11-24.

29. Jahangiri, M.; Adl, J.; Shahtaheri, S. J.; Rashidi, A.; Ghorbanali, A.; Kakooe, H.; Forushani, A. R.; Ganjali, M. R., Preparation of a new adsorbent from activated carbon and carbon nanofiber (AC/CNF) for manufacturing organic-vacbpour respirator cartridge. *Ir.J. environ. hel. sci. eng.* **2013,** *10* (1), 15.

30. Furukawa, H.; Cordova, K. E.; O'Keeffe, M.; Yaghi, O. M., The Chemistry and Applications of Metal-Organic Frameworks. *Science (New York, N.Y.)* **2013,** *341* (6149).

31. Dawson, R.; Stockel, E.; Holst, J. R.; Adams, D. J.; Cooper, A. I., Microporous organic polymers for carbon dioxide capture. *E. & Environ. Sci.* **2011,** *4* (10), 4239-4245.

32. Wang, B.; Cote, A. P.; Furukawa, H.; O/'Keeffe, M.; Yaghi, O. M., Colossal cages in zeolitic imidazolate frameworks as selective carbon dioxide reservoirs. *Nature* **2008,** *453* (7192), 207-211.

33. Haszeldine, R. S., Carbon Capture and Storage: How Green Can Black Be? *Science (New York, N.Y.)* **2009,** *325* (5948), 1647-1652.

34. Yang, R. T.; Hernández-Maldonado, A. J.; Yang, F. H., Desulfurization of Transportation Fuels with Zeolites Under Ambient Conditions. *Science (New York, N.Y.)* **2003,** *301* (5629), 79-81.

35. Choi, S.; Drese, J. H.; Jones, C. W., Adsorbent materials for carbon dioxide capture from large anthropogenic point sources. *ChemSusChem* **2009,** *2* (9), 796-854.

36. Hauser, B. G. Metal Organic Frameworks and Microporous Polymers as Carbon Capture Materials: Effects of Functionality and Alkali Metal Cation Incorporation. 2012.

37. Yazaydin, A. O.; Benin, A. I.; Faheem, S. A.; Jakubczak, P.; Low, J. J.; Willis, R. R.; Snurr, R. Q., Enhanced CO2 Adsorption in Metal-Organic Frameworks via Occupation of Open-Metal Sites by Coordinated Water Molecules. *Chem. Mater.* **2009,** *21* (8), 1425-1430.

38. Maes, M.; Schouteden, S.; Hirai, K.; Furukawa, S.; Kitagawa, S.; De Vos, D. E., Liquid phase separation of polyaromatics on [$Cu_2(BDC)_2(dabco)$]. *Langmuir : the ACS journal of surfaces and colloids* **2011,** *27* (15), 9083-7.

39. Li, J.-R.; Ma, Y.; McCarthy, M. C.; Sculley, J.; Yu, J.; Jeong, H.-K.; Balbuena, P. B.; Zhou, H.-C., Carbon dioxide capture-related gas adsorption and separation in metal-organic frameworks. *Coord. Chem. Rev.* **2011,** *255* (15–16), 1791-1823.

40. Park, J.; Li, J.-R.; Chen, Y.-P.; Yu, J.; Yakovenko, A. A.; Wang, Z. U.; Sun, L.-B.; Balbuena, P. B.; Zhou, H.-C., A versatile metal-organic framework for carbon dioxide capture and cooperative catalysis. *Chem. commun.* **2012,** *48* (80), 9995-9997.

41. McKeown, N. B.; Budd, P. M., Exploitation of Intrinsic Microporosity in Polymer-Based Materials. *Macromolecules* **2010,** *43* (12), 5163-5176.

42. Budd, P. M.; Butler, A.; Selbie, J.; Mahmood, K.; McKeown, N. B.; Ghanem, B.; Msayib, K.; Book, D.; Walton, A., The potential of organic polymer-based hydrogen storage materials. *Phys. Chem. Chem. Phys.* **2007,** *9* (15), 1802-1808.

43. Chang, Z.; Zhang, D. S.; Chen, Q.; Bu, X. H., Microporous organic polymers for gas storage and separation applications. *Phys Chem Chem Phys* **2013,** *15* (15), 5430-42.

44. (a) Zhang, Y.; Riduan, S. N., Functional porous organic polymers for heterogeneous catalysis. *Chem. Soc. Rev.* **2012,** *41* (6), 2083-2094; (b) Ranocchiari, M.; Bokhoven, J. A. v., Catalysis by metal-organic frameworks: fundamentals and opportunities. *Phys. Chem. Chemical Physics* **2011,** *13* (14), 6388-6396.

45. Cote, A. P.; Benin, A. I.; Ockwig, N. W.; O'Keeffe, M.; Matzger, A. J.; Yaghi, O. M., Porous, crystalline, covalent organic frameworks. *Science (New York, N.Y.)* **2005,** *310* (5751), 1166-70.

46. (a) Webster, O. W.; Gentry, F. P.; Farlee, R. D.; Smart, B. E., Hypercrosslinked rigid-rod polymers. *Makromol. Chem., Macromol. Symp.* **1992,** *54/55* (Int. Symp. New Polym. React. React. Mech., 1991), 477-82; (b) Urban, C.; McCord, E. F.; Webster, O. W.; Abrams, L.; Long, H. W.; Gaede, H.; Tang, P.; Pines, A., 129Xe NMR Studies of Hyper-Cross-Linked Polyarylcarbinols: Rigid Versus Flexible Structures. *Chem. Mater.* **1995,** *7* (7), 1325-32.

47. Jiang, J.-X.; Su, F.; Trewin, A.; Wood, C. D.; Niu, H.; Jones, J. T. A.; Khimyak, Y. Z.; Cooper, A. I., Synthetic Control of the Pore Dimension and Surface Area in Conjugated Microporous Polymer and Copolymer Networks. *J. Am. Chem. Soc.* **2008,** *130* (24), 7710-7720.

48. McKeown, N. B.; Makhseed, S.; Budd, P. M., Phthalocyanine-based nanoporous network polymers. *Chem. Commun. (Cambridge, U. K.)* **2002,** (23), 2780-2781.

49. Budd, P. M.; Butler, A.; Selbie, J.; Mahmood, K.; McKeown, N. B.; Ghanem, B.; Msayib, K.; Book, D.; Walton, A., The potential of organic polymer-based hydrogen storage materials. *Phys Chem Chem Phys* **2007,** *9* (15), 1802-8.

50. El-Kaderi, H. M.; Hunt, J. R.; Mendoza-Cortes, J. L.; Cote, A. P.; Taylor, R. E.; O'Keeffe, M.; Yaghi, O. M., Designed synthesis of 3D covalent organic frameworks. *Science (New York, N.Y.)* **2007,** *316* (5822), 268-72.

51. Kahveci, Z.; Islamoglu, T.; Shar, G. A.; Ding, R.; El-Kaderi, H. M., Targeted synthesis of a mesoporous triptycene-derived covalent organic framework. *CrystEngComm* **2013,** *15* (8), 1524-1527.

52. (a) Furukawa, H.; Yaghi, O. M., Storage of hydrogen, methane, and carbon dioxide in highly porous covalent organic frameworks for clean energy applications. *J. Am. Chem. Soc.* **2009,** *131* (25), 8875-83; (b) Han, S. S.; Furukawa, H.; Yaghi, O. M.; Goddard, W. A., 3rd, Covalent organic frameworks as exceptional hydrogen storage materials. *J. Am. Chem. Soc.* **2008,** *130* (35), 11580-1.

53. (a) Xu, Y.; Jin, S.; Xu, H.; Nagai, A.; Jiang, D., Conjugated microporous polymers: design, synthesis and application. *Chem. Soc. Rev.* **2013,** *42* (20), 8012-8031; (b) Tsyurupa, M. P.; Davankov, V. A., Hypercrosslinked polymers: basic principle of preparing the new class of polymeric materials. *Reactive and Functional Polymers* **2002,** *53* (2–3), 193-203.

54. Chinchilla, R.; Najera, C., The Sonogashira reaction: a booming methodology in synthetic organic chemistry. *Chem. Rev. (Washington, DC, U. S.)* **2007,** *107* (3), 874-922.

55. Yuan, D.; Lu, W.; Zhao, D.; Zhou, H.-C., Highly Stable Porous Polymer Networks with Exceptionally High Gas-Uptake Capacities. *Advanced Materials* **2011,** *23* (32), 3723-3725.

56. Lu, W.; Yuan, D.; Sculley, J.; Zhao, D.; Krishna, R.; Zhou, H.-C., Sulfonate-Grafted Porous Polymer Networks for Preferential CO2 Adsorption at Low Pressure. *J. Am. Chem. Soc.* **2011,** *133* (45), 18126-18129.

57. Lu, W. G.; Sculley, J. P.; Yuan, D. Q.; Krishna, R.; Wei, Z. W.; Zhou, H. C., Polyamine-Tethered Porous Polymer Networks for Carbon Dioxide Capture from Flue Gas. *Angew. Chem.-Int. Edit.* **2012,** *51* (30), 7480-7484.

58. Keskin, S.; van Heest, T. M.; Sholl, D. S., Can Metal–Organic Framework Materials Play a Useful Role in Large-Scale Carbon Dioxide Separations? *ChemSusChem* **2010,** *3* (8), 879-891.

59. (a) Dawson, R.; Cooper, A. I.; Adams, D. J., Chemical functionalization strategies for carbon dioxide capture in microporous organic polymers. *Polymer International* **2013,** *62* (3), 345-352; (b) Yang, E.; Li, H.-Y.; Wang, F.; Yang, H.; Zhang, J., Enhancing CO_2 adsorption enthalpy and selectivity via amino functionalization of a tetrahedral framework material. *CrystEngComm* **2013,** *15* (4), 658-661.

60. Lim, H.; Cha, M. C.; Chang, J. Y., Synthesis of microporous polymers by Friedel-Crafts reaction of 1-bromoadamantane with aromatic compounds and their surface modification. *Polymer Chemistry* **2012,** *3* (4), 868-870.

61. Katsoulidis, A. P.; Kanatzidis, M. G., Phloroglucinol Based Microporous Polymeric Organic Frameworks with −OH Functional Groups and High CO_2 Capture Capacity. *Chem. Mater.* **2011,** *23* (7), 1818-1824.

62. Islamoglu, T.; Gulam Rabbani, M.; El-Kaderi, H. M., Impact of post-synthesis modification of nanoporous organic frameworks on small gas uptake and selective CO_2 capture. *J. Mater. Chem. A* **2013,** *1* (35), 10259-10266.

63. Ren, S.; Bojdys, M. J.; Dawson, R.; Laybourn, A.; Khimyak, Y. Z.; Adams, D. J.; Cooper, A. I., Porous, Fluorescent, Covalent Triazine-Based Frameworks Via Room-Temperature and Microwave-Assisted Synthesis. *Adv. Mater.* **2012,** *24* (17), 2357-2361.

64. Liebl, M. R.; Senker, J., Microporous Functionalized Triazine-Based Polyimides with High CO_2 Capture Capacity. *Chem. Mater.* **2013,** *25* (6), 970-980.

65. Ghanem, B. S.; Hashem, M.; Harris, K. D. M.; Msayib, K. J.; Xu, M.; Budd, P. M.; Chaukura, N.; Book, D.; Tedds, S.; Walton, A.; McKeown, N. B., Triptycene-Based Polymers of Intrinsic Microporosity: Organic Materials That Can Be Tailored for Gas Adsorption. *Macromolecules* **2010,** *43* (12), 5287-5294.

66. Chen, Q.; Luo, M.; Hammershøj, P.; Zhou, D.; Han, Y.; Laursen, B. W.; Yan, C.-G.; Han, B.-H., Microporous Polycarbazole with High Specific Surface Area for Gas Storage and Separation. *J. Am. Chem. Soc.* **2012,** *134* (14), 6084-6087.

67. (a) Rabbani, M. G.; Sekizkardes, A. K.; Kahveci, Z.; Reich, T. E.; Ding, R.; El-Kaderi, H. M., A 2D mesoporous imine-linked covalent organic framework for high pressure gas storage applications. *Chem. - Eur. J.* **2013,** *19* (10), 3324-3328; (b) Pandey, P.; Katsoulidis, A. P.; Eryazici, I.; Wu, Y.; Kanatzidis, M. G.; Nguyen, S. B. T., Imine-linked microporous polymer organic frameworks. *Chem. Mater.* **2010,** *22* (17), 4974-4979.

68. Arab, P.; Rabbani, M. G.; Sekizkardes, A. K.; Islamoglu, T.; El-Kaderi, H. M., Copper(I)-Catalyzed Synthesis of Nanoporous Azo-Linked Polymers: Impact of Textural Properties on Gas Storage and Selective Carbon Dioxide Capture. *Chem. Mater.* **2014,** *26* (3), 1385-1392.

69. (a) Rabbani, M. G.; Sekizkardes, A. K.; El-Kadri, O. M.; Kaafarani, B. R.; El-Kaderi, H. M., Pyrene-directed growth of nanoporous benzimidazole-linked nanofibers and their application to selective CO_2 capture and separation. *J. Mater. Chem.* **2012,** *22* (48), 25409-25417; (b) Rabbani, M. G.; Reich, T. E.; Kassab, R. M.; Jackson, K. T.; El-Kaderi, H. M., High CO2 uptake and selectivity by triptycene-derived benzimidazole-linked polymers. *Chem.commun.* **2012,** *48* (8), 1141-3; (c) Rabbani, M. G.; El-Kaderi, H. M., Synthesis and Characterization of Porous Benzimidazole-Linked Polymers and Their Performance in Small Gas Storage and Selective Uptake. *Chem. Mater.* **2012,** *24* (8), 1511-1517; (d) Rabbani, M. G.; El-Kaderi, H. M., Template-Free Synthesis of a Highly Porous Benzimidazole-Linked Polymer for CO2 Capture and H2 Storage. *Chem. Mater.* **2011,** *23* (7), 1650-1653; (e) Altarawneh, S.; Behera, S.; Jena, P.; El-Kaderi, H. M., New Insights into carbon dioxide interactions with benzimidazole-linked polymers. *Chem. commun.* **2014**.

70. (a) McKeown, N. B.; Budd, P. M., Polymers of intrinsic microporosity (PIMs): organic materials for membrane separations, heterogeneous catalysis and hydrogen storage. *Chem. Soci. Rev.* **2006,** *35* (8), 675-683; (b) Thomas, A.; Kuhn, P.; Weber, J.; Titirici, M.-M.; Antonietti, M., Porous Polymers: Enabling Solutions for Energy Applications. *Macromolecular Rapid Communications* **2009,** *30* (4-5), 221-236.

71. Weber, J.; Antonietti, M.; Thomas, A., Mesoporous Poly(benzimidazole) Networks via Solvent Mediated Templating of Hard Spheres. *Macromolecules* **2007,** *40* (4), 1299-1304.

72. (a) Weber, J., Nanostructured Poly(benzimidazole): From Mesoporous Networks to Nanofibers. *ChemSusChem* **2010,** *3* (2), 181-187; (b) von Graberg, T.; Thomas, A.; Greiner, A.; Antonietti, M.; Weber, J., Electrospun Silica—Polybenzimidazole Nanocomposite Fibers. *Macromolecular Materials and Engineering* **2008,** *293* (10), 815-819.

73. Yu, H.; Tian, M.; Shen, C.; Wang, Z., Facile preparation of porous polybenzimidazole networks and adsorption behavior of CO_2 gas, organic and water vapors. *Polymer Chemistry* **2013,** *4* (4), 961-968.

74. Bahrami, K.; Khodaei, M. M.; Kavianinia, I., A simple and efficient one-pot synthesis of 2-substituted benzimidazoles. *Synthesis* **2007,** (4), 547-550.

75. Lin, S.; Yang, L., A simple and efficient procedure for the synthesis of benzimidazoles using air as the oxidant. *Tetrahedron Letters* **2005,** *46* (25), 4315-4319.

76. (a) Fei, F.; Zhou, Z., New substituted benzimidazole derivatives: a patent review (2010 - 2012). *Expert Opin. Ther. Pat.* **2013,** *23* (9), 1157-1179; (b) Zhang, M.; Perry, Z.; Park, J.; Zhou, H.-C., Stable benzimidazole-incorporated porous polymer network for carbon capture with high efficiency and low cost. *Polymer* **2014,** *55* (1), 335-339.

77. Altarawneh, S.; Behera, S.; Jena, P.; El-Kaderi, H. M., New insights into carbon dioxide interactions with benzimidazole-linked polymers. *Chem. commun.* **2014,** *50* (27), 3571-3574.

78. Accelrys, Inc. Materials Studio 4.3 V; Accelrys Inc: San Diego, CA, 2003.

79. Xia, Y.-M.; You, J.; Yang, F.-K., Synthesis of 1,2-bisubstituted benzimidazole: 1,3-Shift mechanism catalyzed by acid or base. *J. Hetero. Chem.* **2011,** *48* (1), 230-236.

80. (a) Shekhah, O.; Wang, H.; Paradinas, M.; Ocal, C.; Schupbach, B.; Terfort, A.; Zacher, D.; Fischer, R. A.; Woll, C., Controlling interpenetration in metal-organic frameworks by liquid-phase epitaxy. *Nat Mater* **2009,** *8* (6), 481-484; (b) Farha, O. K.; Malliakas, C. D.; Kanatzidis, M. G.; Hupp, J. T., Control over Catenation in Metal−Organic Frameworks via Rational Design of the Organic Building Block. *J. Am. Chem. Soc.* **2009,** *132* (3), 950-952.

81. Nelson, A. P.; Farha, O. K.; Mulfort, K. L.; Hupp, J. T., Supercritical Processing as a Route to High Internal Surface Areas and Permanent Microporosity in Metal−Organic Framework Materials. *J. Am. Chem. Soc.* **2008,** *131* (2), 458-460.

82. Farha, O. K.; Mulfort, K. L.; Thorsness, A. M.; Hupp, J. T., Separating solids: purification of metal-organic framework materials. *J. Am. Chem. Soc.* **2008,** *130* (27), 8598-9.

83. Jiang, H.-L.; Makal, T. A.; Zhou, H.-C., Interpenetration control in metal–organic frameworks for functional applications. *Coord. Chem. Rev.* **2013,** *257* (15–16), 2232-2249.

84. (a) Batten, S. R.; Robson, R., Catenane and Rotaxane Motifs in Interpenetrating and Self-Penetrating Coordination Polymers. In *Molecular Catenanes, Rotaxanes and Knots*, Wiley-VCH Verlag GmbH: 2007; pp 77-106; (b) Batten, S. R.; Robson, R., Interpenetrating Nets: Ordered, Periodic Entanglement. *Angew. Chem.-Int. Edit.* **1998,** *37* (11), 1460-1494; (c) Blatov, V. A.; Carlucci, L.; Ciani, G.; Proserpio, D. M., Interpenetrating metal-organic and inorganic 3D networks: a computer-aided systematic investigation. Part I. Analysis of the Cambridge structural database. *CrystEngComm* **2004,** *6* (65), 378-395.

85. Zhang, J.; Wojtas, L.; Larsen, R. W.; Eddaoudi, M.; Zaworotko, M. J., Temperature and Concentration Control over Interpenetration in a Metal−Organic Material. *J. Am. Chem. Soc.* **2009,** *131* (47), 17040-17041.

86. Falkowski, J. M.; Wang, C.; Liu, S.; Lin, W., Actuation of Asymmetric Cyclopropanation Catalysts: Reversible Single-Crystal to Single-Crystal Reduction of Metal–Organic Frameworks. *Angew. Chem.-Int. Edit.* **2011,** *50* (37), 8674-8678.

87. (a) Roberts, J. M.; Farha, O. K.; Sarjeant, A. A.; Hupp, J. T.; Scheidt, K. A., Two Azolium Rings Are Better Than One: A Strategy for Controlling Catenation and Morphology in Zn and Cu Metal–Organic Frameworks. *Crystal Growth & Design* **2011,** *11* (11), 4747-4750; (b)

Eddaoudi, M.; Kim, J.; Rosi, N.; Vodak, D.; Wachter, J.; O'Keeffe, M.; Yaghi, O. M., Systematic design of pore size and functionality in isoreticular MOFs and their application in methane storage. *Science (Washington, DC, U. S.)* **2002,** *295* (5554), 469-472.

88. Eddaoudi, M.; Kim, J.; Rosi, N.; Vodak, D.; Wachter, J.; O'Keeffe, M.; Yaghi, O. M., Systematic Design of Pore Size and Functionality in Isoreticular MOFs and Their Application in Methane Storage. *Science (New York, N.Y.)* **2002,** *295* (5554), 469-472.

89. Ma, S.; Eckert, J.; Forster, P. M.; Yoon, J. W.; Hwang, Y. K.; Chang, J.-S.; Collier, C. D.; Parise, J. B.; Zhou, H.-C., Further Investigation of the Effect of Framework Catenation on Hydrogen Uptake in Metal−Organic Frameworks. *J. Am. Chem. Soc.* **2008,** *130* (47), 15896-15902.

90. Go, Y. B.; Wang, X.; Jacobson, A. J., (6,3)-Honeycomb Structures of Uranium(VI) Benzenedicarboxylate Derivatives: The Use of Noncovalent Interactions to Prevent Interpenetration. *Inorg. chem.* **2007,** *46* (16), 6594-6600.

91. Deshpande, R. K.; Minnaar, J. L.; Telfer, S. G., Thermolabile Groups in Metal–Organic Frameworks: Suppression of Network Interpenetration, Post-Synthetic Cavity Expansion, and Protection of Reactive Functional Groups. *Angew. Chem.-Int. Edit.* **2010,** *49* (27), 4598-4602.

92. Gadzikwa, T.; Zeng, B.-S.; Hupp, J. T.; Nguyen, S. T., Ligand-elaboration as a strategy for engendering structural diversity in porous metal-organic framework compounds. *Chem. commun.* **2008,** (31), 3672-3674.

93. (a) Tedds, S.; Walton, A.; Broom, D. P.; Book, D., Characterisation of porous hydrogen storage materials: carbons, zeolites, MOFs and PIMs. *Faraday Discussions* **2011,** *151* (0), 75-94; (b) Yanik, R., Calculations of isosteric heats of adsorption of neon and hydrogen adsorbed on charcoal in the temperature range 22–90 K. *Vacuum* **1996,** *47* (2), 205-207.

94. (a) Hurly, J. J.; Schmidt, J. W.; Gillis, K. A., Virial equation of state and ideal-gas heat capacities of pentafluoro-dimethyl ether. *Int J Thermophys* **1997,** *18* (1), 137-159; (b) Jagiello, J.; Bandosz, T. J.; Putyera, K.; Schwarz, J. A., Adsorption near Ambient Temperatures of Methane, Carbon Tetrafluoride, and Sulfur Hexafluoride on Commercial Activated Carbons. *J. Chem. Eng. Data* **1995,** *40* (6), 1288-1292.

95. An, J.; Geib, S. J.; Rosi, N. L., High and Selective CO_2 Uptake in a Cobalt Adeninate Metal−Organic Framework Exhibiting Pyrimidine- and Amino-Decorated Pores. *J. Am. Chem. Soc.* **2009,** *132* (1), 38-39.

96. Das, M. C.; Xu, H.; Xiang, S.; Zhang, Z.; Arman, H. D.; Qian, G.; Chen, B., A New Approach to Construct a Doubly Interpenetrated Microporous Metal–Organic Framework of Primitive Cubic Net for Highly Selective Sorption of Small Hydrocarbon Molecules. *Chem. – A Euro. J.* **2011,** *17* (28), 7817-7822.

97. Myers, A. L.; Prausnitz, J. M., Thermodynamics of mixed-gas adsorption. *AIChE Journal* **1965,** *11* (1), 121-127.

98. (a) Herm, Z. R.; Swisher, J. A.; Smit, B.; Krishna, R.; Long, J. R., Metal−Organic Frameworks as Adsorbents for Hydrogen Purification and Precombustion Carbon Dioxide Capture. *J. Am. Chem. Soc.* **2011,** *133* (15), 5664-5667; (b) Belmabkhout, Y.; Pirngruber, G.; Jolimaitre, E.; Methivier, A., A complete experimental approach for synthesis gas separation studies using static gravimetric and column breakthrough experiments. *Adsorption* **2007,** *13* (3-4), 341-349; (c) Belmabkhout, Y.; Sayari, A., Adsorption of CO2 from dry gases on MCM-41 silica at ambient temperature and high pressure. 2: Adsorption of CO_2/N_2, CO_2/CH_4 and CO_2/H_2 binary mixtures. *Chem. Eng. Sci.* **2009,** *64* (17), 3729-3735.

99. Yang, S.; Sun, J.; Ramirez-Cuesta, A. J.; Callear, S. K.; DavidWilliam, I. F.; Anderson, D. P.; Newby, R.; Blake, A. J.; Parker, J. E.; Tang, C. C.; Schröder, M., Selectivity and direct visualization of carbon dioxide and sulfur dioxide in a decorated porous host. *Nat Chem* **2012,** *4* (11), 887-894.

100. Kotha, S.; Kashinath, D.; Lahiri, K.; Sunoj, R. B., Synthesis of C3-symmetric nano-sized polyaromatic compounds by trimerization and Suzuki-Miyaura cross-coupling reactions. *Eur. J. Org. Chem.* **2004,** (19), 4003-4013.

101. Vosko, S. H.; Wilk, L.; Nusair, M., Accurate spin-dependent electron liquid correlation energies for local spin density calculations: a critical analysis. *Cana. J. Phys.* **1980,** *58* (8), 1200-1211.

102. Zhao, Y.; Truhlar, D., The M06 suite of density functionals for main group thermochemistry, thermochemical kinetics, noncovalent interactions, excited states, and transition elements: two new functionals and systematic testing of four M06-class functionals and 12 other functionals. *Theor Chem Account* **2008,** *120* (1-3), 215-241.

103. A primer in Density Functional Theory, ed. C. Fiolhais, F. Nogueira and M. Marques, Springer, Berlin, 2003

104. M. J. Frisch, G. N. Trucks and H. B. Schlegel, et al., Gaussian, Inc.,Wallingford, CT, 2009

105. McLean, A. D.; Chandler, G. S., Contracted Gaussian basis sets for molecular calculations. I. Second row atoms, Z=11–18. *J. Chem. Phy.* **1980,** *72* (10), 5639-5648.

106. Reed, A. E.; Weinstock, R. B.; Weinhold, F., Natural population analysis. *J. Chem. Phys.* **1985,** *83* (2), 735-746.

107. Vogiatzis, K. D.; Mavrandonakis, A.; Klopper, W.; Froudakis, G. E., Ab initio Study of the Interactions between CO_2 and N-Containing Organic Heterocycles. *ChemPhysChem* **2009,** *10* (2), 374-383.

108. Uribe-Romo, F. J.; Hunt, J. R.; Furukawa, H.; Klöck, C.; O'Keeffe, M.; Yaghi, O. M., A Crystalline Imine-Linked 3-D Porous Covalent Organic Framework. *J. Am. Chem. Soc.* **2009,** *131* (13), 4570-4571.

109. Ye, J.; Xu, X.-l., The recent progresses in the synthesis of benzimidazoles. *Zhejiang Huagong* **2012,** *43* (10), 21-24.

110. Dawson, R.; Cooper, A. I.; Adams, D. J., Nanoporous organic polymer networks. *Prog. Poly. Sci.* **2012,** *37* (4), 530-563.

111. Han, S. S.; Jung, D.-H.; Heo, J., Interpenetration of Metal Organic Frameworks for Carbon Dioxide Capture and Hydrogen Purification: Good or Bad? *J. Phys. Chem. C* **2012,** *117* (1), 71-77.

112. Gao, B.; Wang, M.; Cheng, Y.; Wang, L.; Jing, X.; Wang, F., Pyrazine-containing acene-type molecular ribbons with up to 16 rectilinearly arranged fused aromatic rings. *J. Am. Chem. Soc.* **2008,** *130* (26), 8297-306.

113. (a) Moustafa, R. M.; Degheili, J. A.; Patra, D.; Kaafarani, B. R., Synthesis and Detailed Photophysical Studies of Pyrene-Based Molecules Substituted with Extended Chains. *J. Phys. Chem. A* **2009,** *113* (7), 1235-1243; (b) Duncan, N. C.; Hay, B. P.; Hagaman, E. W.; Custelcean, R., Thermodynamic, kinetic, and structural factors in the synthesis of imine-linked dynamic covalent frameworks. *Tetrahedron* **2012,** *68* (1), 53-64.

114. (a) Tong, C.; Zhao, W.; Luo, J.; Mao, H.; Chen, W.; Chan, H. S. O.; Chi, C., Large-Size Linear and Star-Shaped Dihydropyrazine Fused Pyrazinacenes. *Org. lett.* **2012,** *14* (2), 494-497;

(b) More, S.; Bhosale, R.; Choudhary, S.; Mateo-Alonso, A., Versatile 2,7-Substituted Pyrene Synthons for the Synthesis of Pyrene-Fused Azaacenes. *Org. lett.* **2012,** *14* (16), 4170-4173; (c) Figueira-Duarte, T. M.; Müllen, K., Pyrene-Based Materials for Organic Electronics. *Chem. rev.* **2011,** *111* (11), 7260-7314.

115. Nowak, M.; Kauch, B.; Szperlich, P., Determination of energy band gap of nanocrystalline SbSI using diffuse reflectance spectroscopy. *Rev. Sci. Instru.* **2009,** *80* (4), 046107-046107-3.

116. (a) Meador, M. A.; Hart, H., Substituent effects on the photoisomerization of anthracenes to their 9,10-Dewar isomers. *J. Org. Chem.* **1989,** *54* (10), 2336-2341; (b) Sarlauskas, J., Polynitrobenzenes containing alkoxy and alkylenedioxy groups: potential HEMs and precursors of new energetic materials. *Cent. Eur. J. Energ. Mater.* **2010,** *7* (4), 313-324.

117. (a) Han, D.; Tong, X.; Zhao, Y., Synthesis and characterization of six-arm star polystyrene-block-poly (3-hexylthiophene) copolymer by combination of atom transfer radical polymerization and click reaction. *Journal of Polymer Science Part A: Polymer Chemistry* **2012,** *50* (20), 4198-4205; (b) Einsla, B. R.; McGrath, J. E., Synthesis and characterization of hydroxy-functionalized poly(Arylene ether sulfone)s and conversion to proton conducting membranes for fuel cells. *Prepr. Pap.-Am. Chem. Soc., Div. Fuel Chem* **2004,** *49* (2), 616.

118. Makal, T. A.; Wang, X.; Zhou, H.-C., Tuning the Moisture and Thermal Stability of Metal–Organic Frameworks through Incorporation of Pendant Hydrophobic Groups. *Crystal Growth & Design* **2013,** *13* (11), 4760-4768.

119. Tilford, R. W.; Mugavero, S. J.; Pellechia, P. J.; Lavigne, J. J., Tailoring Microporosity in Covalent Organic Frameworks. *Advanced Materials* **2008,** *20* (14), 2741-2746.

120. (a) Henke, S.; Schneemann, A.; Wütscher, A.; Fischer, R. A., Directing the Breathing Behavior of Pillared-Layered Metal–Organic Frameworks via a Systematic Library of

Functionalized Linkers Bearing Flexible Substituents. *J. Am. Chem. Soc.* **2012,** *134* (22), 9464-9474; (b) Yang, J.; Grzech, A.; Mulder, F. M.; Dingemans, T. J., Methoxy-Modified MOF-5: A MOF-5 Framework Prepared by a Mixed Ligand Approach. *Eur. J. Inorg. Chem.* **2013,** *2013* (13), 2336-2341.

121. Tousek, J.; Straka, M.; Sklenar, V.; Marek, R., Origin of the conformational modulation of the 13C NMR chemical shift of methoxy groups in aromatic natural compounds. *J. phys.chem. A* **2013,** *117* (3), 661-9.

122. Biswas, S.; Vanpoucke, D. E. P.; Verstraelen, T.; Vandichel, M.; Couck, S.; Leus, K.; Liu, Y.-Y.; Waroquier, M.; Van Speybroeck, V.; Denayer, J. F. M.; Van Der Voort, P., New Functionalized Metal–Organic Frameworks MIL-47-X (X = −Cl, −Br, $-CH_3$, $-CF_3$, −OH, $-OCH_3$): Synthesis, Characterization, and CO_2 Adsorption Properties. *J. Phys. Chem. C* **2013,** *117* (44), 22784-22796.

123. Henke, S.; Schneemann, A.; Fischer, R. A., Massive Anisotropic Thermal Expansion and Thermo-Responsive Breathing in Metal–Organic Frameworks Modulated by Linker Functionalization. *Adv. Func. Mater.* **2013,** *23* (48), 5990-5996.

124. Deshpande, R. K.; Waterhouse, G. I. N.; Jameson, G. B.; Telfer, S. G., Photolabile protecting groups in metal-organic frameworks: preventing interpenetration and masking functional groups. *Chem. Commun. (Cambridge, U. K.)* **2012,** *48* (10), 1574-1576.

Vita

Suha Saleem Al tarawneh

altarawnehss@vcu.edu, sus.ttu@gmail.com

Date and Place of Birth

February 04, 1979; Al Karak, Jordan

Academic Preparation:

Mutah University, Al Karak-Jordan Chemistry B.Sc., 2001

Mutah University, Al Karak-Jordan Chemistry M.Sc., 2004

Master Thesis : "Synthesis and Characterization of some Transition and Actinide Metal Complexes with Fluorinated Diketone Chelates"

Virginia Commonwealth University, Richmond, VA, USA Chemistry Ph.D., 2014

Professional Appointments:

2010 -Current: Sponsored Graduate student from Tafila Technical University, Tafila, Jordan, at Department of Chemistry, VCU, USA

2008 -2010 Teaching assistant, Chemistry Department, Tafila Technical University, Tafila, Jordan.

2004 -2008 High School Teaching Chemistry- Ministry of education, Jordan

Oral Presentations:

(1) **Suha Al-Tarawneh and Hani El-Kaderi*** "Proton-Conducting membranes Derived from highly porous benzimidazole-linked polymers"

Graduate student Research Poster Session October, 4th 2011

(2) **Suha Al-Tarawneh, Timur Islamoglu and Hani El-Kaderi* "**Acid Catalyzed Formation of Benzimidazole-Linked Polymers and its Impact on Porosity and Selective Gas Admission and Uptake"

Graduate student Research Poster Session October, 5th 2012

(3) **Suha Al-Tarawneh and Hani El-Kaderi*** "Impact of Pre-Functionalization Modification of Benzimidazole-Linked Polymers on the Porosity and Gas Admission and Uptake Graduate student Research Poster Session October, 7th 2013

Publications:

(1) Suha Altarawneh, S. Behera, Puru Jena and Hani M. El-Kaderi* "New insights into carbon dioxide interactions with benzimidazole-linked polymers" *Chem. Commun.***, 2014**, 50, 3571-3574

(2) Suha Altarawneh, Timur Islamoglu, and Hani M. El-Kaderi* "Acid-Catalyzed Formation of Benzimidazole-Linked Polymers: Impact on Porosity and Selective Gas Admission and Uptake" (*in preparation*)

(3) Suha Altarawneh, Limia Nahar, Indika U. Arachchige, Ala'a O. El-Ballouli; Kassem M. Hallal, Bilal R. Kaafarani, and Hani M. El-Kaderi*" Highly Porous and Photoluminescent Pyrazine-Derived Benzimidazole-Linked Polymers" (*Submitted*)

(4) Suha Altarawneh, Timur Islamoglu, Ali Kemal, and Hani M. El-Kaderi* "Alkoxy-Functionalized Benzimidazole-Linked Polymers and their impact of separation applications" (*in preparation*).